

Martin-Luther-Universität Halle-Wittenberg

Naturwissenschaftliche Fakultät II – Chemie, Physik und Mathematik

Institut für Chemie

Synthese und Biokompatibilitätsbewertungen neuartiger, biofunktioneller Polymere für die Medizintechnik

Dissertation

Eingereicht zur Erlangung des akademischen Grades

Doktor der Naturwissenschaften (Dr. rer. nat.)

vorgelegt von

Max Borgolte

geb. am 23.03.1992 in Holzminden

Datum der Verteidigung:

08. März 2023

Erstgutachter: Prof. Dr. René Csuk (Martin-Luther-Universität Halle-Wittenberg)

Zweitgutachter: Prof. Dr. Hans-Peter Deigner (Hochschule Furtwangen)

Drittgutachter: Prof. Dr. Jean-François Stumbe (Universität Haute-Alsace, France)

Die vorliegende Arbeit wurde von Juli 2017 bis August 2022 am Institut für Chemie im Bereich für Organische Chemie, an der Martin-Luther-Universität Halle-Wittenberg in der Arbeitsgruppe von Herrn Prof. Dr. René Csuk sowie am *Institute of Precision Medicine, Fakultät Medical and Life Sciences* an der Hochschule Furtwangen in der Arbeitsgruppe von Herrn Prof. Dr. Hans-Peter Daigner angefertigt. Die Dissertation wurde in kumulativer Form verfasst und die Ergebnisse wurden bereits in internationalen *peer-reviewed Journals* veröffentlicht.

Danksagung

Zuallererst möchte ich Herrn Prof. Hans-Peter Deigner für die Möglichkeit meiner Promotion in seiner Arbeitsgruppe danken, insbesondere auch für den fachlichen Input sowie für das entgegengebrachte Vertrauen und die Freiheiten, die meine Forschungsarbeiten betreffen, außerdem für die Unterstützung und Ermutigung zur Durchführung unzähliger Forschungs-ideen. Vielen Dank hierfür!

Mein weiterer Dank gilt Herrn Prof. Dr. René Csuk für die Übernahme der Betreuung meiner Arbeit seitens der MLU sowie für die hilfreichen Ratschläge zum Schreiben meiner Arbeit. Ferner gilt mein Dank Ihnen und den Mitgliedern Ihrer Arbeitsgruppe zur zwischenzeitlichen Übernahme unzähliger NMR Messungen an der MLU.

Mein Dank gilt ebenso der Arbeitsgruppe um Herrn Prof. Deigner an der Hochschule Furtwan-gen, insbesondere Herrn Oliver Riester, Frau Isabel Quint und Herrn Dr. Lars Kaiser für die vielen konstruktiven Diskussionen und Gespräche sowie den fachlichen Input hinsichtlich der biologischen Experimente. Herrn Oliver Riester danke ich für die Durchführung der Experi-mente zur antimikrobiellen Aktivität der Polymere sowie Frau Isabel Quint für die biochemische Charakterisierung des Kynurenins. Bedanken möchte ich mich ebenso bei den restlichen Mit-gliedern und ehemaligen Mitgliedern der Arbeitsgruppe für ihre Unterstützung.

Bedanken möchte ich mich ebenso bei Tereza Kacerova für die unvergessliche Zeit im Labor, ihre synthetischen Arbeiten, die Durchführung von NMR Messungen sowie die langen Gesprä-che und ihre Unterstützung, die zum Gelingen meiner Arbeit beigetragen haben.

Des Weiteren gilt mein Dank dem alten Team der MCAT GmbH, Herrn Prof. Magnus Schmidt, Dr. Josef Diebold, Dr. Yan Wang und Max Fesenmeyer insbesondere für die unvergessliche Zeit im Labor, die langen Kaffee- und Mittagspausen sowie den fachlichen Input rund um die chemische Synthese.

Inhaltsverzeichnis

Inhaltsverzeichnis	7
Abbildungsverzeichnis	9
Tabellenverzeichnis	11
Abkürzungsverzeichnis	13
1 Einleitung	15
1.1 Bakterielle Infektionen von Implantaten	15
1.1.1 Infektionsproblematik in der Endoprothetik	15
1.1.2 Biofilmbildung und das „Race to the Surface“	15
1.2 Kationische Polymere	17
1.2.1 Wirkmechanismus: Das Shai-Matsuzaki-Huang- (SMH-) Modell	17
1.2.2 Chitin und Chitosan	18
1.2.3 Biomedizinische Anwendungen von Chitosanderivaten	19
1.2.4 Wirkmechanismus: Antimikrobielle Aktivität des Chitosans	19
1.3 Click-Chemie	20
1.3.1 Huisgen 1,3-dipolare Cycloaddition	21
1.3.2 Antimikrobielle Aktivität von 1,2,3-Triazolyl-Clickameren	22
1.4 Beschichtungen von Implantaten	22
1.4.1 PEEK als Implantatmaterial	22
1.4.2 Polydimethacrylamid-co-methacryloylenzophenon Hydrogele	23
1.4.3 UV-induzierte C-H-Insertionsreaktion: Benzophenon Crosslinker	23
1.4.4 Reaktionsmechanismus: UV-induzierte C-H-Insertionsreaktion des Benzophenons	24
1.4.5 UV-induzierte Oberflächenreaktionen des PEEK	25
1.5 Biokompatibilitätsbewertungen nach DIN EN ISO 10993	26
1.5.1 Regulatorische Anforderungen	26
1.5.2 Bewertung der Zytotoxizität nach DIN EN ISO 10993-5	26
1.5.3 Bewertung des inflammatorischen Potentials nach DIN EN ISO 10993-11	27
1.6 Kynurenin als Biomarker für Abstoßungsreaktionen	27
1.6.1 Tryptophanmetabolismus und der Kynureninsignalweg	27
1.6.2 Kynurenin und Abstoßungsreaktionen von Transplantaten	29
1.6.3 Kynurenin und Abstoßungsreaktionen von Implantaten	29
1.6.4 Literaturbekannte Analysemethoden des L-Kynurenins	29
1.6.5 Kynurenin als Biokompatibilitätsmarker	30
2 Zielstellung	31
3 Forschungsergebnisse	33
3.1 GlcNAc-Benzophenon-Dimethacrylamid Copolymere	33
3.1.1 Chemische Synthese der Monomerbausteine und der Copolymere	34

3.1.2	Beschichtung von Oberflächen	36
3.1.3	Biokompatibilität	37
3.1.4	Antimikrobielle Aktivität	37
3.2	Benzophenon-modifizierte Chitosanderivate	38
3.2.1	Chemische Synthese und Beschichtung von Oberflächen	39
3.2.2	Antimikrobielle Aktivität	41
3.2.3	Zytotoxizität	42
3.2.4	Inflammatorisches Potential	44
3.3	Fluoreszent-markiertes L-Kynurenin	45
3.3.1	Synthesestrategie	45
3.3.2	Testentwicklung und Detektion von L-Kynurenin	46
4	Zusammenfassung	47
5	Literaturverzeichnis	49
Anhang		I
Publikationen		I
	P-1: Methacryloyl-GlcNAc Derivatives Copolymerized with Dimethacrylamide as a Novel Antibacterial and Biocompatible Coating	III
	P-2: Synthesis of a biocompatible benzophenone-substituted chitosan hydrogel as novel coating for PEEK with extraordinary strong antibacterial and anti-biofilm properties	V
	P-3: A Fluorescence-Based Competitive Antibody Binding Assay for Kynurenine, a Potential Biomarker of Kidney Transplant Failure	VII
Lebenslauf		IX
Publikationsliste		XI
	Erstautor	XI
	Co-Autor	XI
Erklärung über den Autorenanteil		XIII
Selbstständigkeitserklärung		XV

Abbildungsverzeichnis

Abbildung 1. Schematische Darstellung des <i>Race to the Surface</i> und des <i>Window of Opportunity</i> . Abbildung erstellt mit BioRender, basierend auf Colilla <i>et. al.</i> 2018. ²¹	16
Abbildung 2. Schematische Darstellung des SMH-Modells, Abbildung erstellt mit BioRender basierend auf Shai <i>et. al.</i> 2002. ⁴⁵	18
Abbildung 3. Chitosan (1), Chitin (2) sowie dessen Monomereinheiten Glucosamin (3) bzw. <i>N</i> -Acetylglucosamin (4)	18
Abbildung 4. Schematische Darstellung der thermisch induzierten Huisgen 1,3-dipolaren Cycloaddition ^{85,86} sowie die regioselektiven Varianten unter Cu(I)- ^{89,90} und Ru(II)-Katalyse. ^{91,92}	21
Abbildung 5. Angeregter Tripletzustand des Benzophenons (1 bzw. 1*) und daraus folgende, mögliche Reaktionen. Abbildung basierend auf Dormán <i>et. al.</i> 2016. ¹²⁵	24
Abbildung 6. Chemische Struktur des Polyetheretherketons (PEEK)	25
Abbildung 7. Signalweg des Tryptophan-Metabolismus mit nachgelagertem Kynurenin-Signalweg, deren Endprodukte die Quinolinsäure und Picolinsäure sind. Abbildung basierend auf Simon <i>et. al.</i> 2015. ¹⁸²	28
Abbildung 8. Schematische Übersicht über die synthetisierten Monomere sowie den daraus synthetisierten Polymeren, für eine genaue Übersicht über die Polymere vgl. auch Tabelle 1.	35
Abbildung 9. Reaktionsschema des Chitosans umgesetzt mit 4-Benzoylbenzoesäure in den in Tabelle 2 dargestellten stöchiometrischen Verhältnissen an EDC und 4-Benzylbenzoesäure.	39
Abbildung 10. Ergebnisse der Zytotoxizitätstests in verschiedenen Zellkulturen im Extrakt- und Kontakttest nach DIN EN ISO-10993-5. ¹⁵⁸	43

Tabellenverzeichnis

Tabelle 1. Übersicht über die synthetisierten GlcNAc-MBP-Dimethacrylamid Copolymere mit den jeweiligen stöchiometrischen Verhältnissen an eingesetzten Monomeren sowie die via $^1\text{H-NMR}$ tatsächlich gefundenen Einbauverhältnisse	35
Tabelle 2. Synthetisierte Benzophenon-Chitosan Derivate und deren Substitutionsgrad (ds), bestimmt mittels UV/Vis Spektroskopie.	39
Tabelle 3. Gemessene IC_{90} Werte, log-Werte für antimikrobielle Aktivität der damit beschichteten Oberflächen und die Biofilminhibierung der Oberflächen der unterschiedlich substituierten Benzophenon-Chitosan Derivate aus Tabelle 2.....	41

Abkürzungsverzeichnis

ADME	Absorption, Distribution, Metabolismus, Eliminierung
AFM	Rasterkraftmikroskopie
ALD	Atomlagenabscheidung
ATRP	<i>Atom Transfer Radical Polymerization</i>
BP	Benzophenon
CKD	<i>Chronic kidney disease</i>
CS	Chitosan
DIN	Deutsche Industrie-Norm
DMAm	Dimethacrylamid
DNA	Desoxyribonukleinsäure
ds	Substitutionsgrad
<i>E. coli</i>	<i>Escherichia coli</i>
EDC	1-Ethyl-3-(3-dimethylaminopropyl)carbodiimid
EDS	Energiedispersive Röntgenspektroskopie
ELISA	<i>Enzyme-linked Immunosorbent Assay</i>
EN	Europäische Norm
FDA	<i>Food and Drug Administration</i>
FDM	<i>Fused Deposition Modeling</i>
GlcNAc	N-Acetylglucosamin
GC	Gaschromatographie
HUVEC	<i>Human umbilical vein endothelial cells</i>
IDO	Indolamin-2,3-dioxygenase
IL	Interleukin
IR	Infrarot
ISO	<i>International Organization for Standardization</i>
LB	<i>Lysogeny broth</i>
LC	Flüssigchromatographie
LPS	Lipopolysaccharide
MBP	Methacryloylbenzophenon
MDPI	<i>Multidisciplinary Digital Publishing Institute</i>
MDR	<i>Medical Device Regulation</i>

mRNA	<i>Messenger-RNA</i>
MRSA	Methicillin-resistenter <i>Staphylococcus aureus</i>
MS	Massenspektrometrie
MTT	3-(4,5-Dimethylthiazol-2-yl)-2,5-diphenyltetrazoliumbromid
NHS	<i>N</i> -Hydroxysuccinimid
NMR	Kernspinresonanzspektroskopie
R _a	Mittenrauwert (arithmetisches Mittel)
RNA	Ribonukleinsäure
R _q	quadratische Rauheit (quadratisches Mittel)
<i>S. aureus</i>	<i>Staphylococcus aureus</i>
SEM	Rasterelektronenmikroskopie
SMH-Modell	Shai-Matsuzaki-Huang-Modell
TNF- α	Tumornekrosefaktor- α
<i>P. aeruginosa</i>	<i>Pseudomonas aeruginosa</i>
PEEK	Polyetheretherketon
PEG	Polyethylenglycol
PET	Polyethylenterephthalat
PETG	Polyethylenterephthalat-co-Glycol
PDMAm	Polydimethacrylamid
ppm	<i>parts per million</i>
UV	Ultraviolett
XPS	Röntgenphotoelektronenspektroskopie

1 Einleitung

1.1 Bakterielle Infektionen von Implantaten

Bakterielle Infektionen von Implantaten und Abstoßungsreaktionen von Implantaten sind ein weitverbreitetes Problem in der klinischen Praxis, insbesondere in der Implantationsmedizin.¹ Für Kniegelenke kommt es bei 1 - 2% aller Arthroplastiken zu einer Infektion mit anschließender Revision, bei Hüftgelenken kommt es bei 1% aller Arthroplastiken zu einer Infektion mit erforderlicher Revision.^{2,3} Am Beispiel von Arthroplastiken des Kniegelenks sind die häufigsten Austauschgründe mit 39,9% mechanische Lockerungen, gefolgt von Infektionen mit 27,4%, Instabilitäten 7,5%, Beschädigungen der Endoprothese 4,7% und in 4,5% der Fälle eine Arthrofibrose.⁴ Hierdurch ergibt sich ein adäquater Bedarf an Funktionalisierungen der Implantatoberfläche, insbesondere in Hinblick auf die Infektionsproblematik.

1.1.1 Infektionsproblematik in der Endoprothetik

Hauptsächliche Probleme bei einer Infektion von Implantaten entstehen durch eine bakterielle Biofilmbildung auf der Implantatoberfläche, woraufhin es zu einer signifikant gesteigerten Resistenz, respektive Abschirmung der Bakterien gegenüber äußeren Einflüssen, beispielsweise antibiotischen Verbindungen, kommt.^{1,5,6} Für bakterielle Infektionen von Implantaten mit anschließender Biofilmbildung sind sowohl gram-positive Erreger (Staphylococcaceae-Familie mit insbesondere *Staphylococcus aureus* und *Staphylococcus epidermis* sowie *Enterococcus faecalis*) als auch gram-negative Erreger (*Escherichia coli*, *Klebsiella pneumoniae*, *Pseudomonas aeruginosa*) verantwortlich.⁷

Bei einer Infektion mit anschließender Biofilmbildung wird der bakterielle Infektionsherd vom Immunsystem des Patienten abgekapselt, so dass keine adäquate Bekämpfung der Erreger erfolgen kann.⁸ Die Behandlung nach einer Infektion einer Endoprothese mit entsprechender Biofilmbildung beschränkt sich hier in der gegenwärtigen klinischen Praxis auf eine operative Entfernung des infizierten Implantats mitsamt umliegendem, infiziertem Gewebe, gefolgt von einer antibiotischen Therapie und der Implantation einer neuen Endoprothese.⁹⁻¹² Zusammen mit der steigenden Zahl an multiresistenten Erregern gegen in der Humanmedizin zugelassene Antibiotika handelt es sich hier um ein wachsendes Problem in der klinischen Praxis.¹³

1.1.2 Biofilmbildung und das „Race to the Surface“

Ein Knochenimplantat bzw. ein permanent implantierbares Material muss zelladhäsive Oberflächeneigenschaften für die körpereigene Zelladhäsion aufweisen, damit die Resorption des

Materials in das umliegende Körpergewebe sichergestellt ist. Durch diese Funktionalität bedingt kommt es als Nebeneffekt auch zu einer verbesserten bakteriellen Zelladhäsion auf der Implantatoberfläche. Hierdurch entsteht nach einem chirurgischen Eingriff ein Konkurrenzkampf zwischen den körpereigenen Zellen und potenziellen infektiösen Erregern in der Wunde zur Adhäsion an der Implantatoberfläche, welcher in der wissenschaftlichen Literatur als „*Race to the Surface*“ bezeichnet wird, vgl. auch Abbildung 1.^{14,15} Das kritische Zeitfenster, in der Literatur als „*Window of Opportunity*“ bezeichnet, welches entscheidend für die Zelladhäsion an ein implantiertes Biomaterial ist, beträgt 6 Stunden.¹⁶ Innerhalb dieses Zeitfensters entscheidet sich, ob es zu einer Verwachsung des Implantats im Körpergewebe oder zu einer Biofilmbildung kommt. Ein einzelnes Bakterium kann hier innerhalb von 24 Stunden einen vollständigen Biofilm ausbilden.¹⁶

Sobald sich nach einer bakteriellen Infektion auf der Implantatoberfläche ein Biofilm ausgebildet hat, kommt es zur Abkapselung des Implantats gegenüber dem umliegenden Gewebe und infolgedessen zu einer Abstoßungsreaktion. Diese hat letztlich, bedingt durch eine Entzündungsreaktion an der Grenzfläche des Implantats zum umliegenden Gewebe, eine Abstoßungsreaktion des Implantats zur Folge.¹⁷ Des Weiteren werden die pathogenen Erreger durch den Biofilm gegenüber einer antibiotischen Therapie und dem patienteneigenen Immunsystem abgekapselt, so dass keine effektive antibiotische Therapie oder eine effektive Immunreaktion des körpereigenen Immunsystems gegenüber den im Biofilm eingekapselten Erregern erfolgen kann.^{18,19}

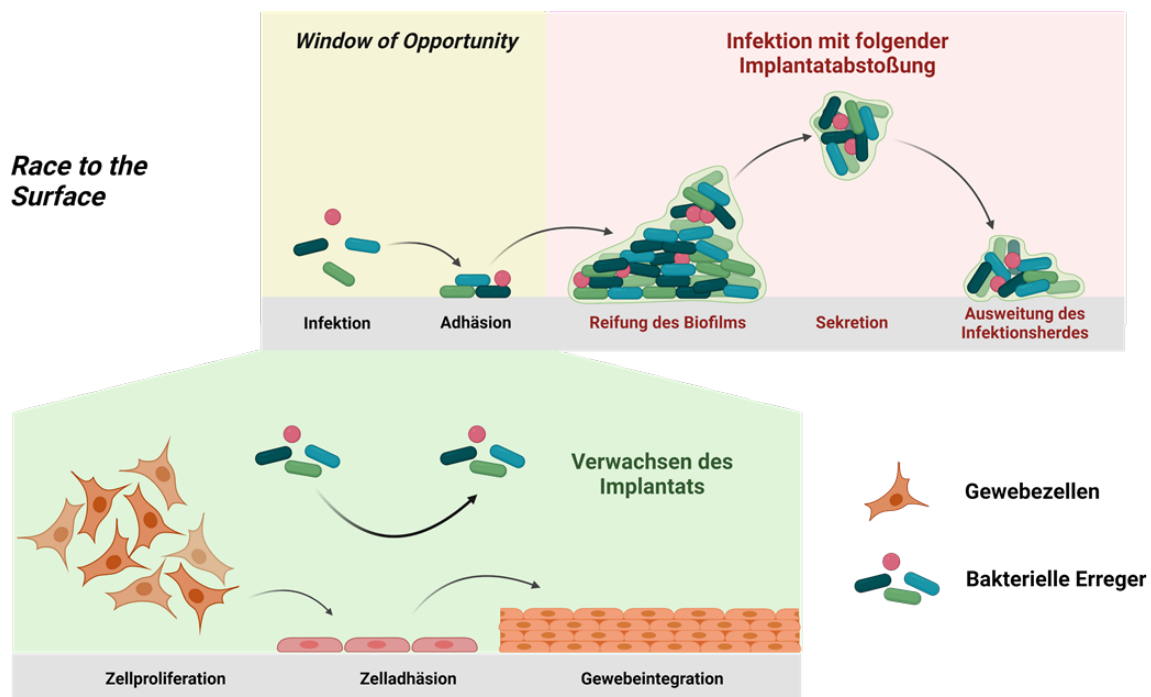


Abbildung 1. Schematische Darstellung des *Race to the Surface* und des *Window of Opportunity*. Abbildung erstellt mit BioRender, basierend auf Colilla *et. al.* 2018.²⁰

Üblicherweise wird zur Prävention einer bakteriellen Infektion eine antibiotische Behandlung zur Prophylaxe von Infektionen an den chirurgischen Eingriff angeschlossen, um das Risiko einer Implantatinfektion mit daraus folgender Biofilmbildung zu minimieren.²¹ Durch den verstärkten Einsatz von Antibiotika in der Humanmedizin besteht allerdings das Resistenzproblem von Mikroorganismen, so dass hier insbesondere durch multiresistente *S. aureus* Stämme eine gesteigerte Infektionsgefahr ausgeht.^{22,23} Hierdurch steigt die wissenschaftliche Relevanz von anderen Ansätzen zur Verhinderung der Infektion und Biofilmbildung von Implantatoberflächen. Ansätze hierfür sind beispielsweise antimikrobielle Modifikationen von Implantatoberflächen mittels antimikrobieller Verbindungen oder Polymere, welche eine bakterielle Infektion des Implantats verhindern und damit eine Biofilmbildung unterdrücken oder reduzieren.^{24,25}

1.2 Kationische Polymere

Ein Ansatz für antimikrobielle Beschichtungen sind antimikrobielle Polymere, welche zur weiteren Oberflächenmodifikation verwendet werden. Hierbei spielen insbesondere Polykationen eine Rolle, von denen die meisten eine quaternäre Ammonium- oder Alkylpyridiniumgruppe als funktionelle Gruppe beinhalten, welche in zahlreichen Artikeln und Reviews für ihre antimikrobiellen Eigenschaften beschrieben sind.^{26–31} Der Mechanismus dieser Polymere kann durch das sogenannte Shai-Matsuzaki-Huang Modell (SMH-Modell) beschrieben werden, welches einen Erklärungsansatz für die Wirkung antimikrobieller, kationischer Peptide liefert, vgl. auch Abschnitt 1.2.1.^{32–37} Die antibakterielle Aktivität von kationischen, polymeren Oberflächenbeschichtungen folgt hier einem ähnlichen Mechanismus,^{27,38–42} wobei einige Publikationen hier einfache *Monolayer* von kationischen Gruppen als antibakteriell beschreiben.⁴³ Die antibakterielle Aktivität folgt aus der Ladung der Oberfläche selbst, welche zu einer Zerstörung der Zellmembran führt, anstelle einer Insertion von kationischen Polymerbrushes in die Zellwand, wie sie durch das SMH-Modell vorhergesagt wird.²⁶ Aufgrund dieser verschiedenen Erklärungsansätze in der Literatur gibt es zurzeit noch keinen Konsens über einen Mechanismus der antibakteriellen Wirkung von kationischen Polymeren. Aufgrund der aktuellen Datenlage liegt hier allerdings eine Kombination beider Mechanismen in Abhängigkeit vom eigentlichen betrachteten Polymer nahe.

1.2.1 Wirkmechanismus: Das Shai-Matsuzaki-Huang- (SMH-) Modell

Der Wirkmechanismus von kationischen Polymeren wurde zuerst am Beispiel von antimikrobiellen, kationischen Peptiden, der Klasse der Magainin-Peptide, von Shai, Matsuzaki und Huang beschrieben.^{35–37} Hierbei kommt es zu einer parallelen Anlagerung^{36,37,44} (vgl. Abbildung 2) der kationischen Peptide an die Zellmembran, welche aus anionischen und zwitterionischen Kopfgruppen besteht. Durch die Zugspannung, die durch daraus folgender Insertion

des Peptides in die Membran entsteht, kommt es zu einer Disruption der Membran und damit zu einer Porenbildung oder zu einer Zerstörung mit Auflösung der Membran.³⁵ Der exakte Mechanismus der Einlagerung selbst ist hier allerdings von den genauen Eigenschaften, insbesondere dem pK_a -Wert des Peptids, der Kettenlänge und der Aminosäuresequenz sowie möglichen Seitenketten des Peptids abhängig.^{44,45}

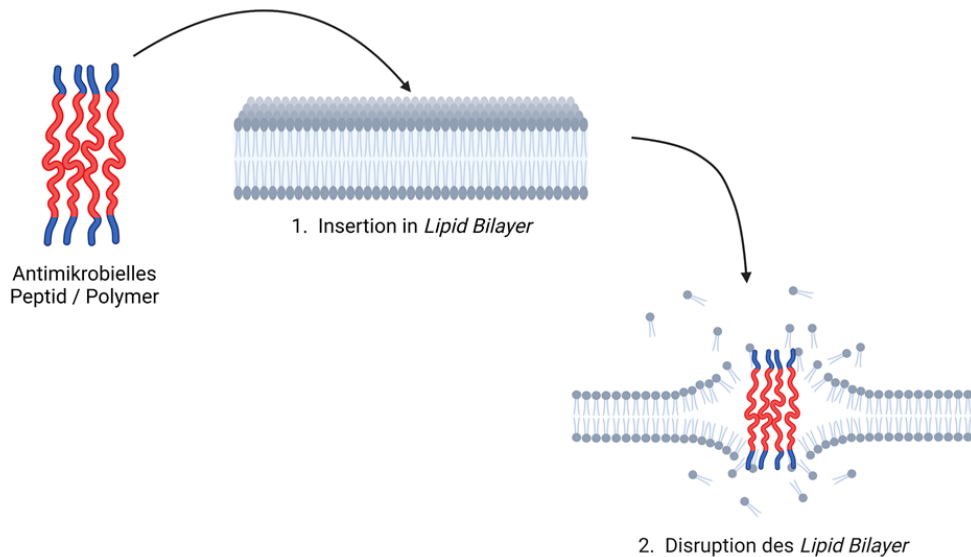


Abbildung 2. Schematische Darstellung des SMH-Modells, Abbildung erstellt mit BioRender basierend auf Shai *et. al.* 2002.⁴⁴

1.2.2 Chitin und Chitosan

Ein Vertreter der Klasse der antimikrobiellen, kationischen Polymere stellt das Chitosan dar, das deacetylierte Derivat des Chitins (vgl. Abbildung 3). Hierbei handelt es sich um ein β -D-(1 \rightarrow 4) vernetztes Polymer des Glucosamins (**3**), respektive des *N*-Acetylglucosamins (**4**). Definitionsgemäß liegt bei mehr als 50% *N*-Acetylglucosamingehalt Chitin vor, während bei Überwiegen des Glucosamins von Chitosan ausgegangen wird.^{46,47} Üblicherweise liegt in Chitosan 60 – 80% *N*-Acetylglucosamin vor, wobei komplett deacetylierte Chitosanpolymere in der Literatur beschrieben sind.⁴⁷

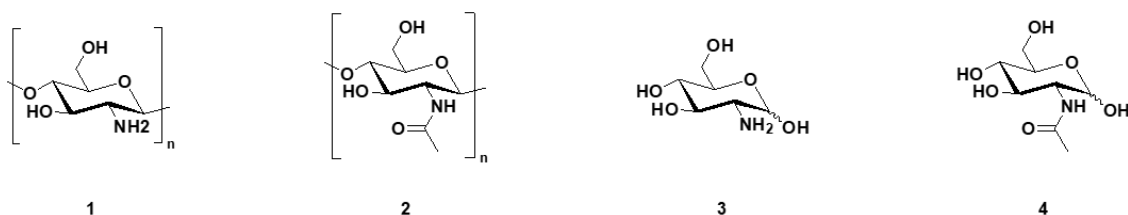


Abbildung 3. Chitosan (**1**), Chitin (**2**) sowie dessen Monomereinheiten Glucosamin (**3**) bzw. *N*-Acetylglucosamin (**4**).

Aufgrund seiner antimikrobiellen Aktivität sind in der Literatur zahlreiche Modifikationen für biomedizinische Anwendungen des Chitosans beschrieben, insbesondere für das *Tissue Engineering* von Knochengewebe,^{48–50} Einkapselung von Stammzellen^{51–53} und Hydrogele für Wundbehandlungen und Wundabdeckungen,^{54,55} um ein paar Beispiele aufzuführen. Da Chitosan nur in sauren, wässrigen Medien, in der Literatur wird üblicherweise 1%ige Essigsäure verwendet,^{56–58} löslich ist und vergleichsweise schlechte mechanische Eigenschaften und Hitzebeständigkeit aufweist,⁵⁹ sind hier chemische Modifikationen des Chitosans essenziell für weitere medizinische Anwendungen.

Durch seine funktionellen Gruppen bedingt liefert Chitosan allerdings gleichzeitig interessante, chemische Anknüpfungspunkte, über welche chemische Modifikationen und spezifische Funktionalisierungen zur Verbesserung der Handhabbarkeit und zur Erweiterung der Funktionalität des Chitosans erfolgen können, beispielsweise für Oberflächenbeschichtungen von Implantatoberflächen.

1.2.3 Biomedizinische Anwendungen von Chitosanderivaten

Bedingt durch die kationischen Eigenschaften des Chitosans, welche zu elektrostatischen Wechselwirkungen mit verschiedenen Gewebetypen führen, weist Chitosan, neben seiner antimikrobiellen Aktivität, mucoadhäsive Eigenschaften auf, was es zu einem interessanten Material zur Zelladhäsion macht.⁶⁰ Beispielsweise wurde thioliertes Chitosan, welches aufgrund der freien Thiole in seinen mucoadhäsiven Eigenschaften noch verstärkt wurde, für orale Anwendungen im Bereich der Dentalmedizin vorgeschlagen. Hierbei kommt es, aufgrund der antimikrobiellen Aktivität, zu einer Verringerung von Karies im Dentalbereich, während keine Toxizität gegenüber menschlichen Zelllinien messbar war.⁶¹ Analog wurde ebenso die Biofilmbildung von *Actinobacillus pleuromoniae* am Beispiel eines weiteren, spezifischen Erregers reduziert.⁶² Weitere Beispiele finden sich in Chitosan-*N*-Halamin Konjugaten, welche für Hämostatika vorgeschlagen wurden. Hier wurden verschiedene *N*-Halamin-Funktionalitäten in Chitosan eingeführt, welche einerseits durch Adhäsion an Thrombozyten die Blutgerinnung triggerten und gleichzeitig antimikrobielle Eigenschaften bis zu 7 log-Stufen gegenüber mikrobieller Kontamination aufwiesen.⁶³

1.2.4 Wirkmechanismus: Antimikrobielle Aktivität des Chitosans

Chitosan weist einen pK_a -Wert zwischen 6,17 und 6,51 in Abhängigkeit der Kettenlänge und des Deacetylierungsgrades auf.^{56,57,64} Dies führt dazu, dass unter physiologischen Bedingungen - bei einem pH-Wert von 7,4 - die freie Aminogruppe am C2 des Glucosamins protoniert vorliegt,⁶⁵ wodurch es sich beim Chitosan unter physiologischen Bedingungen um ein Polykation handelt. Aufgrund dieser kationischen Eigenschaften kann Chitosan die äußere und innere

bakterielle Zellwand durchdringen und in seiner Bilayer-Struktur stören.^{66–69} Dieser Mechanismus folgt aus der Wechselwirkung mit den negativ geladenen Phosphorcholin-Gruppen an der Oberfläche der bakteriellen Zellwand, was einen dem SMH-Modell ähnlichen, antibakteriellen Wirkmechanismus des Chitosans nahelegt.^{33,34} Hinweise auf einen solchen Wirkmechanismus wurden von Li et. al. 2010 geliefert. Hier kam es bei *E. coli* nach Behandlung mit Chitosan zu einer teilweisen Zellauflösung und Lyse aufgrund einer zerstörten Zellmembran, was mittels elektronenmikroskopischer Aufnahmen gezeigt wurde.⁷⁰ Dieser Mechanismus wurde weiterhin am Beispiel von *S. epidermis* auf einer Chitosanbeschichtung demonstriert, wobei es ebenfalls zur Lyse und daraus resultierend zur Freisetzung des Cytosols mit anschließendem Zelltod kam.⁷¹

Als ein potenziell zweiter Wirkmechanismus wurde die Bindung von Chitosan nach Internalisierung in das Cytosol an die DNA vorgeschlagen, gefolgt von einer gehemmten mRNA-Synthese und damit einer Inhibierung des bakteriellen Wachstums.⁷² Dies folgt im Wesentlichen den Erklärungsansätzen des SMH-Modells, nur dass es neben der Bindung an die negativ geladenen Phosphorcholin-Gruppen der Zellmembran noch zu einer Bindung an die negativ geladene Phosphat-Kette der DNA kommt. Dieses Modell wurde für kurzkettige Chitosanmoleküle vorgeschlagen, welche die Zellmembran durchdringen können. Diese Einlagerung in das Cytosol wurde am Beispiel von *E. coli* mit Fluorescein-modifiziertem Chitosan gezeigt; hierbei kam es zu einer Anreicherung des Chitosans innerhalb der Zelle.⁷³

Ein dritter, in der Literatur vorgeschlagener Wirkmechanismus basiert auf der Fähigkeit des Chitosans, Chelatkomplexe mit Metallionen auszubilden.⁷⁴ Aufgrund dieser Chelatoraktivität gegenüber freien Ca^{2+} und Mg^{2+} Ionen, welche in der bakteriellen Zellwand in erhöhten Konzentrationen vorkommen, kann es durch deren Komplexbildung zu einer verringerten Enzymaktivität in der Zellwand kommen. Dies führt zu einer Störung des Aufbaus der bakteriellen Zellwand, was in einer bakteriellen Wachstumsinhibierung und damit in einer antibiotischen Wirkung resultiert.^{66,75–78}

In allen vorgeschlagenen Mechanismen werden, sobald es zum Kontakt mit Chitosan oder Chitosanoberflächen kommt, Bakterien in ihrem Wachstumszyklus beeinträchtigt oder abgetötet, was in einer antibiotischen Wirkung resultiert und damit die Biofilmbildung reduziert.

1.3 Click-Chemie

Der Begriff der *Click-Chemie* wurde 2001 von Hartmuth C. Kolb, M. G. Finn und K. Barry Sharpless in ihrer Publikation „*Click Chemistry: Diverse Chemical Function from a Few Good Reactions*“ geprägt. Die Grundidee der Click-Chemie sind einfach durchführbarer Reaktionen, welche unter milden Reaktionsbedingungen ablaufen, durch ihre Selektivität keine aufwändige

Schutzgruppenchemie erfordern, hohe Ausbeuten liefern und idealerweise keine chromatographische Aufarbeitung benötigen. Das Vorbild hierfür ist die Carbonyl (Aldol-) Chemie des Lebens, welche mittels einfacher Bausteine, unter anderem der Aminosäuren und der Nucleobasen, in wässrigen Umgebungen eine enorm große Vielfalt an chemischen Verbindungen und Funktionalitäten ermöglicht, allerdings deren Nachteile durch hohe Reaktivitäten und Chemoselektivitäten ausgleicht.⁷⁹

1.3.1 Huisgen 1,3-dipolare Cycloaddition

Der bekannteste Vertreter der Click-Reaktionen ist die Huisgen 1,3-dipolare Cycloaddition zwischen Azid und Alkin, welche als Produkt ein 1,2,3-Triazol liefert.^{80,81} Die originale Huisgen 1,3-dipolare Cycloaddition, wie ursprünglich von Rolf Huisgen beschrieben,^{82–85} verläuft als 1,3-dipolare Cycloaddition thermisch induziert und liefert eine Mischung aus 1,4- und 1,5-substituierten Triazolyl-Regioisomeren, vgl. auch Abbildung 4.^{81,86,87}

Weitere Entwicklungen von Meldal und Sharpless et. al. lieferten schließlich die Cu(I)-katalysierte Huisgen 1,3-dipolare Cycloaddition, welche selektiv das 1,4-substituierte 1,2,3-Triazol liefert;^{88,89} ferner lieferten Arbeiten von Sharpless et. al. die Ru(II)-katalysierte Reaktion, welche selektiv 1,5-substituierte 1,2,3-Triazole liefert (vgl. Abbildung 4).^{90,91}

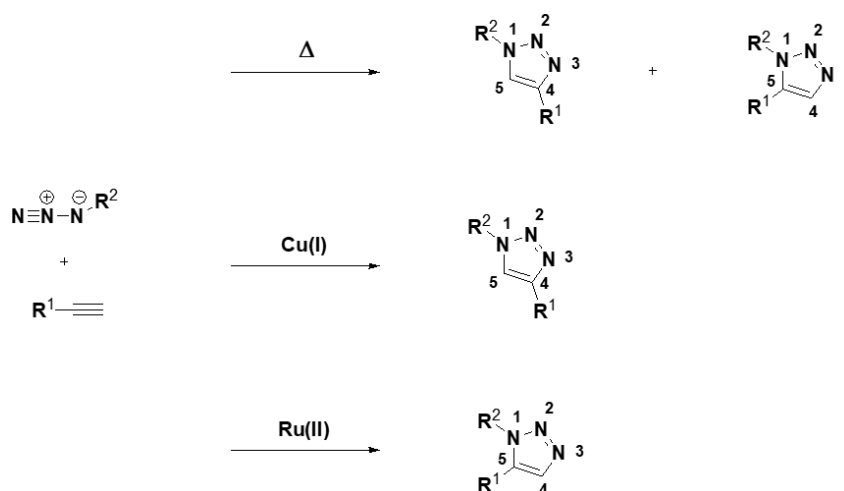


Abbildung 4. Schematische Darstellung der thermisch induzierten Huisgen 1,3-dipolaren Cycloaddition^{84,85} sowie die regioselektiven Varianten unter Cu(I)-^{88,89} und Ru(II)-Katalyse.^{90,91}

Der Cu(I)-katalysierten Huisgen 1,3-dipolaren Cycloaddition kommt hier aufgrund ihrer einfachen Durchführbarkeit, der sehr milden Reaktionsbedingungen, der Tolerierung vieler funktioneller Gruppen und Lösungsmitteln eine besondere Rolle in allen Bereichen der Bio-konjugation, Polymermodifikation⁹² und Peptidsynthese⁸⁸ zu. Die funktionelle Gruppe des

1,2,3-Triazols ist darüber hinaus für Zwecke der Biokonjugation besonders interessant, dass es aufgrund seiner Eigenschaften als Isooster zum Amid fungiert.^{93,94}

Durch diese Eigenschaften eignet sich dieser Heterocyclus insbesondere zum Aufbau und zur Modifikation triterpenoider Leitstrukturen, deren Derivate verschiedene pharmakologische Effekte, beispielsweise zytostatische, antientzündliche oder auch anti-Malaria Wirkungen aufweisen. Hierbei führt die Einführung eines 1,2,3-Triazols an verschiedenen Positionen des Triterpens zu einer erhöhten Hydrophilie, woraus eine erhöhte biologische Wirksamkeit aufgrund verbesserter Absorption, Distribution, Metabolismus sowie Eliminierung (ADME-Parameter) resultiert.⁹⁵

1.3.2 Antimikrobielle Aktivität von 1,2,3-Triazolyl-Clickameren

Die hohe Reaktivität und vergleichsweise einfach durchführbare Reaktionen der Click-Chemie, insbesondere der kupferkatalysierten Huisgen 1,3-dipolaren Cycloaddition, machen diese zum idealen Werkzeug zur Modifikation von Polymeren für medizintechnische Anwendungen.⁹² Verschiedene Polymere, in welche mittels Huisgen 1,3-dipolarer Cycloaddition eine Triazolyl-Gruppe eingeführt wurde, zeigen antimikrobielle Eigenschaften. So beispielsweise verschiedene 1,2,3-Triazol-1-yl-quinazolin-4-one, welche antibakterielle Wirkung gegen gram-positive als auch gram-negative Erreger zeigen.^{96,97} Ferner sind in der Literatur 1,2,3-Triazol-1-yl-Sucrose- als auch Glucose-Clickamere für ihre antimikrobielle Aktivität beschrieben,⁹⁸ was die Huisgen 1,3-dipolare Cycloaddition nicht nur unter chemischen Aspekten, sondern auch unter biofunktionellen Aspekten interessant für chemische Modifikationen von Polymeren zur Einführung diverser biofunktioneller Moleküle in eine Polymermatrix interessant macht.^{99,100}

1.4 Beschichtungen von Implantaten

1.4.1 PEEK als Implantatmaterial

Neben Titanlegierungen kommen in der Medizin insbesondere auch polymere Implantatmaterialien zum Einsatz. Ein Vertreter der polymeren Implantatmaterialien ist das Polyetheretherketon (PEEK), ein Hochleistungspolymer, welches ähnliche mechanische Eigenschaften wie herkömmliche Ti-6Al-4V-Legierungen aufweist, welche für medizinische Anwendungen, beispielsweise in der Endoprothetik, verbreitet sind.¹⁰¹ Die mechanischen Eigenschaften sind hier denen des menschlichen Knochens ähnlich.¹⁰² PEEK ist nicht zytotoxisch, nicht bioabbaubar und setzt keine Abbauprodukte, beispielsweise Schwermetallionen, in das umliegende Gewebe frei.¹⁰³

Diese Eigenschaften machen PEEK zu einem interessanten Material für medizinische Implantate, beispielsweise für Wirbelsäulenkäfige,^{104–107} Endoprothesen für Hüftgelenkersatz^{108–110}

oder Implantate für kraniale Knochenrekonstruktionen.^{111,112} PEEK als Hochleistungspolymer ist ebenso im FDM-3D Druck verarbeitbar.^{113–116}

Aufgrund seiner biologisch inerten Oberfläche, der verzögerten Integration in das umliegende Gewebe, insbesondere der Osseointegration sind hier Oberflächenmodifikationen von PEEK-Implantaten erforderlich.¹¹⁷ Hierfür sind in der Literatur verschiedene Verfahren beschrieben, beispielsweise die Abscheidung von anorganischen Substraten, insbesondere Calciumkomplexen, mittels Atomlagenabscheidung (ALD).¹¹⁸ Neue Entwicklungen schließen ebenso die Verbesserung der mechanischen Eigenschaften von PEEK ein, beispielsweise in Verbund mit Carbonfasern¹¹⁹ oder Calcium-Hydroxyapatit zusammen mit Graphenschichten.¹²⁰ Ein interessanter, neuer Ansatz konzentriert sich hier auf Beschichtungen mit Polymeren des Dopamins auf PEEK, was zu einer Ca^{2+} -Komplexbildung an der Implantatoberfläche führt. Dies führt wiederum zu einer beschleunigten Osseointegration und damit einer beschleunigten Mineralisierung der Oberfläche.¹²¹

1.4.2 Polydimethacrylamid-co-methacryloylbenzophenon Hydrogele

Ein weiterer Ansatz für antimikrobielle Oberflächen sind antiadhäsive Oberflächen, welche die Kolonisierung durch koloniebildende Bakterien verhindern. Derartige Beschichtungen sind auf Basis des Benzophenons im Copolymer mit Dimethacrylamid literaturbekannt und von Pandiyarajan et. al. beschrieben.¹²² Hierbei handelt es sich um ein oberflächenverankertes Polymer Netzwerk, welches aus Polydimethacrylamid-co-Methacryloylbenzophenon besteht und mittels der UV-induzierten C-H-Insertionsreaktion des Benzophenons auf der Oberfläche verankert wurde.¹²³

1.4.3 UV-induzierte C-H-Insertionsreaktion: Benzophenon Crosslinker

Benzophenon ist ein UV-responsiver Crosslinker, welcher in vielen Publikationen der letzten 30 Jahre für einen *grafting-to* Ansatz von Polymeren verwendet wird.^{124–128} Hierauf aufbauend wurden in der Literatur diverse Hydrogele demonstriert, welche zur verbesserten Zelladhäsion,^{129–131} für eine Nanotexturierung von Oberflächen für Diagnostika und diverse Nachweisreaktionen der biomedizinischen Analytik^{131–134} sowie für die Synthese von antiadhäsiven Oberflächen zur physikalischen Verringerung von mikrobieller Kontamination und Biofilmbildung beschrieben wurden.^{128,129,135–137} Weitere Beispiele für ein Benzophenon-basiertes *Photopatterning* finden sich in vielen Publikationen, beispielsweise für oberflächenverankerte Poly-*N,N*-dimethacrylamide, in welche Antikörper eingebracht wurden, zur kontrollierten Zelladhäsion von Tumorzellen aus humanen Blutproben zum Zwecke der Diagnostik.¹³¹

1.4.4 Reaktionsmechanismus: UV-induzierte C-H-Insertionsreaktion des Benzophenons

Bei Absorption eines Photons mit einer diskreten Wellenlänge geht Benzophenon in einen hoch reaktiven Tripletzustand in Form eines Kетоintermediats über. Hierbei handelt es sich um einen $n\text{-}\pi^*$ oder $\pi\text{-}\pi^*$ Übergang, welcher abhängig von der Wellenlänge des absorbierten Photons ist.¹³⁸ Dieser Übergang eines Elektrons aus einem nichtbindenden n-Orbital des Sauerstoffs in das π^* -LUMO der Carbonylgruppe des Benzophenons führt zu einem biradikaloiden Übergangszustand des Benzophenons (vgl. **1** und **1*** Abbildung 5). Das hier gebildete Ketylradikal kann wiederum ein Proton von einer sterisch günstig gelegenen Polymerkette oder einem anderen Substrat abstrahieren, was zu zwei Alkylradikalen (vgl. **2**, Abbildung 5) führt, welche unter Rekombination eine neue C-C Bindung ausbilden, was letztlich zur Vernetzung des Benzophenons mit sterisch günstig gelegenen Alkanen führt (oberer Reaktionsweg aus Abbildung 5 mit **3** als Produkt).¹²⁴

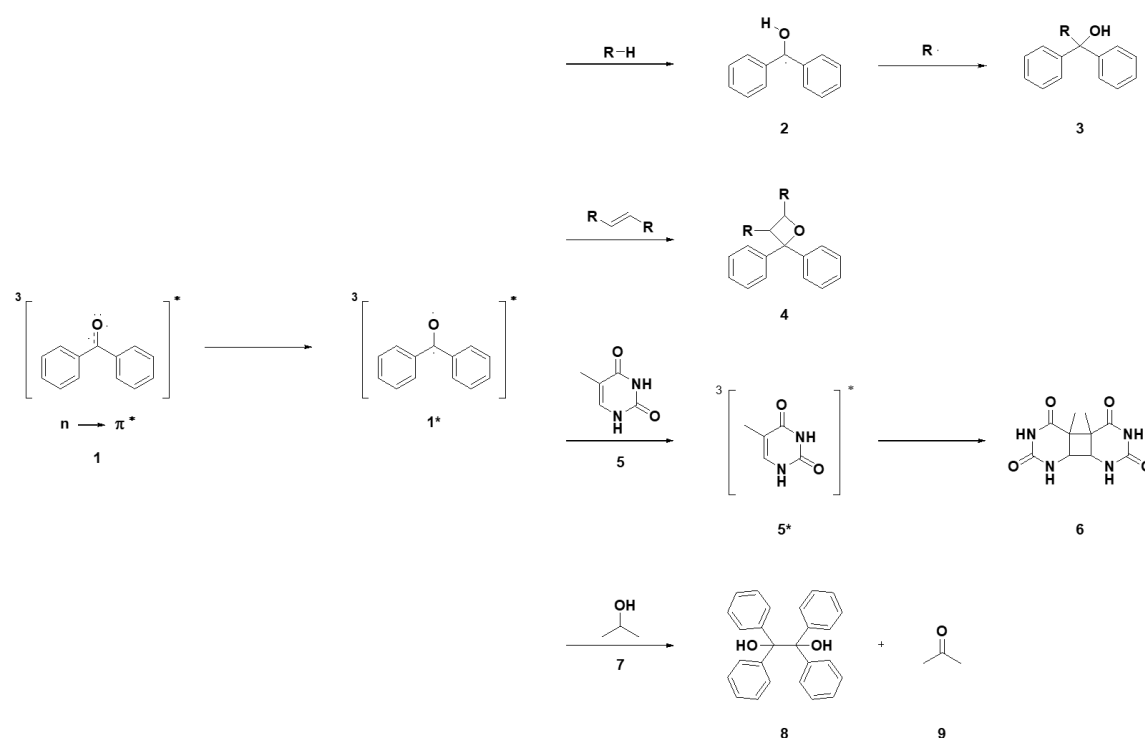


Abbildung 5. Angeregter Tripletzustand des Benzophenons (**1** bzw. **1***) und daraus folgende, mögliche Reaktionen. Abbildung basierend auf Dormán *et. al.* 2016.¹²⁴

Nebenreaktionen beinhalten im Falle von im Substrat vorliegenden Alkenen die Paternó-Büchi Reaktion, wobei es zu einer [2+2]-Cycloaddition zwischen dem Benzophenon-Carbonyl und dem Alken kommt, unter Bildung des Oxetans (**4** aus Abbildung 5).^{124,139} Benzophenon fungiert ebenso als Photosensibilisator, indem es die Cycloaddition zweier Thymidineinheiten der DNA

katalysiert (vgl. Abbildung 5, unterer Reaktionsweg mit **5** über **5*** zum Thymin-Dimer **6**).^{140–142} Des Weiteren kann es zu einer Photoreduktion des Benzophenons kommen, wo unter Rekombination zweier Ketylradikale ein Benzopinakol (vgl. **8** aus Abbildung 5) sowie als Nebenprodukt ein Keton, in diesem Beispiel Aceton (**9**) entsteht. Die die Geschwindigkeitskonstante der Rekombination zweier Ketylradikale zum Benzopinakol, in Abhängigkeit von Substituenteneinflüssen, ist um eine log-Stufe geringer als die der C-H-Insertionsreaktion.¹⁴³

Mechanistische Details hierzu über Lösungsmiteleinflüsse, stereochemische Kontrolle sowie Substituenteneinflüsse auf die C-H-Insertionsreaktion lassen sich in einem Review von Dormán et. al. von 1994 sowie in einem aktuelleren, 117-seitigen Review von 2016 finden.^{124,144}

Die Kinetik dieser C-H-Insertionsreaktionen, welche zu einer UV-induzierten Quervernetzung von Polymeren führt, wurde für 2-dimensionale Oberflächen von Rühle et. al. 2016 beschrieben.¹⁴⁵ Das Quervernetzen folgt hier im Wesentlichen der Perlokationstheorie,¹⁴⁶ bei welcher ab einer kritischen Zahl an Quervernetzungen von einem Hydrogel ausgegangen wird. Da die Quervernetzung mittels UV-Licht bei einer Bestrahlung von oben allerdings durch die Absorption der Schichtdicke beeinflusst wird und damit dem Lambert-Beerschen Gesetz folgt, erfolgt der Umsatz an Benzophenon an der Grenzfläche zum unterliegenden Substrat erst ab einer bestimmten Energiedosis. Demnach ist die Schichtdicke bei derartigen Hydrogelen, bei vollständiger Vernetzung mit UV-Licht durch die gesamte Hydrogelschicht hinweg, allein über die Menge an aufgetragener Beschichtung vorgegeben. Bei einer unvollständigen Vernetzung mit UV-Licht dagegen erfolgt keine Vernetzung mit dem darunter liegenden Substrat.¹⁴⁵

1.4.5 UV-induzierte Oberflächenreaktionen des PEEK

PEEK, als Polyetheretherketon, enthält als Monomereinheit eine Benzophenon-Gruppe, vgl. Abbildung 6.

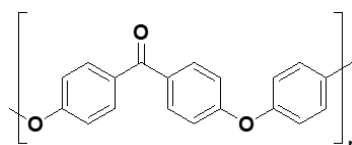


Abbildung 6. Chemische Struktur des Polyetheretherketons (PEEK).

Da sich diese analog zu Benzophenon verhält, kann sie die gleiche UV-induzierte C-H-Insertionsreaktion eingehen, mittels des in Kapitel 1.4.4 beschriebenen $n-\pi^*$ -Übergangs zur Generierung des Ketylradikals. Dies geht entweder im Rahmen der Benzophenon-Photochemie

eine C-H-Insertionsreaktion, Paternó-Büchi Reaktion unter Bildung eines Oxetans oder eine UV-induzierte Pinakol-Kupplung ein. Ferner lässt es sich als Radikalstarter für eine freie radikalische Polymerisation, wie von Kyomoto *et. al.* 2009 am Beispiel einer Funktionalisierung von PEEK mittels eines Methacryloylphosphorcholins demonstriert, nutzen.¹⁴⁷

Hierauf aufbauend wurde eine PEEK Oberfläche als Radikalstarter für *grafting-to* Ansätze von *Polymerbrushes* auf der PEEK Oberfläche beschrieben, beispielsweise mittels freier radikalischer Polymerisation^{148,149} oder mittels ATRP.^{150,151} Insgesamt liefert das PEEK damit, als für die Medizintechnik relevantes Hochleistungspolymer, einen interessanten Ansatz zur weiteren Funktionalisierung dessen Oberfläche.

1.5 Biokompatibilitätsbewertungen nach DIN EN ISO 10993

Die Definition der Biokompatibilität an sich ist abhängig von regulatorischen Begriffen und der für den Zielmarkt des Medizinprodukts geltenden regulatorischen Bestimmungen und ist immer kontextabhängig zu betrachten. Eine allgemeine Definition für Biokompatibilität gibt die *Consensus Conference on Definitions in Biomaterials* der *European Society for Biomaterials* von 1984 vor, die Biokompatibilität als „*the ability of a material to perform with an appropriate host response in a specific application*“ definiert.¹⁵²

1.5.1 Regulatorische Anforderungen

Im europäischen Raum, in welchem die *Medical Device Regulation* (MDR) Gültigkeit besitzt, ist insbesondere die Zweckbestimmung (*intended use*) und die Klassifizierung eines Medizinproduktes für die Bewertung der Biokompatibilität ausschlaggebend.¹⁵³ Ferner fließen in eine adäquate Bewertung der Biokompatibilität eines Materials, respektive eines Medizinprodukts die Betrachtungen eines Risikomanagementprozesses nach DIN EN ISO 14971 ein, welcher auch von der MDR gefordert wird.¹⁵⁴ Hierauf baut eine adäquate Bewertung der toxikologischen Effekte eines Medizinproduktes oder eines Materials für ein Medizinprodukt auf, welche laut MDR also immer kontextabhängig zu betrachten ist. Die DIN EN ISO 10993 besteht aus 23 Teilen, welche hierfür einen entsprechenden, kontextabhängigen Rahmen vorgibt, auf deren Basis Biokompatibilitätsbewertungen erfolgen sollen.^{155,156}

1.5.2 Bewertung der Zytotoxizität nach DIN EN ISO 10993-5

Die DIN EN ISO-10993-5, welche sich auf in-vitro Zytotoxizität beschränkt, verweist für Zytotoxizitätstests auf die *United States Pharmacopeia*.^{157,158} Hierin sind Standardmethoden für Zytotoxizitätsuntersuchungen beschrieben, welche einerseits einen Extrakttest sowie einen Kontakttest beinhalten. Für beide Tests sind nach DIN EN ISO 10993-5 die L-929

Mausfibroblastenzelllinie gefordert.^{159,160} Die Bewertung der Zytotoxizität im Extrakttest erfolgt nach einer Extraktion des Medizinprodukts bzw. Materials mit dem für die Zellkultur verwendeten Medium für 24 Stunden, gefolgt von einer Inkubation der Zellen mit diesem Material für 72 Stunden. Zur Auswertung werden mikroskopische Bilder sowie eine qualitative Erfassung des Zellmaterials oder eine Messung der Zellviabilität, beispielsweise mit dem MTT Test, herangezogen.¹⁵⁹ Für die Bewertung der Toxizität im Kontakttest werden die Zellen direkt auf die Materialoberfläche aufgebracht, respektive das Material direkt auf die Zelloberfläche aufgebracht, und für 24 und 72 Stunden inkubiert, wobei ebenfalls eine mikroskopische und eine qualitative Auswertung der Zellviabilität erfolgt.¹⁶⁰

1.5.3 Bewertung des inflammatorischen Potentials nach DIN EN ISO 10993-11

Für die Bewertung der systemischen Toxizität sowie des inflammatorischen Potenzials eines Biomaterials, respektive eines Medizinprodukts, liefert die DIN EN ISO-10993-11 eine adäquate Grundlage, welche auch von der MDR gefordert wird.¹⁶¹ Hierbei sind bislang noch *in-vivo* Versuche am Kaninchen verbreitet, wobei die Erhöhung der Körpertemperatur als Nachweis für Pyrogenität gilt.¹⁶¹ Für den *in-vivo* Test am Kaninchen wird allerdings eine hohe Zahl an Versuchstieren benötigt, ferner ist die Reproduzierbarkeit über die Versuchstierpopulationen nicht immer gegeben.^{162–164} Ein weiterer, etablierter Test ist der sogenannte Limulustest, bei welchem Limulus-Amöbozyten-Lysat zum Einsatz kommt.^{165–167}

Zur besseren Durchführbarkeit wurde für das inflammatorische Potential der Monozyten-Aktivierungstest vorgeschlagen, welcher seit 2012 in einem *FDA Guidance Document* als Alternativmethode zur Bewertung der systemischen Toxizität geführt wird.¹⁶⁸ Bei diesem werden menschliche Monozyten (Mono Mac-2 oder Mono Mac-6 Zelllinie) *in-vitro* mittels eines ELISA auf Interleukin-Sekretion getestet, in der Regel Interleukin 1b oder Interleukin 6.^{169–173} Diese Tests, basierend auf Monozyten-Zelllinien, weisen in Validierungen noch eine erhöhte Sensitivität gegenüber den herkömmlichen Pyrogenitätstests auf.^{174,175} Dies macht die *in-vitro* Tests mit Monozyten zu einem idealen Werkzeug für Hinweise auf eine systemische Toxizität, eine Immunreaktion gegenüber einem Biomaterial oder einer Pyrogenität des Materials oder einer seiner Bestandteile.

1.6 Kynurenin als Biomarker für Abstoßungsreaktionen

1.6.1 Tryptophanmetabolismus und der Kynureninsignalweg

Kynurenin ist ein Metabolit des Tryptophanmetabolismus, welcher in Zusammenhang mit diversen inflammatorischen Pathologien steht, beispielsweise mit metabolischen, onkogenen und auch psychiatrisch-inflammatorischen Prozessen.^{176–178} Ein Teil des Tryptophans,

welches mit der täglichen Ernährung aufgenommen wird, wird zu Serotonin umgesetzt,¹⁷⁹ während 95% des über die Ernährung zugeführten Tryptophans im Tryptophanmetabolismus über mehrere Abbaumetaboliten bis zur Chinolinsäure und Picolinsäure umgesetzt wird, vgl. auch Abbildung 7.^{180,181} Dies erfolgt mittels einer Reaktionskaskade der Enzymklasse der Indolamin-2,3-dioxygenasen (IDOs).^{181–184}

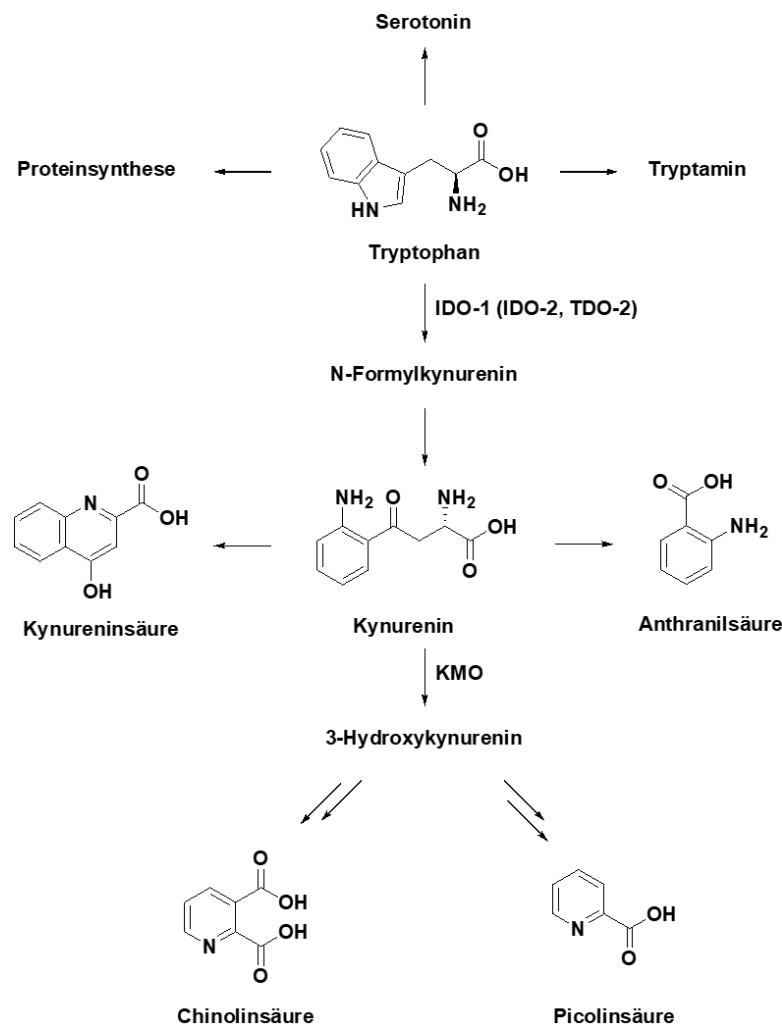


Abbildung 7. Signalweg des Tryptophan-Metabolismus mit nachgelagertem Kynurenin-Signalweg, deren Endprodukte die Chinolinsäure und Picolinsäure sind. Abbildung basierend auf Simon *et. al.* 2015.¹⁸¹

Die Aktivität der IDOs wird mittels diverser immunologischer Faktoren reguliert, beispielsweise durch LPS - vermittelt durch Mikroorganismen,^{185–187} daraus resultierender pro-inflammatorischer Zytokine,^{188,189} beispielsweise IL-1 oder TNF- α .¹⁹⁰ Diese Aktivität der IDOs wird durch erhöhte Kynureninlevel wiederum verringert, was bei einer erhöhten Kynureninkonzentration im Blut zu einer reduzierten Immunreaktion führt. Hierzu wird in der Literatur eine Art Rückkopplungsschleife (*feedback-loop*), vermittelt durch L-Kynurenin, postuliert.^{191–194}

1.6.2 Kynurenin und Abstoßungsreaktionen von Transplantaten

Durch diese Mediatorrolle des Kynurenins innerhalb von entzündlichen Prozessen kommt dem Kynurenin eine interessante Rolle als Biomarker für klinisch relevante Entzündungsprozesse zu. Beispielsweise wurden erhöhte IDO-Expressionslevel und damit erhöhte Kynureninlevel von $3,9 \pm 2,1 \mu\text{M}$ im Serum am Beispiel des chronischen Nierenversagens (*chronic kidney disease*, CKD) bei Patienten im Vordialyse-Stadium gemessen, mit steigenden Werten in Abhängigkeit des CKD-Schweregrades. Die gemessenen Kynureninkonzentrationen betragen bis zu $5,6 \pm 2,3 \mu\text{M}$. Dies wird verursacht durch chronische Entzündungsreaktionen während des Fortschritts des chronischen Nierenversagens.^{195–198} Diese erhöhten Kynurenin-Serumwerte sind nicht lediglich auf CKD beschränkt, sondern lassen sich auch im Zusammenhang mit entzündlichen Prozessen nach einer Nierentransplantation nachweisen. In diesem Falle sind die gemessenen Kynureninkonzentrationen im Serum der betroffenen Patienten invers mit dem Grad der Nierenfunktion korreliert.^{199,200} Bei Patienten mit einer Nierentransplantatabstoßung wurden Kynurenin-Serumwerte von $17,4 \pm 8,4 \mu\text{M}$ gemessen, im Vergleich mit gesunden Kontrollgruppen, welche Werte von $2,7 \pm 0,4 \mu\text{M}$ aufwiesen.²⁰¹

1.6.3 Kynurenin und Abstoßungsreaktionen von Implantaten

Der veränderte Typtophanmetabolismus, verursacht durch eine Änderung der IDO-Expressionslevel, welcher zu erhöhten Kynureninkonzentrationen im Serum führt, wurde ebenso mit Titanimplantaten im Dentalbereich in Verbindung gebracht. Diese werden durch Entzündungsreaktionen während des Osseointegrationsprozesses in den das Implantat umgebenden Knochen verursacht.²⁰² Derartige Entzündungsprozesse, welche zu einem veränderten Typtophanmetabolismus und damit zu einem erhöhten Kynureninspiegel führen, sind ebenso bei Patienten mit Osteoarthritis vorhanden, bei welcher es zu einer Degradierung des Knochengewebes kommt.²⁰³

Ferner wurden diese erhöhten Kynureninlevel im Blut in Zusammenhang mit implantierten Herzunterstützungssystemen, genauer linksventrikulären Unterstützungssystemen, in Verbindung gebracht.²⁰⁴ Diese Beobachtungen legen nahe, Kynurenin ebenso als potenziellen klinischen Biomarker für Abstoßungsreaktionen von Implantaten in Betracht zu ziehen.

1.6.4 Literaturbekannte Analysemethoden des L-Kynurenins

Die meisten Methoden zur Quantifizierung des L-Kynurenins aus Serum oder Speichel fokussieren sich auf LC-MS^{205–209} oder GC-MS.²¹⁰ Hieraus ergeben sich in der klinischen Praxis vor allem lange Diagnosezeiten und damit hohe Kosten sowie verzögerte Diagnosestellungen für den Patienten

In der Literatur sind bereits einige Studien beschrieben, welche auf den Nachweis von Metaboliten des IDO-Signalwegs abzielen, beispielsweise von Ungor et. al. 2019, welche fluoreszente Gold-Nanocluster synthetisiert haben, um L-Kynurenin in physiologisch relevanten Konzentrationsbereichen in PBS mittels eines Fluoreszenz-Quenchingmechanismus nachzuweisen.²¹¹ Die Arbeitsgruppe um Klockow et. al. hat 2013 ein fluoreszierendes Derivat des L-Kynurenins beschrieben, welches mit einem Cumarin als Fluoreszenzmarker verknüpft war. Die Fluoreszenz tritt hier in Abhängigkeit einer Änderung des pH-Werts auf, und ist mechanistisch bedingt durch eine Iminbildung zwischen dem aromatischen Amin des L-Kynurenins und einem freien Aldehyd des verwendeten Cumarinderivats.²¹² Allerdings sind die Nachweisgrenzen weit oberhalb der Konzentrationen, welche eine physiologische Relevanz aufweisen und deshalb für die Entwicklung eines Schnelltests auf L-Kynurenin nicht praktikabel.

Weitere Ansätze, welche auf Schnelldiagnostik unter Zuhilfenahme des Kynurenin-IDO-Systems abzielen, beinhalten die Quantifizierung der IDOs im Rahmen eines Enzymnachweises anstelle eines direkten Nachweises des L-Kynurenins.²¹³ Somit existierte in der Literatur bislang keine hinreichend sensitive Nachweisreaktion für L-Kynurenin als Biomarker, welche über die üblichen, zeit- und kostenintensiven LC-MS und GC-MS Methoden hinaus geht.

1.6.5 Kynurenin als Biokompatibilitätsmarker

Aufgrund dieser vielseitigen Anwendbarkeit des Kynurenins als Biomarker für inflammatorische Prozesse, insbesondere im Zusammenhang mit Abstoßungsreaktionen auf Transplantate sowie Implantate kommt dem Kynurenin eine interessante Rolle als Biomarker in Hinblick auf mögliche Tests auf Abstoßungsreaktionen zu. Dies betrifft insbesondere neben Transplantaten Implantate, bedingt durch die zunehmende Biologisierung von Implantatoberflächen, neuartigen, körpergewebeähnlichen Beschichtungen,^{214,215} der Einkapselung von Stammzellen auf Implantatoberflächen²¹⁶ sowie dem 3D Druck von Implantaten und potenziell künstlichen Organen und Organoiden.²¹⁷

Das Ziel der beschriebenen Untersuchungen, welche im Rahmen dieser Arbeit unter dem Titel *“A Fluorescence-Based Competitive Antibody Binding Assay for Kynurenine, a Potential Biomarker of Kidney Transplant Failure”* in MDPI Diagnostics publiziert wurden (vgl. Publikation P-3 bzw. Referenz ²¹⁸) war die Synthese eines fluoreszierenden Derivats des L-Kynurenins und dessen Untersuchung auf Anwendbarkeit in einem Antikörper-Assay zur Quantifizierung von Kynurenin aus Speichel oder Serum. Dieser Antikörper-Assay soll perspektivisch für die Entwicklung eines Schnelltests auf Kynurenin zur Schnellerkennung einer Abstoßung von Transplantaten und Implantaten verwendet werden. Damit soll perspektivisch dem behandelnden Arzt ein kostengünstiges und schnell verfügbares Werkzeug zum Nachweis von Abstoßungsreaktionen nach chirurgischen Eingriffen zur Verfügung gestellt werden.

2 Zielstellung

Infektionen von Implantaten, insbesondere mit multiresistenten Erregern, wie beispielsweise MRSA, stellen eine enorme Problematik in der Implantationsmedizin dar. So führt eine Infektion der Implantatoberfläche mit anschließender Biofilmbildung zur Abkapselung des Implantats und damit zu einer Abstoßungsreaktion des umliegenden Gewebes gegenüber dem Implantat. Ferner kann es zu einer Streuung der infektiösen Erreger in die Blutbahn kommen, was eine Blutsepsis bis zum septischen Schock zur Folge haben kann.

Aufgrund dieser Problematik war das Ziel der Arbeit die Synthese neuartiger antimikrobieller, biofilmhemmender und gleichzeitig biokompatibler Polymere zur Beschichtung von medizinischen Implantaten zur Vermeidung dieser Infektionsproblematik. Hierzu war ein Ziel der Arbeit einerseits die Synthese von Glucosamin- und Chitosan-basierten Polymeren, deren Bestandteile in der Literatur als antimikrobiell und biofilmhemmend beschrieben sind. Für die Synthese der Glucosamin-basierten Polymere sollte eine Palette an Methacrylaten modifiziert mit *N*-Acetylglucosamin und verschiedenen, verbrückenden Oligoethylenglycol-Linkern mittels der Huisgen 1,3-dipolaren Cycloaddition („Click-Chemie“) synthetisiert und charakterisiert werden. Hieraus sollten Copolymere mit diesen Monomeren zusammen mit Methacryloylbenzophenon als UV-vernetzbares *Crosslinker* für die C-H Insertionsreaktion synthetisiert und charakterisiert werden. Ferner sollte Chitosan selbst modifiziert und für eine UV-vernetzbaare Beschichtung erprobt werden.

Diese so erhaltenen Polymere sollten zur Modifikation von Materialien verwendet werden, welche auch zur Herstellung von Implantaten genutzt werden. Mittels des Ansatzes des *Photopatternings*, welches in der Halbleiterindustrie zum Einsatz kommt und mit welchem Schichten im Nanometerbereich auf Probenstücke aufgebracht werden können, sollten Modellmaterialien für Implantate mit diesen Polymeren modifiziert und die modifizierte Oberfläche chemisch-physikalisch charakterisiert werden, um die Eignung der Polymere für einen Beschichtungsprozess zu evaluieren.

Die synthetisierten Polymere sowie die daraus resultierenden Beschichtungen auf Implantatmaterialien sollten auf ihre antimikrobielle Aktivität sowie auf ihre Biokompatibilität nach DIN EN ISO 10993 untersucht werden, wobei hier insbesondere die Zytotoxizität nach DIN EN ISO 10993-5¹⁵⁷ im Vordergrund stand. Hierauf aufbauend sollten Struktur-Wirkbeziehungen untersucht werden, insbesondere was die chemische Struktur der Polymere in Hinblick auf verbrückende Oligoethylenglycollinker, deren Copolymergehalt sowie das Copolymerverhältnis an Benzophenon betrifft.

Da aufgrund der Gesetzesnovelle von 2017 zu Medizinprodukten, aus welcher die Medical Device Regulation als europaweite Vereinheitlichung der regulatorischen Bestimmungen zu Medizinprodukten hervorging, Bewertung von Medizinprodukten der Klassen IIb und III insbesondere Biokompatibilitätsbewertungen im Rahmen von klinischen Studien erforderlich werden,¹⁵³ sollte im weiteren Verlauf der Arbeit der Aspekt der Bewertung der Biokompatibilität von Implantatmaterialien weiterverfolgt werden. Hierzu wurde das L-Kynurenin als Biomarker für entzündungsbedingte Prozesse, einerseits im Rahmen der Transplantatabstoßung andererseits auch der Implantatabstoßung identifiziert. Es sollte ein fluoreszentes Kynureninderivat mit Rhodamin B als Fluoreszenzmarker synthetisiert und dessen Eignung für die Entwicklung eines Schnelltests auf L-Kynurenin aus Serum oder Speichel evaluiert werden, um hiermit ein kostengünstiges und schnell anwendbares Werkzeug für weitere klinische Biokompatibilitätsprüfungen von Implantatmaterialien zu erhalten.

3 Forschungsergebnisse

Die im Folgenden dargestellten Forschungsergebnisse sind im Rahmen dieser kumulativen Dissertation bereits in Publikationen P-1 bis P-3 in *peer-review* Fachzeitschriften veröffentlicht worden. Hierbei behandeln Publikationen P-1 und P-2 die chemische Synthese, die physikalisch-chemische Oberflächencharakterisierung und die biofunktionelle Charakterisierung von polymeren Oberflächenbeschichtungen, welche auf verschiedene Modellmaterialien aufgebracht und mittels UV-Licht quervernetzt wurden. Dies umfasst ebenso Biokompatibilitätsbewertungen nach DIN EN ISO-10993.

Publikation P-3 erweitert unter anderem den Aspekt der Biofunktionalitäts- und Biokompatibilitätsbewertungen mittels einer Testmethode auf inflammatorische Prozesse auf klinische Anforderungen im Rahmen weiterführender Biokompatibilitätsbewertungen im Rahmen der klinischen Prüfung. Dies betrifft einerseits Abstoßungsreaktionen von Transplantaten, aber insbesondere auch Abstoßungsreaktionen von Implantaten im Rahmen inflammatorischer Prozesse.

Im Folgenden sind die Ergebnisse zusammenfassend dargestellt und in den Gesamtzusammenhang der Dissertation eingeordnet. Experimentelle Details und weiterführende Informationen, insbesondere die diagrammhafte Darstellung der Daten, Abbildungen zur Synthese und zugehörige Syntheschema sowie mikroskopische- und elektronenmikroskopische Aufnahmen der Biofunktionalitätsbewertungen können den jeweiligen Publikationen P-1 bis P-3 im Anhang entnommen werden.

3.1 GlcNAc-Benzophenon-Dimethacrylamid Copolymere

Chitosan selbst zeigt antimikrobielle Eigenschaften durch verschiedene Wirkmechanismen (vgl. auch Kapitel 1.2.4), beispielsweise durch Zerstörung der Integrität der Zellmembran^{219–221} oder durch Disruption der Proteinsynthese durch Bindung an DNA und RNA.^{72,73} Darüber hinaus zeigt es biofilmhemmende Eigenschaften, beispielsweise auf *Actinobacillus pleuromoniae*.²²² Chitosan selbst besteht aus Glucosamin und *N*-Acetylglucosamineinheiten, wobei das *N*-Acetylglucosamin selbst für biofilmhemmende Eigenschaften auf *E. coli* beschrieben ist.²²³ Chitosan selbst weist allerdings schlechte mechanische Eigenschaften und eine schlechte Löslichkeit in wässrigen und organischen Lösungsmitteln auf, was seine Verwendbarkeit in Hinblick auf Biomaterialien und darauf aufbauenden antimikrobiellen Beschichtungen einschränkt.^{56,57,59,224} Ferner zeigen auch glycosidische 1,2,3-Triazole, beispielsweise 1,2,3-Triazolyl-Sucrose Clickamere, antimikrobielle und antibakterielle Eigenschaften.^{225–227}

Das Triazol als funktionelle Gruppe ist mittels der der Huisgen 1,3-dipolaren Cycloaddition („Click-Reaktion“) synthetisch einfach in die molekulare Struktur einführbar.^{88,89} Hieraus ergibt sich ein eleganter Ansatz zur weiteren Umsetzung eines Propargyl-funktionalisierten *N*-Acetylglucosamins mit Azidomethacrylaten. Zusammen mit einem Methacryloylbenzophenon, welches als UV-responsiver Quervernetzer sowie Oberflächenanker fungiert^{126,128,228} sowie einer antiadhäsiven Polydimethacrylamid-Copolymermatrix ergibt sich hier der Ansatz einer UV-vernetzbaaren Beschichtung basierend auf Poly-dimethacrylamid-co-methacryloylbenzophenon, welche als antiadhäsiv in der Literatur beschrieben ist,^{123,128–130} zusammen mit potentiell antimikrobiellen *N*-Acetylglucosamineinheiten zum synthetischen Nachbau einer Chitosanoberfläche, welche allerdings die Vorteile eines wasserlöslichen und einfach handhabbaren Polydimethacrylamid-Hydrogels aufweist.

Somit wurden in diesem Teil der Arbeit verschiedene *N*-Acetylglucosamin-oligoethylenglycol-methacrylate mittels der Click-Chemie synthetisiert, welche verschiedene Oligoethylenglycol-Linker aufweisen, mit welchen sie anomer, d. h. in C1-position, mittels 1,2,3-Triazol verknüpft sind. Diese wurden in verschiedenen Verhältnissen mit Dimethacrylamid sowie einem UV-vernetzbaaren Methacryloylbenzophenon copolymerisiert (vgl. auch Abbildung 8).

Die synthetisierten Copolymere wurden auf PETG Chips als Modellsubstrat einer zu beschichtenden Oberfläche aufgebracht und mittels UV-Licht quervernetzt. Die ausgebildete Beschichtung wurde mittels IR-Spektroskopie, SEM und AFM untersucht. Ferner wurde die Sterilität der Oberfläche im Rahmen des Beschichtungsprozesses untersucht, sowie auf Biokompatibilität getestet. Die antimikrobiellen Eigenschaften wurden mittels MRSA(+) *S. aureus* und *E. coli* als klinisch relevante Pathogene demonstriert.

3.1.1 Chemische Synthese der Monomerbausteine und der Copolymere

Für die chemische Synthese der Monomerbausteine wurden diverse Azidooligoethylenglycol-Methacrylate über literaturbekannte Zwischenschritte^{229–231} synthetisiert und mit einem Propargyl-*N*-Acetylglucosamin mittels der Huisgen 1,3-dipolaren Cycloaddition (Click-Reaktion)^{79,80} zum entsprechenden Triazolylderivat (**2a** – **d**, Abbildung 8) umgesetzt, um an anomerer Position des *N*-Acetylglucosamins einen 1,2,3-Triazolylrest einzuführen. Als Kontrollen für die Biofunktionalitätsbewertungen, insbesondere in Hinblick auf die antimikrobielle Aktivität des Triazols allein in der Dimethacrylamid-Polymermatrix,^{225–227} wurde ebenso Propargylalkohol anstelle von Propargyl-GlcNAc mit den Azido-oligoethylenglycolmethacrylaten umgesetzt (**3a** – **c**). Hiermit sollte ein hydroxy-funktionalisiertes Polymer anstelle eines GlcNAc-funktionalisierten Polymers mit 1,2,3-Triazol an gleicher Position erhalten werden (vgl. Abbildung 8 und Syntheschema in Figure 1, Publikation P-1 im Anhang).

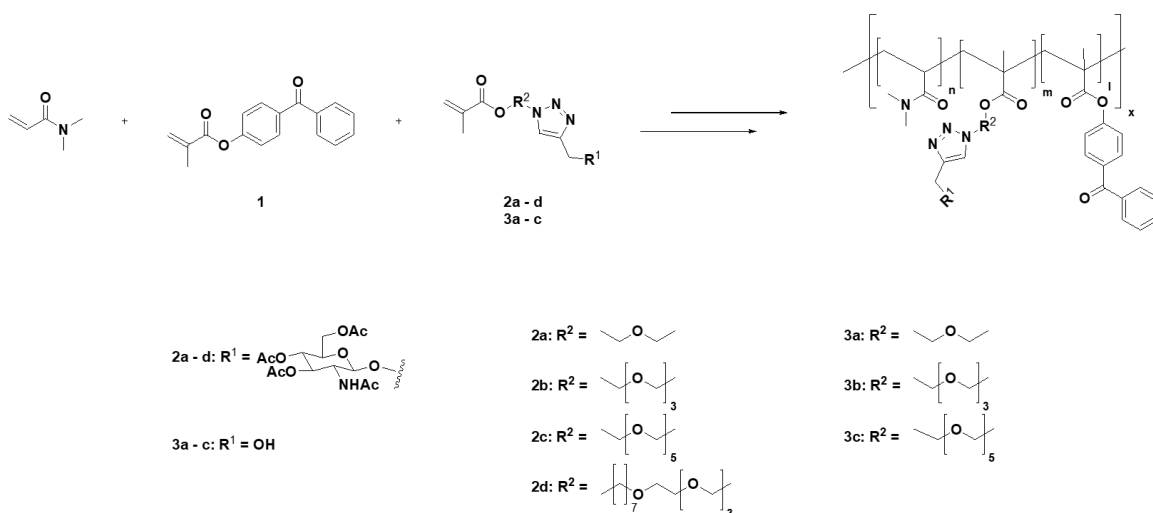


Abbildung 8. Schematische Übersicht über die synthetisierten Monomere sowie den daraus synthetisierten Polymeren, für eine genaue Übersicht über die Polymere vgl. auch Tabelle 1.

Die jeweiligen Methacrylate **2a – d** und **3a - c** wurden zusammen mit Methacryloylbenzophenon **1** sowie Dimethacrylamid copolymerisiert. Experimentelle Details und die exakten Synthesevorschriften können der Publikation P-1 im Anhang entnommen werden. Eine Übersicht über die jeweiligen Polymere mit den jeweils eingesetzten stöchiometrischen Verhältnissen und den gefundenen Einbauverhältnissen, welche mittels ¹H-NMR gefunden wurden, ist in Tabelle 1 aufgeführt.

Tabelle 1. Übersicht über die synthetisierten GlcNAc-MBP-Dimethacrylamid Copolymere mit den jeweiligen stöchiometrischen Verhältnissen an eingesetzten Monomeren sowie die via ¹H-NMR tatsächlich gefundenen Einbauverhältnisse.

Polymer	MBP	Triazolyl-Methacrylat 2 oder 3	Gefundenes Einbauverhältnis via NMR
GlcNAc-2EG	5%	5% 2a	30:1
5%-GlcNAc-4EG	5%	5% 2b	2:1
10%-GlcNAc-4EG	5%	10% 2b	1:2
25%-GlcNAc-4EG	5%	25% 2b	1:5
50%-GlcNAc-4EG	5%	50% 2b	-
GlcNAc-6EG	5%	5% 2c	3:1
GlcNAc-4EG-octyl	5%	5% 2d	6:1
HM-2EG	5%	5% 3a	1:1
HM-4EG	5%	5% 3b	1:1
HM-6EG	5%	5% 3c	1:1
PDMAm	5%	-	-

Insgesamt wurden Copolymere erhalten, wobei die tatsächlichen Copolymerverhältnisse zum Teil erheblich von den stöchiometrisch eingestellten Verhältnissen abweichen. Das Einbauverhältnis wurde mittels des Integralverhältnisses zwischen dem Triazolyl-Proton bei 7,96 ppm und den aromatischen Protonen des Benzophenons bestimmt. Die abweichenden Einbauverhältnisse lassen sich auf unterschiedliche Reaktivitäten, bedingt durch die sterisch anspruchsvolle GlcNAc-Gruppe zurückführen. Die Polymerisation von 50% Methacryloyl-4EG-GlcNAc **2b** zusammen mit 5% MBP und 45% Dimethacrylamid liefert kein Produkt. Die Copolymerisation der Hydroxymethyl-Triazolyl-Methacrylate **3a – c** verläuft dagegen in den stöchiometrisch vorgegebenen Einbauverhältnissen. Insgesamt wurden die benötigten GlcNAc-Benzophenon-Dimethacrylamid Copolymere erfolgreich synthetisiert, welche für weiter Oberflächenfunktionalisierungen verwendet wurden.

3.1.2 Beschichtung von Oberflächen

Die synthetisierten Polymere aus Tabelle 1 wurden zur Ausbildung einer Beschichtung in verschiedenen Konzentrationen auf einen PETG Coverslip als Referenzmaterial aufgebracht und mit UV-Licht quervernetzt. Die erhaltenen Beschichtungen wurden mittels IR-Spektroskopie, SEM und AFM charakterisiert. Die optimierten Bedingungen zur Quervernetzung des Benzophenons nach Rühle et. al. sind 3 J/cm^2 für Polydimethacrylamid-co-methacryloylbenzophenon mit 5% Methacryloylbenzophenon-Copolymer, bei welcher eine stabile Beschichtung ohne mögliche Abbaueffekte erhalten wird.¹²² Folglich wurde diese Energiedosis zur Quervernetzung der Polymere mit UV-Licht verwendet.

Die Beschichtung wurde mittels IR-Spektroskopie untersucht, wobei mit einer Polymerkonzentration von 25 mg/mL bei der verwendeten Methode des Solvent Casting eine hinreichend dicke Schicht erhalten wurde, welche im IR Spektrometer messbar war. Die Beschichtungen wurden anhand der dominanten Peaks des Dimethacrylamids bei 1621 cm^{-1} sowie der Copolymer-Estergruppen bei 1721 cm^{-1} identifiziert. Des Weiteren zeigen die glycosidischen OH-Bindungen Banden bei 3450 cm^{-1} und 2925 cm^{-1} was auf einen erfolgreichen Beschichtungsprozess hindeutet. Die Beschichtung des 5%-4EG-GlcNAc- und 6EG-GlcNAc-PDMAM Polymere wurden weiterhin mittels SEM und AFM untersucht. Hierbei wurde eine glatt texturierte Oberfläche erhalten, welche für die 5%-4EG-GlcNAc-PDMAM Beschichtung mit kleinen Poren bei 500 nm Auflösung durchsetzt ist, wogegen die 6EG-GlcNAc-PDMAM Beschichtung keine Poren erkennen lässt. Insgesamt ist aber eine Textur auf der untexturierten PETG Oberfläche erkennbar, was zusammen mit den IR Daten auf eine erfolgreiche Beschichtung der Oberfläche schließen lässt.

Die Sterilisation mittels UV-Licht ist eine etablierte Methode für Lebensmittel, Wasseraufbereitung sowie Oberflächensterilisierungen in der Medizintechnik,^{232,233} wobei mit einer

Bestrahlung mit UV-C Licht (100 – 280 nm) von 40 mJ/cm² bereits eine log-4-fache Reduzierung der Keimzahl an *P. aeruginosa* auf einer Oberfläche erreicht wird.²³⁴ Insgesamt wird mit 8 mJ/cm² eine Reduzierung der Keimzahl von 90%, also einer log-Stufe, erhalten.²³⁵ Die Quervernetzung mit UV-Licht bei 3 J/cm² liefert somit direkt im Beschichtungsprozess eine sterile Oberfläche, wie sie experimentell durch Inkubation der beschichteten Oberfläche ohne GlcNAc-Copolymer in sterilen LB-Medium ohne Nachweis eines mikrobiellen Wachstums gezeigt wurde.

3.1.3 Biokompatibilität

Die Bewertung der Zytotoxizität der Oberflächen erfolgte nach DIN EN ISO-10993-5,¹⁵⁷ welche die *United States Pharmacopeia* für genaue Protokolle hinsichtlich der Durchführung referenziert.^{158–160} Verwendet wurden L-929 Fibroblasten im Kontakt- und Extrakttest. Experimentelle Details können der zugehörigen Publikation P-1 im Anhang entnommen werden.

Im Extrakttest wurden für alle polymeren Beschichtungen keine Wachstumshemmungen über 30% gemessen. Im Kontakttest wurde lediglich für die Beschichtung mit GlcNAc-verbrückendem Diethylenglycol-Linker eine Wachstumsinhibierung von 32% sowie für einen Tetraethylenglycol-octyl-Linker eine Inhibierung von 37% gemessen, alle andere Beschichtungen weisen Werte von unter 30% auf und können damit als biokompatibel betrachtet werden.²³⁶

In der Literatur sind Toxizitätswerte für verschiedene Oligoethylenglycole beschrieben, so weisen Oligoethylenglycole über PEG200, welches mit einer Molekularmasse von über 200 g/mol ab dem Tetraethylenglycol der Fall ist, die geringste Toxizität auf.^{237–239} Ethylenglycol und Diethylenglycol dagegen sind bekannt für ihre toxischen Effekte, welche mit steigender Kettenlänge der Oligoethylenglycolkette abnehmen.²⁴⁰ Hieraus ergeben sich die entsprechenden Effekte in Hinblick auf die verschiedenen Linkerlängen, so kann für die Beschichtung mit verbrückendem Diethylenglycol-Linker von möglichen Abbauprodukten in direkten Kontakt mit den Zellen ausgegangen werden, was zur Freisetzung von Ethylenglycol führt. Insgesamt sind Effekte in Bezug auf eine Wachstumsinhibierung durchweg gering, abgesehen vom 2EG-GlcNAc-PDMAM und vom 4EG-octyl-GlcNAc-PDMAM Polymer, welche mit über 30% Wachstumsinhibierung über der 30%-Schwelle liegen, unter welcher Biokompatibilität angenommen werden kann.²³⁶

3.1.4 Antimikrobielle Aktivität

Die antimikrobielle Aktivität wurde mit *E. coli* als gram-negativen und MRSA(+) *S. aureus* als gram-positiven Erreger getestet, welche beide eine klinische Relevanz hinsichtlich Pathogenität, Infektiosität und Biofilmbildung aufweisen.²⁴¹ Die experimentellen Details und

weiterführende Daten und mikroskopische Bilder der Färbemethoden können der Publikation P-1 im Anhang entnommen werden. Die experimentellen Arbeiten sowie die Auswertung der Rohdaten hierzu wurden durch Herrn Oliver Riester durchgeführt.

Die antimikrobielle Aktivität der beschichteten Oberflächen wurde unter nährstoffreichen und nährstoffarmen Bedingungen untersucht. In nährstoffreichem Medium zeigt sich keine Inhibierung des mikrobiellen Wachstums, wogegen sich unter nährstoffarmen Bedingungen eine Reduzierung der Keimzahl um 1,2-log Stufen bei MRSA für die 5%-GlcNAc-4EG-PDMAm Beschichtung zeigt. Ebenso wurde die Biofilmmasse auf den Oberflächen nach 24, 48 und 72 Stunden mittels Kristallviolett-Färbung, Lebend-Tot-Färbung und Phenol-Schwefelsäure-Methode analysiert. Die Beschichtungen 5%-GlcNAc-4EG-PDMAm und GlcNAc-6EG-PDMAm weisen die stärkste Inhibierung der Biofilmbildung durchweg über einen Zeitraum von bis zu 72 Stunden in allen Messmethoden auf, ferner ist eine signifikante Reduktion des Biofilms in der Lebend-Tot-Färbung sichtbar.

Eine Verringerung der Biofilmbildung verursacht durch GlcNAc ist für *E. coli* in der Literatur bekannt, allerdings nicht sicher für *S. aureus* beschrieben.²²³ Da die antimikrobiellen und biofilmmhemmenden Effekte lediglich unter nährstoffarmen Bedingungen zu beobachten sind, liegt hier eine Beeinträchtigung von Stoffwechsellenzymen nahe. Für Chitosan wurde bereits gezeigt, dass einer der antimikrobiellen Wirkmechanismen die Beeinträchtigung der RNA- und Proteinsynthese ist,^{242–245} was einen Hinweis auf den Wirkmechanismus unter lediglich nährstoffarmen Bedingungen liefert. Unter nährstoffreichen Wachstumsbedingungen der Bakterien liegt genug Substrat für eine RNA- und Proteinsynthese vor.

Insgesamt konnte gezeigt werden, dass sich mit synthetischen Acrylaten im Copolymer mit einem GlcNAc-Methacrylat eine Nachbildung der antimikrobiellen Aktivität des Chitosans erreichen lässt, bei gleichzeitig gegebener Biokompatibilität.

3.2 Benzophenon-modifizierte Chitosanderivate

Da Chitosan selbst antimikrobielle Eigenschaften zeigt, welche abhängig vom Deacetyllierungsgrad sind,⁷⁵ sollte im weiteren Verlauf Chitosan selbst in verschiedenen Verhältnissen mit einer Benzophenoneinheit als Quervernetzer synthetisiert werden und auf die antimikrobiellen und anti-Biofilm Eigenschaften hin untersucht werden. Ferner stand die Zytotoxizität der Oberfläche sowie potenziell inflammatorische oder anti-inflammatorische Effekte der Oberfläche im Zentrum der Untersuchungen. Die Synthese, Charakterisierung der Beschichtung sowie die Untersuchungen auf antimikrobielle Aktivität und Zytotoxizität / Pyrogenität wurden in Publikation P-2 („*Synthesis of a biocompatible benzophenone-substituted chitosan hydrogel as novel coating for PEEK with extraordinary strong antibacterial and anti-biofilm properties*“)

veröffentlicht. Die genauen Details der experimentellen Durchführung der Untersuchungen sowie detaillierte Abbildungen zur Oberflächencharakterisierung, antimikrobiellen Aktivität und Biokompatibilitätsbewertungen können der Publikation P-2 im Anhang sowie dem zugehörigen *Supplementary Material* entnommen werden.

3.2.1 Chemische Synthese und Beschichtung von Oberflächen

Für die Synthese der Benzophenon-Chitosan Polymere wurde Chitosan mittels der freien Aminogruppe mit 4-Benzoylbenzoesäure umgesetzt. Insgesamt wurden 5 verschiedene, stöchiometrische Verhältnisse an 4-Benzoylbenzoesäure eingesetzt, um verschiedene Substitutionsgrade an Benzophenon zu erhalten, vgl. Abbildung 9.

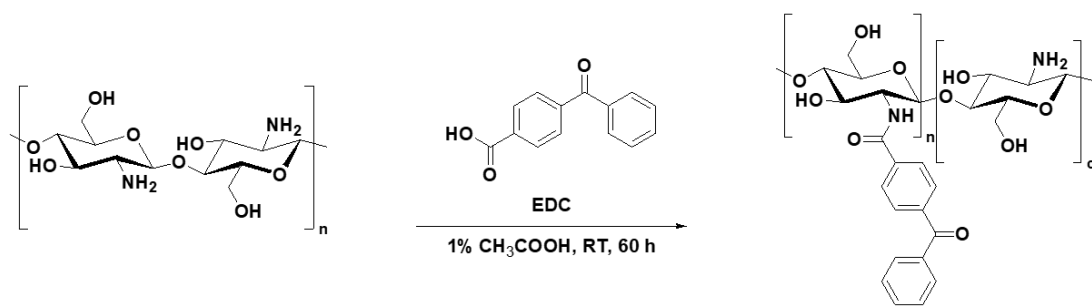


Abbildung 9. Reaktionsschema des Chitosans umgesetzt mit 4-Benzoylbenzoesäure in den in Tabelle 2 dargestellten stöchiometrischen Verhältnissen an EDC und 4-Benzoylbenzoesäure.

Die Substitutionsgrade wurden photometrisch über das Absorptionsmaximum des Benzophenons bei 263 nm gegen eine Kalibrierkurve von 4-Benzoylbenzoesäure in Ethanol bestimmt und sind in Tabelle 2 aufgeführt

Tabelle 2. Synthetisierte Benzophenon-Chitosan Derivate und deren Substitutionsgrad (ds), bestimmt mittels UV/Vis Spektroskopie.

Polymer	EDC	4-Benzoylbenzoesäure	Substitutionsgrad nach Stöchiometrie	Substitutionsgrad bestimmt mittels UV/Vis
100%-BP-CS	1 äq	1 äq	100%	100%
50%-BP-CS	1 äq	0.5 äq	50%	50%
30%-BP-CS	1 äq	0.25 äq	25%	30%
12%-BP-CS	1 äq	0.1 äq	10%	12%
7%-BP-CS	1 äq	0.05 äq	5%	7%

Insgesamt wurde, innerhalb von bis zu 5% Abweichung, das stöchiometrisch eingestellte Einbauverhältnis an Benzophenon zu Glucosamin-Monomeren des Chitosans erhalten. Mittels $^1\text{H-NMR}$ Spektroskopie konnte weiterhin gezeigt werden, dass die Umsetzung selektiv am freien Amin des Chitosans erfolgt, vgl. auch P-2 im Anhang.

Die synthetisierten Chitosanderivate wurden zur Beschichtung von PEEK als Modellmaterial für Implantate verwendet, welches für diverse Knochenimplantate, wie beispielsweise Wirbelsäulenkäfige^{104–107} oder Hüftgelenke^{108–110} verwendet wird. Da PEEK selbst in seiner Monomereinheit eine 4-Phenoxyphenyl-Einheit aufweist, welche chemisch dem Benzophenon ähnlich ist und ebenso eine UV-vermittelte Quervernetzungsreaktion wie das Benzophenon eingehen kann,¹⁴⁷ ist dieses Material insbesondere interessant für die Benzophenon-vermittelte Vernetzungsreaktion der Chitosanbeschichtungen. Die eigentliche Beschichtung wurde mittels *Solvent Casting* der Benzophenon-Chitosan Derivate aus Tabelle 2 auf PEEK-Chips aufgebracht, mittels UV-Licht mit 254 nm Wellenlänge quervernetzt und anschließend physikochemisch mittels IR, XPS, SEM-EDS und AFM charakterisiert.

Der erfolgreiche Beschichtungs- und Quervernetzungsprozess konnte mittels der XPS-Spektren am Beispiel der 100%-BP-CS und 30%-BP-CS Derivate gezeigt werden, in welchen die Elementarverhältnisse an Stickstoff, Sauerstoff und Kohlenstoff den theoretisch ermittelten Werten entsprechen. Diese Werte wurden mittels SEM-EDS reproduziert, wobei die ermittelten Elementarverhältnisse an N, O und C mit 3% Abweichung der 100%-BP-CS Beschichtung dem der XPS-Messungen entsprechen (vgl. Abbildungen S2 und S3 aus dem *Supplementary Material*, Publikation P-2). Hierbei wurde ebenso die Anwesenheit der Carbonylgruppe, der Hydroxygruppe als Reaktionsprodukt der C-H Insertionsreaktion und die Anwesenheit des Chitosan-Benzoesäureamids nachgewiesen. Ferner wurde die Anwesenheit der C-H sowie Hydroxylgruppen im IR-Spektrum durch die Anwesenheit der Banden 2929 cm^{-1} , 2881 cm^{-1} (beides C-H) sowie 3284 cm^{-1} (O-H) für alle Beschichtungen nachgewiesen, was die Anwesenheit von einer Chitosanbeschichtung auf der PEEK Oberfläche bestätigt.

Die Topologie der Oberfläche wurde mittels SEM, AFM und eines Surface Profilers analysiert. In Abhängigkeit vom Substitutionsgrad der Chitosankette ergibt sich entweder eine porenartige Oberfläche oder eine relativ glatte Oberfläche, wobei die Dicke der Beschichtung zwischen $1\text{ }\mu\text{m}$ und $4\text{ }\mu\text{m}$ beträgt. Die Unterschiede in der Oberflächentopologie wurden hier auf verschiedene Gehalte an Benzophenon als Quervernetzer zurückgeführt. Einerseits werden durch Löslichkeitsunterschiede im wässrigen Medium, bedingt durch unterschiedlichen Amidgehalt durch die Funktionalisierung des Chitosans, verschiedene Oberflächentopologien erhalten, wie auch am Beispiel anderer Polymere, beispielsweise Poly- ϵ -Caprolacton, in der Literatur bekannt ist.²⁴⁶ Des Weiteren wurde die gleiche Belichtungszeit mit UV-Licht (3 J/cm^2) auf alle Beschichtungen mit unterschiedlichem Benzophenongehalt angewendet, so dass sich

auch hieraus, bedingt durch unterschiedlich starke Aktivierung des Benzophenons in den biradikaloiden Übergangszustand mit anschließender unterschiedlicher Rekombinationskinetik in der C-H Insertionsreaktion unterschiedliche Ausbeuten an aktiven Crosslinker ergeben. Daraus resultieren anschließend verschiedene Vernetzungsgrade und unterschiedliche Oberflächentopologien der Beschichtung.

3.2.2 Antimikrobielle Aktivität

Die antimikrobiellen Eigenschaften der Chitosanderviate wurden zuerst als Verbindungen in Lösung in einer Konzentrationsreihe untersucht, um den Einfluss der Benzophenonmodifikation sowie des Substitutionsgrades auf die antimikrobiellen Eigenschaften zu evaluieren. Die experimentellen Arbeiten zur antimikrobiellen Aktivität der Oberfläche sowie die Auswertung der Rohdaten wurden durch Oliver Riester durchgeführt. Es wurde mit einer Verdünnungsreihe die IC_{90} der Derivate auf *E. coli* und MRSA(+) *S. aureus* bestimmt, vgl. Tabelle 3. Die bestimmten IC_{90} Werte liegen zwischen 60 und 75 $\mu\text{g/mL}$ für *E. coli* und zwischen 60 und 86 $\mu\text{g/mL}$ für MRSA(+) *S. aureus*, was den bekannten Literaturwerten der MIC von nativem Chitosan von 50 $\mu\text{g/mL}$ gegen *E. coli* und 100 $\mu\text{g/mL}$ gegen *S. aureus* relativ nahe kommt.²⁴⁷ Somit liegt keine signifikante Beeinträchtigung der antimikrobiellen Aktivität durch die Funktionalisierung mit 4-Benzylbenzoesäure vor.

Hierauf aufbauend wurden die mit den Polymeren beschichteten Oberflächen auf antimikrobielle Aktivität untersucht, wobei nach 24 h mit der zu 30%-Benzophenon modifizierten Chitosanverbindung eine antimikrobielle Aktivität der Oberfläche von 5,1 log-Stufen gegen MRSA(+) *S. aureus* und 4,8 log-Stufen gegen *E. coli* erreicht wurde (vgl. Tabelle 3). Analog ist nach 72 Stunden eine Biofilmreduzierung von $98,1 \pm 9 \%$ am Beispiel von *E. coli* und $96,8 \pm 0,1 \%$ am Beispiel von MRSA(+) *S. aureus* im Vergleich zur am wenigsten aktiven Beschichtung (normiert auf 100 %) auf der Oberfläche messbar.

Tabelle 3. Gemessene IC_{90} Werte, log-Werte für antimikrobielle Aktivität der damit beschichteten Oberflächen und die Biofilminhibierung der Oberflächen der unterschiedlich substituierten Benzophenon-Chitosan Derivate aus Tabelle 2.

Polymer	IC_{90} in Lösung		Wachstumshinibierung (log-10) auf Oberfläche		Biofilm auf Beschichtung nach 72 h (in %)	
	<i>E. coli</i>	<i>S. aureus</i>	<i>E. coli</i>	<i>S. aureus</i>	<i>E. coli</i>	<i>S. aureus</i>
100%-BP-CS	75,30 $\mu\text{g/mL}$	65,63 $\mu\text{g/mL}$	2,8	2,8	100 \pm 0 %	97,7 \pm 2,6 %
50%-BP-CS	74,08 $\mu\text{g/mL}$	85,88 $\mu\text{g/mL}$	3,8	2,1	82,1 \pm 5,1 %	87,1 \pm 10,2 %
30%-BP-CS	72,38 $\mu\text{g/mL}$	82,18 $\mu\text{g/mL}$	4,8	5,1	1,9 \pm 9%	3,2 \pm 0,1 %
12%-BP-CS	59,04 $\mu\text{g/mL}$	63,53 $\mu\text{g/mL}$	1,4	5,0	98 \pm 8 %	75,0 \pm 27,5 %
7%-BP-CS	62,71 $\mu\text{g/mL}$	62,74 $\mu\text{g/mL}$	0,7	1,5	63,5 \pm 1,1 %	100 \pm 0 %

3.2.3 Zytotoxizität

Chitosan selbst ist als ein gut biokompatibles Polymer, insbesondere für pharmazeutische Formulierungen als *Drug Delivery Device* bekannt und in zahllosen Publikationen und Reviews hierfür charakterisiert,^{248–251} wobei allerdings in Abhängigkeit von der Dosis zytotoxische Effekte auftreten können.

Die Tests auf Zytotoxizität wurden nach den Protokollen der *United States Pharmacopeia* durchgeführt, welche von der DIN EN ISO-10993-5 referenziert wird.¹⁵⁷ Hierbei kommt die L-929 Fibroblastenzelllinie zum Einsatz, Inkubationszeiten für Kontakttests sind 24 und 72 Stunden, für Extrakttests 24 Stunden.^{159,160} Diese Zelllinie wird ebenso in der wissenschaftlichen Literatur für *in-vitro* Biokompatibilitätsstudien von Medizinprodukten verwendet.^{252,253} Kommt es bei einem Extrakt eines Medizinproduktes zu weniger als 30% Wachstumsinhibierung in den Fibroblastenzellkulturen, kann nach DIN EN ISO-10993-5 davon ausgegangen werden, dass keine Zytotoxizität vorliegt.¹⁵⁷ Experimentelle Details können der Publikation P-2 im Anhang entnommen werden, ebenso detaillierte Auswertungen und mikroskopische Bilder der eingesetzten Zellen in Abbildung 4 der Publikation.

Insgesamt wurde im Extrakttest in Fibroblastenzellkulturen keine Wachstumsinhibierung von mehr als 30% erreicht. Im Kontakttest kam es zu eindeutig zytotoxischen Effekten, teilweise mit mehr als 50% Wachstumsinhibierung für Chitosanderivate mit 100%, 50%, 12% und 7% Benzophenongehalt nach 24 h und auch nach 72 h, wogegen das Chitosanderivat mit 30% Benzophenongehalt die geringste Toxizität, respektive Wachstumsinhibierung mit 20% aufweist. Demnach kann bei der 30%-BP-CS Beschichtung von Biokompatibilität in Hinblick auf Zytotoxizität ausgegangen werden.

Da die Biokompatibilitätsbewertungen immer gewebespezifisch sein sollten, und es sich bei der L-929 Zelllinie um Mausfibroblasten handelt, wurden ferner Zytotoxizitätstests mit humanen Osteoblasten (Saos-2), Endothelzellen (HUVECs) sowie Monozyten (Mono Mac-6) durchgeführt. Im Extrakttest kann auch mit humanen Endothelzellen von Biokompatibilität ausgegangen werden, da weniger als 30% Wachstumsinhibierung vorliegt.²³⁶ Im Kontakttest zeigen Chitosanderivate 100%-BP-CS, 50%-BP-CS, 12%-BP-CS und 7%-BP-CS stark zytotoxische Effekte mit über 60% Wachstumsinhibierung nach 24 h und 72 h wogegen die 30%-BP-CS Beschichtung lediglich 20% Wachstumsinhibierung aufweist und damit als biokompatibel bewertet werden kann (vgl. Abbildung 10). Die stärkeren Werte der Wachstumsinhibierung sind hier durch den Charakter der HUVECs als einer humanen Primärzelllinie bedingt, aufgrund derer es zu einer erhöhten Empfindlichkeit der Zelllinie gegenüber toxischen Einflüssen kommt.

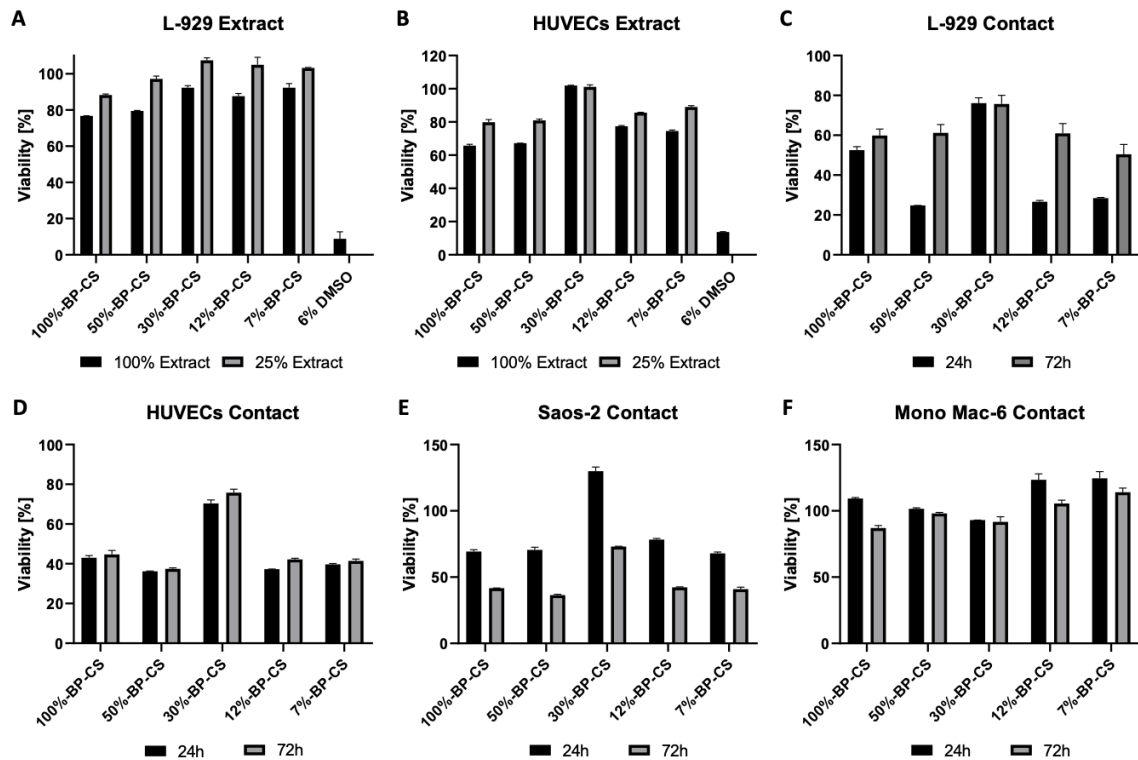


Abbildung 10. Ergebnisse der Zytotoxizitätstests in verschiedenen Zellkulturen im Extrakt- und Kontakttest nach DIN EN ISO-10993-5.¹⁵⁷

Die Saos-2 Osteoblastenzelllinie zeigt die höchste Wachstumsinhibierung nach 72 Stunden, was in diesem Fall durch die langen Verdopplungszyklen der Saos-2 von 40 Stunden bedingt ist.²⁵⁴ Hierdurch kommt es erst nach 72 Stunden zu messbaren Beeinträchtigungen des Zellwachstums, in diesem Falle bei allen Benzophenon-modifizierten Chitosanpolymeren. Benzophenonderivate des *N*-Acetylglucosamins und kurzkettiger Chitooligosaccharide sind für ihre Wirkung als Inhibitoren der Enzymklasse der Matrixmetallopeptidasen bekannt, welche eine starke Aktivität gegenüber Krebszellen des Sarkom-Typs zeigt.^{255,256} Des Weiteren wurde für Glucosamin gezeigt, dass dies das Wachstum von MG-63 und Saos-2 Zelllinien beeinträchtigt.^{257–259} Da es sich bei der Saos-2 Zelllinie um eine Krebszelllinie eines Sarkom-Typs handelt,²⁵⁴ kann hier von einer entsprechenden Aktivität gegenüber den Matrixmetallopeptidasen ausgegangen werden, was wiederum zu einer erhöhten Zytotoxizität der Chitosanbeschichtungen gegenüber diesen Zelllinien führt. Somit ist die Aussagekraft dieses Tests auf Osteokompatibilität begrenzt, da eine Überexpression der MMP-Familie charakteristisch für Osteosarkomzelllinien ist²⁶⁰ und die Inhibierung dieser das Wachstum wiederum beeinträchtigt.^{257–259} Da es sich bei allen Osteoblastenzelllinien, welche sich gegenwärtig permanent in Kultur halten lassen, um Krebszelllinien des Osteosarkom-Typs handelt,²⁵⁴ besteht diese Problematik insgesamt bei Testungen dieser Beschichtung auf Osteokompatibilität.

Diese Unterschiede der Zytotoxizitätsdaten bei Verwendung verschiedener Zelllinien, welche allerdings mit Osteoblasten, Fibroblasten und Endothelzellen sehr gewebespezifisch sind, zeigen gleichzeitig die Problematik der gewebespezifischen Biokompatibilitätsbewertung mit *in-vitro* Tests auf. Für genaue Daten muss hier demnach auf gewebespezifische, idealerweise humane Primärzelllinien, respektive Stammzellen, zurückgegriffen werden, um aussagekräftige Daten über zytotoxische Effekte von Implantaten auf das umliegende Gewebe zu generieren.

Insgesamt wurde aber, abgesehen von den spezifischen Effekten des Chitosans, seiner Monomere und der synthetisierten Chitosanderivate auf die Saos-2 Zelllinie, welche für die spezifischen Verbindungen auf literaturbekannte Effekte zurückgeführt werden konnte, eine nicht-zytotoxische Beschichtung bei Verwendung der L-929 Fibroblastenzelllinie nach DIN EN ISO-10993-5 für das 30% Benzophenon-funktionalisierte Chitosanderivat erhalten.

3.2.4 Inflammatorisches Potential

Zur Bewertung des inflammatorischen Potentials hinsichtlich Pyrogenität und systemische Toxizität werden bislang nach DIN EN ISO-10993-11 *in-vivo* Versuche am Kaninchen durchgeführt, wobei die Erhöhung der Körpertemperatur als Nachweis für Pyrogenität gilt.¹⁶¹ Hierfür werden allerdings eine hohe Zahl an Versuchstieren benötigt, ferner ist die Reproduzierbarkeit über die Versuchstierpopulationen nicht immer gegeben.^{162–164} Zur besseren Durchführbarkeit wurde hier der Monozyten-Aktivierungstest vorgeschlagen, bei welchem menschliche Monozyten (Mono Mac-2 oder Mono Mac-6 Zelllinie) *in-vitro* auf Interleukin-Sekretion, in der Regel IL-1b oder IL-6, getestet werden.^{169–173} Zur Bewertung des inflammatorischen oder potenziell anti-inflammatorischen Potentials wurden Mono Mac-6 Zellen mit und ohne LPS auf den Beschichtungen inkubiert, gefolgt von der Messung der IL-6 Sekretion sowie der IL-1b, IL-8 und IL-10 Genexpression. Experimentelle Details können der Publikation P-2 im Anhang entnommen werden.

Es wurden um ca. 100% erhöhte IL-6-Konzentrationen im überstehenden Medium für die 100%-BP-CS, 50%-BP-CS und 12%-BP-CS Beschichtung gemessen, während die 30%-BP-CS Beschichtung keine signifikant erhöhte IL-6 Sekretion verursacht. Die 7%-BP-CS Beschichtung zeigt eine um ca. 40% erhöhte IL-6 Sekretion. Die geringere IL-6 Sekretion geht hier einher mit einer glatteren Oberflächentextur, welche mittels SEM und AFM bestimmt wurde, womit die erhöhten Werte für die 100%, 50% und 12%-BP-CS Beschichtung auf die schwammartige Texturierung der Oberfläche zurückgeführt werden kann. Dies entspricht den Beobachtungen zu Oberflächenstrukturierung und Biokompatibilität, wobei die Oberflächenrauigkeit und -textur einen signifikanten Einfluss auf Biokompatibilität und inflammatorische Eigenschaften einer Implantatoberfläche hat.²⁶¹ Die gemessenen Daten über die IL-6

Sekretion werden ebenso von den Genexpressionsdaten von IL-1b, IL-8 und IL-10 bestätigt, bei welchen die 30%-BP-CS Beschichtung keine erhöhte Genexpression dieser Interleukine zur Folge hat.

3.3 Fluoreszent-markiertes L-Kynurenin

Kynurenin ist ein vielversprechender Biomarker für Abstoßungsreaktionen von Transplantaten^{199–201,262} sowie von Implantaten.^{202,204,263} Bislang ist in der Literatur aber kein hinreichend sensitiver Schnelltest mittels eines Antikörpers auf L-Kynurenin bekannt, welcher eine hinreichende Sensitivität unter physiologischen Bedingungen auf die physiologisch relevanten Konzentrationen an L-Kynurenin liefert. Der Ansatz von Klockow et. al.,²¹² funktioniert über eine Umsetzung des aromatischen Amins des L-Kynurenins mit einem Aldehyd. Hier kommt es durch ein Cumarin-Derivat *in-situ* durch Ausbildung eines Imins zwischen dem aromatischen Amin des Kynurenins und eines Aldehyds am Cumarinderivat zu einer pH-Wert abhängigen Fluoreszenz mit Emissionsmaximum bei 555 nm.²¹² Da allerdings die Epitoperkennung von Aminosäuren, insbesondere bei kurzkettigen Epitopen oder gar Epitopen, welche aus einzelnen Aminosäuren bestehen, über die Seitenkette erfolgt,²⁶⁴ ist hier die Erkennung mittels eines Anti-Kynurenin-Antikörpers fraglich. Des Weiteren wäre eine Änderung des pH-Wertes zur Induzierung einer Fluoreszenz erforderlich, was die Entwicklung eines Schnelltests hieraus ausschließt.

3.3.1 Synthesestrategie

Aufbauend auf diesen literaturbekannten Verbindungen wurde der Ansatz eines fluoreszenten Rhodamin B gewählt, welches mittels eines verbrückenden Azidotetraethylenglycol-Linkers an die freie Carboxygruppe des L-Kynurenins sowie mit der Azidogruppe mittels Huisgen 1,3-dipolarer Cycloaddition („Click-Chemie“⁷⁹) an ein Propargyl-Rhodamin B ligiert wurde. Hierzu wurde die freie Aminogruppe des Kynurenins Boc-geschützt, gefolgt von einer Veresterung der (aktivierten) Carboxygruppe *via* Steglich mit einem Azidotetraethylenglycol, welche Ausbeuten von 33% liefert. Die weitere Umsetzung mit einem Propargyl-Rhodamin B liefert Ausbeuten von 90%, welche charakteristisch für die *Click-Chemie* mittels der Huisgen 1,3-dipolare Cycloaddition sind.⁷⁹ Entschützen der Boc-Aminogruppe liefert das finale Produkt nach Aufarbeitung in 26% Ausbeute. Als Kontrolle für die Antikörper-Bindung wurde ebenso das Propargyl-Rhodamin B mit einem Azidotetraethylenglycol-Linker mittels der ClickChemie umgesetzt, was Ausbeuten von 95% liefert.

Die Emissionsmaxima der Rhodamin B Konjugate wurden zu 586 nm bestimmt, welchem mit den Literaturwerten für natives Rhodamin B übereinstimmen. Die Absorptionsmaxima sind um 6 nm zu 560 nm verschoben, im Vergleich zu 554 nm für natives Rhodamin B.²⁶⁵

3.3.2 Testentwicklung und Detektion von L-Kynurenin

Als Modell für eine Schnelltestentwicklung wurden die Anti-Kynurenin Antikörper mittels EDC/NHS an magnetische Beads konjugiert und in einem kompetitiven Assay die Verdrängung von nativem L-Kynurenin bestimmt. Die experimentellen Arbeiten hierzu wurden seitens von Frau Isabel Quint durchgeführt, experimentelle Details können der Publikation P-3 entnommen werden. Es wurde kein K_D -Wert von 5,9 μM für die Bindung des Rhodamin B markierten L-Kynurenins an den Antikörper gefunden, womit unspezifische Interaktionen ausgeschlossen werden konnten. Ferner konnte die IC_{50} zur Verdrängung von nativem L-Kynurenin zu 4,0 μM in PBS und 10,2 μM in künstlichem Speichel bestimmt werden.

4 Zusammenfassung

Im ersten Teil der Dissertation wurde eine Reihe an *N*-Acetylglucosamin-methacryloyl Derivaten synthetisiert und mit Methacryloylbenzophenon und Dimethacrylamid in verschiedenen stöchiometrischen Verhältnissen copolymerisiert. Die stöchiometrisch vorgesehenen Verhältnisse an Methacryloyl-GlcNAc und Dimethacrylamid wurden erhalten. Die Polymere wurden mittels einer C-H Insertionsreaktion, vermittelt durch das copolymerisierte Methacryloylbenzophenon, erfolgreich in ein polymeres Hydrogel auf einer PETG Oberfläche als Modellmaterial quervernetzt. Die Beschichtungen mit GlcNAc-Methacrylat im Copolymer zeigen antimikrobielle Aktivität von bis zu 1,2 log-Stufen gegenüber MRSA(+) *S. aureus*. Die Biofilmbildung wird am Beispiel von *E. coli* und MRSA(+) *S. aureus* verhindert. Die Zytotoxizität wurde nach DIN EN ISO-10993-5 mit L-929 Fibroblasten getestet, wobei nur eine geringe Wachstumsinhibierung kleiner als 30% festgestellt wurde. Insgesamt zeigt diese Beschichtung einen interessanten Ansatz hinsichtlich der Oberflächenfunktionalisierung von Implantaten, welche antiadhäsive und antimikrobielle Verbindungen enthalten bei gleichzeitig geringer Zytotoxizität.

Der Ansatz der Benzophenon-vernetzten Polymere als kovalent gebundene Oberflächenbeschichtung wurde demnach weiter auf Chitosan selbst ausgedehnt. Chitosan wurde in fünf verschiedenen stöchiometrischen Verhältnissen mit 4-Benzylbenzoesäure umgesetzt, um verschiedene Substitutionsgrade an Benzophenon am Chitosan zu erhalten. Die Reaktion verläuft regioselektiv an der freien Aminogruppe des Chitosans. Die stöchiometrisch vorhergesehenen Verhältnisse (100%, 50%, 25%, 10% und 5%) wurden im Substitutionsgrad mit 100%, 50%, 30%, 12% und 7% ungefähr erhalten und photometrisch bestimmt. Die daraus erhaltenen Oberflächenbeschichtungen wurden mittels IR, XPS, SEM-EDS chemisch charakterisiert. Die entsprechenden Substitutionsgrade von 100% und 30% Benzophenon finden sich im XPS-Spektrum der zugehörigen Beschichtungen wieder, des Weiteren im SEM-EDS Spektrum. Chitosan selbst wurde mittels IR, XPS und SEM-EDS nachgewiesen. Die Oberflächeneigenschaften wurden mittels SEM, AFM und eines *Surface Profilers* analysiert, wobei raue Oberflächen mit Rauigkeiten von 300 – 700 nm (R_a und R_q) erhalten wurden. Die Dicke der Beschichtungen wurde zu 1 – 4 μm bestimmt.

Die Zytotoxizität wurde nach DIN EN ISO-10993-5 mit vier verschiedenen Zelllinien bestimmt, wobei die 30%-BP-CS Beschichtung die geringste Zytotoxizität aufweist und mit unter 30% Wachstumshemmung als nicht-zytotoxisch betrachtet werden kann. Ferner ist kein inflammatorisches Potential der Oberfläche (Pyrogenität) bei einem Monozyten-Aktivierungstest auf sekretierte (IL-6) oder überexprimierte (IL-1b, IL-8, IL-10) Interleukine nachweisbar. Diese Beschichtung zeigt ebenso eine antimikrobielle Aktivität von 5,1 log-Stufen gegen MRSA(+) *S. aureus* und *E. coli*.

Mit diesen beiden Ansätzen, welche beide in Publikationen in Peer Review Journals veröffentlicht wurden (vgl. P-1 und P-2 im Anhang) wurde die Machbarkeit einer antibakteriellen Oberflächenbeschichtung, welche sich für photolithographische Zwecke eignet, am Beispiel von PEEK als Implantatmaterial demonstriert. Ferner wurden Zusammenhänge zwischen dem Gehalt an Benzophenon *Crosslinker* und der Biokompatibilität, der antimikrobiellen Aktivität und der erhaltenen Oberflächentopologie der Beschichtung untersucht. Zusammenhänge zwischen verbrückenden Oligoethylenglycol-Linkern und den Copolymergehalt an *N*-Acetylglucosamin und der antimikrobiellen Aktivität der Polymere wurden untersucht und hergestellt, wobei sich ein GlcNAc-Gehalt von 5% in Verbindung mit einem Tetraethylenglycol-Linker als am wirkungsvollsten herausgestellt hat. Hierbei wurde eine antimikrobielle Aktivität von 1,2 log-Stufen gegen MRSA(+) *S. aureus* erreicht. Ferner wurde der Einfluss der Linkerlänge auf die Zytotoxizität, respektive Biokompatibilität untersucht, wobei sich Linkerlängen mit mehr als vier Ethylenglycoleinheiten als am besten biokompatibel herausgestellt haben. Die antimikrobielle Aktivität dieser Polymere als Oberflächenbeschichtungen wurde durch Benzophenon-modifizierte Chitosanderivate noch übertroffen, bei welchen eine antimikrobielle Aktivität von 5,1 log-Stufen gegen MRSA(+) *S. aureus* erreicht wurde, bei gleichzeitig geringer Zytotoxizität und damit gegebener Biokompatibilität.

Im weiteren Teil der Arbeit (vgl. Publikation P-3) wurde gezeigt, dass sich ein fluoreszent markiertes L-Kynurenin Derivat mittels eines Antikörpers gegen L-Kynurenin als Biomarker für Abstoßungsreaktionen nachweisen lässt, wobei die Nachweisgrenze den Bereich der physiologisch relevanten Konzentrationen für L-Kynurenin bei Abstoßungsreaktionen umfasst. Hiermit besteht ebenso ein interessantes Werkzeug zur weiteren klinischen Bewertung von möglichen Abstoßungsreaktionen im Rahmen der Biokompatibilitätsbewertung von Medizinprodukten.

5 Literaturverzeichnis

1. Weinstein RA, Darouiche RO. *Clin. Infect. Dis.* 2001; 33: 1567–1572.
2. Kurtz SM, Ong KL, Lau E, Bozic KJ, Berry D, Parvizi J. *Clin. Orthop. Relat. Res.* 2010; 468: 52–56.
3. Dale H, Hallan G, Espehaug B, Havelin LI, Engesaeter LB. *Acta Orthop.* 2009; 80: 639–645.
4. Sharkey PF, Lichstein PM, Shen C, Tokarski AT, Parvizi J. *J. Arthroplasty.* 2014; 29: 1774–1778.
5. Costerton JW, Stewart PS, Greenberg EP. *Science.* 1999; 284: 1318.
6. Zimmerli W, Widmer AF, Blatter M, Frei R, Ochsner PE. *J. Am. Med. Assoc.* 1998; 280: 1537–1541.
7. Davey ME, O’toole GA. *Microbiol. Mol. Biol. Rev.* 2000; 64: 847–867.
8. Dapunt U, Hänsch G, Arciola C. *Materials.* 2016; 9: 387.
9. Lin J, Yang X, Bostrom MPG. *J. Chemother.* 2001; 13: 54–65.
10. Westrich GH, Walcott-Sapp S, Bornstein LJ, Bostrom MP, Windsor RE, Brause BD. *J. Arthroplasty.* 2010; 25: 1015–1021.
11. Lieberman JR, Callaway GH, Salvati EA, Pellicci PM, Brause BD. *Clin. Orthop. Relat Res.* 1994; 301: 205–212.
12. Toulson C, Walcott-Sapp S, Hur J, Salvati E, Bostrom M, Brause B, Westrich GH. *J. Arthroplasty.* 2009; 24: 1051–1060.
13. Teerawattanapong N, Panich P, Kulpokin D, Na Ranong S, Kongpakwattana K, Saksinanon A, Goh BH, Lee LH, Apisarnthanarak A, Chaiyakunapruk N. *Infect. Control. Hosp. Epidemiol.*, 2018, 39, 525–533.
14. Gristina AG. *Science.* 1987; 237: 1588.
15. Busscher HJ, van der Mei HC, Subbiahdoss G, Jutte PC, van den Dungen JJAM, Zaat SAJ, Schultz MJ, Grainger DW. *Sci. Transl. Med.* 2012; 4: 153rv10–153rv10.
16. Poelstra KA, Barekzi NA, Rediske AM, Felts AG, Slunt JB, Grainger DW. *J. Biomed. Mater. Res.* 2002; 60: 206–215.
17. Darouiche RO, Landon GC, Patti JM, Nguyen LL, Fernau RC, Mcdevitt D, Greene C, Foster T, Klima M. *J. Med. Microbiol.* 1997; 46: 75–79.
18. Fux CA, Costerton JW, Stewart PS, Stoodley P. *Trends. Microbiol.* 2005; 13: 34–40.
19. Vuong C, Voyich JM, Fischer ER, Braughton KR, Whitney AR, DeLeo FR, Otto M. *Cell Microbiol.* 2004; 6: 269–275.
20. Colilla M, Izquierdo-Barba I, Vallet-Regí M. *Medicines.* 2018; 5: 125.
21. Schmidmaier G, Lucke M, Wildemann B, Haas NP, Raschke M. *Injury.* 2006; 37: S105–S112.
22. de Kraker MEA, Stewardson AJ, Harbarth S. *PLoS Med.* 2016; 13: e1002184.
23. Humphreys G, Fleck F. United Nations: *Bull. World. Health. Organ*, 2016, 94, 638–639.
24. Kargupta R, Bok S, Darr CM, Crist BD, Gangopadhyay K, Gangopadhyay S, Sengupta S. *Wiley Interdiscip Rev. Nanomed. Nanobiotechnol.* 2014; 6: 475–495.
25. Brooks BD, Brooks AE. *Adv. Drug Deliv. Rev.*, 2014, 78, 14–27.
26. Murata H, Koepsel RR, Matyjaszewski K, Russell AJ. *Biomaterials.* 2007; 28: 4870–4879.
27. Tiller JC, Liao C-J, Lewis K, Klibanov AM. *Proc. Natl. Acad. Sc. U.S.A.* 2001; 98: 5981–5985.
28. Samal SK, Dash M, van Vlierberghe S, Kaplan DL, Chiellini E, van Blitterswijk C, Moroni L, Dubruel P. *Chem. Soc. Rev.* 2012; 41: 7147–7194.
29. Huang J, Murata H, Koepsel RR, Russell AJ, Matyjaszewski K. *Biomacromolecules.* 2007; 8: 1396–1399.

30. Lee SB, Koepsel RR, Morley SW, Matyjaszewski K, Sun Y, Russell AJ. *Biomacromolecules*. 2004; 5: 877–882.
31. Madkour AE, Dabkowski JM, Nüsslein K, Tew GN. *Langmuir*. 2009; 25: 1060–1067.
32. Yang L, Weiss TM, Lehrer RI, Huang HW. *Biophys. J.* 2000. 2002–2009.
33. Shai Y. *Biochimica et Biophysica Acta (BBA) - Biomembranes*. 1999; 1462: 55–70.
34. Matsuzaki K. *Biochimica et Biophysica Acta (BBA) - Biomembranes*. 1999; 1462: 1–10.
35. Ludtke SJ, He K, Heller WT, Harroun TA, Yang L, Huang HW. *Biochemistry*. 1996; 35: 13723–13728.
36. Matsuzaki K, Murase O, Tokuda H, Funakoshi S, Fujii N, Miyajima K. *Biochemistry*. 1994; 33: 3342–3349.
37. Gazit E, Miller IR, Biggin PC, Sansom MSP, Shai Y. *J. Mol. Biol.* 1996; 258: 860–870.
38. Milović NM, Wang J, Lewis K, Klibanov AM. *Biotechnol. Bioeng.* 2005; 90: 715–722.
39. Lin J, Tiller JC, Lee SB, Lewis K, Klibanov AM. *Biotechnol. Lett.* 2002; 24: 801–805.
40. Lin J, Murthy SK, Olsen BD, Gleason KK, Klibanov AM. *Biotechnol. Lett.* 2003; 25: 1661–1665.
41. Ikeda T, Hirayama H, Yamaguchi H, Tazuke S, Watanabe M. *Antimicrob Agents Chemother.* 1986; 30: 132–136.
42. Ikeda T, Yamaguchi H, Tazuke S. *Antimicrob. Agents Chemother.* 1984; 26: 139–144.
43. Isquith AJ, Abbott EA, Walters PA. *Appl. Microbiol.* 1972; 24: 859–863.
44. Shai Y. *Biopolymers*. 2002; 66: 236–248.
45. Bocchinfuso G, Palleschi A, Orioni B, Grande G, Formaggio F, Toniolo C, Park Y, Hahn K-S, Stella L. *J. Pept. Sc.* 2009; 15: 550–558.
46. Yeul VS, Rayalu SS. *J. Polym. Environ.* 2013; 21: 606–614.
47. Mima S, Miya M, Iwamoto R, Yoshikawa S. *J. Appl. Polym. Sci.* 1983; 28: 1909–1917.
48. Luz GM, Boesel L, Campo A del, Mano JF. *Langmuir*. 2012; 28: 6970–6977.
49. Wang Y, Shi R, Gong P, Li J, Li J, Ao D, Wang P, Yang Y, Man Y, Qu Y. *J. Bioact. Compat. Polym.* 2012; 27: 122–132.
50. Kim I-Y, Seo S-J, Moon H-S, Yoo M-K, Park I-Y, Kim B-C, Cho C-S. *Biotechnol. Adv.* 2008; 26: 1–21.
51. Sivashankari PR, Prabakaran M. *Int. J. Biol. Macromol.* 2016; 93: 1382–1389.
52. Liu Z, Wang H, Wang Y, Lin Q, Yao A, Cao F, Li D, Zhou J, Duan C, Du Z, Wang Y, Wang C. *Bio-materials*. 2012; 33: 3093–3106.
53. Shi W, Nie D, Jin G, Chen W, Xia L, Wu X, Su X, Xu X, Ni L, Zhang X, Zhang X, Chen J. *Biomaterials*. 2012; 33: 3119–3126.
54. Jayakumar R, Prabakaran M, Sudheesh Kumar PT, Nair SV, Tamura H. *Biotechnol. Adv.* 2011; 29: 322–337.
55. Jayakumar R, Prabakaran M, Nair SV, Tokura S, Tamura H, Selvamurugan N. *Prog. Mater. Sci.* 2010; 55: 675–709.
56. Vårum KM, Ottøy MH, Smidsrød O. *Carbohydr. Polym.* 1994; 25: 65–70.
57. Sorlier P, Viton C, Domard A. *Biomacromolecules*. 2002; 3: 1336–1342.
58. Blagodatskikh I v., Kulikov SN, Vyshivannaya O v., Bezrodnykh EA, Yamskov IA, Tikhonov VE. *Carbohydr. Res.* 2013; 381: 28–32.
59. Diab MA, El-Sonbati AZ, Bader DMD. *Spectrochim. Acta. A Mol. Biomol. Spectrosc.* 2011; 79: 1057–1062.
60. He P, Davis SS, Illum L. *Int. J. Pharm.* 1998; 166: 75–88.
61. Samprasit W, Kaomongkolgit R, Sukma M, Rojanarata T, Ngawhirunpat T, Opanasopit P. *Carbohydr. Polym.* 2015; 117: 933–940.

-
62. Izano EA, Sadovskaya I, Vinogradov E, Mulks MH, Velliyagounder K, Ragunath C, Kher WB, Ramasubbu N, Jabbouri S, Perry MB, Kaplan JB. *Microb. Pathog.* 2007; 43: 1–9.
 63. Zheng Y, Pan N, Liu Y, Ren X. *Carbohydr. Polym.* 2021; 253: 117205.
 64. Wang QZ, Chen XG, Liu N, Wang SX, Liu CS, Meng XH, Liu CG. *Carbohydr. Polym.* 2006; 65: 194–201.
 65. Kurtzman NA. In *Urolithiasis* Springer US: Boston, MA, 1989; 19–22.
 66. Helander IM, Nurmiaho-Lassila EL, Ahvenainen R, Rhoades J, Roller S. *Int. J. Food. Microbiol.* 2001; 71: 235–244.
 67. Je JY, Kim SK. *J Agric Food Chem.* 2006; 54: 6629–6633.
 68. Divya K, Vijayan S, George TK, Jisha MS. *Fibers and Polymers.* 2017; 18: 221–230.
 69. Chien RC, Yen MT, Mau JL. *Carbohydr. Polym.* 2016; 138: 259–264.
 70. Li X, Feng X, Yang S, Fu G, Wang T, Su Z. *Carbohydr. Polym.* 2010; 79: 493–499.
 71. Carlson RP, Taffs R, Davison WM, Stewart PS. *J Biomater. Sci. Polym. Ed.* 2008; 19: 1035–1046.
 72. Liu X, Song L, Li L, Li S, Yao K. *J. Appl. Polym. Sci.* 2007; 103: 3521–3528.
 73. Fei Liu X, Lin Guan Y, Zhi Yang D, Li Z, de Yao K. *J. Appl. Polym. Sci.* 2001; 79: 1324–1335.
 74. Varma AJ, Deshpande SV, Kennedy JF. *Carbohydr. Polym.* 2004; 55: 77–93.
 75. Sahariah P, Másson M. *Biomacromolecules.* 2017; 18: 3846–3868.
 76. Chung Y. *Bioresour. Technol.* 2003; 88: 179–184.
 77. Liu H. *Carbohydr. Polym.* 2004; 55: 291–297.
 78. Liu H, Du Y, Wang X, Sun L. *Int. J. Food Microbiol.* 2004; 95: 147–155.
 79. Kolb HC, Finn MG, Sharpless KB. *Angew. Chem. Int. Ed.* 2001; 40: 2004–2021.
 80. Kolb HC, Sharpless KB. *Drug. Discov. Today*, 2003, 8, 1128–1137.
 81. Huisgen R. *Pure Appl. Chem.* 1989; 61: 613–628.
 82. Huisgen R, Szeimies G, Möbius L. *Chem. Ber.* 1967; 100: 2494–2507.
 83. Huisgen R, Knorr R, Möbius L, Szeimies G. *Chem. Ber.* 1965; 98: 4014–4021.
 84. Huisgen R. *Angew. Chem.* 1963; 75: 604–637.
 85. Huisgen R. *Angew. Chem.* 1963; 75: 742–754.
 86. Huisgen R, Szeimies G, Möbius L. *Chem. Ber.* 1967; 100: 2494–2507.
 87. Huisgen R, Knorr R, Möbius L, Szeimies G. *Chem. Ber.* 1965; 98: 4014–4021.
 88. Tornøe CW, Christensen C, Meldal M. *J. Org. Chem.* 2002; 67: 3057–3064.
 89. Rostovtsev V v., Green LG, Fokin V v., Sharpless KB. *Angew. Chem. Int. Ed.* 2002; 41: 2596–2599.
 90. Zhang L, Chen X, Xue P, Sun HHY, Williams ID, Sharpless KB, Fokin V v., Jia G. *J. Am. Chem. Soc.* 2005; 127: 15998–15999.
 91. Rasmussen LK, Boren BC, Fokin V v. *Org. Lett.* 2007; 9: 5337–5339.
 92. Golas PL, Matyjaszewski K. *Chem. Soc. Rev.* 2010; 39: 1338–1354.
 93. Bonandi E, Christodoulou MS, Fumagalli G, Perdicchia D, Rastelli G, Passarella D. *Drug Discov Today*. 2017; 22: 1572–1581.
 94. Tron GC, Piralì T, Billington RA, Canonico PL, Sorba G, Genazzani AA. *Med. Res. Rev.* 2008; 28: 278–308.
 95. Csuk R, Deigner H-P. *Bioorg. Med. Chem. Lett.* 2019; 29: 949–958.
 96. Wang L, Chen J, Shi L, Shi Z, Ren L, Wang Y. *ChemComm.* 2014; 50: 975–977.
 97. Głowacka IE, Grzonkowski P, Lisiecki P, Kalinowski Ł, Piotrowska DG. *Arch. Pharm. (Weinheim)*. 2019; 352: 1800302.
 98. el Malah T, Nour HF, Satti AAE, Hemdan BA, El-Sayed WA. *Molecules.* 2020; 25: 790.
 99. Kolb HC, Finn MG, Sharpless KB. *Angew. Chem. Int. Ed.* 2001; 40: 2004–2021.
-

100. Kolb HC, Sharpless KB. *Drug. Discov. Today*. 2003; 8: 1128–1137.
101. Garcia-Gonzalez D, Rusinek A, Jankowiak T, Arias A. *Compos. Struct.* 2015; 124: 88–99.
102. Kurtz SM, Devine JN. *Biomaterials*. 2007; 28: 4845–4869.
103. Godara A, Raabe D, Green S. *Acta Biomater.* 2007; 3: 209–220.
104. Brantigan JW, Steffee AD, Lewis ML, Quinn LM, Persenaire JM. *Spine*. 2000; 25: 1437–1446.
105. Cho D-Y, Liao W-R, Lee W-Y, Liu J-T, Chiu C-L, Sheu P-C. *Neurosurgery*. 2002; 51: 1343–1350.
106. Brantigan JW, Neidre A, Toohey JS. *Spine J.* 2004; 4: 681–688.
107. Toth JM, Wang M, Estes BT, Scifert JL, Seim HB, Turner AS. *Biomaterials*. 2006; 27: 324–334.
108. Wang A, Lin R, Stark C, Dumbleton JH. *Wear*. 1999; 225–229: 724–727.
109. Glassman AH, Crowninshield RD, Schenck R, Herberts P. In *Clin. Orthop. Relat. Res.* 2001; 393: 128–136.
110. Akhavan S, Matthiesen MM, Schulte L, Penoyar T, Kraay MJ, Rimnac CM, Goldberg VM. *J. Bone. Joint Surg. Am.* 2006; 88: 1308–1314.
111. el Halabi F, Rodriguez JF, Rebolledo L, Hurtós E, Doblaré M. *J Mech Behav Biomed Mater.* 2011; 4: 1819–1832.
112. Lovald S, Kurtz SM. In *PEEK Biomaterials Handbook* Elsevier, 2012; 243–260.
113. Hoskins TJ, Dearn KD, Kukureka SN. *Polym Test.* 2018; 70: 511–519.
114. Rinaldi M, Ghidini T, Cecchini F, Brandao A, Nanni F. *Compos B Eng.* 2018; 145: 162–172.
115. Hu B, Duan X, Xing Z, Xu Z, Du C, Zhou H, Chen R, Shan B. *Mech. Mater.* 2019; 137: 103139.
116. Berretta S, Evans K, Ghita O. *Mater Des.* 2018; 139: 141–152.
117. Najeeb S, BDS ZK, BDS SZ, BDS MSZ. *J Oral Implantol.* 2016; 42: 512–516.
118. Blendinger F, Seitz D, Ottenschläger A, Fleischer M, Bucher V. *ACS Appl Mater Interfaces.* 2021; 13: 3536–3546.
119. Diouf-Lewis A, Farahani RD, Iervolino F, Pierre J, Abderrafai Y, Lévesque M, Piccirelli N, Therriault D. *Mater Today Commun.* 2022; 31: 103445.
120. Oladapo BI, Zahedi SA. *Mater Chem Phys.* 2021; 266: 124485.
121. Hu K, Yang Z, Zhao Y, Wang Y, Luo J, Tuo B, Zhang H. *Langmuir.* 2022; 38: 5924–5933.
122. Pandiyarajan CK, Prucker O, Zieger B, Rühle J. *Macromol Biosci.* 2013; 13: 873–884.
123. Pandiyarajan CK, Prucker O, Zieger B, Rühle J. *Macromol Biosci.* 2013; 13: 873–884.
124. Dormán G, Nakamura H, Pulsipher A, Prestwich GD. *Chem Rev.* 2016; 116: 15284–15398.
125. Dormán G, Prestwich GD. *Biochemistry.* 1994; 33: 5661–5673.
126. Prucker O, Brandstetter T, Rühle J. *Biointerphases.* 2018; 13: 010801.
127. Hassan MM, Olaoye OO. *Molecules.* 2020; 25: 2285.
128. Prucker O, Naumann CA, Rühle J, Knoll W, Frank CW. *J Am Chem Soc.* 1999; 121: 8766–8770.
129. Pidhatika B, Zhao N, Zinggeler M, Rühle J. *J. Polym. Res.* 2019; 26: 1–12.
130. Samyn P, Biesalski M, Prucker O, Rühle J. *J Photochem Photobiol A Chem.* 2019; 377: 80–91.
131. Scherag FD, Niestroj-Pahl R, Krusekopf S, Lücke K, Brandstetter T, Rühle J. *Anal Chem.* 2017; 89: 1846–1854.
132. Scherag FD, Mader A, Zinggeler M, Birsner N, Kneusel RE, Brandstetter T, Rühle J. *Biomacromolecules.* 2018; 19: 4641–4649.
133. Yuan L, Qu B, Chen J, Lv H, Yang X. *Polym Chem.* 2019; 10: 4859–4865.
134. Iwasaki Y, Bunuasunthon S, Hoven VP. *ChemComm.* 2020; 56: 5472–5475.
135. Liu Q, Locklin JL. *ACS Omega.* 2020; 5: 9204–9211.
136. Ishihara K, Suzuki K, Inoue Y, Fukazawa K. *J Biomater Sci Polym Ed.* 2020; 32: 419–437.

137. Koc J, Schönemann E, Wanka R, Aldred N, Clare AS, Gardner H, Swain GW, Hunsucker K, Laschewsky A, Rosenhahn A. *Biofouling*. 2020; 36: 646–659.
138. Orelma H, Vuoriluoto M, Johansson LS, Campbell JM, Filpponen I, Biesalski M, Rojas OJ. *RSC Adv*. 2016; 6: 85100–85106.
139. Büchi G, Inman CG, Lipinsky ES. *J Am Chem Soc*. 1954; 76: 4327–4331.
140. Encinas S, Belmadoui N, Climent MJ, Gil S, Miranda MA. *Chem Res Toxicol*. 2004; 17: 857–862.
141. Varghese AJ. *Photochem Photobiol*. 1975; 21: 147–151.
142. Belmadoui N, Encinas S, Climent MJ, Gil S, Miranda MA. *Eur. J. Chem*. 2006; 12: 553–561.
143. Demeter A, Horváth K, Böör K, Molnár L, Soós T, Lendvay G. *Journal of Physical Chemistry A*. 2013; 117: 10196–10210.
144. Dorman G, Prestwich GD. *Biochemistry*. 1994; 33: 5661–5673.
145. Körner M, Prucker O, Rühle J. *Macromolecules*. 2016; 49: 2438–2447.
146. Broadbent SR, Hammersley JM. *Math. Proc. Cambridge Philos. Soc*. 1957; 53: 629–641.
147. Kyomoto M, Ishihara K. *ACS Appl Mater Interfaces*. 2009; 1: 537–542.
148. Kyomoto M, Moro T, Yamane S, Hashimoto M, Takatori Y, Ishihara K. *Biomaterials*. 2013; 34: 7829–7839.
149. Kyomoto M, Moro T, Takatori Y, Kawaguchi H, Nakamura K, Ishihara K. *Biomaterials*. 2010; 31: 1017–1024.
150. Fristrup CJ, Jankova K, Hvilsted S. *Polym. Chem*. 2010; 1: 1696–1701.
151. Yameen B, Álvarez M, Azzaroni O, Jonas U, Knoll W. *Langmuir*. 2009; 25: 6214–6220.
152. Peters K, Unger RE, Kirkpatrick CJ. In *Biomedical Materials* Springer International Publishing: Cham, 2021; 423–453.
153. European Union. Regulation (EU) 2017/745 of the European Parliament and of the Council of 5 April 2017 on medical devices, amending Directive 2001/83/EC, Regulation (EC) No 178/2002 and Regulation (EC) No 1223/2009 and repealing Council Directives 90/385/EEC and 93/42/EE. *Official Journal of the European Union*. 2017.
154. DIN EN ISO 14971:2013 Medical devices - Application of risk management to medical devices, .
155. ISO 10993-1:2009 - Biological evaluation of medical devices -- Part 1: Evaluation and testing within a risk management process, 2009.
156. Goode J. FDA Guidance Document: Use of International Standard ISO 10993-1, “Biological evaluation of medical devices - Part 1: Evaluation and testing within a risk management process,” 2016.
157. ISO 10993-5:2009 Biological evaluation of medical devices — Part 5: Tests for in vitro cytotoxicity, .
158. The United States pharmacopeia. The National formulary, Rockville, Md. : United States Pharmacopoeial Convention, Inc., 1979.
159. In *The United States pharmacopeia. The National formulary* Rockville, Md. :United States Pharmacopoeial Convention, Inc., 1979; Vol. 35, pp 92–94.
160. In *The United States pharmacopeia. The National formulary* Rockville, Md. :United States Pharmacopoeial Convention, Inc., 1979; pp 94–98.
161. ISO 10993-11:2017 Biological evaluation of medical devices — Part 11: Test for systemic toxicity.
162. Wilsnack RE. *Biomater Med Devices Artif Organs*. 1976; 4: 235–261.
163. Greisman SE, Hornick RB. *Exp Biol Med*. 1969; 131: 1154–1158.
164. Lipton JM, Ticknor CB. *J Physiol*. 1979; 295: 263–272.
165. Levin J. *Prog Clin Biol Res*. 1985; 189: 3–30.
166. Fink PC, Lehr L, Urbaschek RM, Kozak J. *Klin Wochenschr*. 1981; 59: 213–218.

-
167. Pearson FC, Bohon J, Lee W, Bruszer G, Sagona M, Jakubowski G, Dawe R, Morrison D, Dinarello C. *Appl Environ Microbiol.* 1984; 48: 1189–1196.
 168. Food and Drug Administration: FDA Guidance Document: Guidance for Industry Pyrogen and Endotoxins Testing: Questions and Answers. 2012; 1–10.
 169. Stang K, Fennrich S, Krajewski S, Stoppelkamp S, Burgener IA, Wendel H-P, Post M. *J Mater Sci Mater Med.* 2014; 25: 1065–1075.
 170. Mazzotti F, Beuttler J, Zeller R, Fink U, Schindler S, Wendel A, Hartung T, von Aulock S. *J Biomed Mater Res A.* 2007; 80A: 276–282.
 171. Moesby L, Jensen S, Hansen EW, Christensen JD. *Int J Pharm.* 1999; 191: 141–149.
 172. Brown J. *ALTEX.* 2021: 151–156.
 173. Nakagawa Y, Maeda H, Murai T. *Clinical and Vaccine Immunology.* 2002; 9: 588–597.
 174. Pardo-Ruiz Z, Menéndez-Sardiñas DE, Pacios-Michelena A, Gabilondo-Ramírez T, Montero-Alejo V, Perdomo-Morales R. *Eur J Pharm Sci.* 2016; 81: 18–26.
 175. Hoffmann S, Peterbauer A, Schindler S, Fennrich S, Poole S, Mistry Y, Montag-Lessing T, Spreitzer I, Löschner B, van Aalderen M, Bos R, Gommer M, Nibbeling R, Werner-Felmayer G, Loitzl P, Jungi T, Brcic M, Brügger P, Frey E, Bowe G, Casado J, Coecke S, de Lange J, Mogster B, Næss LM, Aaberge IS, Wendel A, Hartung T. *J Immunol Methods.* 2005; 298: 161–173.
 176. Cervenka I, Agudelo LZ, Ruas JL. *Science.* 2017; 357.
 177. Dantzer R. *Curr Top Behav Neurosci.* 2017; 31: 117.
 178. Adams S, Teo C, McDonald KL, Zinger A, Bustamante S, Lim CK, Sundaram G, Braidy N, Brew BJ, Guillemin GJ. *PLoS One.* 2014; 9: e112945.
 179. Badawy AA-B. *Int. J. Tryptophan Res.* 2017; 10: 1–20.
 180. Stone TW, Stoy N, Darlington LG. *Trends Pharmacol Sci.* 2013; 34: 136–143.
 181. Jones SP, Franco NF, Varney B, Sundaram G, Brown DA, de Bie J, Lim CK, Guillemin GJ, Brew BJ. *PLoS One.* 2015; 10: e0131389.
 182. Badawy AA-B. *Nutr Res Rev.* 2002; 15: 123–152.
 183. Bender DA. *Mol Aspects Med.* 1983; 6: 101–197.
 184. HJ B, HJ Y, CJ A, S W, NH H. *Int J Biochem Cell Biol.* 2009; 41: 467–471.
 185. Fujigaki S, Saito K, Sekikawa K, Tone S, Takikawa O, Fujii H, Wada H, Noma A, Seishima M. .
 186. Divanovic S, Sawtell NM, Trompette A, Warning JI, Dias A, Cooper AM, Yap GS, Arditi M, Shimada K, DuHadaway JB, Prendergast GC, Basaraba RJ, Mellor AL, Munn DH, Aliberti J, Karp CL. *J Infect Dis.* 2012; 205: 152–161.
 187. Suzuki Y, Suda T, Asada K, Miwa S, Suzuki M, Fujie M, Furuhashi K, Nakamura Y, Inui N, Shirai T, Hayakawa H, Nakamura H, Chida K. *Clin. Vaccine Immunol.* 2012; 19: 436–442.
 188. Taylor MW, Feng G. *The FASEB Journal.* 1991; 5: 2516–2522.
 189. Hassanain HH, Chon SY, Gupta SL. *J Biol Chem.* 1993; 268: 5077–5084.
 190. Babcock TA, Carlin JM. *Cytokine.* 2000; 12: 588–594.
 191. Fallarino F, Grohmann U, Vacca C, Bianchi R, Orabona C, Spreca A, Fioretti MC, Puccetti P. *Cell Death Differ.* 2002; 9: 1069–1077.
 192. Hill M, Tanguy-Royer S, Royer P, Chauveau C, Asghar K, Tesson L, Lavainne F, Rémy S, Brion R, Hubert FX, Heslan M, Rimbert M, Berthelot L, Moffett JR, Josien R, Grégoire M, Anegón I. *Eur J Immunol.* 2007; 37: 3054–3062.
 193. Mellor AL, Munn DH. *Nat Rev Immunol.* 2004; 4: 762–774.
 194. Wood KJ, Sawitzki B. *Trends Immunol.* 2006; 27: 183–187.
-

-
195. Schefold JC, Zeden J-P, Fotopoulou C, von Haehling S, Pschowski R, Hasper D, Volk H-D, Schuett C, Reinke P. *Nephrol. Dial. Transplant.* 2009; 24: 1901–1908.
 196. Bao Y-S, Ji Y, Zhao S-L, Ma L-L, Xie R-J, Na S-P. *Biomarkers.* 2013; 18: 379–385.
 197. Gagnebin Y, Jaques DA, Rudaz S, Seigneux S de, Boccard J, Ponte B. *Sci Rep.* 2020; 10.
 198. Konje VC, Rajendiran TM, Bellovich K, Gadegbeku CA, Gipson DS, Afshinnia F, Mathew A v. *Clin Kidney J.* 2021; 14: 1097–1105.
 199. Marzinzig M. *Ann Transplant.* 2015; 20: 327–337.
 200. Lahdou I, Sadeghi M, Daniel V, Schenk M, Renner F, Weimer R, Löb S, Schmidt J, Mehrabi A, Schnitzler P, Königsrainer A, Döhler B, Opelz G, Terness P. *Hum Immunol.* 2010; 71: 1067–1072.
 201. Kaden J, Abendroth D, Marzinzig M, May G. *Transplantationsmedizin: Organ der Deutschen Transplantationsgesellschaft.* 2007; 19: 110–116.
 202. Merino JJ, Cabaña-Muñoz ME, Toledano Gasca A, Garcimartín A, Benedí J, Camacho-Alonso F, Parmigiani-Izquierdo JM. *J Clin Med.* 2019; 8: 1368.
 203. Zhang Q, Li H, Zhang Z, Yang F, Chen J. *Dis Markers.* 2015; 2015: 1–7.
 204. Clendenen N, Cornwell W, Pal J, Weitzel N. *J. Heart Lung Transplant.* 2019; 38: S245.
 205. Sousa A, Ribeiro C, Gonçalves VMF, Barbosa J, Peixoto B, Andrade A, Silva P, Andrade JP, Leal S. *J Pharm Biomed Anal.* 2021; 198: 113997.
 206. Fuertig R, Ceci A, Camus SM, Bezard E, Luippold AH, Hengerer B. *Bioanalysis.* 2016; 8: 1903–1917.
 207. Linderholm KR, Skogh E, Olsson SK, Dahl M-L, Holtze M, Engberg G, Samuelsson M, Erhardt S. *Schizophr Bull.* 2012; 38: 426–432.
 208. Flieger J, Świąch-Zubilewicz A, Śniegocki T, Dolar-Szczasny J, Pizoń M. *Molecules.* 2018; 23: 3012.
 209. Sundaram G, Brew BJ, Jones SP, Adams S, Lim CK, Guillemin GJ. *J Neuroinflammation.* 2014; 11: 204.
 210. Notarangelo FM, Wu HQ, Macherone A, Graham DR, Schwarcz R. *Anal Biochem.* 2012; 421: 573–581.
 211. Ungor D, Horváth K, Dékány I, Csapó E. *Sens Actuators B Chem.* 2019; 288: 728–733.
 212. Klockow JL, Glass TE. *Org Lett.* 2013; 15: 235–237.
 213. Seegers N, van Doornmalen AM, Uitdehaag JCM, de Man J, Buijsman RC, Zaman GJR. *SLAS Discovery.* 2014; 19: 1266–1274.
 214. Rößler S, Scharnweber D, Born R, Worch H, Sewing A, Dard M. In *15th European Conference on Biomaterials (ESB)* 1999;
 215. Müller WEG, Wang S, Ackermann M, Gerich T, Neufurth M, Wiens M, Schröder HC, Wang X. *Adv Funct Mater.* 2019; 29: 1905220.
 216. Pflaum M, Dahlmann J, Engels L, Naghilouy-Hidaji H, Adam D, Zöllner J, Otto A, Schmeckeber S, Martin U, Haverich A, Olmer R, Wiegmann B. *Micromachines (Basel).* 2021; 12: 981.
 217. Ho CMB, Ng SH, Yoon Y-J. *Int. J. Precis. Eng.* 2015; 16: 1035–1046.
 218. Borgolte M, Quint I, Kaiser L, Csuk R, Deigner H-P. *Diagnostics.* 2022; 12: 1380.
 219. Helander IM, Nurmiaho-Lassila EL, Ahvenainen R, Rhoades J, Roller S. *Int J Food Microbiol.* 2001; 71: 235–244.
 220. Je JY, Kim SK. *J Agric Food Chem.* 2006; 54: 6629–6633.
 221. Divya K, Vijayan S, George TK, Jisha MS. *Fibers and Polymers.* 2017; 18: 221–230.
 222. Izano EA, Sadovskaya I, Vinogradov E, Mulks MH, Velliyagounder K, Ragunath C, Kher WB, Ramasubbu N, Jabbouri S, Perry MB, Kaplan JB. *Microb Pathog.* 2007; 43: 1–9.
 223. Sicard JF, Vogeleer P, Le Bihan G, Rodriguez Olivera Y, Beaudry F, Jacques M, Harel J. *Gut Pathog.* 2018; 10: 26.
-

-
224. Blagodatskikh I V., Kulikov SN, Vyshivannaya O V., Bezrodnykh EA, Yamskov IA, Tikhonov VE. *Carbohydr Res.* 2013; 381: 28–32.
225. Petrova KT, Potewar TM, Correia-Da-Silva P, Barros MT, Calhelha RC, Ćiric A, Soković M, Ferreira ICFR. *Carbohydr Res.* 2015; 417: 66–71.
226. Holla BS, Mahalinga M, Karthikeyan MS, Poojary B, Akberali PM, Kumari NS. *Eur J Med Chem.* 2005; 40: 1173–1178.
227. Abdel-Wahab, F. B, Mohamed, H. A, Awad, E., A. G. *Eur Chem Bull.* 2015; 4: 106–109.
228. Prucker O, Naumann CA, Rühle J, Knoll W, Frank CW. *J Am Chem Soc.* 1999; 121: 8766–8770.
229. Öztürk T, Meyvacı E, Arslan T. *J. Macromol. Sci. Phys. A.* 2020; 57: 171–180.
230. Mahou R, Wandrey C. *Polymers (Basel).* 2012; 4: 561–589.
231. Sumerlin BS, Tsarevsky N v., Louche G, Lee RY, Matyjaszewski K. *Macromolecules.* 2005; 38: 7540–7545.
232. Kowalski W. *Ultraviolet Germicidal Irradiation Handbook*, Springer Berlin Heidelberg: Berlin, Heidelberg, 2009; 233–254.
233. Cutler TD, Zimmerman JJ. *Anim Health Res Rev.* 2011; 12: 15–23.
234. Bak J, Begovic T. *J. Hosp. Infec.* 2013; 84: 173–177.
235. Gora SL, Rauch KD, Ontiveros CC, Stoddart AK, Gagnon GA. *Water Res.* 2019; 151: 193–202.
236. ISO 10993-5:2009 Biological evaluation of medical devices — Part 5: Tests for in vitro cytotoxicity, .
237. Thiele W, Kyjacova L, Köhler A, Sleeman JP. *Lab Anim.* 2020; 54: 391–396.
238. Gu YZ, Chu X, Houle R, Vlasakova K, Koeplinger KA, Bourgeois I, Palyada K, Anderson KD, Brynczka C, Bhatt B, Chen F, Smith R, Amin R, Glaab WE, Lebron J, Cox K, Sistare FD. *Toxicol. Sci.* 2019; 172: 155–166.
239. Li B, Dong X, Fang S, Gao J, Yang G, Zhao H. *Drug Chem Toxicol.* 2011; 34: 208–212.
240. Smyth HF, Carpenter CP, Weil CS. *J. Am. Pharm. Assoc.* 1950; 39: 349–354.
241. Donlan RM. In *Emerging Infectious Diseases Centers for Disease Control and Prevention (CDC)*, 2001; Vol. 7, 277–281.
242. Liu XF, Guan YL, Yang DZ, Li Z, Yao K De. *J Appl Polym Sci.* 2001; 79: 1324–1335.
243. Li M, Chen C, Xia X, Garba B, Shang L, Wang Y. *Food Sci. Technol.* 2020; 40: 250–257.
244. Khan F, Pham DTN, Oloketuyi SF, Manivasagan P, Oh J, Kim Y-M. *Colloids Surf B Biointerfaces.* 2020; 185: 110627.
245. Tantala J, Thumanu K, Rachtanapun C. *Int. J. Biol. Macromol.* 2019; 135: 386–393.
246. Tang ZG, Black RA, Curran JM, Hunt JA, Rhodes NP, Williams DF. *Biomaterials.* 2004; 25: 4741–4748.
247. Hu L, Meng X, Xing R, Liu S, Chen X, Qin Y, Yu H, Li P. *Bioorg. Med. Chem. Lett.* 2016; 26: 4548–4551.
248. Baldrick P. *Regul. Toxicol. Pharmacol.* 2010; 56: 290–299.
249. Kumar MNVR, Muzzarelli RAA, Muzzarelli C, Sashiwa H, Domb AJ. *Chem Rev.* 2004; 104: 6017–6084.
250. Ishihara M, Fujita M, Obara K, Hattori H, Nakamura S, Nambu M, Kiyosawa T, Kanatani Y, Takase B, Kikuchi M, Maehara T. *Curr. Drug Deliv.* 2006; 3: 351–358.
251. Fonte P, Andrade F, Araújo F, Andrade C, Neves J das, Sarmiento B. In *Methods in enzymology Methods Enzymol*, 2012; Vol. 508,295–314.
252. Cannella V, Altomare R, Chiaramonte G, di Bella S, Mira F, Russotto L, Pisano P, Guercio A. *Biomed Res Int.* 2019; 2019: 1–5.
-

-
253. Cannella V, Altomare R, Leonardi V, Russotto L, di Bella S, Mira F, Guercio A. *Biomed Res Int.* 2020; 2020: 1–6.
 254. Rodan SB, Imai Y, Thiede MA, Wesolowski G, Thompson D, Bar-Shavit Z, Shull S, Mann K, Rodan GA. *Cancer Res.* 1987; 47: 4961–4966.
 255. Baxter AD, Bhogal R, Bird J, Keily JF, Manallack DT, Montana JG, Owen DA, Pitt WR, Watson RJ, Wills RE. *Bioorg. Med. Chem. Lett.* 2001; 11: 1465–1468.
 256. Heath EI, Grochow LB. *Drugs.* 2000; 59: 1043–1055.
 257. Quastel JH, Cantero A. *Nature.* 1953; 171: 252–4.
 258. Chesnokov V, Gong B, Sun C, Itakura K. *Cancer Cell Int.* 2014; 14: 45.
 259. Pohlig F, Ulrich J, Lenze U, Mühlhofer HML, Harrasser N, Suren C, Schauwecker J, Mayer-Kuckuk P, von Eisenhart-Rothe R. *BMC Complement Altern Med.* 2016; 16: 313.
 260. Zhang M, Zhang X. *Int. J. Clin. Exp. Pathol.* 2015; 8: 14965–70.
 261. Refai AK, Textor M, Brunette DM, Waterfield JD. *J Biomed Mater Res.* 2004; 70A: 194–205.
 262. Abendroth D, Marzinzig M, Stangl M. In *American Transplant Congress*. American Transplant Congress, Chicaco. IL, USA 2017. Abstract No. 131.
 263. Lechner J, Noubbissi S, von Baehr V. *EPMA Journal.* 2018; 9: 331–343.
 264. Hebbes TR, Turner CH, Thorne AW, Crane-Robinson C. *Mol Immunol.* 1989; 26: 865–873.
 265. Helttunen K, Prus P, Luostarinen M, Nissinen M. *New Journal of Chemistry.* 2009; 33: 1148.
-

Anhang

Publikationen

Die folgenden Publikationen (P-1 bis P-3) liegen dieser Arbeit zugrunde:

- P-1: *Methacryloyl-GlcNAc Derivatives Copolymerized with Dimethacrylamide as a Novel Antibacterial and Biocompatible Coating.*
- P-2: *Synthesis of a biocompatible benzophenone-substituted chitosan hydrogel as novel coating for PEEK with extraordinary strong antibacterial and anti-biofilm properties.*
- P-3: *A Fluorescence-Based Competitive Antibody Binding Assay for Kynurenine, a Potential Biomarker of Kidney Transplant Failure.*
-

P-1: Methacryloyl-GlcNAc Derivatives Copolymerized with Dimethacrylamide as a Novel Antibacterial and Biocompatible Coating

Borgolte, M.; Riester, O.; Kacerova, T.; Rentschler, S.; Schmidt, M.S.; Jacksch, S.; Egert, M.; Laufer, S.; Csuk, R.; Deigner, H.-P. Methacryloyl-GlcNAc Derivatives Copolymerized with Dimethacrylamide as a Novel Antibacterial and Biocompatible Coating. *Pharmaceutics* **2021**, *13*, 1647.

Abstract

Improving medical implants with functional polymer coatings is an effective way to further improve the level of medical care. Antibacterial and biofilm-preventing properties are particularly desirable in the area of wound healing, since there is a generally high risk of infection, often with a chronic course in the case of biofilm formation. To prevent this we here report a polymeric design of polymer-bound *N*-acetyl-glucosamine-oligoethylene glycol residues that mimic a cationic, antibacterial, and biocompatible chitosan surface. The combination of easy to use, crosslinkable, thin, potentially 3D-printable polymethacrylate layering with antibacterial and biocompatible functional components will be particularly advantageous in the medical field to support a wide range of implants as well as wound dressings. Different polymers containing a *N*-acetylglucosaminemethacryloyl residue with oligoethylene glycol linkers and a methacryloyl benzophenone crosslinker were synthesized by free radical polymerization. The functional monomers and corresponding polymers were characterized by ¹H, ¹³C NMR, and infrared (IR) spectroscopy. The polymers showed no cytotoxic or antiadhesive effects on fibroblasts as demonstrated by extract and direct contact cell culture methods. Biofilm formation was reduced by up to 70% and antibacterial growth by 1.2 log, particularly for the 5% GlcNAc-4EG polymer, as observed for *Escherichia coli* and *Staphylococcus aureus* as clinically relevant Gram-negative and Gram-positive model pathogens.

Keywords

carbohydrates; glycosides; antibacterial; antibiofilm; MRSA; *E. coli*; biocompatible

Article

Methacryloyl-GlcNAc Derivatives Copolymerized with Dimethacrylamide as a Novel Antibacterial and Biocompatible Coating

Max Borgolte ^{1,2} , Oliver Riestler ^{1,3,4} , Tereza Kacerova ^{5,6} , Simone Rentschler ^{1,3} , Magnus S. Schmidt ¹ , Susanne Jacksch ¹ , Markus Egert ¹ , Stefan Laufer ^{3,4} , René Csuk ²  and Hans-Peter Deigner ^{1,4,7,*} 

- ¹ Institute of Precision Medicine, Furtwangen University, Jakob-Kienzle Str. 17, 78054 Villingen-Schwenningen, Germany; Max.Borgolte@hs-furtwangen.de (M.B.); Oliver.Riestler@hs-furtwangen.de (O.R.); S.Rentschler@hs-furtwangen.de (S.R.); Magnus.Schmidt@hs-furtwangen.de (M.S.S.); Susanne.Jacksch@hs-furtwangen.de (S.J.); Markus.Egert@hs-furtwangen.de (M.E.)
- ² Department of Organic Chemistry, Martin-Luther University Halle-Wittenberg, Kurt-Mothes Str. 2, 06120 Halle (Saale), Germany; Rene.csuk@chemie.uni-halle.de
- ³ Department of Pharmaceutical and Medicinal Chemistry, Institute of Pharmaceutical Sciences, Eberhard Karls University Tuebingen, Auf der Morgenstelle 8, 72076 Tuebingen, Germany; Stefan.laufer@uni-tuebingen.de
- ⁴ Faculty of Science, Eberhard Karls University Tuebingen, Auf der Morgenstelle 8, 72076 Tuebingen, Germany
- ⁵ Department of Chemistry, Czech University of Life Sciences, Kamýcká 129, 16500 Prague, Czech Republic; tereza.kacerova.18@ucl.ac.uk
- ⁶ Department of Chemistry, University College London, London WC1H 0AJ, UK
- ⁷ EXIM Department, Fraunhofer Institute IZI (Leipzig), Schillingallee 68, 18057 Rostock, Germany
- * Correspondence: dei@hs-furtwangen.de



Citation: Borgolte, M.; Riestler, O.; Kacerova, T.; Rentschler, S.; Schmidt, M.S.; Jacksch, S.; Egert, M.; Laufer, S.; Csuk, R.; Deigner, H.-P. Methacryloyl-GlcNAc Derivatives Copolymerized with Dimethacrylamide as a Novel Antibacterial and Biocompatible Coating. *Pharmaceutics* **2021**, *13*, 1647. <https://doi.org/10.3390/pharmaceutics13101647>

Academic Editors: Ewa Kłodzińska; and Marek Konop

Received: 3 August 2021
Accepted: 2 October 2021
Published: 9 October 2021

Publisher's Note: MDPI stays neutral with regard to jurisdictional claims in published maps and institutional affiliations.



Copyright: © 2021 by the authors. Licensee MDPI, Basel, Switzerland. This article is an open access article distributed under the terms and conditions of the Creative Commons Attribution (CC BY) license (<https://creativecommons.org/licenses/by/4.0/>).

Abstract: Improving medical implants with functional polymer coatings is an effective way to further improve the level of medical care. Antibacterial and biofilm-preventing properties are particularly desirable in the area of wound healing, since there is a generally high risk of infection, often with a chronic course in the case of biofilm formation. To prevent this we here report a polymeric design of polymer-bound *N*-acetyl-glucosamine-oligoethylene glycol residues that mimic a cationic, antibacterial, and biocompatible chitosan surface. The combination of easy to use, crosslinkable, thin, potentially 3D-printable polymethacrylate layering with antibacterial and biocompatible functional components will be particularly advantageous in the medical field to support a wide range of implants as well as wound dressings. Different polymers containing a *N*-acetylglucosamine-methacryloyl residue with oligoethylene glycol linkers and a methacryloyl benzophenone crosslinker were synthesized by free radical polymerization. The functional monomers and corresponding polymers were characterized by ¹H, ¹³C NMR, and infrared (IR) spectroscopy. The polymers showed no cytotoxic or antiadhesive effects on fibroblasts as demonstrated by extract and direct contact cell culture methods. Biofilm formation was reduced by up to 70% and antibacterial growth by 1.2 log, particularly for the 5% GlcNAc-4EG polymer, as observed for *Escherichia coli* and *Staphylococcus aureus* as clinically relevant Gram-negative and Gram-positive model pathogens.

Keywords: carbohydrates; glycosides; antibacterial; antibiofilm; MRSA; *E. coli*; biocompatible

1. Introduction

Bacterial wound infections are a major health problem, comparable to infections subsequent to surgical procedures, especially when a biofilm is formed significantly reducing the susceptibility of bacteria to antibiotics [1–3]. In combination with the increasing number of reported multidrug-resistant pathogens, antibiotic resistant bacterial infections are a clinical problem that will become even more acute in the future [4]. An implant or scaffold has to be functional for fibroblast or stem cells adhesion to ensure proper resorption of

the implant into the surrounding tissue. This functionalization promotes adhesion often unspecifically for all cells and organisms, including bacteria, leading to a “race to the surface” [5,6], whereby the patient’s cells and bacteria compete to adhere to an implant’s surface. The critical time window for this competition between body tissue and bacteria has been determined to be the first 6 h after implantation, while a single bacteria can form a biofilm within 24 h [7]. After 48–96 h, the biofilm becomes resistant to therapeutic treatment as the formed matrix renders the encapsulated bacteria less susceptible to host defense mechanisms and antibiotic therapy [8–12]. Conventionally, antibiotic prophylaxis is used in both implant surgery and traumatic wound care to reduce the likelihood of bacterial infections [13,14]. However, the problem of increasing multidrug-resistant bacteria, particularly in clinical settings, has led to a re-evaluation of the extensive use of antibiotics [15,16]. To some degree, reducing the usage of systemic antibiotics can prevent the emergence of new multidrug-resistant pathogens. In order to prevent infections even with reduced administration of antibiotics, other antimicrobial mechanisms must also be applied, such as antimicrobial modification of surfaces or addition of nanoparticles [17–19].

Cationic polymers have been widely described in articles and reviews with regard to their antibacterial properties and use in self-disinfecting surfaces; most contain a quaternary ammonium group or alkyl pyridinium group as the functional component [20–25]. The mechanism of action of these cationic polymers in solution is well described by the Shai-Matsuzaki-Huang (SMH) model [26–28]. The antibacterial action of surfaces coated with cationic polymers is thought to follow a similar mechanism through polymeric brushes [21,29–33], but some publications describe a simple monolayer of cationic groups as being antibacterial as well [34]. Murata et al. propose a mechanism driven mainly by surface charge instead of insertion of cationic polymer brushes into the bacterial cell wall, following an SMH-like mechanism [20]. The exact mechanism of the antibacterial effect of cationic polymers requires further discussion and clarification.

Chitosan is a cationic polymeric aminoglycan, consisting of *N*-acetylglucosamine (GlcNAc) and glucosamine repeating units; it is used in tissue engineering applications such as bone tissue engineering [35–37], stem cell encapsulation [38–40], and wound dressing [41,42]. The polymer is thought to exhibit its antibacterial properties through a cationic mechanism via glucosamine’s amino group by disrupting the outer and inner bacterial cell membrane [43–45] and has been shown to mediate biofilm formation of *Actinobacillus pleuromoniae* [46]. The corresponding monomer, GlcNAc, has been shown to prevent biofilm formation by *Escherichia coli* [47]. Because of its insolubility in water and organic solvents, except ionic liquids, chitosan has been used in several polymeric modifications to combine its proliferative and antibacterial properties with the mechanical stiffness of other polymers, taking advantage of different synthetic polymers or nanoparticles, rendering it useful for biomedical applications [48].

Another group of antimicrobial compounds is the 1,2,3-triazoles, which exhibit antibacterial activity mainly through formation of hydrogen bonds of the triazole ring with other moieties, forming a cationic surface and possibly leading to an SMH-like antibacterial mechanism [49]. These 1,2,3-triazoles can easily be introduced by Huisgen 1,3-dipolar cycloaddition of an azide and alkyne, without the need for complicated workup procedures or toxic and expensive reagents, making it suitable for polymer modifications [50,51]. Several polymers modified in this way are listed in a library of (1,2,3-triazol-1-yl)quinazolin-4-ones and have shown antibacterial properties against Gram-positive and Gram-negative bacteria [52,53]. In addition, a library of 1,2,3-triazol-sucrose derivatives showed antifungal and antibacterial properties while maintaining low cytotoxicity against non-tumor cell lines [54–56].

An additional approach is the design of antiadhesive surfaces to prevent colonization of implant surfaces. Pandiyarajan et al. [57] described a surface-attached hydrogel network, consisting of poly-dimethacrylamide copolymerized with methacryloyl benzophenone (MBP), that had antiadhesive properties against proteins and blood platelets. Surface anchoring was accomplished via photoactive UV crosslinking of the benzophenone moi-

ety [57]. The benzophenone undergoes a UV-induced, radical C–H insertion reaction, as reviewed by Prucker et al. [58] rendering it suitable for functionalization of polymeric surfaces to obtain stable, covalently attached hydrogel networks [58]. To the best of our knowledge, there is no description of combining the antimicrobial properties of a cationic GlcNAc residue with an antiadhesive, UV-crosslinkable acrylamide hydrogel in order to reduce microbial contamination of implant surfaces in the literature.

In this study, we combined the previously described approaches that resulted in a surface-bound poly-dimethacrylamide methyl (PDMAM) network with UV-induced anchoring via benzophenone, combining it with a GlcNAc residue containing a triazole and a distinct linker to the PDMAM network backbone. We thereby mimicked an antimicrobial chitosan surface while taking advantage of the antiadhesive PDMAM hydrogel as base layer. The hydrogel network can be easily obtained via solvent casting of the polymer solution, followed by UV crosslinking. We investigated the effect of the combinatorial approach of triazole functional groups and chitosan-mimicking surfaces on the antimicrobial, antibiofilm, and biocompatible properties of such coatings.

2. Experimental Section

2.1. Chemical Synthesis and Characterization

2.1.1. General Methods

TLC was carried out on Silica Gel 60 F254 (Merck KGaA, Darmstadt, Germany, layer thickness 0.2 mm) with detection by UV light (254 nm) or by charring with 1% KMnO_4 in 1N NaOH. Flash column chromatography (FC) was performed on M&N Silica Gel 60 (0.063–0.200 mm, MACHEREY-NAGEL GmbH, Düren, Germany). ^1H NMR and ^{13}C NMR spectra were recorded on a Bruker Avance I 200, Bruker Avance II 400 (Bruker Corporation, Billerica, MA, USA), or Varian Unity 500 (Varian, Palo Alto, CA, USA) spectrometer. Chemical shifts are reported in parts per million relative to solvent signals (CDCl_3 : $\delta\text{H} = 7.26$ ppm, $\delta\text{C} = 77.0$ ppm; DMSO-d_6 : $\delta\text{H} = 2.49$ ppm, $\delta\text{C} = 39.7$ ppm; CD_3OD : $\delta\text{H} = 4.78$ ppm, $\delta\text{C} = 49.3$ ppm). Signals were assigned by first-order analysis, and assignments were supported, where feasible, by 2-dimensional ^1H , ^1H and ^1H , ^{13}C correlation spectroscopy. Coupling constants are reported in hertz. Chemicals and reagents were purchased from Acros Organics (Geel, Belgium), Sigma-Aldrich (Munich, Germany), Carl Roth (Karlsruhe, Germany), ABCR (Karlsruhe, Germany), or MCAT (Donaueschingen, Germany) and were used without further purification.

2.1.2. Synthesis of Azido Linkers 2, 4, 5, 6

Azido linkers were synthesized according to a procedure published by Mahou and Wandrey [59], following a cascade of sequential tosylation and NaN_3 substitution steps. For diethylene glycol linker 2, 2-(2-chloro-ethoxy)-ethanol was chosen as the starting material instead of the tosylated diethylene glycol residue, according to another published procedure [60].

2.1.3. General Tosylation Procedure

Tosylation was carried out according to a literature report [59]. The corresponding linker (1 eq) and *p*-toluenesulfonyl chloride (1.1 eq) were dissolved in dichloromethane (DCM) at 0 °C and NEt_3 (2 eq) was added. After stirring for 2 h, the ice bath was removed and the mixture stirred overnight at room temperature. Washing twice with water and once with brine, followed by evaporation of the solvent, yielded the tosylated linker as a yellowish oil.

2.1.4. Chain Prolongment of Azido Linkers via Tosylate 5, 6

Chain prolongment was carried out according to the literature [59]. Tosylated azido linker 4 (1 eq) and NaH (1.1 eq) were suspended in water-free tetrahydrofuran (THF) under Ar atmosphere. After stirring for 30 min at room temperature, diethylene glycol for product 5 or 1,8-octanediol for product 6 (5 eq) was added dropwise to the mixture. After

stirring for 48 h under reflux, H₂O was added, the solvent evaporated, and the aqueous layer extracted 3× with DCM Washing 2× with NaOH, followed by evaporation of the solvent and column chromatography (ethyl acetate/methanol 19:1, R_f = 0.4), yielded the pure products **5** and **6** as yellowish oils.

8-(2-[2-[2-(2-Azido-ethoxy)-ethoxy]-ethoxy]-ethoxy)-octan-1-ol **6**

Yield: 71%

¹H-NMR (CDCl₃, 400 MHz): 3.71–3.63 (m, 14H, O–CH₂), 3.59 (dt, *J* = 4.5, 1.2 Hz, 2H, O–CH₂), 3.46 (t, *J* = 6.8 Hz, 2H, O–CH₂), 3.40 (t, *J* = 5.1 Hz, 2H, N₃–CH₂), 1.57 (dt, *J* = 13.2, 6.5 Hz, 4H, CH₂), 1.40–1.29 (m, *J* = 17.9 Hz, 8H, CH₂).

¹³C-NMR (CDCl₃, 100 MHz): 71.48 (O–CH₂), 70.72 (O–CH₂), 70.70 (O–CH₂), 70.65 (O–CH₂), 70.61 (O–CH₂), 70.08 (O–CH₂), 70.04 (O–CH₂), 63.01 (O–CH₂), 50.70 (N₃–CH₂), 32.77 (CH₂), 29.60 (CH₂), 29.39 (CH₂), 29.33 (CH₂), 26.00 (CH₂), 25.66 (CH₂).

2.1.5. General Procedure for the Synthesis of Azidomethacrylates **7–10**

Azido methacrylates were synthesized as published [61]. Briefly, azido linker (1 eq) and NEt₃ (1.3 eq) were dissolved in water-free DCM in a sealed Schlenk flask under Ar atmosphere cooled in an ice bath to 0 °C. Methacryloyl chloride (1.2 eq) was added dropwise to the mixture. The solution was allowed to warm to room temperature and stirred at room temperature overnight. Washing with 1M H₂SO₄ (3×, equal volume to solvent) followed by drying over Na₂SO₄ and evaporation of the solvent yielded the crude product. Further purification by column chromatography (ethyl acetate/hexane 1:10) yielded the pure products.

2-Methyl-acrylic acid 2-(2-azido-ethoxy)-ethyl ester **7**

Yield: 81%

¹H-NMR (CDCl₃, 400 MHz): 6.17 (s, 1H, CH₂), 5.60 (s, 1H, CH₂), 4.34 (t, *J* = 4.7 Hz, 2H, O–CH₂), 3.78 (t, *J* = 4.7, 2H, O–CH₂), 3.71 (t, *J* = 5.0, 2H, O–CH₂), 3.40 (t, *J* = 4.9, 2H, CH₂–N₃), 1.98 (s, 3H, CH₃).

¹³C-NMR (CDCl₃, 100 MHz): 167.3 (C=O), 136.1 [C(CH₃)(CH₂)], 125.9 (C=CH₂), 70.1 (O–CH₂), 69.2 (O–CH₂), 63.7 (O–CH₂), 50.7 (N₃–CH₂), 18.3 (CH₃).

2-Methyl-acrylic acid 2-[2-[2-(2-azido-ethoxy)-ethoxy]-ethoxy]-ethyl ester **8**

Yield: 71%

¹H-NMR (CDCl₃, 400 MHz): 6.16 (s, 1H, CH₂), 5.60 (s, 1H, CH₂), 5.33 (t, *J* = 4.9 Hz, 2H, O–CH₂), 3.77 (t, *J* = 3.8 Hz, 2H, O–CH₂), 3.70 (s, 10H, O–CH₂), 3.41 (t, *J* = 5.0 Hz, 2H, CH₂–N₃), 1.97 (s, 3H, CH₃).

¹³C-NMR (CDCl₃, 100 MHz): 136.2 [C(CH₃)(CH₂)], 125.8 (C=CH₂), 70.8 (O–CH₂), 70.1 (O–CH₂), 69.2 (O–CH₂), 63.8 (O–CH₂), 50.7 (N₃–CH₂), 18.3 (CH₃).

2-Methyl-acrylic acid 2-[2-[2-[2-(2-azido-ethoxy)-ethoxy]-ethoxy]-ethoxy]-ethoxy]-ethyl ester **9**

Yield: 55%

¹H-NMR (CDCl₃, 400 MHz): 6.17 (s, 1H, CH₂), 5.60 (s, 1H, CH₂), 4.34 (t, *J* = 4.7 Hz, 2H, O–CH₂), 3.78 (t, *J* = 4.7, 2H, O–CH₂), 3.71 (t, *J* = 5.0, 2H, O–CH₂), 3.40 (t, *J* = 4.9, 2H, CH₂–N₃), 1.98 (s, 3H, CH₃).

¹³C-NMR (CDCl₃, 100 MHz): 167.4 (C=O), 136.2 [C(CH₃)(CH₂)], 125.7 (C=CH₂), 70.7 (O–CH₂), 70.6 (O–CH₂), 70.0 (O–CH₂), 69.2 (O–CH₂), 63.9 (O–CH₂), 50.7 (N₃–CH₂), 18.3 (CH₃).

2-Methyl-acrylic acid 8-(2-[2-[2-(2-azido-ethoxy)-ethoxy]-ethoxy]-ethoxy)-octyl ester **10**

Yield: 66%

¹H-NMR (CDCl₃, 400 MHz): 6.11 (s, 1H, CH₂), 5.56 (s, 1H, CH₂), 4.15 (t, *J* = 6.7 Hz, 2H, O–CH₂), 3.72–3.64 (m, 14H, O–CH₂), 3.62–3.57 (m, 2H, O–CH₂), 3.46 (t, *J* = 6.8 Hz, 2H,

O-CH₂), 3.41 (t, *J* = 5.1 Hz, 2H, N₃-CH₂), 1.96 (s, 2H, O-CH₂), 1.73–1.64 (m, 2H, O-CH₂), 1.62–1.57 (m, 2H, O-CH₂), 1.44–1.26 (m, 8H, O-CH₂).

¹³C-NMR (CDCl₃, 100 MHz): 167.56 (C=O), 136.55 [C(CH₃)(CH₂)], 125.16 (C=CH₂), 71.48 (O-CH₂), 70.72 (O-CH₂), 70.70 (O-CH₂), 70.65 (O-CH₂), 70.64 (O-CH₂), 70.62 (O-CH₂), 70.08 (O-CH₂), 70.05 (O-CH₂), 64.80 (O-CH₂), 50.70 (N₃-CH₂), 29.61 (CH₂), 29.36 (CH₂), 29.21 (CH₂), 28.60 (CH₂), 26.02 (CH₂), 25.93 (CH₂), 18.34 (CH₃).

2.1.6. General Procedure for Click Reaction of Azidomethacrylates with **13**

The click reaction was carried out under optimized conditions according to Schmidt et al. 2014 [62]. Azido methacrylate (1 eq) and propargyl GlcNAc **13** (1 eq) were dissolved in a mixture of dichloromethane/methanol/water (10:10:3). Then, CuSO₄ (0.04 eq), tris(benzyltriazolylmethyl)amine (TBTA) (0.01 eq), and sodium ascorbate (0.22 eq) were added, and the mixture was heated to reflux for 1 h. After cooldown and adding water, the solution was extracted 3 times with dichloromethane, the organic layer dried over Na₂SO₄, and the solvent evaporated in vacuum. Column chromatography yielded the products as yellowish oil.

2-Methyl-acrylic acid 2-[2-[4-(3-acetylamino-4,5-dihydroxy-6-hydroxymethyl-tetrahydro-pyran-2-yloxymethyl)-[1,2,3]triazol-1-yl]-ethoxy]-ethyl ester **11a**

Yield: 75%

¹H-NMR (CDCl₃, 400 MHz): 7.67 (s, 1H, Ar-H), 6.03 (s, 1H, CH₂), 5.84 (s, 1H, H-1), 5.54 (s, 1H, CH₂), 5.16 (t, *J* = 9.2 Hz, 1H, H-3), 5.04 (t, *J* = 9.4 Hz, 1H, H-4), 4.83–4.75 (m, 3H, O-CH₂ + H-2), 4.49 (s, 2H, O-CH₂), 4.24–4.19 (m, 2H, O-CH₂), 4.07 (dd, *J* = 16.3, 9.5 Hz, 1H, H-6), 3.92 (s, 1H, H-6), 3.82 (s, 2H, O-CH₂), 3.68–3.65 (m, 1H, H-5), 3.63 (t, *J* = 4.7 Hz, 2H, O-CH₂), 2.03 (s, 3H, C(O)CH₃), 1.96 (s, 3H, C(O)CH₃), 1.95 (s, 3H, C(O)CH₃), 1.87 (s, 3H, C(O)CH₃), 1.79 (s, 3H, CH₃).

2-Methyl-acrylic acid 2-[2-(2-[2-[4-(4,5-diacetoxy-6-acetoxymethyl-3-acetylamino-tetrahydro-pyran-2-yloxymethyl)-[1,2,3]triazol-1-yl]-ethoxy]-ethoxy)-ethoxy]-ethyl ester **11b**

Yield: 63%

¹H-NMR (CDCl₃, 400 MHz): 7.58 (s, 1H, Ar-H), 5.96 (s, 1H, CH₂), 5.71 (d, *J* = 8.5 Hz, 1H, H-1), 5.42 (s, 1H, CH₂), 5.05 (t, *J* = 9.9 Hz, 1H, H-3), 4.95 (t, *J* = 9.6 Hz, 1H, H-4), 4.78 (d, *J* = 12.3 Hz, 1H, H-2), 4.68 (dd, *J* = 23.6, 10.5 Hz, 2H, O-CH₂-Ar), 4.39 (t, *J* = 4.7 Hz, 2H, O-CH₂), 4.17–4.10 (m, 3H, O-CH₂ + H-6), 3.99 (dd, *J* = 12.4, 2.1 Hz, 1H, H-6), 3.82 (dd, *J* = 18.0, 8.5 Hz, 1H, H-5), 3.72 (t, *J* = 5.0 Hz, 2H, O-CH₂), 3.60–3.57 (m, 2H, O-CH₂), 3.53–3.45 (m, 10H, O-CH₂), 1.94 [s, 2H, C(O)CH₃], 1.87 [s, 3H, C(O)CH₃], 1.86 [s, 3H, C(O)CH₃], 1.79 [s, 3H, C(O)CH₃], 1.69 (s, 3H, CH₃).

2-Methyl-acrylic acid

2-(2-[2-[2-[2-[4-(3-acetylamino-4,5-dihydroxy-6-hydroxymethyl-tetrahydro-pyran-2-yloxymethyl)-[1,2,3]triazol-1-yl]-ethoxy]-ethoxy]-ethoxy]-ethoxy)-ethyl ester **11c**

Yield: 56%

¹H-NMR (CDCl₃, 400 MHz): 7.76 (s, 1H, Ar-H), 6.12 (s, 1H, CH₂), 6.05 (d, *J* = 8.4 Hz, 1H, H-1), 5.57 (d, *J* = 1.6 Hz, 1H, CH₂), 5.23 (t, *J* = 9.9 Hz, 1H, H-3), 5.09 (t, *J* = 9.6 Hz, 1H, H-4), 4.94 (d, *J* = 12.6 Hz, 1H, H-2), 4.84 (dd, *J* = 33.4, 10.4 Hz, 2H, O-CH₂-Ar), 4.54 (t, *J* = 4.8 Hz, 2H, O-CH₂), 4.32–4.23 (m, 3H, O-CH₂ + H-6), 4.14 (dd, *J* = 12.4, 2.1 Hz, 1H, H-6), 3.87 (t, *J* = 5.0 Hz, 2H, O-CH₂), 3.77–3.71 (m, 3H, O-CH₂ + H-5), 3.68–3.59 (m, 20H, O-CH₂), 2.09 (s, 3H, C(O)CH₃), 2.02 (s, 3H, C(O)CH₃), 2.01 (s, 3H, C(O)CH₃), 1.94 (s, 3H, C(O)CH₃), 1.85 (s, 3H, CH₃).

2-Methyl-acrylic acid

8-[2-[2-(2-[2-[4-(4,5-diacetoxy-6-acetoxymethyl-3-acetylamino-tetrahydro-pyran-2-yloxymethyl)-[1,2,3]triazol-1-yl]-ethoxy]-ethoxy)-ethoxy]-ethoxy]-octyl ester **11d**

Yield: 86%

¹H-NMR (CDCl₃, 400 MHz): 7.61 (s, 1H, Ar-H), 5.94 (s, 1H, CH₂), 5.85 (d, *J* = 8.6 Hz, 1H, H1), 5.39 (s, 1H, CH₂), 5.08 (t, *J* = 9.9 Hz, 1H, H3), 4.94 (t, *J* = 9.6 Hz, 1H, H4), 4.82–4.60 (m, 3H, H2 + Ar-CH₂-O), 4.41–4.34 (m, 2H, O-CH₂), 4.25–4.08 (m, 2H, H6), 4.02–3.92 (m, 2H, O-CH₂), 3.63–3.54 (m, 1H, H5), 3.51–3.45 (m, 10H, O-CH₂), 3.43–3.39 (m, 2H, O-CH₂), 3.28 (t, *J* = 6.8 Hz, 2H, O-CH₂), 1.94 (s, 3H, CH₃), 1.87 (s, 3H, CH₃), 1.86 (s, 3H, CH₃), 1.78 (s, 3H, CH₃), 1.69 (s, 3H, CH₃), 1.56–1.37 (m, 5H, CH₂), 1.22–1.13 (m, 9H, CH₂).

2.1.7. General Procedure for Click Reaction of Azidomethacrylates with Propargyl Alcohol

The click reaction with propargyl alcohol was carried out under conditions as previously published [62]. Briefly, azido methacrylate (1 eq) and propargyl alcohol (1.3 eq) were dissolved in a mixture of dichloromethane/methanol/water (10:10:3). Then, CuSO₄ (0.04 eq), TBTA (0.01 eq), and sodium ascorbate (0.22 eq) were added, and the mixture was heated to reflux overnight. After cooldown and adding water, the solution was extracted 3 times with dichloromethane, the organic layer dried over Na₂SO₄, and the solvent evaporated in vacuo. Column chromatography (ethyl acetate/methanol, 4:1) yielded the products as yellow oils.

2-Methyl-acrylic acid 2-[2-(4-hydroxymethyl-[1,2,3]triazol-1-yl)-ethoxy]-ethyl ester **12a**

Yield: 18%

¹H-NMR (CDCl₃, 200 MHz): 7.68 (s, 1H, Ar-H), 6.10 (dd, *J* = 1.5, 1.0 Hz, 1H, CH₂), 5.60 (p, *J* = 1.6 Hz, 1H, CH₂), 4.77 (s, 2H, CH₂), 4.54 (t, *J* = 5.0 Hz, 2H, O-CH₂), 4.29 (t, *J* = 4.7 Hz, 2H, O-CH₂), 3.87 (t, *J* = 5.1 Hz, 2H, O-CH₂), 3.69 (ddd, *J* = 5.4, 4.0, 2.1 Hz, 2H, O-CH₂), 1.94 (dd, *J* = 1.5, 1.0 Hz, 3H, CH₃).

¹³C-NMR (CDCl₃, 50 MHz): 125.88 (C=CH₂), 115.58, 69.40 (O-CH₂), 69.20 (O-CH₂), 69.04 (O-CH₂), 63.42 (O-CH₂), 50.30 (N-CH₂), 18.21 (CH₃).

2-Methyl-acrylic acid 2-[2-(4-hydroxymethyl-[1,2,3]triazol-1-yl)-ethoxy]-ethyl ester **12b**

Yield: 39%

¹H-NMR (CDCl₃, 200 MHz): 7.76 (s, 1H, Ar-H), 6.11 (dd, *J* = 1.5, 0.9 Hz, 1H, CH₂), 5.57 (p, *J* = 1.6 Hz, 1H, CH₂), 4.78 (s, 2H, CH₂), 4.53 (t, *J* = 5.3 Hz, 2H, CH₂), 4.29 (dd, *J* = 5.7, 4.2 Hz, 2H, CH₂), 3.86 (t, *J* = 5.2 Hz, 2H, CH₂), 3.74 (dd, *J* = 5.5, 4.2 Hz, 2H, CH₂), 3.67–3.57 (m, 8H, CH₂), 1.93 (s, 3H, CH₃).

¹³C-NMR (CDCl₃, 50 MHz): 125.68 [C(CH₃)(CH₂)], 122.87 (C=CH₂), 70.62 (O-CH₂), 70.58 (O-CH₂), 70.51 (O-CH₂), 70.48 (O-CH₂), 69.41 (O-CH₂), 69.12 (O-CH₂), 63.74 (O-CH₂), 56.52 (O-CH₂), 50.23 (N-CH₂), 18.21 (CH₃).

2-Methyl-acrylic acid 2-[2-(2-[2-(2-(4-hydroxymethyl-[1,2,3]triazol-1-yl)-ethoxy]-ethoxy)-ethoxy)-ethoxy]-ethyl ester **12c**

Yield: 96%

¹H-NMR (CDCl₃, 600 MHz): 7.86 (s, 1H, Ar-H), 6.12 (dd, *J* = 1.6, 1.0 Hz, 2H, CH₂), 5.56 (q, *J* = 1.6 Hz, 2H, CH₂), 4.79 (s, 2H, CH₂), 4.54 (t, *J* = 4.9 Hz, 2H, CH₂), 4.30–4.27 (m, 2H, CH₂), 3.86 (t, *J* = 4.9 Hz, 2H, CH₂), 3.72 (dd, *J* = 5.5, 4.3 Hz, 2H, CH₂), 3.65–3.59 (m, 16H, CH₂), 2.37 (s, 1H, OH), 1.94 (dd, *J* = 1.5, 1.0 Hz, 3H, CH₃).

¹³C-NMR (CDCl₃, 200 MHz): 136.12 [C(CH₃)(CH₂)], 125.72 (C=CH₂), 70.60 (O-CH₂), 70.57 (O-CH₂), 70.56 (O-CH₂), 70.54 (O-CH₂), 70.53 (O-CH₂), 70.48 (O-CH₂), 70.46 (O-CH₂), 70.38 (O-CH₂), 69.38 (O-CH₂), 69.10 (O-CH₂), 64.34 (O-CH₂), 63.81 (O-CH₂), 57.20 (O-CH₂), 56.62 (O-CH₂), 50.34 (N₃-CH₂), 30.57 (CH₂), 18.28 (CH₃).

2.1.8. General Procedure for Free Radical Polymerization

Combined monomers (in general, dimethacrylamide, benzophenone methacrylate **14** and functional methacrylate **11a–d** or **12a–c** in given ratios (Table 1) were dissolved in water-free THF under Ar atmosphere to a total monomer concentration of 2 M. Azobisisobutyronitrile (AIBN) (0.01 mol%) was added and the reaction mixture heated to reflux for 16 h. Cooldown followed by precipitation of the polymers in 10-fold excess iso-hexane yielded the product as a white precipitate. The precipitate was dissolved in water and lyophilized to obtain the product as a white powder.

Table 1. Overview of the synthesized PDMAm-polymers.

Polymer	Calculated Ratio		Found Ratio (via NMR)
	MBP 14 [%] ^(a)	11 or 12 [%] ^(b)	MBP vs. 11/12
GlcNAc-2EG	5%	5% 11a	30:1
5%-GlcNAc-4EG	5%	5% 11b	2:1
10%-GlcNAc-4EG	5%	10% 11b	1:2
25%-GlcNAc-4EG	5%	25% 11b	1:5
50%-GlcNAc-4EG ^(c)	5%	50% 11b	-
GlcNAc-6EG	5%	5% 11c	3:1
GlcNAc-4EG-octyl	5%	5% 11d	6:1
HM-2EG	5%	5% 12a	1:1
HM-4EG	5%	5% 12b	1:1
HM-6EG	5%	5% 12c	1:1
PDMAm ^(d)	5%	-	-

^(a) 4-methacryloyloxy-benzophenone (MBP). ^(b) Functional GlcNAc monomers (**11**), Functional 4-hydroxymethyl monomers (**12**). ^(c) The 50%-GlcNAc-4EG polymer could not be obtained; instead, the reaction resulted in ester hydrolysis of the methacrylic acid ester, yielding the GlcNAc-tetraethylene glycol clickamer only. ^(d) The PDMAm polymer is the dimethacrylamide-co-methacryloyl benzophenone copolymer without additional functionality, serving as control for cell culture and microbiology experiments.

2.1.9. General Deprotection Procedure of GlcNAc Polymers

Deprotection was carried out according to a standard Zemplén procedure [63]. GlcNAc polymers were dissolved in dry methanol in a sealed tube under Ar atmosphere. NaOMe (30% solution in methanol; 0.2 eq referring to glycoside content) was added and the mixture stirred at room temperature overnight. Water was added until the precipitated polymers were dissolved. Addition of ion exchange resin (Dowex 50WX8, 200–400 mesh, Carl Roth, Karlsruhe, Germany) followed by filtration and lyophilization yielded the products as yellowish powders. The crude polymer was further purified by 3 times dissolving in methanol and precipitation in 10-fold excess of Et₂O, followed by dissolution in ddH₂O and lyophilization. Pure polymers were obtained as white powder.

2.2. Preparation of Polymer Coatings

Polymers were diluted to a concentration of 25 or 5 mg/mL in a H₂O/ethanol 5:1 mixture. The mixture was sterile filtered before use. From the mixture, 20 µL was pipetted into each well of a 48-well plate, 34.6 µL into each well of a 24-well plate, or 5.76 µL into each well of a 96-well plate. The plates were allowed to dry under sterile conditions for at least 4 h and crosslinked with 3 J/cm² UV light at 254 nm, followed by 3× washings with 250 µL of phosphate-buffered saline (PBS).

Coverslips were coated by carefully pipetting 10 µL of each polymer solution on a 13-mm PETG coverslip (Tissue Culture Coverslips 13 mm, Sarstedt, Nümbrecht, Germany) to obtain a fully coated surface. The coverslips were let dry in air for at least 4 h, followed by crosslinking with 3 J/cm² at 254 nm. Washing 3× with ddH₂O and 3× with ethanol, followed by drying in an N₂ stream yielded the final coating, which was used directly for IR spectroscopy.

2.3. Physicochemical Surface Characterization

IR data was recorded on a Tensor 27 FT-IR Spectrometer (Bruker, Germany). Scanning electron microscope (SEM) images were obtained with an XL-30 SEM (Philips, Amsterdam, Netherlands) at 10 kV. The samples were dried in vacuum and thereafter coated with an approx. 5 nm thick Au/Pd layer (SC7620 sputter coater, Quorum, Laughton, UK). Images were taken at a 40° tilted angle. Atomic force microscope (AFM) images were obtained using a CoreAFM (Nanosurf, Liestal, Switzerland) with a TAP150GD-G tip (BudgetSensors, Sofia, Bulgaria, tip radius <10 nm) in tapping mode.

2.4. Biological Evaluation

2.4.1. L-929 Mouse Fibroblast Cell Culture

L-929 mouse fibroblasts were a gift from Dr. Oliver Podlech (CleanControlling GmbH, Emmingen-Liptingen, Germany). Media and reagents were purchased from Sigma-Aldrich (Taufkirchen, Germany). Sterile cell cultureware was purchased from VWR, Germany. Fibroblasts were cultured in low-glucose Dulbecco's Modified Eagle Medium (DMEM), supplemented with 10% (v/v) fetal calf serum (FCS), 1% (v/v) penicillin-streptomycin (10,000 U/mL) and 1% (v/v) L-glutamine. Cells were incubated at 37 °C and 5% CO₂ in a humidified incubator (CB series C150, Binder, Tuttlingen, Germany) and subculturing was performed using trypsin/Ethylenediaminetetraacetic acid (EDTA) before reaching confluency, approximately every third day.

2.4.2. Extract Test Using the MTT Assay

Polymer extracts were prepared according to USP standard [64]. Briefly, after coating a 24-well plate with polymers followed by washing steps, 317 µL of DMEM (20 mL for 120-cm² coated surface) was added and the coating incubated for 24 h at 37 °C in a humidified 5% CO₂ atmosphere. A cell suspension of L-929 in DMEM (100,000 cells/mL) was added to an uncoated 96-well plate (treated for cell culture, 100 µL/well) and grown to adherence overnight. Medium in each well was replaced by prepared extract medium (100 µL) or medium containing 6% Dimethyl sulfoxide (DMSO) for the cytotoxicity positive control and incubated for 72 h at 37 °C in a humidified 5% CO₂ atmosphere. After 72 h, medium was replaced by 110 µL of DMEM containing 10% of a 10mM MTT solution in PBS. After incubating for 4 h in the incubator, 100 µL of 10% SDS in 0.01M HCl solution was added and incubated for 4 h. Absorbance was measured at 570 nm using a Tecan Infinite M2000 microplate reader. Cell viability was calculated as the percentage ratio of averaged absorbance of triplicate wells containing extract versus the averaged absorbance of untreated control wells.

2.4.3. Direct Contact Test Using the MTT Assay

Cell suspension (100,000 cells/mL) was added to a polymer-coated 96-well plate (treated for cell culture, 100 µL each) and incubated over 24 and 48 h at 37 °C and 5% CO₂ in a humidified incubator. At the end of incubation, the medium was removed, and 110 µL of medium containing 10% of a 10 mM MTT solution in PBS was added. After incubating the cells for 4 h at 37 °C in a humidified 5% CO₂ atmosphere, 100 µL of 10% SDS in 0.01M HCl was added and incubated for 4 h at 37 °C in 5% CO₂. The absorbance was measured at 570 nm using a microplate reader. Cell viability was calculated as the percentage ratio of averaged absorbance of each triplicate well containing the same polymer coating versus the averaged absorbance of uncoated control wells.

2.4.4. Bacterial Cell Culture

For antimicrobial tests, bacteria cell lines of *Staphylococcus aureus* (MRSA, DSM 28766) and *Escherichia coli* (K12, DSM 498) were used. Bacterial strains were stored at −80 °C in glycerol stocks. For each experiment, a new vial of bacterial strain was thawed and incubated (Minitron, Infors HT, Bottmingen, Switzerland) overnight at 37 °C and 100 rpm in LB medium before use in the experiments.

2.4.5. Antibacterial Assay by Optical Density

The antibacterial effects of the polymers were evaluated using a direct contact method according to ISO 22196 [65] with a thin film of bacteria solution in LB medium (high-nutrition) or PBS (low-nutrition) between the polymer to be analyzed and a polymer slide to ensure direct contact. A 24-well cell culture tissue plate coated with the polymers to be tested was inoculated with 100 μL of bacterial suspension at a concentration of 3×10^5 cells/mL and sealed with a PETG coverslip. Bacterial solutions were prepared in LB medium for the high-nutrition condition and in PBS for the low-nutrition condition. As controls, wells without polymer coating were treated with bacteria suspension and medium without cells. After incubating the plate for 24 h at 37 °C and 90% humidity, bacteria were removed from the plates by addition of 1 mL of soybean casein digest lecithin polysorbate broth (SCDLP), followed by pipetting up and down 4 times to detach all bacteria. From this mixture, 200 μL was transferred to a 96-well plate in a series of dilutions. The 96-well plate was sealed with parafilm and placed in a plate reader preheated to 37 °C. Optical density at 600 nm was measured every 30 min over the next 12 h. The plate was shaken briefly every 10 min to ensure distribution of nutrients. Measured values from each sample were compared to determine the viability relative to that of untreated samples. The evaluation time point was chosen to be in the exponential phase before reaching the inflection point. For evaluation, the last time point was used for which Equation (1) was still fulfilled:

$$\frac{\log(\text{OD}_{600\text{nm},t_{+1}}) - 2 \times \log(\text{OD}_{600\text{nm},t}) + \log(\text{OD}_{600\text{nm},t_{-1}})}{t - t_{-1}} > 0 \quad (1)$$

where $\text{OD}_{600\text{nm}}$ is the optical density at 600 nm for the different measuring points; t is the measuring time of the data point to be evaluated; t_{+1} is the measuring point of the subsequent data point and t_{-1} is the measuring point of the previous data point.

2.4.6. Antibacterial Assay by Colony-Forming Units

The antibacterial effects of the polymers were evaluated using a direct contact method as a droplet of bacteria solution in PBS on top of the polymer. A bacterial overnight culture in LB medium was centrifuged (10 min, $4000 \times g$) and resuspended in PBS to an OD_{600} value of 0.2. Coated and uncoated PETG coverslips were inoculated in a 6-well tissue culture plate with 100 μL of the prepared bacteria suspension. Uncoated PETG coverslips were used as reference. The samples were cultured for 24 h at 37 °C and 90% humidity in a humid chamber. Solutions were removed and transferred to a sterile tube. Each coverslip was transferred to a 15 mL Falcon tube, covered with 900 μL of PBS, and treated in an ultrasonic bath at 50 Hz for 15 min to remove bacteria. Both PBS fractions were combined, vortexed for 1 min, and pipetted in a series of dilutions on LB agar plates in duplicate (100 μL per dilution and plate). Agar plates were cultured at 37 °C in an incubator, followed by counting of colony-forming units (CFU) after 24 h.

2.4.7. Crystal Violet Assay for Biofilm Assessment

Biofilm formation was assessed in 96-well plates by staining with crystal violet dye. Briefly, 200 μL of a bacterial overnight culture, adjusted to a concentration of 3×10^5 cells/mL in lysogeny broth (LB) medium, was added to each sample. Empty wells (in the outer row, in particular) were filled with 200 μL of PBS to prevent the samples from drying out. The closed well plate was incubated for 24, 48, or 72 h at 37 °C in an incubator without shaking. Then, OD_{600} was measured to ensure comparable cell growth in each well. The medium was gently discarded without removing the biofilm, and the samples were washed carefully 3 times with PBS, followed by fixing with 200 μL of absolute ethanol. The ethanol was aspirated, and the samples were dried for 10 min under sterile conditions. For biofilm staining, 200 μL of 0.5 wt% (*wt/vol*) crystal violet staining solution in PBS was added to each sample, and the plate was incubated for 2 min at room temperature. The staining solution was removed and the samples washed $6 \times$ with 200 μL

of PBS to remove excess dye. The samples were left to dry overnight under a sterile bench, followed by addition of 100 μ L of ethanol to release the dye. After a 10 min incubation, the mixture in each well was transferred to a new 96-well plate, and absorbance at 595 nm was measured using a plate reader.

2.4.8. Extracellular Polymeric Substance (EPS) Assessment by Phenol-Sulfuric Acid Method

In addition, the biofilm formation was assessed by analyzing the carbohydrates in the formed biofilm. Therefore, the phenol-sulfuric acid method according to Masuko et al. [66] was performed. Briefly, polymer coatings were treated in a 96-well plate as previously described for the crystal violet assay and incubated for 24, 48 and 72 h at 37 °C in an incubator without shaking. OD₆₀₀ was measured to ensure comparable cell growth in each well, and the medium was gently discarded. After 3 wash steps with sterile PBS, the samples were fixed with 200 μ l of absolute ethanol. The ethanol was gently aspirated, and the samples were dried for 10 min under sterile conditions. A volume of 150 μ l of concentrated sulfuric acid was added to each well, immediately followed by 30 μ l of 5% phenol in water. The plate was incubated at 90 °C for 5 min and then cooled in an ice bath for an additional 5 min. The absorbance at 490 nm was measured using a plate reader to quantify EPS.

2.4.9. Live/Dead Staining

Besides the Crystal violet staining and EPS assessment, we also performed live/dead staining using the bacteria live/dead staining kit (PromoCell GmbH, Heidelberg, Germany). Polymer coatings were treated in a 96-well plate as previously described for the crystal violet assay and incubated for 24, 48 and 72 h at 37 °C in an incubator without shaking and stained accordingly to the manufacturer's instructions. Briefly, biofilm samples were washed 3 times with sterile 150 mM NaCl solution and stained for 15 min at room temperature in the dark with an appropriate mixture of DMAO (ex/em 490/540) and EthD-III (ex/em 530/630). Live bacteria with an intact cell membrane are stained fluorescent green, whereas dead bacteria with a disrupted cell membrane are stained fluorescent red. Labeled cells were imaged using the fluorescent microscope Observer.Z1 (Carl Zeiss AG, Oberkochen, Germany) and processed using the software ZEN blue edition (Version 3.4, Carl Zeiss AG, Oberkochen, Germany).

2.4.10. Statistical Analysis

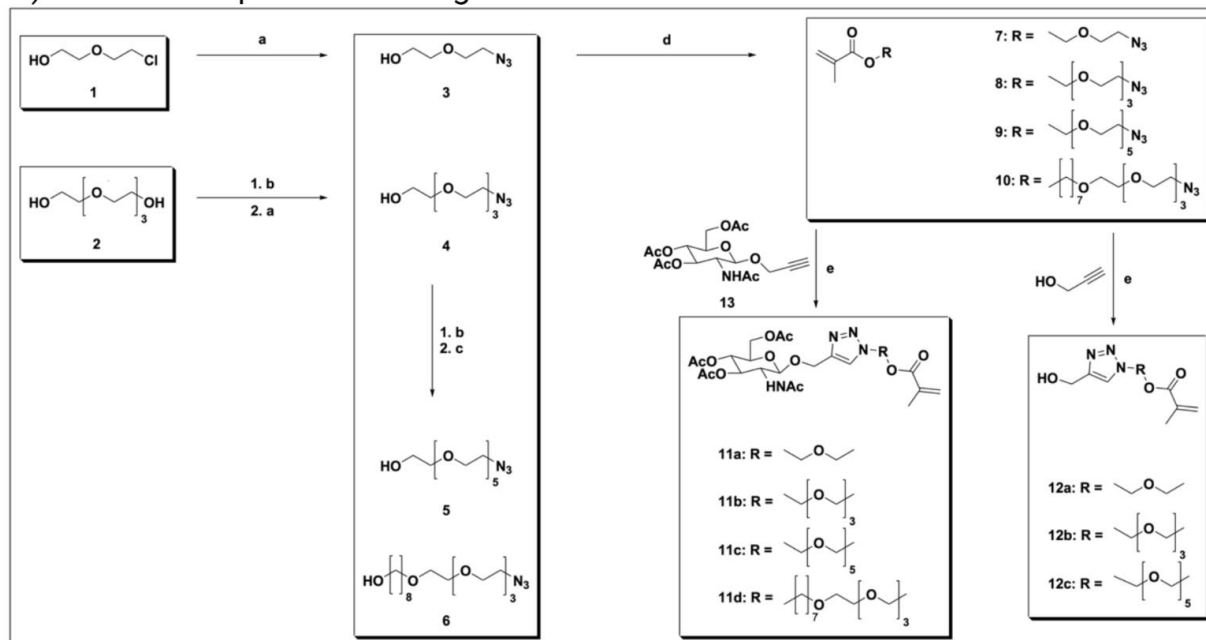
Measurements for biological evaluation (bacterial and cell culture) were replicated with $n = 3$ and expressed as mean \pm standard deviation (SD) unless stated otherwise. Statistical significance was analyzed with pairwise Student's *t*-test, and statistically significant values were defined as $p < 0.05$ (*).

3. Results and Discussion

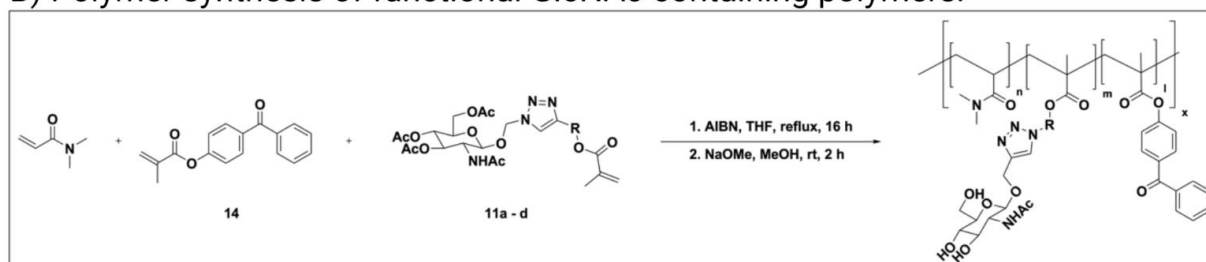
3.1. Monomer Synthesis

Azido linkers 3–6 were synthesized by sequential tosylation steps, followed by substitution with either sodium azide or another linker fragment. Those prolonged linkers were reacted to azido methacrylate 7–10, followed by click reaction to either functional GlcNAc methacrylate 11a–d or their corresponding 4-hydroxymethyl methacrylate derivatives 12a–c. The detailed reaction sequences are shown in Figure 1.

A) Reaction sequences leading to functional monomers:



B) Polymer synthesis of functional GlcNAc-containing polymers:



C) Polymer synthesis of functional 4-hydroxymethyl derivatives:

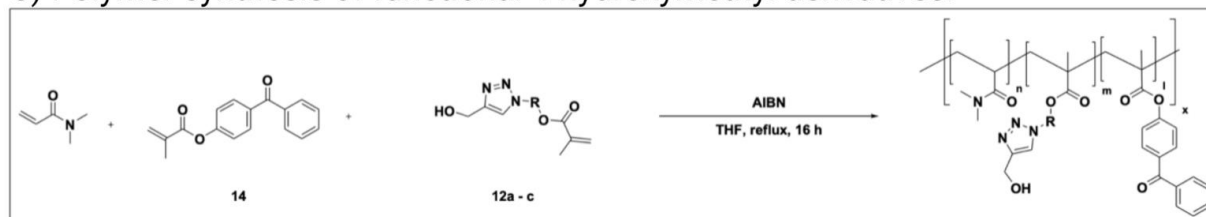


Figure 1. Chemical Synthesis. (A) Reaction sequences leading to functional monomers **11a–d** or **12a–c**, respectively. Reaction conditions: (a) NaN_3 , CH_3CN , reflux, 16 h; (b) TsCl , NEt_3 , CH_2Cl_2 , rt, 16 h; (c) NaH , THF, reflux, 48 h; (d) methacryloyl chloride, NEt_3 , CH_2Cl_2 , 0°C –rt, 16 h; and (e) CuSO_4 , TBTA, Na ascorbate, $\text{H}_2\text{O}/\text{MeOH}/\text{CH}_2\text{Cl}_2$ 3:10:10, 60°C , 1 h. (B) Polymer synthesis of functional *N*-acetylglucosamine (GlcNAc)-containing polymers. Benzophenone methacrylate **14** was copolymerized with glycosidic monomers **11a–d** by free radical polymerization with AIBN, followed by Zemplén deprotection. (C) Polymer synthesis of functional 4-hydroxymethyl derivatives using 4-hydroxymethyl-[1,2,3]-triazolo-1-yl derivatives of functional monomers **12a–c** of the polymers with AIBN.

Azido linker **3** was synthesized by reacting 2-(2-chloroethoxy)-ethanol with sodium azide (a) according to the literature [60]. Azido linkers **4–6** were synthesized via sequen-

tial tosylation (**b**) and substitution steps with either sodium azide (**a**) or another linker for chain prolongment. For the azido hexaethylene glycol linker **5**, diethylene glycol was used for chain prolongment as published Mahou et al. [59], and for the difunctional azido tetraethyleneglycol octyl linker **6**, 1,8-octanediol was used for chain prolongment. Azidomethacrylates **7–10** were synthesized following published protocols, using methacryloyl chloride and triethylamine [61].

The functional glycoside, propargyl GlcNAc **13**, was synthesized as described by Schmidt et al. [62]. *N*-Acetylglucosamine was used as starting material, followed by protection with acetyl groups, conversion of the peracetylated *N*-acetylglucosamine into an oxazoline as glycoside donor, and further glycosidation using propargyl alcohol to *N*-acetylpropargylglucosamine **13**. For click functionalization, the optimized conditions reported by Schmidt et al. [62] were used, yielding the GlcNAc-functionalized monomers **11a–d**. To further elucidate antimicrobial properties of the combined triazole and linker in the polymers, azido oligoethylene glycol methacrylates **7–9** were reacted under the same conditions with propargyl alcohol to their 4-hydroxymethyl-[1,2,3]-triazole-1-yl counterparts **12a–c**. The 4-hydroxymethyl derivatives **12a–c** and the GlcNAc derivatives **11a–d** were used as functional monomers directly for polymerization.

3.2. Polymer Synthesis

Functional GlcNAc monomers **11a–d** were successfully polymerized using free radical polymerization with AIBN as radical starter (Figure 1B), followed by several purification steps with precipitation and *O*-acetyl deprotection to the functional glycosidic polymer. Functional 4-hydroxymethyl monomers **12a–c** were polymerized using free radical polymerization with AIBN (Figure 1C) followed by purification and used directly because no protection groups were involved. The 4-methacryloyloxy-benzophenone **14** was synthesized according to the literature [57]. All synthesized polymers with their corresponding abbreviations are listed in Table 1.

Analysis of the polymers and the copolymer ratio between MBP **14** and functional monomers **11** or **12** was performed by ¹H NMR spectroscopy, followed by 2-dimensional measurements for glycosidic structure determination. The triazole proton, showing a relatively isolated singlet at 7.96 ppm, was integrated against the benzophenone aromatic protons and against the *N*-acetyl group of the glycosidic monomers **11a–d**. For the 4-hydroxymethyl derivatives **12a–c** without glycoside, the triazole proton at 7.96 ppm was integrated against the benzophenone protons only. The dimethacrylamide methyl (DMAM) groups showed a broad multiplet at 2.98–2.75 ppm, which overlapped with the ethylene glycol signals of comonomers **11** and **12**; therefore, the integral ratio of those signals did not match the actual copolymer ratio as shown in Figure 2. The multiplet integral was relatively constant over all three copolymers of **11b**, which had decreasing dimethacrylamide content from 90% to 70%, whereas the content of **11b** with a tetraethylene glycol linker increased from 2.5% to 25%. Therefore, the DMAM content was not calculated using the integral ratios. Successful deprotection of GlcNAc-containing polymers was confirmed by disappearance of the *O*-acetyl groups in ¹H NMR after the deprotection step. For the 4-hydroxymethyl-derivative comonomers **12a–c**, adjusted copolymer ratios of 1:1 MBP **14** vs. **12** were obtained. In the GlcNAc copolymer group, consisting of copolymers with comonomers **11a–d**, different copolymer ratios of MBP **14** vs. **11** were obtained. Possible mechanisms are ester hydrolysis during the Zemplén deprotection step of the GlcNAc residue, because the 4-hydroxymethyl-containing polymeric counterparts did not show different copolymer ratios of the benzophenone. Interestingly, the GlcNAc-4EG copolymers showed no reduction in MBP content relative to the GlcNAc residue (Figure 2). Therefore, different reactivities of benzophenone in combination with several GlcNAc-methacrylates and oligoethylene glycol linkers are possible explanations.

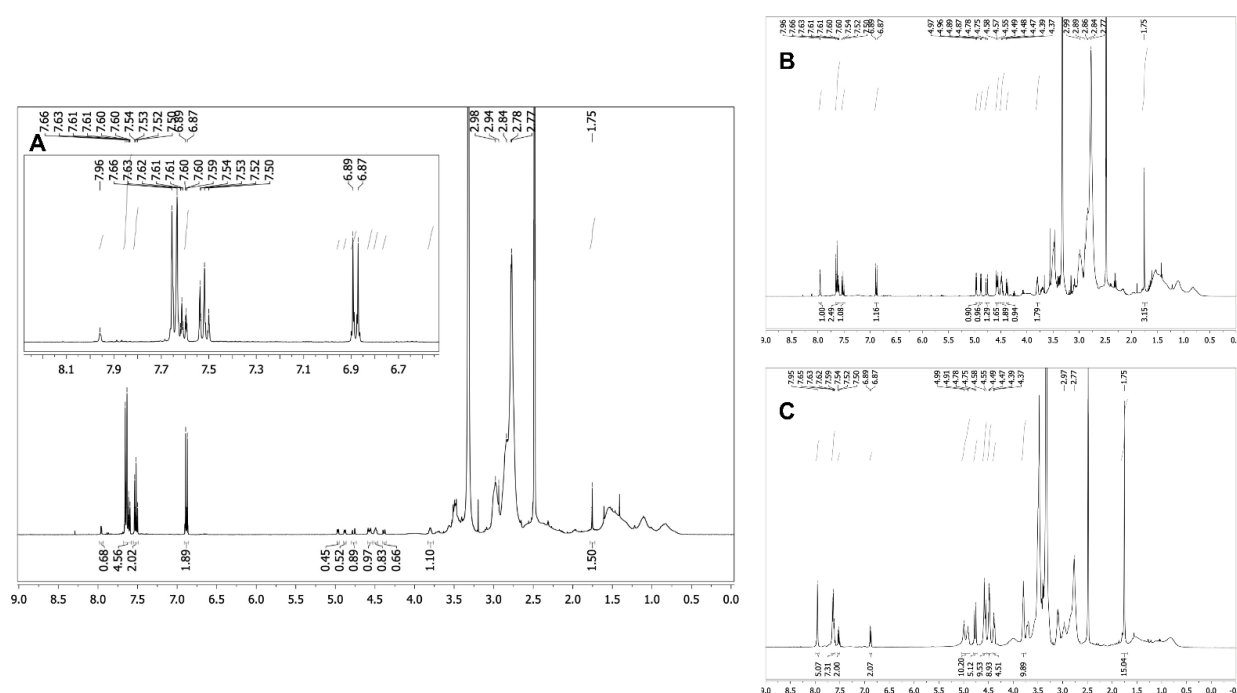


Figure 2. $^1\text{H-NMR}$ spectra (600 MHz) of the 5%—(A), 10%—(B) and 25%—(C) GlcNAc-4EG polymers (Table 1). The GlcNAc and 4-hydroxymethyl triazoles proton gave a distinct singlet at 7.96 ppm, whereas the benzophenones aromatic protons gave signals from 7.66 to 6.67 ppm. Furthermore, the GlcNAc acetyl group singlet showed a signal at 1.75 ppm. The broad multiplet from 2.98 to 2.75 ppm belongs to the dimethacrylamide methyl groups. Copolymer ratio was calculated by the integral ratios of triazole-H vs. NAc vs. aromatic benzophenone-H. For the 4-hydroxymethyl comonomers, only triazole-H was integrated vs. aromatic benzophenone-H. The figure shows the increasing triazole singlet (7.96 ppm) and NAc singlet (1.75 ppm) with increasing comonomer ratio of **11b** vs. the aromatic protons of MBP **14**. The dimethacrylamide multiplet between 2.98 and 2.75 ppm was relatively constant in all three spectra because it overlays the tetraethylene glycol.

Interestingly, the copolymerization of 50% GlcNAc-4EG-methacrylate monomer resulted in ester hydrolysis of the methacrylate ester during polymerization, leading to the propargyl GlcNAc tetraethylene glycol clickamer **15** (data not shown, cf. Supplementary Materials), following the same workup procedure as for the other polymers.

3.3. Coating of PETG Coverslips

As the model material, polyethylene terephthalate glycol (PETG) coverslips were coated with the functional polymers. Previous studies with MBP UV crosslinker in different acrylamide scaffolds indicated that 3 J/cm^2 was the optimum dose of UV irradiation to obtain proper coating stability with minimum unreacted MBP left and minimum coating degradation [57]. Following the crosslinking protocol with UV light (3 J/cm^2 , 254 nm) and several washing steps with ddH₂O and ethanol, stable polymer coatings were obtained using the polymers listed in Table 1. Two concentrations of polymer solutions were applied to the coverslips to obtain coatings of different thicknesses, which were investigated via IR spectroscopy. Recorded spectra of four selected coatings are shown in Figure 3.

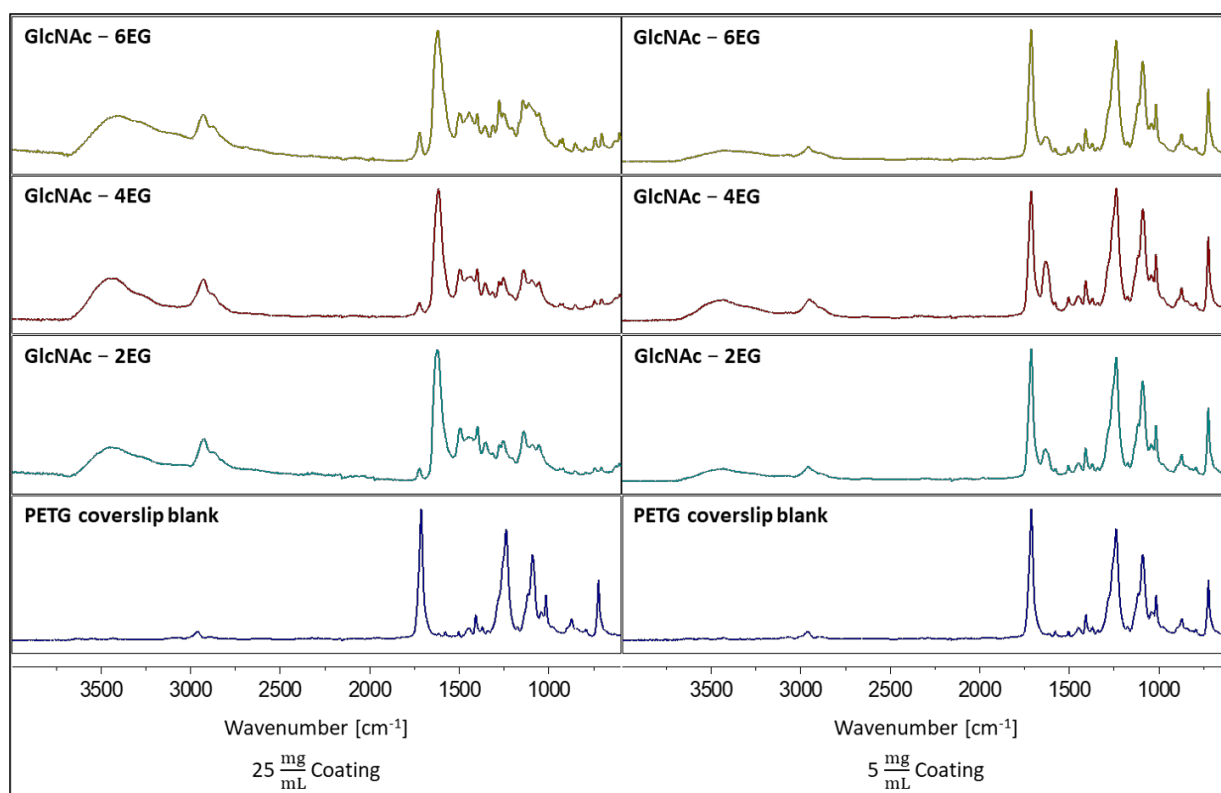


Figure 3. Recorded Fourier transform-infrared spectra of selected functional PDMAm-co-P-benzophenone-MA-co-P-GlcNAc-OEG-MA coatings (Table 1) containing 5% GlcNAc copolymer and linkers with 2, 4 and 6 ethylene glycol (EG) units. Coatings obtained with 25 mg mL^{-1} coatings could be analyzed properly, whereas with 5 mg mL^{-1} coatings, the terephthalate group of the PETG was the dominant signal in the recorded IR spectra.

The dominant peak at 1713 cm^{-1} of the terephthalate of PETG from the coverslip blank disappeared in all polymeric coatings obtained by drop casting a 25 mg/mL solution after crosslinking, wherein the peak of the dimethacrylamide dimethyl-carboxamide group at 1621 cm^{-1} became visible as well as the copolymer ester groups at 1721 cm^{-1} . The presence of the GlcNAc residue was confirmed through the presence of glycosidic OH groups, showing broad peaks at 3450 cm^{-1} and at 2925 cm^{-1} . The stable coatings were obtained using the polymers as listed in Table 1 with the given MBP copolymer ratios. Therefore, apart from the synthesis, stable coatings using a 25 mg/mL casting solution were obtained.

In coatings obtained by casting a 5 mg/mL polymer solution, the most dominant peak in the IR spectra of the coatings was the PETG terephthalate peak at 1713 cm^{-1} , followed by a smaller peak of the dimethacrylamide dimethyl-carboxamide group at 1621 cm^{-1} . The copolymer ester groups at 1721 cm^{-1} were not visible at all compared with those of the thicker 25 mg/mL coatings, possibly being overlaid by the dominant terephthalate peak. As a result, the polymer coatings for antimicrobial studies and cytotoxicity evaluations were prepared by casting a 25 mg/mL solution to obtain an appropriate coating thickness.

3.4. Surface Morphology

The surface morphology of the bioactive polymer coatings 5%-GlcNAc-6EG-PDMAm and 5%-GlcNAc-4EG-PDMAm was investigated by SEM and AFM as shown in Figure 4. SEM images were recorded at a tilted angle of 40 degrees. For the 5%-GlcNAc-4EG-PDMAm, in the SEM image (Figure 4A), a textured surface showing small pores and a sponge-like structure can be observed. Furthermore, small particles in the size of up to

500 nm are present. The AFM surface topography (Figure 4B) confirms the topography. Similar observations can be made for the GlcNAc-6EG coating (Figure 4C,D), but showing less pore-like structures than the 5%-GlcNAc-PDMAm coating.

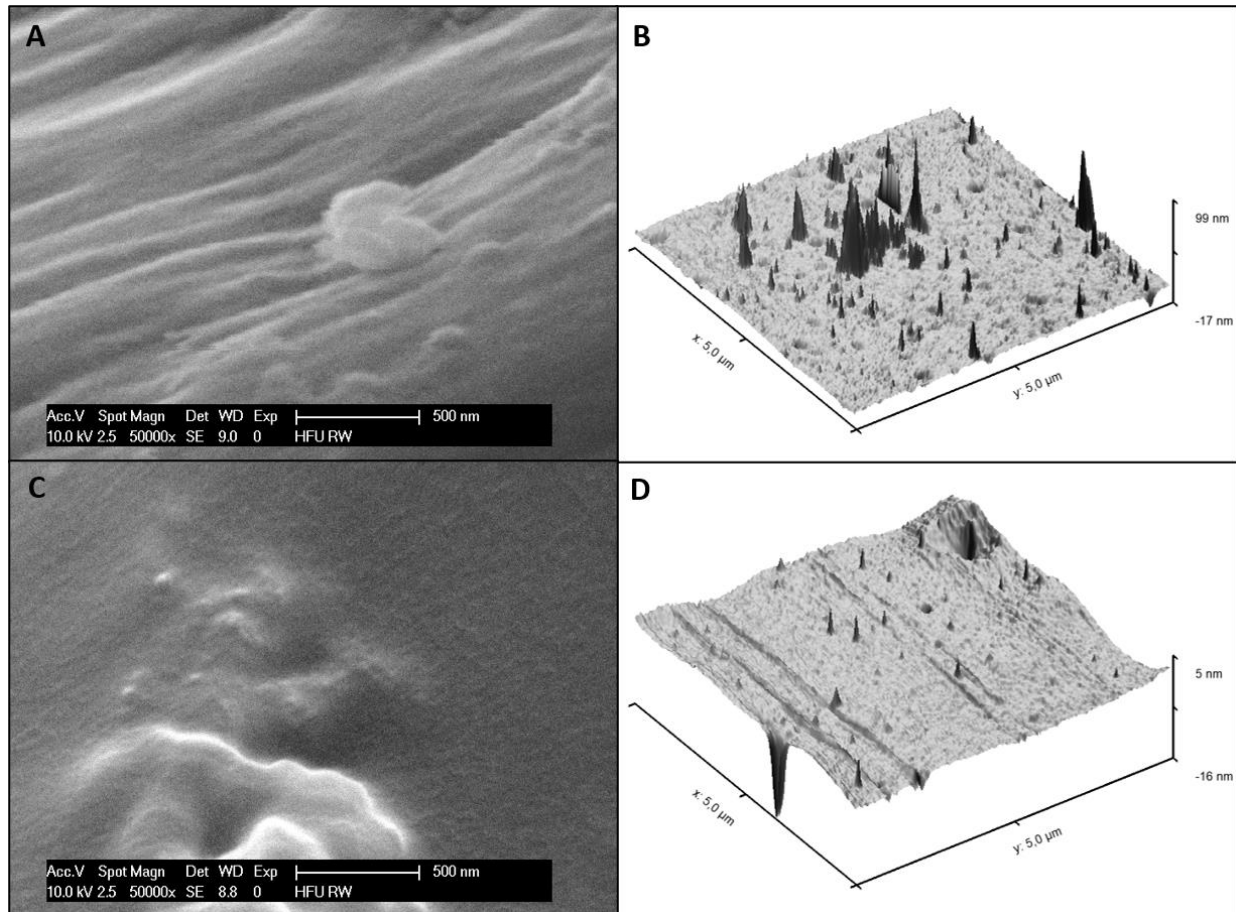


Figure 4. SEM (A,C) and AFM (B,D) images of the bioactive PDMAm coatings, 5%-GlcNAc-4EG (A,B) and GlcNAc-6EG (C,D).

3.5. Coating Sterilization

Due to the sterile demands for biocompatibility testing as well as for antimicrobial activity testing against specified bacterial strains, the successful sterilization of the coating was established prior to testing. Therefore, polymer solutions were sterile filtered with a 0.2 μm sterile filter and handled under sterile condition in a biosafety cabinet during coating of the corresponding surfaces, followed by crosslinking with 3 J/cm^2 UV-C light (254 nm). The polymer coated surfaces were then incubated for 24 h at 37 $^\circ\text{C}$ and further 24 h at room temperature in LB media in order to assess the sterility by absence of bacterial growth. No bacterial growth could be observed for the coated chips under these conditions.

UV sterilization is an established method in food packing, water treatment, and surface sterilization in medical settings [67,68]. For example, according to Bak et. al. [69], a 4-log fold reduction in *P. aeruginosa* in catheter disinfection was obtained, using UV-C light with a dosage of 40 mJ/cm^2 . In addition, clinical studies have shown the efficacy of UV-C light against different fungi, by using a dosage of 41.25 mJ/cm^2 from a commercially available disinfecting device for medical settings [70,71]. In general, for a 90% inactivation of bacterial pathogens, a UV-C dosage of 8 mJ/cm^2 is needed [71], whereas, for ssRNA viruses, an irradiation dose of 1.32–3.20 mJ/cm^2 is needed [72]. Therefore, it can be

concluded that residing pathogens as well as possible viral contaminations are eliminated after the combination of sterile filtration and UV crosslinking of the benzophenone residue in order to form the stable coating.

3.6. Antibacterial Activity

The antibacterial properties of the synthesized polymers were evaluated using *Escherichia coli* (*E. coli*) as a Gram-negative model organism and multidrug-resistant *Staphylococcus aureus* (MRSA) as a Gram-positive model organism. These organisms were chosen as model organisms with clinical relevance for infections and biofilm formation [73]. The bacteria were cultured in high-nutrition (LB medium) and low-nutrition (PBS) environments to assess the effect of the polymers in different nutritional conditions.

In the high-nutrition environment, no effect of coatings on bacterial growth of *E. coli* and *S. aureus* could be observed (Figure 5A). In contrast, under low-nutrition conditions (Figure 5B), the 5%-GlcNAc-4EG (4061 ± 2184 CFU/cm²) and 5%-GlcNAc-6EG (22,883 ± 5172 CFU/cm²) modified PDMAm coatings showed a reduction in bacterial viability, compared with the untreated PETG chip (63,625 ± 13,320 CFU/cm²) and the unmodified PDMAm coating (60,009 ± 17,207 CFU/cm²).

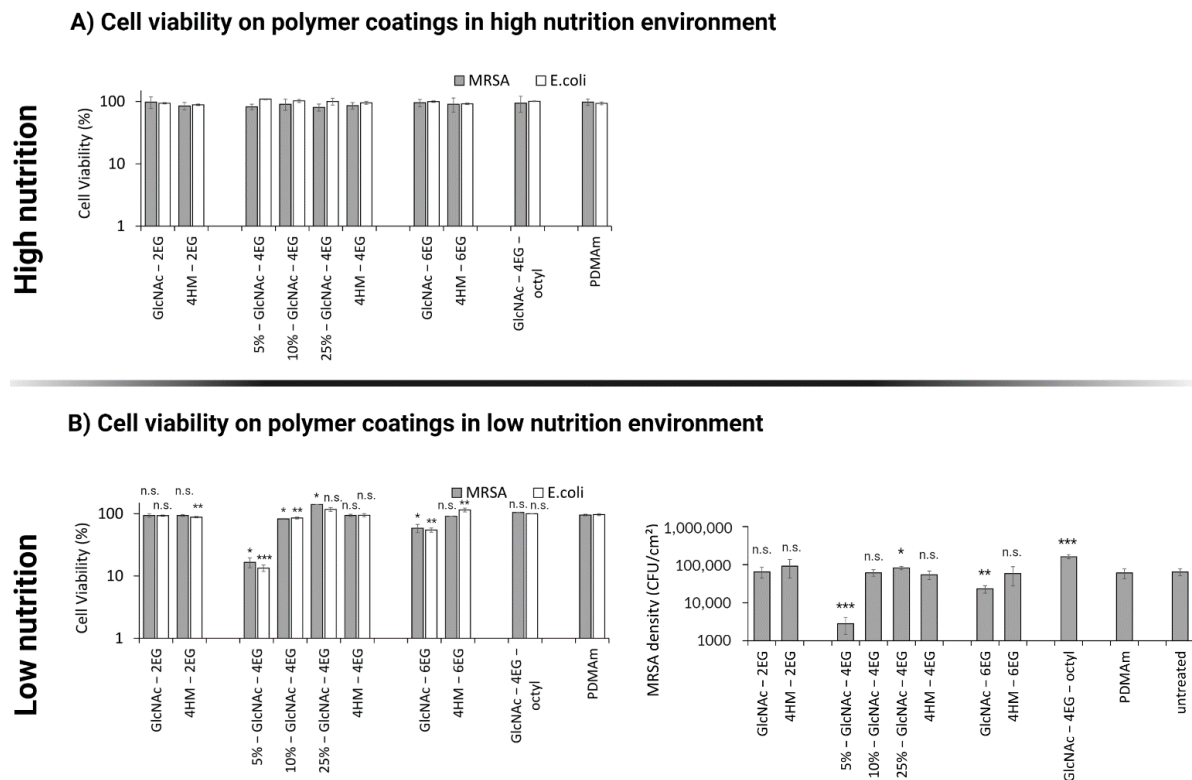


Figure 5. Antibacterial evaluation of polymer coatings in high- and low-nutrition environments. PDMAm corresponds to the unmodified acrylate coating. **(A)** Cell viability of *Escherichia coli* (*E. coli*) and multidrug-resistant *Staphylococcus aureus* (MRSA) on polymer coatings in the high-nutrition environment was assessed according to antibacterial assay (optical density, OD). Values are shown relative to that of the untreated sample. **(B)** Cell viability on polymer coatings in the low-nutrition environment was assessed for *E. coli* ($n = 4$) and MRSA ($n = 2$) according to antibacterial assay (optical density, OD, left graph) and in addition for MRSA ($n = 3$) according to the more sensitive antibacterial assay (colony-forming units, CFU, right graph). Values are shown as mean ± SD. Significant changes were assessed by pairwise Student's *t*-test (n.s., not significant; * $p < 0.05$; ** $p < 0.01$; *** $p < 0.001$).

Both the GlcNAc-2EG modified polymer and the triazole-bearing 4-hydroxymethyl derivatives (4HM-2EG, 4HM-4EG and 4HM-6EG) did not show a considerable effect compared with unmodified PDMAM, whereas the polymers 5%-GlcNAc-4EG and 5%-GlcNAc-6EG showed a significant reduction in viable MRSA and *E. coli* in direct contact testing under low-nutrition conditions (Figure 5B). Thus, viability was reduced by 1.2 log for the GlcNAc-4EG modified hydrogel and by 0.4 log for the GlcNAc-6EG modified hydrogel. Higher ratios of GlcNAc-4EG copolymer in the hydrogel network did not result in a stronger antibacterial effect but resulted in bacterial viabilities similar to those of 4-hydroxymethyl functionalized coatings.

In addition to evaluating the antibacterial effect on bacterial growth, we assessed biofilm formation on the different hydrogels. The crystal violet assay for biofilm assessment showed a decrease in biofilm formation for several polymers, as shown in Figure 6A,B. In particular, the polymers 5%-GlcNAc-4EG and 5%-GlcNAc-6EG showed a significant decrease in biofilm formation compared with the unfunctionalized PDMAM coating. They showed a decrease in absorption at 595 nm for *S. aureus* of 0.46 ± 0.07 and 0.52 ± 0.12 compared with 0.89 ± 0.14 , respectively. Biofilm formation for *E. coli* decreased even more: 0.23 ± 0.07 and 0.42 ± 0.11 compared with 1.06 ± 0.11 . Higher GlcNAc-4EG copolymer content resulted in less biofilm inhibition (60–80% biofilm content) compared with the unmodified PDMAM hydrogel. The effect was observed over a cultivation time of 72 h (Figure 6B) and was confirmed by EPS analysis with the phenol-sulfuric acid method described by Masuko et al. (Figure 6C) [66]. In addition, we analyzed the quantity and viability of bacteria on the polymer coatings after 24, 48 and 72 h incubation, using live/dead staining (Figure 6D). Even though the live staining with DMAO in combination with the polymer coating resulted in high background noises, so that a low exposure time had to be selected and the intensity of the fluorescent stained bacteria was low, the overall effect of the polymer coatings could be confirmed. The quantity of bacteria was significantly lower for the polymers 5%-GlcNAc-4EG and 5%-GlcNAc-6EG compared to their respective controls 4HM-4EG and 4HM-6EG as can be seen in the brightfield images (Figure 6D). Furthermore, it was observed that the proportion of dead cells, especially on the 5%-GlcNAc-4EG, was higher than on the corresponding controls and particularly on the unmodified PDMAM, where a mix of dead and alive cells was visible. Additional images taken at 24, 48 and 72 h are shown in the supplementary materials (Figures S2–S4).

The inhibition of biofilm formation by GlcNAc was previously observed by Sicard et al. for different *E. coli* strains, but not for *S. aureus* [47]. However, under high-nutrition conditions, there was no longer any effect on bacterial growth observed. Antibacterial effects in the low-nutrition environment were evaluated using the OD-method to identify potential candidates and additionally evaluated for MRSA using the more sensitive CFU-method, which is more conclusive, particularly in the lower measurement range. This is attributed to the measurement procedure itself, since in the OD-method, although cells in the process of dying make up only a small part of the population, they also lead to a signal in the measurement. In contrast, only the most vital cells are taken into account in the CFU-method, as these must be able to form their own colony. The observations in the nutrient-rich environment may indicate that the polymer interferes in the metabolism of specific substrates, as studies have shown that chitosan interferes with RNA and protein synthesis [74–77]. Therefore, these substrates can no longer be used for biofilm formation or as a source of nutrients. This would explain the observed decrease in biofilm formation (high-nutrition) and bacteria viability under nutrient-poor conditions, whereas under nutrient-rich conditions, the bacteria can use other substrates as a source of nutrients, negating the growth-inhibiting effect. Another possible explanation for the lack of effect on growth under high-nutrient levels is that a higher mortality rate might have been present but was not measurable because it was obscured by significantly greater bacterial proliferation. As a result, the effect of the coatings was only observable in the low-nutrition medium, where bacterial growth was negligible and thus the increased mortality rate could be observed [78]. Nevertheless, the antibiofilm effect was observed under the nutrient-rich

conditions, so the effect seems to be only partially dependent on the nutrient condition. The exact mechanism underlying the antibacterial and antibiofilm effect needs further elucidation [76].

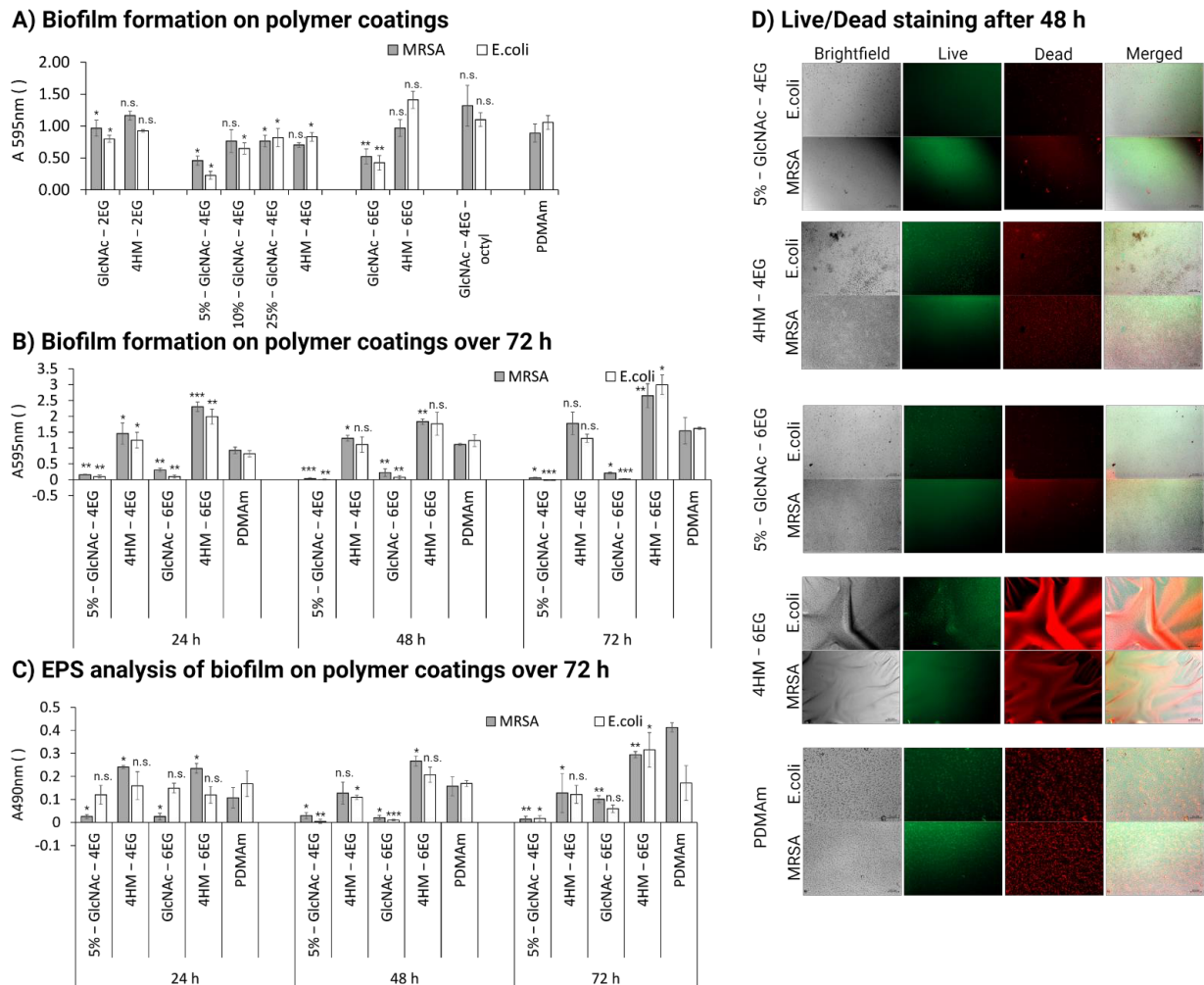


Figure 6. Evaluation of biofilm formation of polymer coatings. PDMAm corresponds to the unmodified acrylate coating. (A) Biofilm formation of *E. coli* and MRSA in the high-nutrient environment was assessed by crystal violet staining after 24 h of cultivation for all coatings as a first evaluation. (B) Biofilm formation of *E. coli* and MRSA in the high-nutrient environment was assessed by crystal violet staining after 24, 48 and 72 h of cultivation for the most active polymer coatings and their respective controls. Corresponding brightfield images are available in the supplementary materials (Figure S1) (C) Extracellular polymeric substance (EPS) analysis of formed biofilm by *E. coli* and MRSA in the high-nutrient environment was assessed by phenol-sulfuric acid method after 24, 48 and 72 h of cultivation for the most active polymer coatings and their respective controls. (D) Live/Dead staining of *E. coli* and MRSA in the high-nutrient environment after 24, 48 and 72 h of cultivation for the most active polymer coatings and their respective controls. Magnification is 100 \times ; scale bar measures 0.1 mm. Values are shown as mean \pm SD. Significant changes were assessed by pairwise Student's *t*-test (n.s., not significant; * $p < 0.05$; ** $p < 0.01$; *** $p < 0.001$).

Comparison of the different synthesized coatings showed that linker length and the amount of GlcNAc are critical parameters for the antibacterial and antibiofilm functionality of the polymers. We found that the 4EG linker yielded the best results, whereas the 2EG and 6EG linkers had decreased functionality. In addition, GlcNAc content affected the antimicrobial and antibiofilm properties: the highest effect was achieved at 5% GlcNAc and

decreased with higher GlcNAc contents for the 4EG linker. This shows that the 4EG linker itself and therefore the length of the oligoethylene glycol brush affect biofilm formation and antimicrobial properties. The reason for this is most likely the steric arrangement of the functional groups and their distance from the sample surface. Depending on the distance, different interaction possibilities exist between the modified groups and the cell wall or membrane of the bacteria [79].

3.7. Cytotoxicity

A cytotoxicity evaluation of the polymeric coatings was carried out according to ISO 10993-5 standards using the extract method and the contact method. Extracts of the coatings were prepared according to ISO 10993-12 and 6% DMSO was chosen as the positive control for cytotoxicity. Cell viability was assessed by the MTT assay.

Cell viability was measured after 72 h of incubation with the prepared extracts (undiluted and diluted 4-fold with medium); results are shown in Figure 7A. No notable cytotoxic effect was observed for any GlcNAc-containing copolymer in the extract test. This included the antimicrobial and antibiofilm polymer, 5% GlcNAc-containing PDMAm hydrogel (5%-GlcNAc-4EG), whose extracts resulted in no loss of fibroblast viability. The 4-hydroxymethyl copolymers containing a tetraethylene glycol (HM-4EG) or a hexaethylene glycol linker (HM-6EG) showed minor decreases in cell viability: a 23% decrease for the 4EG linker and a 12% decrease for the 6EG linker. The extract of the 4-hydroxymethyl derivative with diethylene glycol linker (HM-2EG) showed no cytotoxicity.

For the direct contact test, the cell culture dish was directly coated with the polymers, followed by crosslinking with UV light, 3 washing steps with phosphate buffer, and seeding of cells onto the generated scaffolds. The observed cell viability after 24 and 48 h, determined by MTT assay, is shown in Figure 7B. After 24 h, cell viability was generally lower than that of the untreated cell culture dish, ranging between 60% and 80% for all polymers including the non-modified PDMAm. After 48 h, the most functional polymer against biofilms (5%-GlcNAc-4EG) and most other tested polymers showed only minor reductions in cell viability, within the range of biological systems. Only the GlcNAc-containing polymer with a diethylene glycol linker and the tetraethylene glycol octyl linker showed decreases in cell viability after 48 h (32% and 37%, respectively).

Furthermore, images of the cells grown directly on the polymer coatings were taken, as shown in Figure 8. Morphology of the cells grown directly on the coatings (Figure 8A–E) is altered compared to the uncoated cell culture dish (Figure 8F). It can be observed that the cell morphology is more spheroid like, which implies a lesser adhesion. Due to the experimental conditions, where the coatings were washed after 24 or 48 h incubation prior to addition of fresh media with MTT, an adequate adherence of the cells to the coatings should be given or else the cells would have been washed away in these steps. Thereby, it can be concluded that the L-929 Fibroblasts show adherent behavior to the coatings, albeit lower than on standard cell culture plates. According to ISO 10993:5—evaluation of cytotoxicity of biomaterials, growth inhibition of >30% compared with an untreated control is considered indicative of cytotoxicity [80]. No polymers, except the GlcNAc-2EG and GlcNAc-4EG-octyl polymers showed greater growth inhibition than 30%, and therefore, all polymers except the GlcNAc-2EG and GlcNAc-4EG-octyl polymers can be considered noncytotoxic.

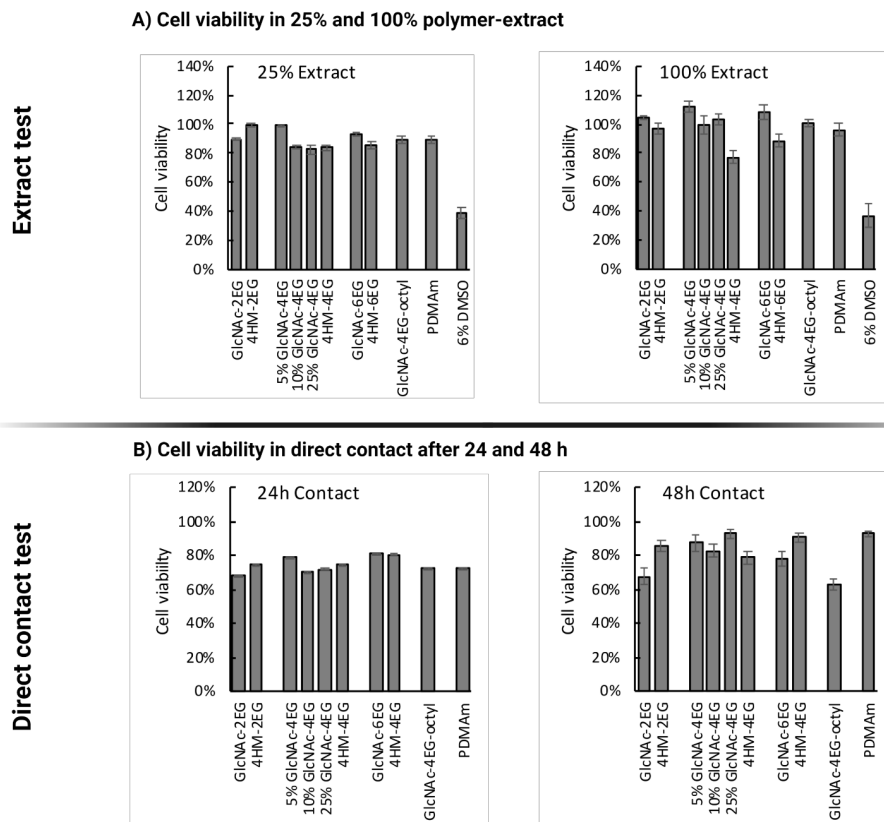


Figure 7. Cytotoxicity determination according to ISO 10993-5. (A) Cell viability measured with MTT assay after 72 h of incubation with 100% and 25% extracts; 6% DMSO was used as positive control for cytotoxicity. In both cases, no cytotoxicity was observed for the antimicrobial 5%-GlcNAc-4EG polymer. (B) Cell viability in direct contact test after 24 and 48 h, determined by MTT assay. The main functional polymer, 5%-GlcNAc-4EG, showed no more than a 20% decrease in cell viability by the direct contact test.

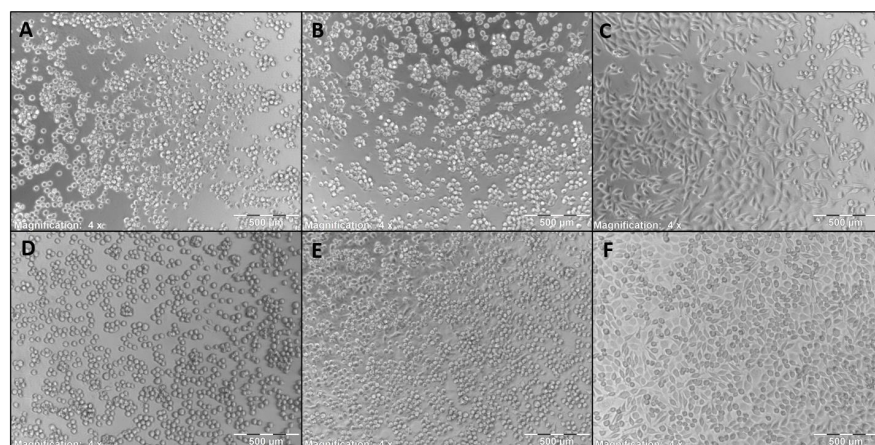


Figure 8. L-929 mouse fibroblasts grown on the coatings for 48 h. (A) GlcNAc-2EG-PDMAm, (B) GlcNAc-4EG-PDMAm, (C) 10%-GlcNAc-4EG-PDMAm, (D) GlcNAc-6EG-PDMAm, (E) PDMAm, (F) untreated cell culture dish. Morphology is altered to some extent, but cell viability is still given as shown via MTT test in Figure 7, in which the shown polymers show no more than 20% reduction in cell viability, so no cytotoxicity can be assumed.

4. Conclusions

In summary, we demonstrated the successful synthesis of functionalized PDMAM hydrogel networks, suitable for polymer surface coating via UV-induced C–H insertion reaction. Stable coatings were obtained using benzophenone crosslinker chemistry. A proper sterility of the surface after UV treatment for crosslinking was shown by the absence of bacterial growth in sterile medium. The functionalized coatings showed antimicrobial and antibiofilm properties, leading to a significant reduction of microbial biofilm formation on the coated surface, for both Gram-positive (*S. aureus*) and Gram-negative (*E. coli*) bacteria. We showed up to a 1.2 log decrease in colony-forming units of the clinically relevant pathogen MRSA on surfaces treated with polymer coating. Non-cytotoxicity and biocompatibility toward fibroblast cells, evaluated according to ISO 10993-5 standards, was maintained. Overall, this work describes an interesting approach for decreasing bacterial adhesion to surfaces by selective functionalization with antiadhesive and antimicrobial molecules, preventing bacterial colonization and contamination of wound dressings or surgical implants. The use of such coatings can not only prevent many surgically induced infections or the formation of biofilms in chronic wounds but also help to accelerate wound healing by favoring fibroblasts.

Supplementary Materials: The following are available online at <https://www.mdpi.com/article/10.3390/pharmaceutics13101647/s1>. Figure S1: Brightfield images after crystal violet staining of biofilm formation on polymer coatings. Figure S2: Fluorescent images after Live/Dead staining of *E. coli* and MRSA in the high-nutrition environment after 24 h of cultivation. Figure S3: Fluorescent images after Live/Dead staining of *E. coli* and MRSA in the high-nutrition environment after 48 h of cultivation. Figure S4: Fluorescent images after Live/Dead staining of *E. coli* and MRSA in the high-nutrition environment after 72 h of cultivation.

Author Contributions: Conceptualization, H.-P.D.; data curation, M.B. and O.R.; funding acquisition, H.-P.D.; investigation, M.B., O.R., T.K. and S.J.; methodology, M.B., O.R. and S.J.; project administration, S.R.; resources, M.S.S., M.E. and H.-P.D.; supervision, S.L., R.C. and H.-P.D.; visualization, M.B. and O.R.; writing—original draft, M.B., O.R. and H.-P.D.; writing—review and editing, M.B., O.R., S.R., M.S.S., S.J., M.E., S.L., R.C. and H.-P.D. All authors have read and agreed to the published version of the manuscript.

Funding: This research was funded by Europäischer Fonds für regionale Entwicklung (EFRE) in the program “Interreg VOberrhein” (Ref: 5115/3.17), by the project “CoHMed MS-Tox Test” (FKZ: 13FH5E01IA; BMBF), and the CoHMed-project “FunktioMed” (FKZ: 13FH5I02IA; BMBF).

Data Availability Statement: The data presented in this study is available in the supplementary material.

Acknowledgments: The authors thank Oliver Podlech, CleanControlling GmbH, for sharing the L-929 cell line and helpful advice regarding cell handling and biocompatibility tests according to ISO 10993-5, and Felix Blendinger for taking the SEM and AFM images. We are grateful to S. the R. for management of all the projects. The authors are grateful for funding of this work provided by the project “TriMaBone–Trinationale Forschungsinitiative: 3D-Druck Materialien für resorbierbare Knochen-implantate” (Europäischer Fonds für regionale Entwicklung—EFRE) in the program “Interreg VOberrhein” (Ref: 5115/3.17), by the project “CoHMed MS-Tox Test” (FKZ: 13FH5E01IA; BMBF) and the CoHMed-project “FunktioMed” (FKZ: 13FH5I02IA; BMBF). The article processing charge was funded by the Baden-Wuerttemberg Ministry of Science, Research, and Culture and the Furtwangen University in the funding program Open Access Publishing.

Conflicts of Interest: The authors declare no conflict of interest.

References

1. Darouiiche, R.O. Device-Associated Infections: A Macroproblem That Starts with Microadherence. *Clin. Infect. Dis.* **2001**, *33*, 1567–1572. [[CrossRef](#)]
2. Zhang, A.; Mu, H.; Zhang, W.; Cui, G.; Zhu, J.; Duan, J. Chitosan Coupling Makes Microbial Biofilms Susceptible to Antibiotics. *Sci. Rep.* **2013**, *3*, 1–7. [[CrossRef](#)]
3. Olivares, E.; Badel-Berchoux, S.; Provot, C.; Prévost, G.; Bernardi, T.; Jehl, F. Clinical Impact of Antibiotics for the Treatment of *Pseudomonas aeruginosa* Biofilm Infections. *Front. Microbiol.* **2020**, *10*, 2894. [[CrossRef](#)]

4. Teerawattanapong, N.; Panich, P.; Kulpokin, D.; Na Ranong, S.; Kongpakwattana, K.; Saksinanon, A.; Goh, B.-H.; Lee, L.-H.; Apisarnthanarak, A.; Chaiyakunapruk, N. A Systematic Review of the Burden of Multidrug-Resistant Healthcare-Associated Infections among Intensive Care Unit Patients in Southeast Asia: The Rise of Multidrug-Resistant *Acinetobacter baumannii*. *Infect. Control Hosp. Epidemiol.* **2018**, *39*, 525–533. [[CrossRef](#)] [[PubMed](#)]
5. Gristina, A.G. Biomaterial-Centered Infection: Microbial Adhesion versus Tissue Integration. *Science* **1987**, *237*, 1588. [[CrossRef](#)]
6. Busscher, H.J.; van der Mei, H.C.; Subbiahdoss, G.; Jutte, P.C.; van den Dungen, J.J.A.M.; Zaat, S.A.J.; Schultz, M.J.; Grainger, D.W. Biomaterial-Associated Infection: Locating the Finish Line in the Race for the Surface. *Sci. Transl. Med.* **2012**, *4*, 153rv10. [[CrossRef](#)] [[PubMed](#)]
7. Poelstra, K.A.; Barekzi, N.A.; Rediske, A.M.; Felts, A.G.; Slunt, J.B.; Grainger, D.W. Prophylactic Treatment of Gram-Positive and Gram-Negative Abdominal Implant Infections Using Locally Delivered Polyclonal Antibodies. *J. Biomed. Mater. Res.* **2002**, *60*, 206–215. [[CrossRef](#)] [[PubMed](#)]
8. Fux, C.A.; Costerton, J.W.; Stewart, P.S.; Stoodley, P. Survival Strategies of Infectious Biofilms. *Trends Microbiol.* **2005**, *13*, 34–40. [[CrossRef](#)] [[PubMed](#)]
9. Vuong, C.; Voyich, J.M.; Fischer, E.R.; Braughton, K.R.; Whitney, A.R.; DeLeo, F.R.; Otto, M. Polysaccharide Intercellular Adhesion (PIA) Protects *Staphylococcus epidermidis* against Major Components of the Human Innate Immune System. *Cell. Microbiol.* **2004**, *6*, 269–275. [[CrossRef](#)] [[PubMed](#)]
10. Attinger, C.; Wolcott, R. Clinically Addressing Biofilm in Chronic Wounds. *Adv. Wound Care* **2012**, *1*, 127–132. [[CrossRef](#)]
11. Costerton, J.W.; Stewart, P.S.; Greenberg, E.P. Bacterial Biofilms: A common Cause of Persistent Infections. *Science* **1999**, *284*, 1318. [[CrossRef](#)]
12. Zimmerli, W.; Widmer, A.F.; Blatter, M.; Frei, R.; Ochsner, P.E. Role of Rifampin for Treatment of Orthopedic Implant-Related Staphylococcal Infections: A Randomized Controlled Trial. *J. Am. Med. Assoc.* **1998**, *279*, 1537–1541. [[CrossRef](#)] [[PubMed](#)]
13. Schmidmaier, G.; Lucke, M.; Wildemann, B.; Haas, N.P.; Raschke, M. Prophylaxis and Treatment of Implant-Related Infections by Antibiotic-Coated Implants: A Review. *Injury* **2006**, *37*, 105–112. [[CrossRef](#)]
14. Ghafouri, H.B.; Bagheri-Behzad, B.; Yasinzadeh, M.R.; Modirian, E.; Divsalar, D.; Farahmand, S. Prophylactic Antibiotic Therapy in Contaminated Traumatic Wounds: Two Days versus Five Days Treatment. *BiolImpacts* **2012**, *2*, 33–37. [[CrossRef](#)] [[PubMed](#)]
15. De Kraker, M.E.A.; Stewardson, A.J.; Harbarth, S. Will 10 Million People Die a Year due to Antimicrobial Resistance by 2050? *PLoS Med.* **2016**, *13*, e1002184. [[CrossRef](#)] [[PubMed](#)]
16. Nations, U.; Assembly, G.; York, N.; Humphreys, G.; Fleck, F. United Nations Meeting on Antimicrobial Resistance. *Bull. World Health Organ.* **2016**, *94*, 638–639.
17. Kargupta, R.; Bok, S.; Darr, C.M.; Crist, B.D.; Gangopadhyay, K.; Gangopadhyay, S.; Sengupta, S. Coatings and Surface Modifications Imparting Antimicrobial Activity to Orthopedic Implants. *Wiley Interdiscip. Rev. Nanomed. Nanobiotechnology* **2014**, *6*, 475–495. [[CrossRef](#)]
18. Brooks, B.D.; Brooks, A.E. Therapeutic Strategies to Combat Antibiotic Resistance. *Adv. Drug Deliv. Rev.* **2014**, *78*, 14–27. [[CrossRef](#)]
19. Hebeish, A.; El-Rafie, M.H.; EL-Sheikh, M.A.; Seleem, A.A.; El-Naggar, M.E. Antimicrobial Wound Dressing and Anti-Inflammatory Efficacy of Silver Nanoparticles. *Int. J. Biol. Macromol.* **2014**, *65*, 509–515. [[CrossRef](#)] [[PubMed](#)]
20. Murata, H.; Koepsel, R.R.; Matyjaszewski, K.; Russell, A.J. Permanent, Non-Leaching Antibacterial Surfaces-2: How High Density Cationic Surfaces Kill Bacterial Cells. *Biomaterials* **2007**, *28*, 4870–4879. [[CrossRef](#)]
21. Tiller, J.C.; Liao, C.-J.; Lewis, K.; Klibanov, A.M. Designing Surfaces That Kill Bacteria on Contact. *Proc. Natl. Acad. Sci. USA* **2001**, *98*, 5981–5985. [[CrossRef](#)]
22. Samal, S.K.; Dash, M.; Van Vlierberghe, S.; Kaplan, D.L.; Chiellini, E.; van Blitterswijk, C.; Moroni, L.; Dubruel, P. Cationic Polymers and Their Therapeutic Potential. *Chem. Soc. Rev.* **2012**, *41*, 7147. [[CrossRef](#)]
23. Huang, J.; Murata, H.; Koepsel, R.R.; Russell, A.J.; Matyjaszewski, K. Antibacterial Polypropylene via Surface-Initiated Atom Transfer Radical Polymerization. *Biomacromolecules* **2007**, *8*, 1396–1399. [[CrossRef](#)]
24. Lee, S.B.; Koepsel, R.R.; Morley, S.W.; Matyjaszewski, K.; Sun, Y.; Russell, A.J. Permanent, Nonleaching Antibacterial Surfaces, 1. Synthesis by Atom Transfer Radical Polymerization. *Biomacromolecules* **2004**, *5*, 877–882. [[CrossRef](#)] [[PubMed](#)]
25. Madkour, A.E.; Dabkowski, J.M.; Nüsslein, K.; Tew, G.N. Fast Disinfecting Antimicrobial Surfaces. *Langmuir* **2009**, *25*, 1060–1067. [[CrossRef](#)] [[PubMed](#)]
26. Yang, L.; Weiss, T.M.; Lehrer, R.I.; Huang, H.W. Crystallization of Antimicrobial Pores in Membranes: Magainin and Protegrin. *Biophys. J.* **2000**, *79*, 2002–2009. [[CrossRef](#)]
27. Shai, Y. Mechanism of the Binding, Insertion and Destabilization of Phospholipid Bilayer Membranes by α -Helical Antimicrobial and Cell Non-Selective Membrane-Lytic Peptides. *Biochim. Biophys. Acta-Biomembr.* **1999**, *1462*, 55–70. [[CrossRef](#)]
28. Matsuzaki, K. Why and How are Peptide–Lipid Interactions Utilized for Self-Defense? Magainins and Tachyplesins as Archetypes. *Biochim. Biophys. Acta-Biomembr.* **1999**, *1462*, 1–10. [[CrossRef](#)]
29. Milović, N.M.; Wang, J.; Lewis, K.; Klibanov, A.M. Immobilized N-Alkylated Polyethylenimine Avidly Kills Bacteria by Rupturing Cell Membranes with No Resistance Developed. *Biotechnol. Bioeng.* **2005**, *90*, 715–722. [[CrossRef](#)]
30. Lin, J.; Tiller, J.C.; Lee, S.B.; Lewis, K.; Klibanov, A.M. Insights into Bactericidal Action of Surface-Attached Poly(Vinyl-N-Hexylpyridinium) Chains. *Biotechnol. Lett.* **2002**, *24*, 801–805. [[CrossRef](#)]

31. Lin, J.; Murthy, S.K.; Olsen, B.D.; Gleason, K.K.; Klivanov, A.M. Making Thin Polymeric Materials, Including Fabrics, Microbicidal and Also Water-Repellent. *Biotechnol. Lett.* **2003**, *25*, 1661–1665. [[CrossRef](#)] [[PubMed](#)]
32. Ikeda, T.; Hirayama, H.; Yamaguchi, H.; Tazuke, S.; Watanabe, M. Polycationic Biocides with Pendant Active Groups: Molecular Weight Dependence of Antibacterial Activity. *Antimicrob. Agents Chemother.* **1986**, *30*, 132–136. [[CrossRef](#)]
33. Ikeda, T.; Yamaguchi, H.; Tazuke, S. New Polymeric Biocides: Synthesis and Antibacterial Activities of Polycations with Pendant Biguanide Groups. *Antimicrob. Agents Chemother.* **1984**, *26*, 139–144. [[CrossRef](#)] [[PubMed](#)]
34. Isquith, A.J.; Abbott, E.A.; Walters, P.A. Surface-Bonded Antimicrobial Activity of an Organosilicon Quaternary Ammonium Chloride. *Appl. Microbiol.* **1972**, *24*, 859–863. [[CrossRef](#)]
35. Luz, G.M.; Boesel, L.; Campo, A.D.; Mano, J.F. Micropatterning of Bioactive Glass Nanoparticles on Chitosan Membranes for Spatial Controlled Biomineralization. *Langmuir* **2012**, *28*, 6970–6977. [[CrossRef](#)] [[PubMed](#)]
36. Wang, Y.; Shi, R.; Gong, P.; Li, J.; Li, J.; Ao, D.; Wang, P.; Yang, Y.; Man, Y.; Qu, Y. Bioelectric Effect of a Chitosan Bioelectret Membrane on Bone Regeneration in Rabbit Cranial Defects. *J. Bioact. Compat. Polym.* **2012**, *27*, 122–132. [[CrossRef](#)]
37. Kim, I.-Y.; Seo, S.-J.; Moon, H.-S.; Yoo, M.-K.; Park, I.-Y.; Kim, B.-C.; Cho, C.-S. Chitosan and its Derivatives for Tissue Engineering Applications. *Biotechnol. Adv.* **2008**, *26*, 1–21. [[CrossRef](#)]
38. Sivashankari, P.R.; Prabakaran, M. Prospects of Chitosan-Based Scaffolds for Growth Factor Release in Tissue Engineering. *Int. J. Biol. Macromol.* **2016**, *93*, 1382–1389. [[CrossRef](#)]
39. Liu, Z.; Wang, H.; Wang, Y.; Lin, Q.; Yao, A.; Cao, F.; Li, D.; Zhou, J.; Duan, C.; Du, Z.; et al. The Influence of Chitosan Hydrogel on Stem Cell Engraftment, Survival and Homing in the Ischemic Myocardial Microenvironment. *Biomaterials* **2012**, *33*, 3093–3106. [[CrossRef](#)]
40. Shi, W.; Nie, D.; Jin, G.; Chen, W.; Xia, L.; Wu, X.; Su, X.; Xu, X.; Ni, L.; Zhang, X.; et al. BDNF Blended Chitosan Scaffolds for Human Umbilical Cord MSC Transplants in Traumatic Brain Injury Therapy. *Biomaterials* **2012**, *33*, 3119–3126. [[CrossRef](#)]
41. Jayakumar, R.; Prabakaran, M.; Sudheesh Kumar, P.T.; Nair, S.V.; Tamura, H. Biomaterials Based on Chitin and Chitosan in Wound Dressing Applications. *Biotechnol. Adv.* **2011**, *29*, 322–337. [[CrossRef](#)]
42. Jayakumar, R.; Prabakaran, M.; Nair, S.V.; Tokura, S.; Tamura, H.; Selvamurugan, N. Novel Carboxymethyl Derivatives of Chitin and Chitosan Materials and Their Biomedical Applications. *Prog. Mater. Sci.* **2010**, *55*, 675–709. [[CrossRef](#)]
43. Helander, I.M.; Nurmiho-Lassila, E.L.; Ahvenainen, R.; Rhoades, J.; Roller, S. Chitosan Disrupts the Barrier Properties of the Outer Membrane of Gram-Negative Bacteria. *Int. J. Food Microbiol.* **2001**, *71*, 235–244. [[CrossRef](#)]
44. Je, J.Y.; Kim, S.K. Chitosan Derivatives Killed Bacteria by Disrupting the Outer and Inner Membrane. *J. Agric. Food Chem.* **2006**, *54*, 6629–6633. [[CrossRef](#)] [[PubMed](#)]
45. Divya, K.; Vijayan, S.; George, T.K.; Jisha, M.S. Antimicrobial Properties of Chitosan Nanoparticles: Mode of Action and Factors Affecting Activity. *Fibers Polym.* **2017**, *18*, 221–230. [[CrossRef](#)]
46. Izano, E.A.; Sadovskaya, I.; Vinogradov, E.; Mulks, M.H.; Velliagounder, K.; Ragunath, C.; Kher, W.B.; Ramasubbu, N.; Jabbouri, S.; Perry, M.B.; et al. Poly-N-Acetylglucosamine Mediates Biofilm Formation and Antibiotic Resistance in *Actinobacillus pleuropneumoniae*. *Microb. Pathog.* **2007**, *43*, 1–9. [[CrossRef](#)] [[PubMed](#)]
47. Sicard, J.F.; Voegelé, P.; Le Bihan, G.; Rodríguez Olivera, Y.; Beaudry, F.; Jacques, M.; Harel, J. N-Acetyl-Glucosamine Influences the Biofilm Formation of *Escherichia coli*. *Gut Pathog.* **2018**, *10*, 26. [[CrossRef](#)] [[PubMed](#)]
48. Blagodatskikh, I.V.; Kulikov, S.N.; Vyshivannaya, O.V.; Bezrodnykh, E.A.; Yamskov, I.A.; Tikhonov, V.E. Influence of Glucosamine on Oligochitosan Solubility and Antibacterial Activity. *Carbohydr. Res.* **2013**, *381*, 28–32. [[CrossRef](#)]
49. Dheer, D.; Singh, V.; Shankar, R. Medicinal Attributes of 1,2,3-Triazoles: Current Developments. *Bioorg. Chem.* **2017**, *71*, 30–54. [[CrossRef](#)]
50. Kolb, H.C.; Finn, M.G.; Sharpless, K.B. Click Chemistry: Diverse Chemical Function from a Few Good Reactions. *Angew. Chemie Int. Ed.* **2001**, *40*, 2004–2021. [[CrossRef](#)]
51. Kolb, H.C.; Sharpless, K.B. The Growing Impact of Click Chemistry on Drug Discovery. *Drug Discov. Today* **2003**, *8*, 1128–1137. [[CrossRef](#)]
52. Wang, L.; Chen, J.; Shi, L.; Shi, Z.; Ren, L.; Wang, Y. The Promotion of Antimicrobial Activity on Silicon Substrates Using a “click” Immobilized Short Peptide. *Chem. Commun.* **2014**, *50*, 975–977. [[CrossRef](#)] [[PubMed](#)]
53. Glowacka, I.E.; Grzonkowski, P.; Lisiecki, P.; Kalinowski, Ł.; Piotrowska, D.G. Synthesis and Antimicrobial Activity of Novel 1,2,3-Triazole-Conjugates of Quinazolin-4-Ones. *Arch. Pharm.* **2019**, *352*, 1800302. [[CrossRef](#)] [[PubMed](#)]
54. Petrova, K.T.; Potewar, T.M.; Correia-Da-Silva, P.; Barros, M.T.; Calhelha, R.C.; Ćirić, A.; Soković, M.; Ferreira, I.C.F.R. Antimicrobial and Cytotoxic Activities of 1,2,3-Triazole-Sucrose Derivatives. *Carbohydr. Res.* **2015**, *417*, 66–71. [[CrossRef](#)] [[PubMed](#)]
55. Holla, B.S.; Mahalinga, M.; Karthikeyan, M.S.; Poojary, B.; Akberali, P.M.; Kumari, N.S. Synthesis, Characterization and Antimicrobial Activity of Some Substituted 1,2,3-Triazoles. *Eur. J. Med. Chem.* **2005**, *40*, 1173–1178. [[CrossRef](#)]
56. Abdel-Wahab, F.B.; Mohamed, H.A.; Awad, E.A.G. Synthesis and Biological Activity of Some New 1,2,3-Triazole Hydrazone Derivatives. *Eur. Chem. Bull.* **2015**, *4*, 106–109. [[CrossRef](#)]
57. Pandiyarajan, C.K.; Prucker, O.; Zieger, B.; Rühle, J. Influence of the Molecular Structure of Surface-Attached Poly(N-alkyl Acrylamide) Coatings on the Interaction of Surfaces with Proteins, Cells and Blood Platelets. *Macromol. Biosci.* **2013**, *13*, 873–884. [[CrossRef](#)]
58. Prucker, O.; Brandstetter, T.; Rühle, J. Surface-Attached Hydrogel Coatings via C,H-Insertion Crosslinking for Biomedical and Bioanalytical Applications (Review). *Biointerphases* **2018**, *13*, 010801. [[CrossRef](#)]

59. Mahou, R.; Wandrey, C. Versatile Route to Synthesize Heterobifunctional Poly(Ethylene Glycol) of Variable Functionality for Subsequent Pegylation. *Polymers* **2012**, *4*, 561–589. [[CrossRef](#)]
60. Öztürk, T.; Meyvacı, E.; Arslan, T. Synthesis and Characterization of Poly(Vinyl Chloride-g-ε-Caprolactone) Brush Type Graft Copolymers by Ring-Opening Polymerization and “Click” Chemistry. *J. Macromol. Sci. Part. A* **2020**, *57*, 171–180. [[CrossRef](#)]
61. Sumerlin, B.S.; Tsarevsky, N.V.; Louche, G.; Lee, R.Y.; Matyjaszewski, K. Highly Efficient “Click” Functionalization of Poly(3-azidopropyl methacrylate) Prepared by ATRP. *Macromolecules* **2005**, *38*, 7540–7545. [[CrossRef](#)]
62. Schmidt, M.S.; Leitner, K.; Welter, M.; Wurmthaler, L.A.; Ringwald, M. Carbohydrate-Based Cu(I) Stabilizing Ligands and Their Use in the Synthesis of Carbohydrate–Ferrocene Conjugates. *Carbohydr. Res.* **2014**, *387*, 42–45. [[CrossRef](#)] [[PubMed](#)]
63. Waldvogel, S.R. Zemplén Deacetylation. In *Comprehensive Organic Name Reactions and Reagents*; John Wiley & Sons, Inc.: Hoboken, NJ, USA, 2010; Volume 2010, p. 892.
64. 87: Biological Reactivity Tests, in Vitro. In *The United States Pharmacopeia-The National Formulary*; Pharmacopeial Convention, Inc.: Rockville, MD, USA, 1979; Volume 35, pp. 92–94.
65. Japan Food Research Laboratories. *Measurement of Antibacterial Activity on Plastics and Other Non-Porous Surfaces*; ISO: London, UK, 2011; pp. 1–24.
66. Masuko, T.; Minami, A.; Iwasaki, N.; Majima, T.; Nishimura, S.I.; Lee, Y.C. Carbohydrate Analysis by a Phenol-Sulfuric Acid Method in Microplate Format. *Anal. Biochem.* **2005**, *339*, 69–72. [[CrossRef](#)] [[PubMed](#)]
67. Kowalski, W. *Ultraviolet Germicidal Irradiation Handbook*; Springer: Berlin/Heidelberg, Germany, 2009; ISBN 9783642019982.
68. Cutler, T.D.; Zimmerman, J.J. Ultraviolet Irradiation and the Mechanisms Underlying its Inactivation of Infectious Agents. *Anim. Health Res. Rev.* **2011**, *12*, 15–23. [[CrossRef](#)]
69. Bak, J.; Begovic, T. A Prototype Catheter Designed for Ultraviolet C Disinfection. *J. Hosp. Infect.* **2013**, *84*, 173–177. [[CrossRef](#)]
70. Yang, J.-H.; Wu, U.-I.; Tai, H.-M.; Sheng, W.-H. Effectiveness of an Ultraviolet-C Disinfection System for Reduction of Healthcare-Associated Pathogens. *J. Microbiol. Immunol. Infect.* **2019**, *52*, 487–493. [[CrossRef](#)] [[PubMed](#)]
71. Gora, S.L.; Rauch, K.D.; Ontiveros, C.C.; Stoddart, A.K.; Gagnon, G.A. Inactivation of Biofilm-Bound Pseudomonas Aeruginosa Bacteria Using UVC Light Emitting Diodes (UVC LEDs). *Water Res.* **2019**, *151*, 193–202. [[CrossRef](#)]
72. Tseng, C.-C.; Li, C.-S. Inactivation of Viruses on Surfaces by Ultraviolet Germicidal Irradiation. *J. Occup. Environ. Hyg.* **2007**, *4*, 400–405. [[CrossRef](#)]
73. Donlan, R.M. Biofilms and Device-Associated Infections. In *Proceedings of the Emerging Infectious Diseases*; Centers for Disease Control and Prevention (CDC): Atlanta, GA, USA, 2001; Volume 7, pp. 277–281.
74. Liu, X.F.; Guan, Y.L.; Yang, D.Z.; Li, Z.; Yao, K. De Antibacterial Action of Chitosan and Carboxymethylated Chitosan. *J. Appl. Polym. Sci.* **2001**, *79*, 1324–1335. [[CrossRef](#)]
75. LI, M.; CHEN, C.; XIA, X.; GARBA, B.; SHANG, L.; WANG, Y. Proteomic Analysis of the Inhibitory Effect of Chitosan on *Penicillium expansum*. *Food Sci. Technol.* **2020**, *40*, 250–257. [[CrossRef](#)]
76. Khan, F.; Pham, D.T.N.; Oloketuyi, S.F.; Manivasagan, P.; Oh, J.; Kim, Y.-M. Chitosan and Their Derivatives: Antibiofilm Drugs against Pathogenic Bacteria. *Colloids Surf. B Biointerfaces* **2020**, *185*, 110627. [[CrossRef](#)] [[PubMed](#)]
77. Tantala, J.; Thumanu, K.; Rachtanapun, C. An Assessment of Antibacterial Mode of Action of Chitosan on *Listeria innocua* Cells Using Real-Time HATR-FTIR Spectroscopy. *Int. J. Biol. Macromol.* **2019**, *135*, 386–393. [[CrossRef](#)] [[PubMed](#)]
78. Andres, Y.; Giraud, L.; Gerente, C.; Le Cloirec, P. Antibacterial Effects of Chitosan Powder: Mechanisms of Action. *Environ. Technol.* **2007**, *28*, 1357–1363. [[CrossRef](#)] [[PubMed](#)]
79. Liu, H.; Du, Y.; Wang, X.; Sun, L. Chitosan Kills Bacteria through Cell Membrane Damage. *Int. J. Food Microbiol.* **2004**, *95*, 147–155. [[CrossRef](#)] [[PubMed](#)]
80. ISO. *Biological Evaluation of Medical Devices-Part. 5: Tests for In Vitro Cytotoxicity*; ISO: London, UK, 2009.

Supplementary Material

Methacryloyl-GlcNAc Derivatives Copolymerized with Dimethacrylamide as a Novel Antibacterial and Biocompatible Coating

Max Borgolte ^{1,2}, Oliver Riester ^{1,3,4}, Tereza Kacerova ^{5,6}, Simone Rentschler ^{1,3}, Magnus S. Schmidt ¹, Susanne Jacksch ¹, Markus Egert ¹, Stefan Laufer ^{3,4}, René Csuk ² and Hans-Peter Deigner ^{1,4,7,*}

- ¹ Institute of Precision Medicine, Furtwangen University, Jakob-Kienzle Str. 17, 78054 Villingen-Schwenningen, Germany; Max.Borgolte@hs-furtwangen.de (M.B.); Oliver.Riester@hs-furtwangen.de (O.R.); S.Rentschler@hs-furtwangen.de (S.R.); Magnus.Schmidt@hs-furtwangen.de (M.S.S.); Susanne.Jacksch@hs-furtwangen.de (S.J.); Markus.Egert@hs-furtwangen.de (M.E.)
 - ² Department of Organic Chemistry, Martin-Luther University Halle-Wittenberg, Kurt-Mothes-Str. 2, 06120 Halle/Saale, Germany; Rene.csuk@chemie.uni-halle.de
 - ³ Department of Pharmaceutical and Medicinal Chemistry, Institute of Pharmaceutical Sciences, Eberhard Karls University Tuebingen, Auf der Morgenstelle 8, 72076 Tübingen, Germany; Stefan.laufer@uni-tuebingen.de
 - ⁴ Faculty of Science, Eberhard Karls University Tuebingen, Auf der Morgenstelle 8, 72076 Tübingen, Germany
 - ⁵ Department of Chemistry, Czech University of Life Sciences, Kamýcká 129, 16500 Prague, Czech Republic; tereza.kacerova.18@ucl.ac.uk
 - ⁶ Department of Chemistry, University College London, London WC1H 0AJ, UK
 - ⁷ EXIM Department, Fraunhofer Institute IZI (Leipzig), Schillingallee 68, 18057 Rostock, Germany
- * Correspondence: dei@hs-furtwangen.de

Citation: Borgolte, M.; Riester, O.; Kacerova, T.; Rentschler, S.; Schmidt, M.S.; Jacksch, S.; Egert, M.; Laufer, S.; Csuk, R.; Deigner, H.-P. Methacryloyl-GlcNAc Derivatives Copolymerized with Dimethacrylamide as a Novel Antibacterial and Biocompatible Coating. *Pharmaceutics* **2021**, *13*, 1647. <https://doi.org/10.3390/pharmaceutics13101647>

Academic Editors: Ewa Klodzińska, Marek Konop

Received: 3 August 2021

Accepted: 2 October 2021

Published: 9 October 2021

Publisher's Note: MDPI stays neutral with regard to jurisdictional claims in published maps and institutional affiliations.



Copyright: © 2021 by the authors. Licensee MDPI, Basel, Switzerland. This article is an open access article distributed under the terms and conditions of the Creative Commons Attribution (CC BY) license (<http://creativecommons.org/licenses/by/4.0/>).

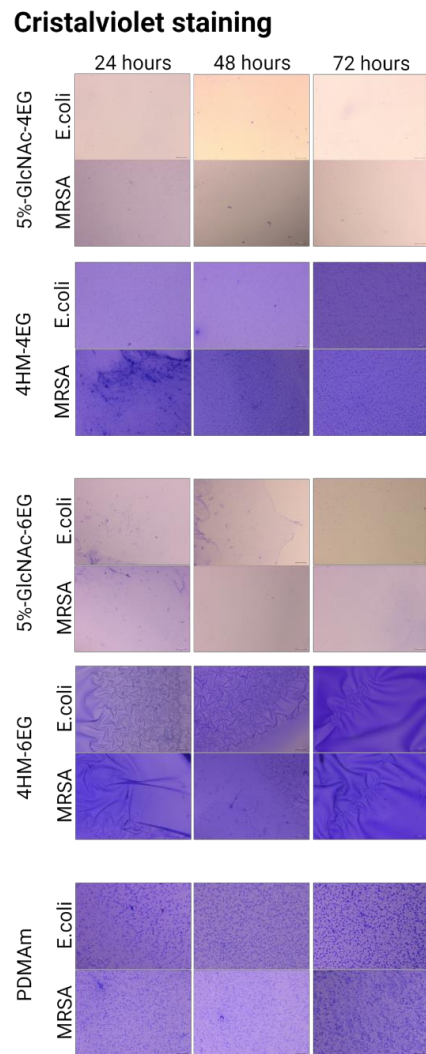


Figure S1. Brightfield images after crystal violet staining of biofilm formation on polymer coatings. PDMAM corresponds to the unmodified acrylate coating. Images were taken with 100× magnification using the microscope Observer.Z1 (Zeiss, Germany) after 24, 48 and 72 h of cultivation. Scale bar measures 0.1 mm.

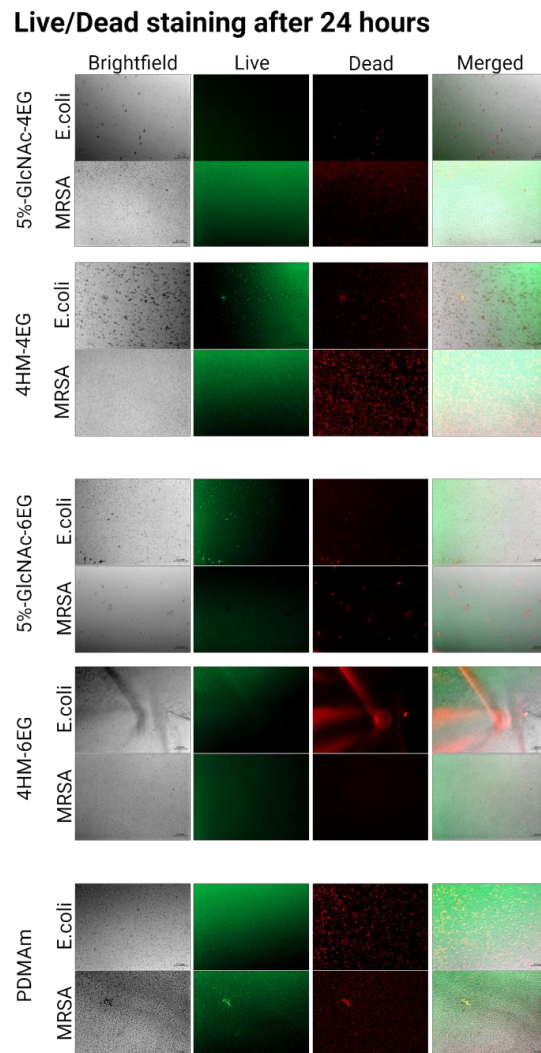


Figure S2. Fluorescent images after Live/Dead staining of *E. coli* and MRSA in the high-nutrition environment after 24 h of cultivation. PDMAm corresponds to the unmodified acrylate coating. Images were taken with 100× magnification using the microscope Observer.Z1 (Zeiss, Germany). Scale bar measures 0.1 mm.

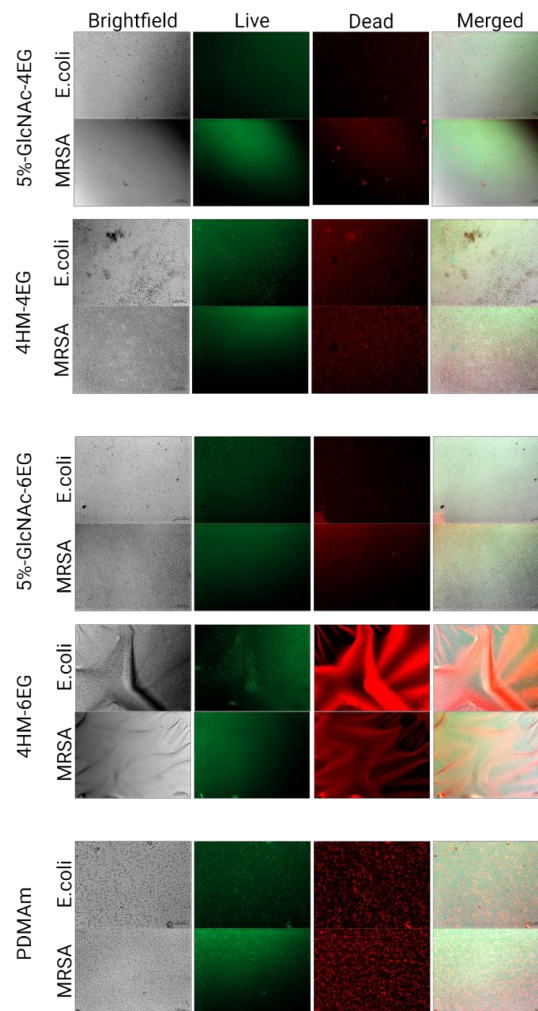
Live/Dead staining after 48 hours

Figure S3. Fluorescent images after Live/Dead staining of *E. coli* and MRSA in the high-nutrition environment after 48 hours of cultivation. PDMAm corresponds to the unmodified acrylate coating. Images were taken with 100x magnification using the microscope Observer.Z1 (Zeiss, Germany). Scale bar measures 0.1 mm.

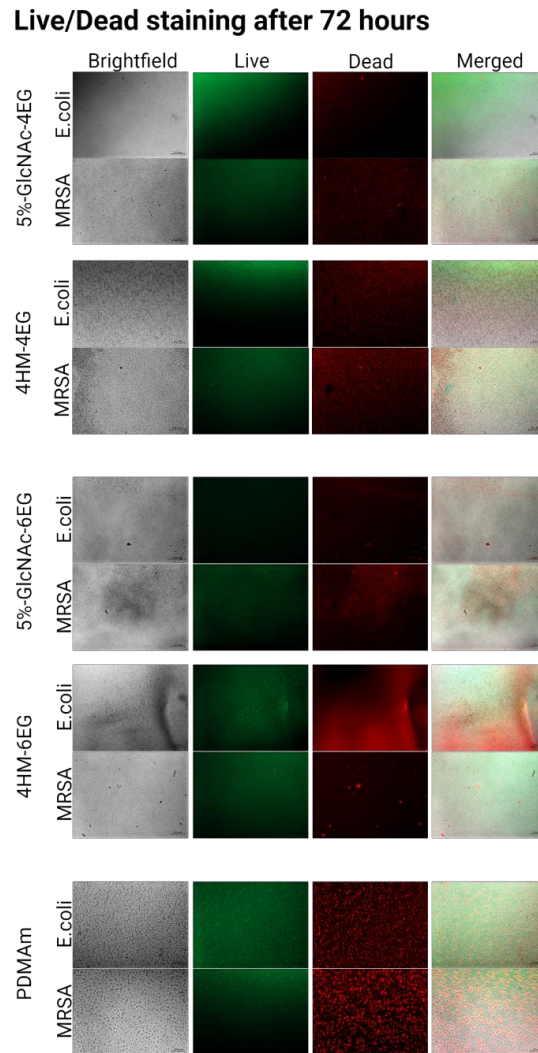
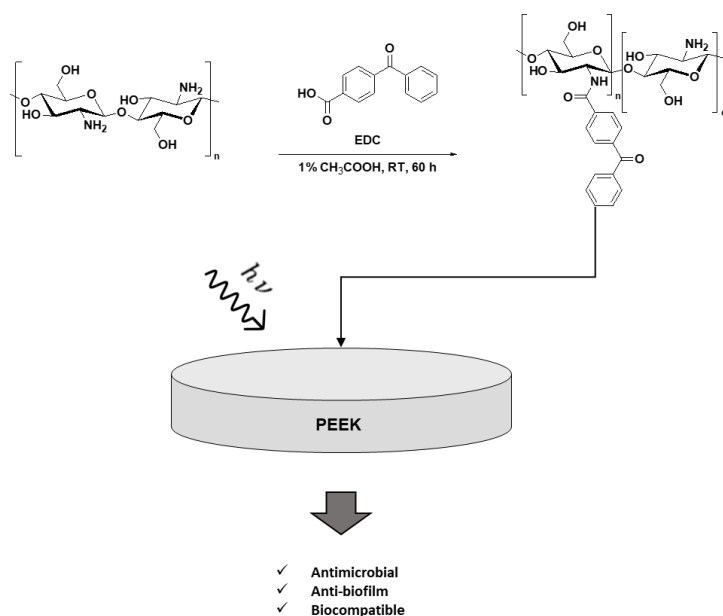


Figure S4. Fluorescent images after Live/Dead staining of *E. coli* and MRSA in the high-nutrition environment after 72 h of cultivation. PDMAm corresponds to the unmodified acrylate coating. Images were taken with 100× magnification using the microscope Observer.Z1 (Zeiss, Germany). Scale bar measures 0.1 mm.

P-2: Synthesis of a biocompatible benzophenone-substituted chitosan hydrogel as novel coating for PEEK with extraordinary strong antibacterial and anti-biofilm properties

Borgolte, M.; Riestler, O.; Quint, I.; Blendinger, F.; Bucher, V.; Laufer, S.; Csuk, R.; Scotti, L.; Deigner H.-P. Synthesis of a biocompatible benzophenone-substituted chitosan hydrogel as novel coating for PEEK with extraordinary strong antibacterial and anti-biofilm properties. *Mater. Today Chem.* **2022**, *26*, 101176.

Graphical Abstract



Abstract

Chitosan derivatives substituted with benzophenone groups that can be cross-linked by ultra-violet light were synthesized as coatings for PEEK substrates used in the construction of lumbar cages. The IC₉₀ values of the benzophenone-modified chitosan polymers in solution before crosslinking were in the same range as those reported for native chitosan. The resulting hydrogel surface after crosslinking exhibited excellent antimicrobial properties and was highly effective (up to 5 log-fold) against clinically relevant strains of methicillin-resistant *S. aureus* and *E. coli*. As a result, the coated surface also significantly reduced biofilm formation. The coatings show good biocompatibility with numerous cell lines as well as low levels of cytotoxicity (ISO 10993-5) and pyrogenicity (ISO 10993-11). The coatings also exhibited strong oxidant properties toward formed hydroxyl radicals in an in-vitro Fenton reaction. Overall, substitution of chitosan with benzophenone residues is an interesting and important approach to the functionalization of materials used for medical implants that are prone to microbial contamination and mechanical failure. Biocompatible antimicrobial coatings might also be employed in photopatterning methods used in the design of medical devices.

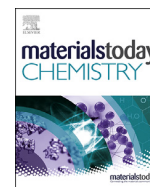
Keywords

Chitosan; UV-crosslinker; antimicrobial coating; anti-biofilm coating; biocompatible



Contents lists available at ScienceDirect

Materials Today Chemistry

journal homepage: www.journals.elsevier.com/materials-today-chemistry/

Synthesis of a biocompatible benzophenone-substituted chitosan hydrogel as novel coating for PEEK with extraordinary strong antibacterial and anti-biofilm properties



M. Borgolte^{a, b}, O. Riester^{a, c}, I. Quint^{a, c}, F. Blendinger^{d, e}, V. Bucher^d, S. Laufer^{c, f}, R. Csuk^b, L. Scotti^g, H.-P. Deigner^{a, h, i, *}

^a Institute of Precision Medicine, Furtwangen University, Jakob-Kienzle Str. 17, 78054 Villingen-Schwenningen, Germany

^b Martin-Luther University Halle-Wittenberg, Organic Chemistry, Kurt-Mothes-Str. 2, 06120, Halle, Saale, Germany

^c Institute of Pharmaceutical Sciences, Department of Pharmacy and Biochemistry, Eberhard-Karls-University Tuebingen, Auf der Morgenstelle 8, Tuebingen, 72076, Germany

^d Institute for Microsystems Technology (iMST), Furtwangen University, Neckartal 142, Rottweil, 78628, Germany

^e Institute for Applied Physics, Eberhard Karls University Tuebingen, Auf der Morgenstelle 8, Tuebingen, 72076, Germany

^f Tuebingen Center for Academic Drug Discovery & Development (TüCAD2), Tuebingen, 72076, Germany

^g Department of Medical, Oral and Biotechnological Sciences, University "G. D'Annunzio" of Chieti-Pescara, Via Dei Vestini, 66100, Chieti, Italy

^h Faculty of Science, Eberhard Karls University Tuebingen, Auf der Morgenstelle 8, Tuebingen, 72076, Germany

ⁱ EXIM Department, Fraunhofer Institute IZI (Leipzig), Schillingallee 68, 18057, Rostock, Germany

ARTICLE INFO

Article history:

Received 17 May 2022

Received in revised form

10 August 2022

Accepted 28 August 2022

Available online 5 October 2022

Keywords:

Chitosan

UV-Crosslinker

Antimicrobial coating

Anti-biofilm coating

Biocompatible

ABSTRACT

Chitosan derivatives substituted with benzophenone groups that can be cross-linked by ultraviolet light were synthesized as coatings for PEEK substrates used in the construction of lumbar cages. The IC₉₀ values of the benzophenone-modified chitosan polymers in solution before crosslinking were in the same range as those reported for native chitosan. The resulting hydrogel surface after crosslinking exhibited excellent antimicrobial properties and was highly effective (up to 5 log-fold) against clinically relevant strains of methicillin-resistant *S. aureus* and *E. coli*. As a result, the coated surface also significantly reduced biofilm formation. The coatings show good biocompatibility with numerous cell lines as well as low levels of cytotoxicity (ISO 10993–5) and pyrogenicity (ISO 10993–11). The coatings also exhibited strong antioxidant properties toward formed hydroxyl radicals in an in-vitro Fenton reaction. Overall, substitution of chitosan with benzophenone residues is an interesting and important approach to the functionalization of materials used for medical implants that are prone to microbial contamination and mechanical failure. Biocompatible antimicrobial coatings might also be employed in photopatterning methods used in the design of medical devices.

© 2022 The Author(s). Published by Elsevier Ltd. This is an open access article under the CC BY license (<http://creativecommons.org/licenses/by/4.0/>).

1. Introduction

Chitosan is the deacetylated derivative of chitin that exhibits antimicrobial properties due to the positive charge of the amino groups of its constituent glucosamines. Due to this cationic properties, chitosan is able to disrupt the outer and inner bacterial cell membrane [1–4], via interactions of its polycationic properties with the negatively charged phosphocholine groups of the bacterial cell wall as suggested by the Shai-Matsuzaki-Huang (SMH) model

of the behavior of cationic antimicrobial peptides in solution, leading to the antimicrobial properties of chitosan as well [5,6]. This is backed by a publication from Li et al., 2010, who investigated *E. coli* after chitosan treatment under an electron microscope, finding partly cell lysis and dissolved cell membranes of *E. coli* [7]. Another publication, analyzing an experimental chitosan coating, showed cell lysis and cytosol leakage of *S. epidermidis* on the substrate [8]. As second potential mechanism, chitosan has been proposed to bind DNA inside the bacterial cytosol, inhibiting mRNA synthesis and therefore, inhibiting microbial growth and biofilm formation. This ability also follows the electrostatic interaction model, proposed by the SMH model, but refers to shorter chained chitosan molecules, which are able to penetrate the cell wall. A

* Corresponding author.

E-mail address: dei@hs-furtwangen.de (H.-P. Deigner).

study on *E. coli* using fluorescein-modified chitosan, analyzed with a confocal laser microscope, shows an accumulation of chitosan inside the bacteria [9]. A third proposed mechanism of chitosan is based on its metal chelating ability [10]. Through this chelating ability free Ca^{2+} and Mg^{2+} cations, present in the bacterial cell wall, are bound, leading to decreased enzyme activity in the cell wall and, therefore, inhibition and disruption of bacterial growth [1,11–14]. In all cases, the bacteria are disturbed in their metabolism upon contact with the coated chitosan surface and, therefore, ultimately killed and unable to biofilm formation.

Due to these unique antimicrobial properties, several publications describe the use of chitosan for its antimicrobial properties in medicine-related applications. For example, thiolated mucoadhesive chitosan fibers prevent the growth of bacteria that cause dental caries while exhibiting no cytotoxicity against relevant cell lines [15]. Similarly, chitosan limits the formation of biofilms of *Actinobacillus pleuromoniae* [16]. Findings reported in another recent publication revealed that the introduction of chitosan *N*-halamine conjugates in hemostatic wound dressings resulted in a one million-fold reduction in the extent of microbial contamination [17]. Other applications for chitosan that have been widely described in the literature include bone tissue engineering [18–20], stem cell encapsulation [21–23], and wound dressings [24,25]. Unmodified chitosan has only limited solubility in both aqueous and organic solvents and exhibits comparatively poor mechanical properties and heat resistance. Thus, the use of chitosan as an antimicrobial coating for medical implants remains limited. However, the aforementioned studies revealed that chitosan may serve as an attractive substrate for specific functionalization designed to improve its properties and use on implant surfaces prone to microbial infection.

Benzophenone is a UV-responsive crosslinker, described in several publications over the last 30 years regarding photopatterning, including the generation of surface-anchored benzophenone hydrogels that promote cell adhesion [26–28] and micropatterning for analytical purposes [28–31] as well as for the design of antimicrobial and anti-adhesive surfaces [26,32–35]. We recently published a description of the synthesis of a benzophenone-acrylamide hydrogel in which *N*-acetyl glucosamine units were connected by various oligoethylene glycol chains. This hydrogel was used successfully to prevent microbial growth and biofilm formation when used as a coating for polyethylene terephthalate glycol (PETG) coverslips [36]. The mechanism of the underlying crosslinking reaction has been extensively reviewed [37–40]. Briefly, by activation through photons, benzophenone forms a highly reactive triplet radical via $n\text{-}\pi^*$ or $\pi\text{-}\pi^*$ transition, while the exact orbital transition depends on the wavelength [41]. This transition of a nonbonding n orbital of the oxygen into the π^* -LUMO of the carbonyl group leads to a biradicaloid state of the benzophenone. The then formed electrophilic ketyl radical can abstract a hydrogen atom from a nearby substrate or polymer chain, leading to two alkyl radicals, undergoing recombination, and therefore, crosslinking [42]. The kinetics of such C–H crosslinking reactions, leading to surface-anchored polymer networks and their surface-bond gelling kinetics, have also been described by R  he et al. [2016], showing unique, non-linear kinetics of the crosslinking reaction inside the coating hydrogel network [43].

Functionalization of glycosidic polymers with benzophenone has been described primarily for the design of UV-protective scaffolds. For example, Heo et al. [44] described the modification of pullulan with benzophenone that exhibited UV-absorption properties while maintaining good biocompatibility, thereby suggesting its use in the formulations of sunscreens [38]. Similarly, Morimoto et al. [38] described the synthesis of UV-absorbing phenolic chitosan derivatives with formaldehyde in a Mannich reaction [37]. Likewise, Hong et al. [45] described the antimicrobial activity of benzophenone-modified

cotton; in this case, benzophenone functioned as an antimicrobial agent after UV irradiation and radical activation [45].

Polyether ether ketone (PEEK) is a high-performance thermoplastic, showing similar mechanical properties like the Ti6Al4V titanium alloy which is commonly used in medical applications [46] and displaying properties similar to human bone [47]. It is not cytotoxic, nor does it degrade or leach ions into the surrounding tissue [48]. Given these properties, it has been used for manufacturing of a variety of medical implants, for example, spinal cages [49–52], endoprotheses for hip replacement [53–55], or implants for cranial reconstructions [56,57] which can also be manufactured in a 3D printing process [58–61]. Given its otherwise bioinert surface, tissue integration and osseointegration of PEEK is still an issue of concern, leading to the need of proper surface functionalization of PEEK implants [62]. Therefore, multiple approaches for surface functionalization have been described, for example, deposition of inorganic substrates via atomic layer deposition (ALD) [63]. Newer works aim at further improving the mechanical properties of PEEK, for example by blending with other polymers and incorporation of carbon fibers [64] or calcium hydroxyapatite together with graphene [65]. A newer approach focusses on polydopamine coating on PEEK, able to complex Ca^{2+} ions in order to improve biocompatibility and bone mineralisation on the PEEK surface [66]. Since the PEEK consists of a diphenyl ketone group, similar to those present in benzophenone, this functional group is able to undergo the same radical generation mechanism via the $n\text{-}\pi^*$ transition induced by UV light as used with benzophenone, [67]. Further, it been employed as radical starter for grafting-on approaches of polymer brushes using free radical polymerization [68,69] and ATRP [70,71], to mention a few examples.

While the antimicrobial properties of benzophenone-modified polysaccharides have been studied extensively, to the best of our best knowledge, there are no publications that describe benzophenone-mediated, covalent surface anchoring of chitosan to polymeric surfaces, especially PEEK, in order to exhibit its antimicrobial action on a real-world material used for medical implants and devices. In this study, we describe the successful synthesis of benzophenone-modified chitosan derivatives with varying degrees of substitution. We herein report the successful surface functionalization of PEEK with these chitosan derivatives including chemical and physical surface characterization. We also examine their antimicrobial activities, their biocompatibility according to ISO 10993–5, and their pyrogenicity as well as potentially anti-inflammatory properties.

2. Experimental

2.1. Synthesis of chitosan derivatives

Chitosan (molecular weight 100,000–300,000 g/mol, Sigma Aldrich, Germany) was dissolved in 1% (v/v) CH_3COOH in ddH_2O . A mixture of 4-benzoyl-benzoic acid in tetrahydrofuran (THF, 100 mg/mL) was added, followed by 1-ethyl-3-(3-dimethylaminopropyl)carbodiimide (EDC, 1 eq) was added and the mixture was then stirred at room temperature for 60 h. Derivatized chitosan was precipitated in 5-fold excess of acetone, the precipitate filtered, and re-precipitated two more times. The resulting material was dissolved in 100 mL ddH_2O and dialyzed 5 times against an excess of 1 mM hydrochloric acid. After lyophilization, the benzophenone-substituted chitosan derivatives were obtained as a white powder.

2.2. UV/vis and nuclear magnetic resonance (NMR) measurements

Benzophenone-substituted chitosan derivatives were dissolved to 5 mg/mL in 1 mM HCl. The UV/Vis absorbance (220–600 nm) of

various dilutions was measured in a Perkin Elmer Lambda XLS + photometer. Absorption at 263 nm was used to determine the degree of functionalization, which was calculated from a standard curve of 4-benzoyl-benzoic acid dissolved in ethanol, cf. Fig. S1 in Supplementary Material. Degree of substitution is given as the ratio between determined benzophenone concentration in the measured solutions and total polymer amount. NMR measurements were performed in 1 mM deuterium chloride (DCl) in D₂O in a Varian Unity 500 NMR spectrometer. Chemical shifts are reported in parts per million relative to the solvent signal (D₂O). Signals were assigned by first-order analysis.

2.3. Coating formation

To generate polyether ether ketone (PEEK) sample coatings, a rod of PEEK polymer (2 m length, 25 mm diameter, Schmidt + Bartl GmbH, Villingen-Schwenningen, Germany) was cut into 2 mm chips using a lathe; the cut edges were deburred, and a smooth surface was obtained by grinding with a lathe. The PEEK chips were washed extensively with acetone, ethyl acetate, ethanol and water in an ultrasonic bath. After drying of the chips, a 100 μ L sterile-filtered solution of the benzophenone-chitosan derivatives dissolved in 1 mM HCl to a concentration of 10 mg/mL was added to cover the entire surface of the PEEK chip. The PEEK chip immersed in solution was permitted to dry overnight in a sterile cabinet to prevent dust contamination and then subjected to crosslinking with UV-light (254 nm, 3 J/cm²) using a UV-crosslinker (AnalytikJena UVP Crosslinker 254 nm). After washing 2 times with excess 1 mM HCl and ddH₂O, the chips were vacuum-dried for 16 h and then used directly in the following experiments.

For cell culture dishes, a sterile-filtered solution of the benzophenone-chitosan derivatives in 1 mM HCl (10 mg/mL for 625 μ g/cm², 5 mg/mL for 312 μ g/cm², and 1 mg/mL for 62.5 μ g/cm²) was added at 20 μ L per well for 96-well plates or 60 μ L per well for 24-well plates. The plate was permitted to dry overnight under a sterile cabinet to prevent contamination and when then subjected to crosslinking with UV light (254 nm, 3 J/cm²) as described above. The plates were washed two times with 1 mM HCl and once with ddH₂O (200 μ L per well for 96-well plates or 1 mL per well for 24-well plates). The plates were then dried to generate the final coatings that were evaluated in cell culture and microbiology experiments.

2.4. Physicochemical surface characterization

Infrared (IR) spectra of the coated PEEK chips were obtained using a PerkinElmer Spotlight 200 FT-IR microscope that was attached to a PerkinElmer Frontier FT-IR spectrometer unit. A blank PEEK chip was used as background. Difference spectra between coated and uncoated PEEK chips were recorded to eliminate interference from PEEK signals. Microscopic images were collected using the FT-IR microscope in illumination mode and are shown without any further processing. Scanning electron microscope (SEM) images were taken at a 40° tilted angle using an XL-30 SEM (Philips, Amsterdam, Netherlands) operating at 10 kV. Samples were dried in a vacuum chamber, followed by coating with a 5 nm thick Au/Pd layer (SC7620 sputter coater, Quorum, Laughton, UK). X-ray photoelectron spectroscopy (XPS) was carried out using a Physical Instruments Quantera SXM (Physical Instruments, Chanhassen, MN, USA) equipped with a monochromatic Al K _{α} (1486.6 eV) X-ray source. X-ray beam had a diameter of 200 μ m at 50 W, area of investigation was a square of 1.4 \times 1.4 mm. SEM coupled energy dispersive X-ray spectroscopy (SEM-EDS) was carried out using a Phenom XL (Thermo Fisher Scientific, USA) equipped with BDS, SED, and EDS detectors (15 kW of acceleration voltages under high vacuum level). The sample was coated with

carbon prior to analysis and a copper wire was used for electrical conduction between the sample and the manifold. The acquisition data are present in the figures acquired with the instrument. Atomic force microscope (AFM) images were recorded using a CoreAFM (Nanosurf, Liestal, Switzerland) equipped with a TAP150GD-G tip (BudgetSensors, Sofia, Bulgaria, tip radius <10 nm) in tapping mode. Coating roughness on PEEK was measured with an Alphastep 500 surface profiler (KLA Tencor) using a tip with 12.5 μ m radius and a force of 61 mg. Profiles with a length of 1000 μ m were obtained with a scanning speed of 50 μ m/s. Coating thickness was determined by measuring the surface profile with 1000 μ m length over a border of the coating to uncoated PEEK and calculated by the difference in surface levels.

2.5. Biocompatibility studies

2.5.1. Cell culture

L-929 mouse fibroblasts were obtained from Dr. Oliver Podlech (CleanControlling GmbH, Emmingen-Liptingen, Germany) and cultured in low-glucose Dulbecco's Modified Eagle Medium (DMEM), containing 10% (v/v) fetal calf serum (FCS), 1% penicillin-streptomycin (10,000 U/mL) and 1% (v/v) L-glutamine. Human umbilical vein endothelial cells (HUVECs, neonatal, pooled) were obtained from Sigma Aldrich, Germany, and cultured in endothelial cell growth medium (Sigma Aldrich, Germany). Saos-2 human osteogenic sarcoma cells (Sigma Aldrich, Germany, DSMZ No. ACC 243) were cultured in McCoy's 5a medium supplemented with 10% (v/v) FCS, 2 mM L-glutamine, and 1% penicillin-streptomycin (10,000 U/mL). Mono Mac-6 monocytes (Sigma Aldrich, Germany, DSMZ No. ACC 124) were maintained in RPMI-1640 (Sigma Aldrich, Germany) supplemented with 10% (v/v) FCS, 1 mM sodium pyruvate, 10 μ g/mL human insulin (Sigma Aldrich, Germany) and 1% penicillin-streptomycin (10,000 U/mL). All cell lines used in these studies were maintained in a humidified atmosphere supplemented with 5% CO₂ at 37 °C in a tissue culture incubator (CB series C150, Binder, Tuttlingen, Germany).

2.5.2. Cytotoxicity testing: extracts

Cytotoxicity testing of polymer extracts was performed according to United States Pharmacopeia (USP) standards as previously described [36,72]. Polymer extracts were obtained by coating the wells of a 24-well plate with final polymers (Fig. 1) followed by the addition of 317 μ L cell culture media identified as suitable for the cell line to be evaluated. After incubation for 24 h at 37 °C in a humidified atmosphere, 100 μ L of each polymer extract was added to cells grown to adherence overnight (100,000 cells/mL). Medium supplemented with 6% (v/v) DMSO was used as a positive control. After 72 h, the medium was removed from each well and replaced with 110 μ L fresh media supplemented with 10% of a 10 mM 3-(4,5-dimethylthiazol-2-yl)-2,5-diphenyltetrazolium bromide (MTT) solution in phosphate-buffered saline (PBS), followed by 4 h incubation at 37 °C and 5% CO₂ in a humidified atmosphere. in the incubator. The formed formazan crystals were solubilized with 100 μ L 10% sodium dodecyl sulfate (SDS; w/v) in 10 mM HCl followed by incubation at 37 °C and 5% CO₂ in an H₂O-saturated atmosphere. Absorbance measurements (570 nm) obtained using a Tecan Infinite M200 microplate reader provide a measurement of cell viability in response to each extract; this value was calculated from the ratio/percentage of the average absorbance measured in triplicate wells of extract-treated versus non-treated cells. Standard deviations for each of the triplicate samples are shown as error bars.

2.5.3. Cytotoxicity testing: contact

Cytotoxicity testing based on contact with the polymer was performed as described in our previous publication [36]. A 100 μ L

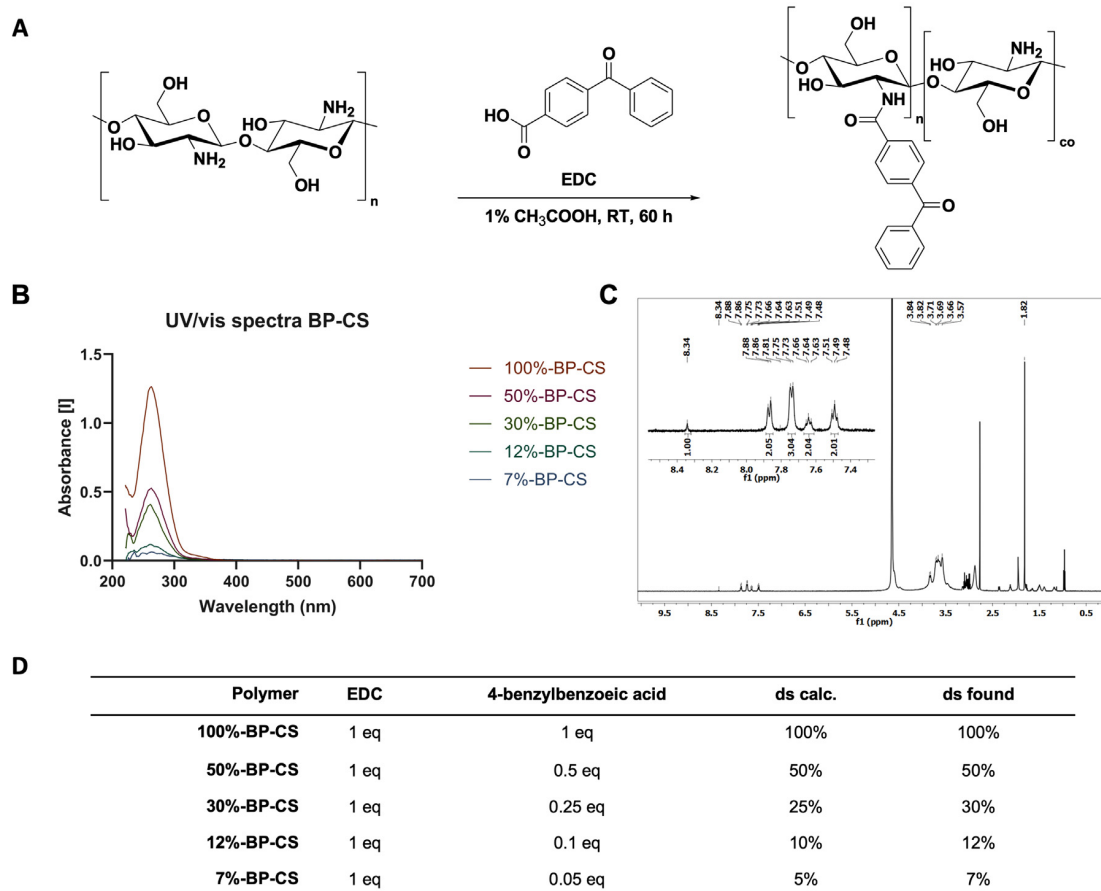


Fig. 1. Synthesis (A) and degree of substitution (ds) (D) of the chitosan derivatives. The degree of substitution determined calculated by stoichiometry matches that determined by UV/vis spectroscopy (B). The ^1H NMR spectrum confirms that the reaction between chitosan and 4-benzoylbenzoic acid is chemoselective and results in substitution at the amino group only (C).

cell suspension containing 100,000 cells/mL was added to a coated 96-well plate which was then incubated for 24 or 72 h. The medium was removed from each well and replaced with 110 μL of fresh medium containing 10% of a 10 mM MTT solution in PBS. The cells were then incubated for 4 h in an incubator. This was followed by the addition of 100 μL of a 10% SDS solution in 10 mM HCl and another incubation for 4 h in an incubator. Absorbance (570 nm) was then measured using a Tecan Infinite M200 pro microplate reader. Cell viability was calculated as mean absorbance measured in wells containing polymer coatings *versus* uncoated control wells. Each measurement was performed in triplicate with error bars indicating standard deviation.

2.5.4. Interleukin (IL)-6 ELISA

Mono Mac-6 cells were used for quantitative evaluation of IL-6 expression. A 200 μL suspension containing 200,000 cells/mL was aliquoted into wells of a polymer-coated 96-well plate, followed by a 16 h incubation either with or without lipopolysaccharide (LPS, 500 ng/mL). Cells in uncoated wells treated with LPS (500 ng/mL) and untreated cells served as positive and negative controls, respectively. After 16 h incubation, the cells were collected by centrifugation (300 g, 5 min at room temperature). Levels of immunoreactive IL-6 were assessed in 100 μL samples of the resulting supernatant by ELISA according to the manufacturer's

instructions (PeproTech Human IL-6 Standard ABTS ELISA Development Kit). Absorbance after reaction quenching was measured at 450 nm using a Tecan Infinite M200 microplate reader. The IL-6 concentration in each biological replicate was calculated using mean values from three triplicate wells. Error bars are used to indicate standard deviation.

2.5.5. Expression of *IL-1b*, *IL-8*, and *IL-10*

One million Mono Mac-6 cells in 2 mL of medium were seeded in wells of a 12-well plate coated with final benzophenone-chitosan polymers and incubated for 16 h. LPS (500 ng/mL) was used as a positive control for cytokine expression. The cells were collected by centrifugation at 350g for 5 min at 4 $^{\circ}\text{C}$. The cell pellets were washed with 1 mL PBS and collected again by centrifugation. RNA was extracted from the cell pellet using the MACHERY-NAGEL NucleoSpin $^{\text{®}}$ RNA Plus Kit according to the manufacturer's instructions. From the extracted RNA, 1 μg of each sample was converted into cDNA using the Thermo Scientific RevertAid First Strand cDNA Synthesis Kit according to the manufacturer's instructions. GAPDH was used as the reference gene. Quantitative gene expression analysis was performed in triplicate experiments using the Roche Light LightCycler $^{\text{®}}$ 480 II with Roche SYBR Green I mix according to the manufacturer's instructions. Data shown are the calculated ratios of interleukin RNA to GAPDH. Error bars are used to indicate standard deviation over three replicates.

Primer sequences include

IL-1b fwd: 5'-GAAGATGCTGGTTC-3'
 IL-1b rev: 5'-TCCCATGTGTCCAAGAAGATAG-3'
 IL-8 fwd: 5'-GAGCACTCCATAAGGCACAAA-3'
 IL-8 rev: 5'-ATGGTTCCTCCGGTGGT-3'
 IL-10 fwd: 5'-CATAAATTAGAGGTCTCCAAAATCG-3'
 IL-10 rev: 5'-AAGGGGCTGGGTCAGCTAT-3'
 GAPDH fwd: 5'-CTCTGCTCCTCTGTTCCGAC-3'
 GAPDH rev: 5'-CAATACGACCAATCCGTTGAC-3'

2.6. Microbiology

2.6.1. Bacterial cell culture

Methicillin-resistant *Staphylococcus aureus* (MRSA, DSM 28766) and *Escherichia coli* (K12, DSM 498) were used in the antimicrobial assays. Glycerol stocks of these bacterial strains were stored at $-80\text{ }^{\circ}\text{C}$. A new overnight culture was initiated for each experiment. Bacteria were incubated (Minitron, Infors HT, Bottmingen, Switzerland) at $37\text{ }^{\circ}\text{C}$ with aeration (rotation at 100 rpm) in lysogeny broth (LB) medium. All bacterial suspensions were prepared in LB medium.

2.6.2. Antibacterial assay for the evaluation of polymer coatings

A modified version of the direct contact method based on ISO 22196 and Skytta et al. was used to evaluate the antibacterial properties of the polymer coatings [73,74]. Briefly, 200 μL of bacterial suspension a concentration of 5×10^3 cells/mL was added to each well of a coated 96-well plate. A well without polymer treatment was used for reference. The plate was sealed with parafilm to reduce evaporation and incubated for 24 h at $37\text{ }^{\circ}\text{C}$ in a humidified incubator. The bacterial cell suspension was removed, and the wells were washed twice with 200 μL of sterile PBS. Adherent bacteria that remained in direct contact with the coating were removed with 200 μL of soybean casein digest lecithin polysorbate broth (SCDLP); the suspension was mixed thoroughly and transferred to a new 96-well plate. In addition, serial dilution of a suspension with 10^4 cells/well in SCDLP was added to the plate layout for the calculation of a calibration curve to determine the absolute reduction in bacterial count. After all empty wells were filled with sterile PBS, the plate was sealed with parafilm and placed in a Tecan Infinite M200 microplate reader that was preheated to $37\text{ }^{\circ}\text{C}$. Optical density at 600 nm was measured every 20 min over the next 16 h. The first derivative of the maximum rate of growth shown in each curve was calculated using GraphPad Prism 8 (San Diego, CA, USA). The live bacteria count was then determined from the calibration curve (Fig. S5) and logarithmic reductions were determined compared to results from the untreated well.

2.6.3. Bacteriostatic assay

The bacteriostatic impact of the chitosan polymers before crosslinking was evaluated according to a modified version of the assay described by Skytta et al. [73]. Briefly, 20 μL of polymer solution (concentrations including 10 mg/mL, 5 mg/mL, 1 mg/mL, 500 $\mu\text{g}/\text{mL}$, 100 $\mu\text{g}/\text{mL}$, 50 $\mu\text{g}/\text{mL}$, 10 $\mu\text{g}/\text{mL}$, 100 ng/mL, and 1 ng/mL) dissolved in 1 mM HCl, or 20 μL of 1 mM HCl as vehicle control were added to 180 μL of a bacterial suspension containing 5×10^4 cells/mL in a 96-well plate. In addition, serial dilution of 10^4 cells/well in LB media was added to the plate layout as a negative control. After all empty wells were filled with sterile PBS, the plate was sealed with parafilm and placed in a Tecan Infinite M200 microplate reader that was preheated to $37\text{ }^{\circ}\text{C}$. Optical density at 600 nm was measured every 20 min over the next 16 h.

The area under the growth curves between the two thresholds was calculated using GraphPad Prism 8; the lower threshold was

defined as the baseline and the upper threshold was defined as the endpoint of the exponential growth phase. The areas under the growth curves for each sample were compared to those observed in suspensions exposed to vehicle control to determine relative bacterial growth. The inhibitory concentration (IC_{90}) value was calculated from these findings.

2.6.4. Crystal violet assay for biofilm assessment

Staining with crystal violet was performed to quantify biofilm formation as described previously [36]. Briefly, an overnight bacterial culture was diluted in LB medium to a concentration of 3×10^5 cells/mL. These suspensions were added to each well in a 96-well plate after the coating was washed twice with 200 μL sterile PBS. All empty wells were filled with 200 μL sterile PBS to prevent samples from drying out. The plate was then sealed with parafilm and incubated for 24 or 72 h at $37\text{ }^{\circ}\text{C}$ in a humidified incubator without shaking. The medium was then carefully removed, and the samples were washed three times with 200 μL sterile PBS, with care taken to avoid detaching any biofilm that may have formed. This was followed by fixation with 200 μL of absolute EtOH. EtOH was then aspirated, and the samples were dried for 10 min in a sterile hood. Biofilms were then stained for 2 min in 200 μL of a 0.1% (w/v) crystal violet solution in PBS. The staining solution was removed, and samples were washed six times with 200 μL sterile PBS to remove excess dye. The samples were then dried overnight to avoid dilution errors and the dye was then released from the bacteria by adding 100 μL of absolute EtOH. The crystal violet-containing solution was transferred to a new well after 10 min incubation at room temperature and was quantified by measuring the absorbance at 595 nm in a microplate reader.

2.6.5. Live/dead staining

Live/Dead Staining was performed according to the manufacturer's instructions of the live/dead staining kit (PromoCell GmbH, Heidelberg, Germany). Briefly, polymer coatings were crosslinked in a 96-well plate and washed three times with 200 μL sterile PBS to remove residues. The sterile PBS was removed and coatings were inoculated with 200 μL of overnight bacterial culture (*E. coli* or MRSA) diluted to 3×10^5 cells/mL with LB medium. Samples were incubated for 24 h at $37\text{ }^{\circ}\text{C}$ in a humidified incubator without shaking. For staining, medium was carefully removed and samples were washed three times with 200 μL sterile 150 mM NaCl solution and stained with an appropriate mixture of DMAO (ex/em 490/540) and EthD-III.

(ex/em 530/630) for 15 min at room temperature protected from light. Images were taken with the fluorescent microscope Observer Z1 (Carl Zeiss AG, Oberkochen, Germany) and processed with ZEN blue edition (Version 3.4, Carl Zeiss AG, Oberkochen, Germany). The membrane-permeable DNA dye DMAO stains all cells (live and dead), while the membrane-impermeable DNA dye EthD-III stains only dead cells with damaged cell membranes.

3. Results and discussion

3.1. Synthesis

The reaction of chitosan with 4-benzoyl-benzoic acid in presence of EDC in the ratios shown in Fig. 1D results in the corresponding, substituted benzophenone-chitosan (BP-CS) derivatives (Fig. 1A). The degree of substitution at the chitosan glucosamine moiety was determined by UV/vis spectroscopy using a calibration curve of 4-benzoyl-benzoic acid dissolved in EtOH. The UV/vis spectrum of the benzophenone group shows a strong absorbance peak at 263 nm. The degree of chitosan substitution determined by UV/vis spectroscopy (Fig. 1B) approximately matches the values

that were calculated theoretically. Thus, the degree of chitosan functionalization could be determined stoichiometrically and is shown in Fig. 1D.

To determine whether substitution occurred at one of the hydroxyl groups or was limited to the free amino groups, we performed NMR measurements of the most highly substituted chitosan derivative (100%-BP-CS) in 1 mM DCl in D₂O (Fig. 1C). The aromatic region of the spectrum includes nine aromatic protons of the benzophenone group in two doublets (at 7.9 ppm and 7.7 ppm) and two triplets (at 7.6 ppm and 7.5 ppm). The spectrum also includes an amide signal at 8.3 ppm that is detected in an integral ratio that matches the benzophenone protons. Collectively, these results indicate that the benzophenone modification of chitosan occurs chemoselectively, as this moiety is linked to the amino but not the free hydroxyl groups. These findings confirm the structure of the benzophenone-chitosan amide derivative shown in Fig. 1A.

3.2. Surface functionalization

PEEK is a ductile polymer with mechanical properties that are similar to those of human bone [47]. This compound is not cytotoxic nor does it degrade or leach ions into the surrounding tissue [48]. Given these properties, it has been used to generate a variety of medical implants, for example, spinal cages [49–52] and endoprostheses for hip replacement [53–55]. Given its otherwise bioinert surface, multiple approaches for surface functionalization have been described, for example, deposition of inorganic substrates via atomic layer deposition (ALD) [63]. Here, the BP-CS containing solutions were solvent-cast on PEEK chips, used as a model substrate for PEEK implants, followed by UV-crosslinking at 254 nm, washing, and drying *in vacuo*. The surfaces of the solvent-cast coatings were then further investigated by XPS, SEM-EDS and IR spectroscopy.

Recorded XPS spectra of 100%-BP-CS and 30%-BP-CS coatings are shown in Fig. 2A. In general, the presence of oxygen, nitrogen and carbon could be confirmed. Al, Si, S and Cl could be detected in traces <1% (for determined atom ratios cf. Fig. S2). Due to the high presence of nitrogen in the measured coating areas, the successful coating with chitosan could be confirmed. The element ratios of carbon, nitrogen and oxygen in the 100%-BP-CS coating were also determined using SEM-EDS (cf. Fig. S3) and match the values determined via XRD within deviations of 3%, thus showing consistent data over different methods applied.

The C1s signals between 290 and 282 eV show the presence of C–C, C–H, C=C, C–O, C–N and C=O bonds. The ratio in C=O bonds, which is present in non-crosslinked benzophenone, matches the ratio 3:1 between 100%-BP-CS and 30%-BP-CS, and, therefore, is in accordance with the measurements of the degree of substitution, where 100% and 30% benzophenone content could be determined in the coatings. The relatively high difference in C–O bonds between 100%-BP-CS and 30%-BP-CS also shows successful crosslinking, since the content of C–O and C–N resulting from chitosan itself is constant, while the benzophenone carbonyl is converted into a biradicaloid triplet state, followed by hydrogen abstraction from a neighboring C–H bond and formation of a hydroxy ketyl radical, which undergoes recombination into a C–C bond while a hydroxy group is left as residue [37]. Therefore, the content of hydroxyl groups, as shown in 100%-BP-CS C1s and 30%-BP-CS C1s graphs (Fig. 2A), also differs to a certain factor, which indicates successful crosslinking of the benzophenone photophore through the C–H insertion reaction. Further, it is an additional confirmation of the degrees of substitution as determined on the chitosan polymers.

Microscopic images (200x magnification) of the coatings are shown in Fig. S4. The coarse structure of the PEEK substrate (final panel) caused by milling while cutting PEEK into slices on a lathe

includes circular, groove-like structures of approximately 40 μm thickness. Coatings 100%-BP-CS, 50%-BP-CS, 12%-BP-CS, and 7%-BP-CS applied to the PEEK substrate cover these structures; by contrast, the groove-like structures remain in evidence in PEEK substrates coated with 30%-BP-CS polymer.

IR spectra of those microscopically analyzed areas are shown in Fig. 2B. The IR spectrum of the coating is generally characterized by dominant C–H bands at 2929 cm⁻¹ and 2881 cm⁻¹ as well as the O–H band detected at 3284 cm⁻¹ which are the result of glycosidic carbon backbone C–H stretching vibrations and the free glycosidic hydroxyl groups, respectively. These measurements are consistent with literature reports of bands associated with the parent chitosan molecule [75]. Of these, the most dominant bands are those associated with the glycosidic hydroxyl groups at 3284 cm⁻¹; these are also detected in compound 30%-BP-CS, which was not visible microscopically as noted above. Collectively, these results lead us to conclude that all five coatings were formed appropriately upon UV-crosslinking of the benzophenone group with the PEEK substrate.

3.3. Surface topology

The surface topology of the coatings formed on the PEEK substrate was examined further using AFM and SEM measurements for the formed nanoscale surface topology. SEM images of the surfaces with each of the five coatings are shown in Fig. 3A. Coatings 100%-BP-CS, 50%-BP-CS, and 12%-BP-CS appear as coarse, sponge-like structures with pore diameters of ~2 μm (100%-BP-CS and 50%-BP-CS) and ~4–5 μm (12%-BP-CS). Coatings 30%-BP-CS and 7%-BP-CS appear relatively flat with lamellar-like structures. The uncoated PEEK substrate is also relatively flat; the 40 μm grooves cannot be detected at this resolution. The surface topology of the PEEK substrate measured by AFM reveals grooves of ~40 μm within the borders of resolution (Fig. 3B). The sponge-like structures associated with coatings 100%-BP-CS, 12%-BP-CS, and (to some extent) 50%-BP-CS can also be detected by this method. By contrast, coatings 30%-BP-CS and 7%-BP-CS appear as flat surfaces with underlying grooves that can be attributed to the PEEK substrate.

The surface thickness has been determined using a surface profiler, measuring over a formed edge of the polymer coating. Measured values are shown in Table 1. Overall, a surface thickness ranging between 1 and 4 μm was obtained for the coatings using the solvent casting method. The standard derivatives determined by triplicate measurements of the thickness approximately match the determined values for surface roughness, where R_a is the arithmetic average of the profile height deviations and R_q the quadratic average of profile height deviations.

Differences in the topology, resulting in either sponge-like structures or relatively flat surfaces, could be caused by differences in the degree of substitution, resulting in different solubilities in the used solvent (1 mM HCl). Chitosan itself is insoluble in water or 1 mM HCl, therefore, the reaction with 4-benzoylbenzoic acid was carried out in 1% CH₃COOH. The solubility in 1 mM HCl is, therefore, caused by the conversion of the amine into the amide functionality (cf. Fig. 1), which still leads to different solubilities through different amide-amine ratios. Solubility differences in solvent casting have been shown to influence the formation of topology using the solvent casting method and leading to inconsistencies [76]. Furthermore, the same crosslinking conditions of 3 J/cm² UV-light of 254 nm were applied to all coatings with different benzophenone content; we, therefore, expected differences in coating topology as shown in the SEM and AFM images. Nevertheless, the surface thickness is relatively constant in the range of 1–4 μm over all coatings as well as the determined surface roughness is.

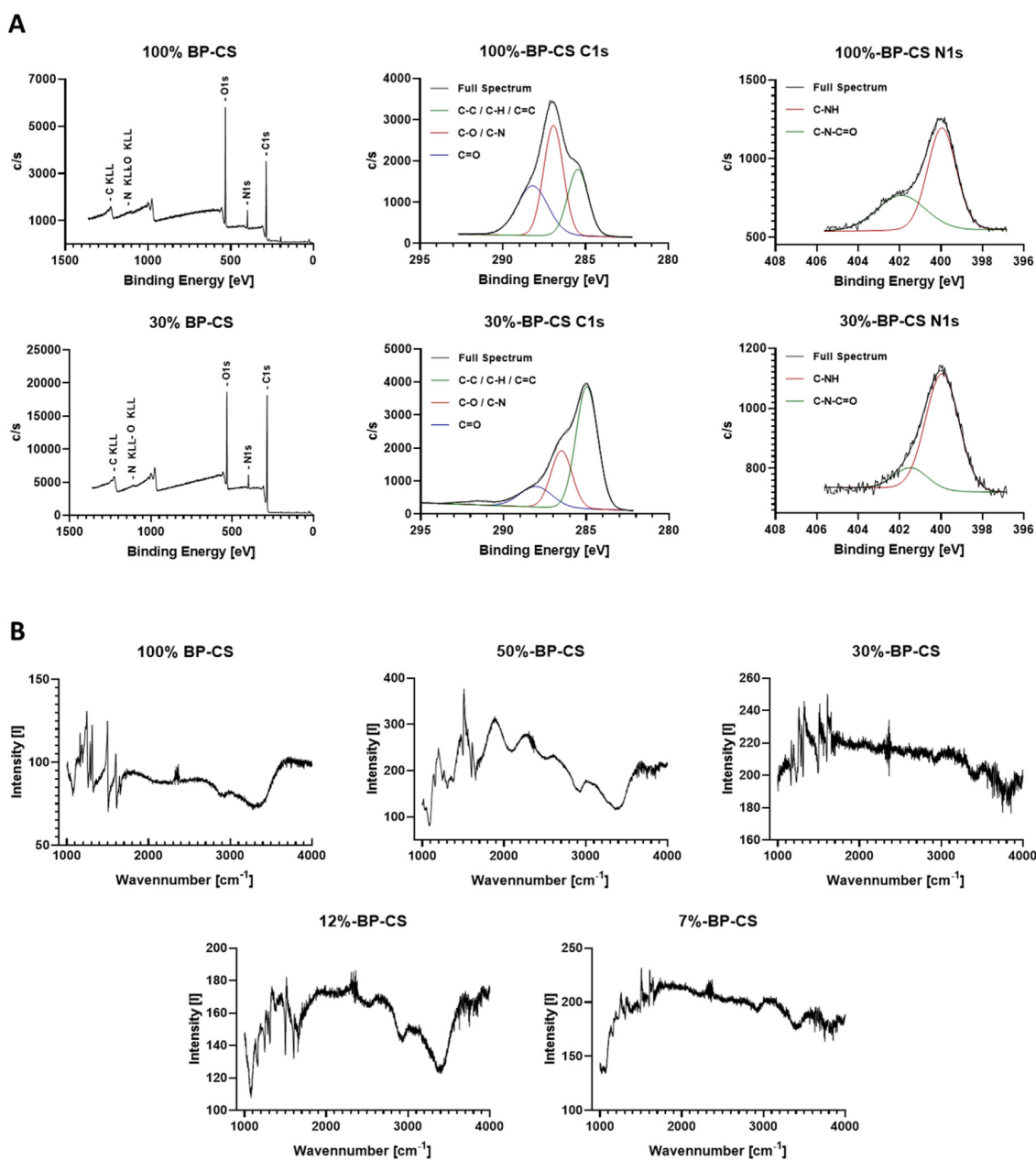


Fig. 2. XPS spectra of 100%-BP-CS and 30%-BP-CS coating on PEEK after crosslinking with UV light at 254 nm. The presence of nitrogen confirms the presence of chitosan on the coating, furthermore, the presence of C=O bonds in spectra C1s for both coatings confirm the presence of benzophenone through non-reacted residues (A). IR spectra of the material (B). The most dominant peaks in IR spectra are the glycosidic O–H bounds at 3284 cm⁻¹, followed by the glycosidic C–H stretching vibrations at both 2929 cm⁻¹ and 2881 cm⁻¹. These spectra match those obtained for chitosan in this region [75] and indicate successful crosslinking of this material on the surface of the PEEK chip.

3.4. Cytotoxicity

Cytotoxicity of the synthesized coatings was determined in experiments targeting the L-929 mouse embryonal fibroblast cell line, human umbilical vein endothelial cells (HUVECs), Saos-2 osteosarcoma cell line, and Mono Mac-6 monocytes. Both extract and direct contact methods were used according to ISO 10993–5 [72,77,78]. Growth inhibition of L-929 cells in response to all extract dilutions was comparatively low (Fig. 4A). By contrast, these same dilutions (except for 30%-BP-CS) promote somewhat more substantial growth inhibition of the HUVEC cell line (Fig. 4B). Overall, little to no growth inhibition was observed in response to the 30% substituted chitosan derivative (30%-BP-CS). More substantial

growth inhibition of both L-929 cells and HUVECs was observed in response to functionalized chitosan derivatives with both higher as well lower benzophenone content.

Direct contact cytotoxicity tests were performed that targeted HUVECs as well as the L929, Saos-2, and Mono Mac-6 cell lines (Fig. 4C–F). The results of these cytotoxicity tests were similar to one another. Similar to the extract tests, the 30% benzophenone-substituted chitosan derivative was minimally cytotoxic in direct contact assays targeting both HUVECs and L929 cells. Among our other results, inhibition of Saos-2 cell growth was enhanced after 72 h of contact with all chitosan derivatives evaluated; inhibition in response to compound 30%-BP-CS increased from <0% at 24 h to 40% at this time point (Fig. 4E). By contrast, the proliferation of

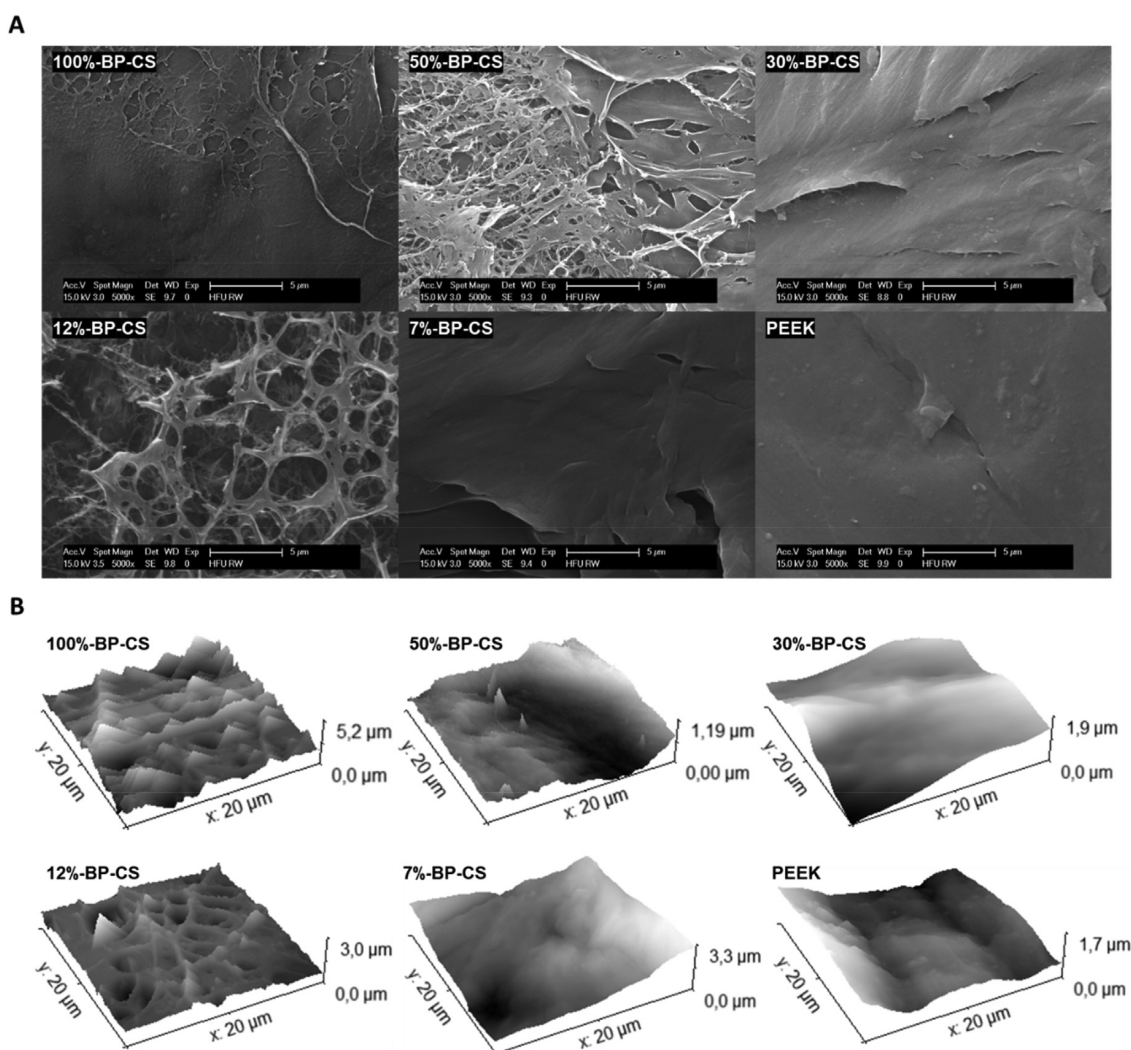


Fig. 3. SEM images (A) and AFM measurements (B) of the coatings, applied to the PEEK substrate (final panel).

Table 1

Surface thickness and surface roughness of the BP-CS coatings determined using a surface profiler.

Sample	Surface thickness [μm]	Surface roughness R_q [nm]	Surface roughness R_q [nm]
100%-BP-CS	2.15 ± 0.13	456.1	509.2
50%-BP-CS	1.46 ± 0.41	615.5	739.5
30%-BP-CS	1.51 ± 0.48	287.2	334.4
12%-BP-CS	3.75 ± 0.60	271.6	339.7
7%-BP-CS	2.12 ± 0.98	323.3	398.6

Mono Mac-6 cells remained constant, with slightly less inhibition observed in response to coatings 12%-BP-CS and 7%-BP-CS (Fig. 4F).

Benzophenone derivatives of N-acetyl glucosamine and short-chain chitooligosaccharides have been characterized as matrix metalloproteinase (MMP) inhibitors with potent activity against cancer cells [79] with potential utility as adjuvant anti-cancer therapy [80]. The activity of these compounds against sarcoma-type cells may explain some of the growth inhibition and decreased cell viability observed in cytotoxicity assays performed in this study. The doubling time of the Saos-2 sarcoma cell line is 40 h [81]. Thus, the growth inhibition of this cell type is observed most

prominently at the 72 h time point, most notably in experiments performed with coating 30%-BP-CS. Downregulation of MMP2 and MMP-9 has also been linked to diminished angiogenesis and reduced migration of human endothelial cells [82]; these findings may explain the decreased viability observed in HUVEC cultures at 24 and 72 h. Results from previous studies suggest that chitosan may form polyelectrolyte complexes in culture medium that sequester growth factors provided by FCS and that this will ultimately result in decreased fibroblast proliferation. In literature, this effect was not observed in cell cultures that were not supplemented with FCS [83]. In the current study, exposure to the 30% substituted chitosan derivative 30%-BP-CS results in the retention of ~70% of the original proliferative activity relative to untreated cells at both 24 and 72 h in all cell lines evaluated. Thus, derivative 30%-BP-CS has been identified as non-cytotoxic. Interestingly, the 30%-BP-CS chitosan derivative is also most effective at inhibiting the growth and viability of both *E. Coli* and *S. aureus* bacterial strains.

3.5. Anti-inflammatory potential

The pyrogenicity of the coating surface and/or the presence of potential pyrogenic residues or contaminants was elucidated by a

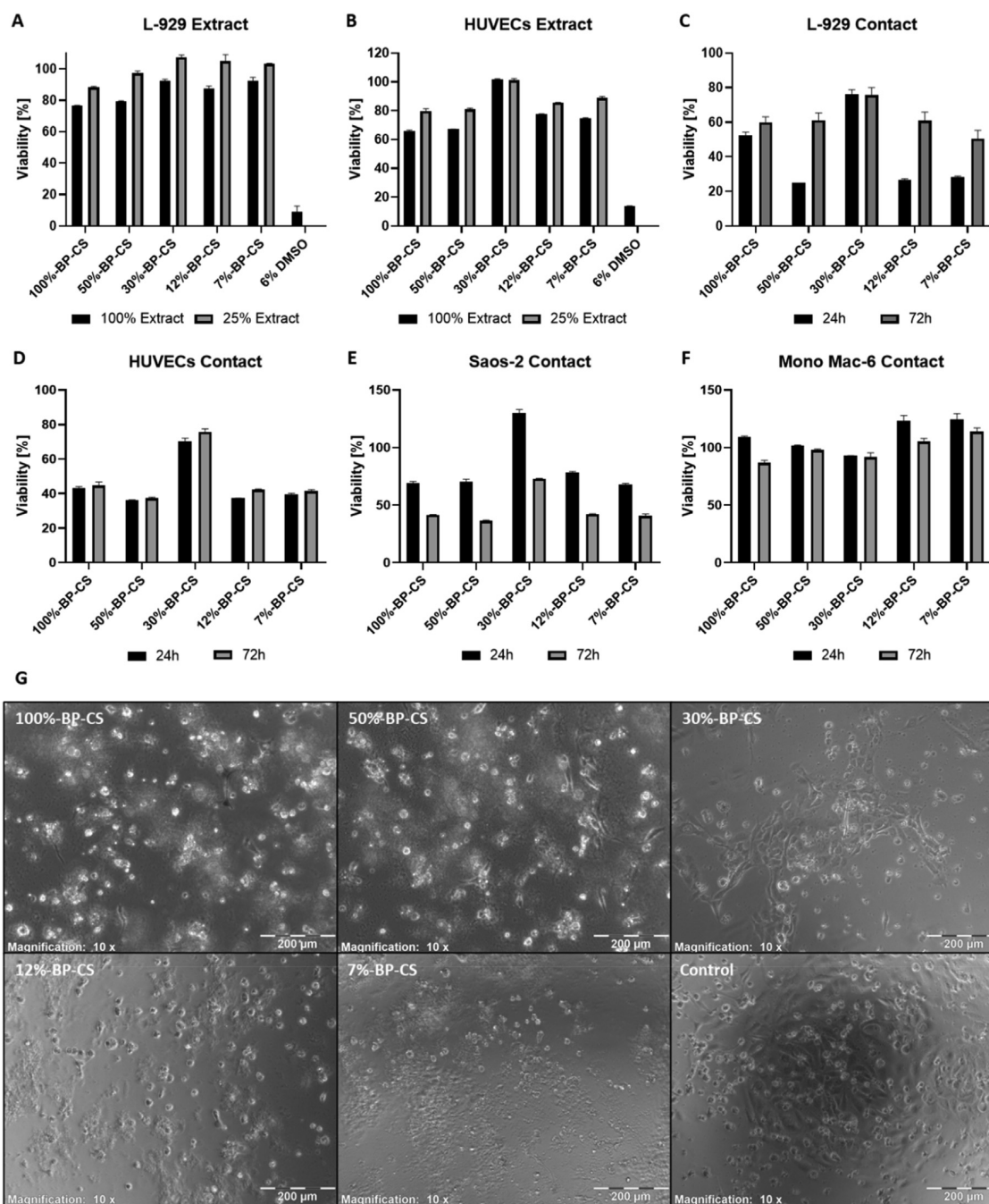


Fig. 4. Cytotoxicity at 24 and 72 h associated with exposure to extracts of BP-CS coatings in L-929 cells and HUVECs with 6% DMSO as positive control (A, B). Cytotoxicity at 24 and 72 h associated with direct contact of L-929, HUVECs, Saos-2, and Mono Mac-6 with BP-CS coatings (C–F). Error bars are given as standard deviation of triplicates each. In (G) L-929 mouse fibroblasts growing on the coated surface at 72 h before the addition of the MTT reagent. Cytotoxicity is observed in response to contact with polymers 100%-BP-CS, 50%-BP-CS, 12%-BP-CS, and 7%-BP-CS. By contrast, relatively little cytotoxicity is observed in response to contact with polymer 30%-BP-CS. This result was confirmed by the cell viability test evaluated quantitatively in (C); the images shown are at 10x magnification.

monocyte activation test using the Mono Mac-6 cell line and an enzyme-linked immunosorbent assay (ELISA) for quantitative detection of IL-6 secretion [84,85]. An approximately two-fold increase in IL-6 was detected in the medium of cultures grown in wells with 625 $\mu\text{g}/\text{cm}^2$ of 100%-BP-CS, 50%-BP-CS, 12%-BP-CS and 7%-BP-CS coatings compared to negative controls (Fig. 5A, left). By contrast, no increase in IL-6 levels was detected in wells coated with 30%-BP-CS derivative. No significant increases in IL-6 release

were observed over control levels in cultures grown in wells coated with lower concentrations of these chitosan derivatives. Thus, all coatings can be considered non-pyrogenic when used at concentrations at or below 312.5 $\mu\text{g}/\text{cm}^2$; 30%-BP-CS derivative is non-pyrogenic at concentrations as high as 625 $\mu\text{g}/\text{cm}^2$. We also evaluated the expression of genes encoding the cytokines IL-1b, IL-8, and IL-10 in monocytes that were cultivated for 16 h in coated wells. We detected no significant increase in IL-1b expression in

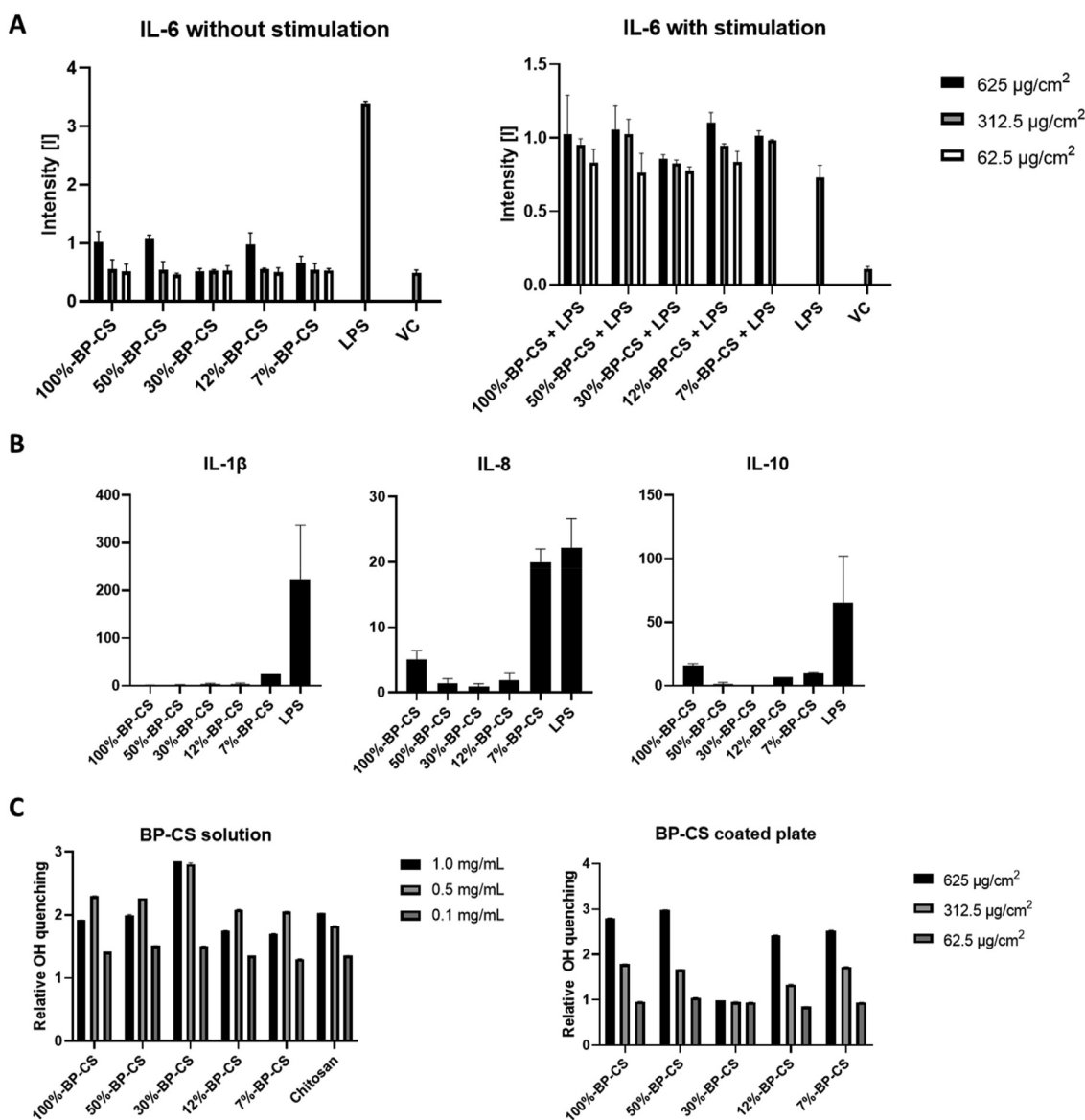


Fig. 5. Secreted IL-6 from Mono Mac-6 monocytes (A) detected in the medium by ELISA at 16 h both with (left) and without (right) stimulation with 500 ng/mL LPS together with LPS and vehicle control (VC) alone. IL-6 levels are twice as high in LPS-stimulated monocytes exposed to 625 $\mu\text{g}/\text{cm}^2$ coatings compared to vehicle control (VC). By contrast, IL-6 levels remain at baseline in cell cultures exposed to lower coating concentrations. IL-6 levels remained at baseline in all cultures exposed to coating 30%-BP-CS. Expression of IL-1 β , IL-8, and IL-10 genes (B) determined by qPCR after 16 h cultivation on a benzophenone-substituted chitosan-coated microtiter plate (625 $\mu\text{g}/\text{cm}^2$). Expression of all three cytokine genes remained at or near baseline in cultures exposed to polymer 30%-BP-CS. (C) Radical (OH \cdot) quenching mediated by benzophenone-substituted chitosan polymers in solution compared to unmodified chitosan (left) and as coatings on microtiter plates.

Mono Mac 6 cells cultured with derivatives 100%-, 50%-, 30%- and 12%-BP-CS, compared to the LPS-positive control [63]. A similar pattern was observed for IL-8; this might be related to findings indicating that IL-8 expression is induced by exogenous IL-1 β in monocytes [86]. The lowest level of IL-8 expression was detected in cells cultured with 30%-BP-CS derivative; expression levels increase from 50%-BP-CS to 100%-BP-CS and from 12%-BP-CS, reaching a maximum in the presence of 7%-BP-CS, approaching the levels observed in response to the LPS positive control. Expression of the anti-inflammatory cytokine, IL-10 increases in a similar pattern, which may represent its capacity to modulate the responses of the proinflammatory cytokines IL-1 β , IL-6, and IL-8. Interestingly, the expression of IL-10 is more prominent in response to 100%-BP-CS derivative than 7%-BP-CS; the 100%-BP-CS derivative also elicits comparatively lower levels of both IL-6 and IL-8. Overall, we can

conclude that the 30%-BP-CS coating is non-inflammatory, while the 100%-BP-CS coating exhibits anti-inflammatory properties as described above.

LPS induces oxidative stress via the production of reactive oxygen species (ROS) in both monocytes and macrophages. LPS-mediated monocyte activation also leads to the synthesis and release of proinflammatory cytokines, including IL-1 β , followed by IL-6 and IL-8, which are cytokines that stimulate local inflammation [87–89]. Chitosan has characterized antioxidative properties and is capable of quenching hydroxyl- and superoxide radicals in solution [90]. Chitosan also exhibits anti-inflammatory properties including its capacity to limit the expression of cyclooxygenase (COX)-2 [91–93]. We tested the radical scavenging potential of each coating and examined their capacity to suppress monocyte-mediated IL-6 release in response to 500 ng/mL LPS. ROS is generated in biological

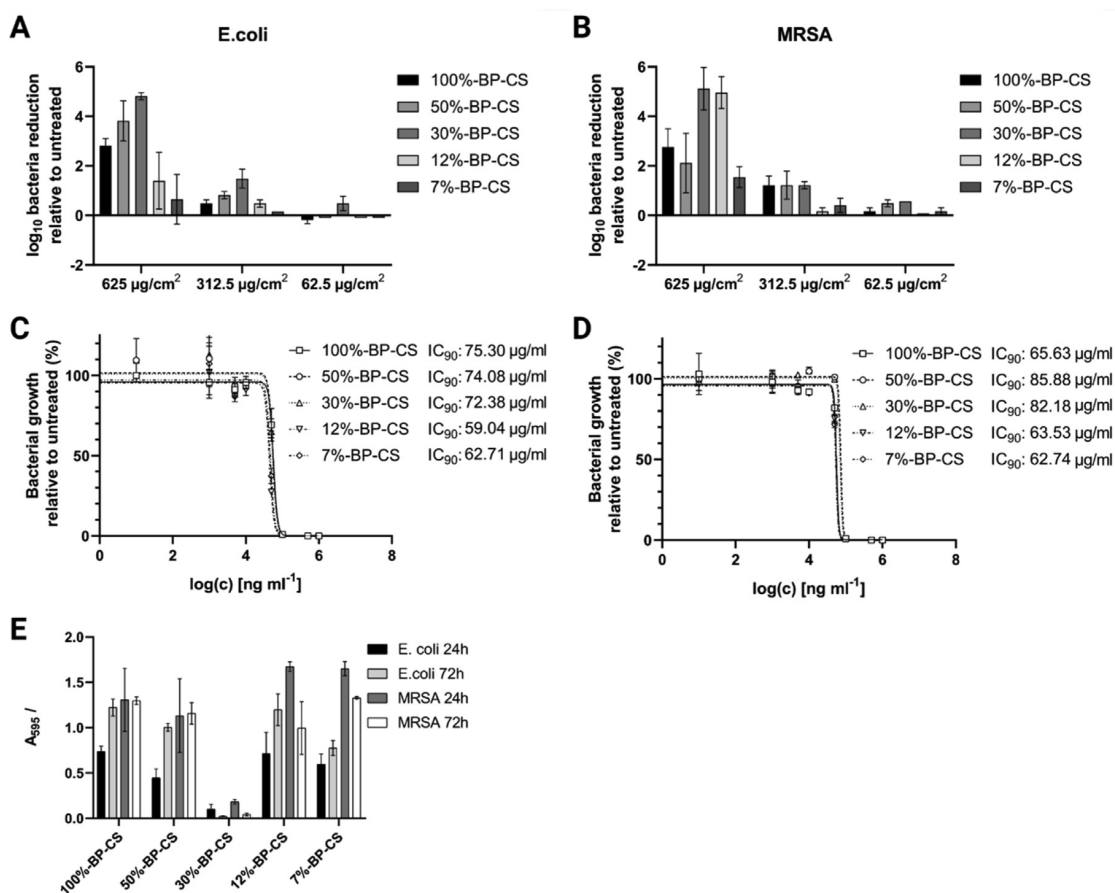


Fig. 6. Antimicrobial activity of benzophenone-substituted chitosan coatings and solubilized chitosan derivatives. Shown are reductions in the number of viable *E. coli* (A) and MRSA (B) that are adherent to coatings relative to the untreated surface of a tissue culture plate. The impact of solubilized chitosan derivatives at various concentrations on the growth of *E. coli* (C) and MRSA (D) and the calculated IC₉₀ values. (E) Biofilms of *E. coli* and MRSA at 24 and 72 h were evaluated by crystal violet staining. All values represent means \pm standard deviations; $n = 3$.

systems mainly via the Fenton reaction [94]. Thus, we performed this reaction in an *ex vivo* as described by Li et al. [90] that utilized photometric measurements of Safranin O degradation mediated by hydroxyl radicals [90]. We found that compound 30%-BP-CS was most effective at radical quenching; exposure to polymers of this compound in solution resulted in a 3-fold increase in OH-quenching compared to the negative control (Fig. 5C). Interestingly, the effectiveness of coating 30%-BP-CS exceeds that of chitosan alone by a factor of 1.5, also compared to the negative control. However, these anti-oxidant activities were not detected when compound 30%-BP-CS was evaluated as a coating. Furthermore, and despite their capacity for radical quenching, none of the coatings had an impact on monocytes-mediated IL-6 secretion compared to the responses of unstimulated monocytes alone (see Fig. 5A, right).

In conclusion, we found that exposure to coating 30%-BP-CS resulted in no increase in proinflammatory cytokine release; this coating also had a negligible effect on modulating the responses of LPS-stimulated monocytes. Monocyte viability remained at or near 100% after 24 or 72 h in a contact with this coating. Based on these results, we identify coating 30%-BP-CS as both inert and biocompatible in experiments performed in relevant *ex vivo* settings.

3.6. Antimicrobial properties

The antibacterial properties of soluble chitosan are well-characterized. Among these findings, Li et al. [95] reported that

chitosan at ~0.1% (w/v) resulted in >80% inhibition of several bacterial strains. In this study, we tested our compounds within a general range of concentrations to determine the 90% inhibitory concentration (IC₉₀) based on the results of growth curves of *E. coli* and MRSA (Fig. S3). Our findings revealed that all five BP-CS derivatives retained their antibacterial properties when evaluated in solution (Fig. 6C and D). The IC₉₀s determined for benzophenone chitosan derivatives targeting *E. coli* were 75, 74, 72, 59, and 63 µg/mL, respectively; IC₉₀s determined for chitosan derivatives targeting MRSA were 66, 86, 82, 64, and 63 µg/mL, respectively. These calculated IC₉₀ values are comparable to the minimum inhibitory concentrations previously reported for non-functionalized chitosan against *E. coli* (50 µg/mL) and MRSA (100 µg/mL) [96]. Interestingly, although benzophenone is considered toxic to bacteria [97], higher IC₉₀ values were observed for compounds with higher benzophenone content. The reduced impact associated with more extensive substitution may be explained by reductions in the number of free amino groups contributing to the overall cationic charge of the polymer. Of note, according to the SMH model, cationic charge is the critical feature underlying chitosan-mediated antimicrobial activity [5,6]. Thus, our results suggest that the impact of the loss of cationic charge may exceed the potential for increased toxicity associated with an increase in the benzophenone content. This net effect may result in an overall reduction of its antibacterial properties.

We then examined the antibacterial properties of coatings prepared from the dissolved chitosan derivatives after UV-

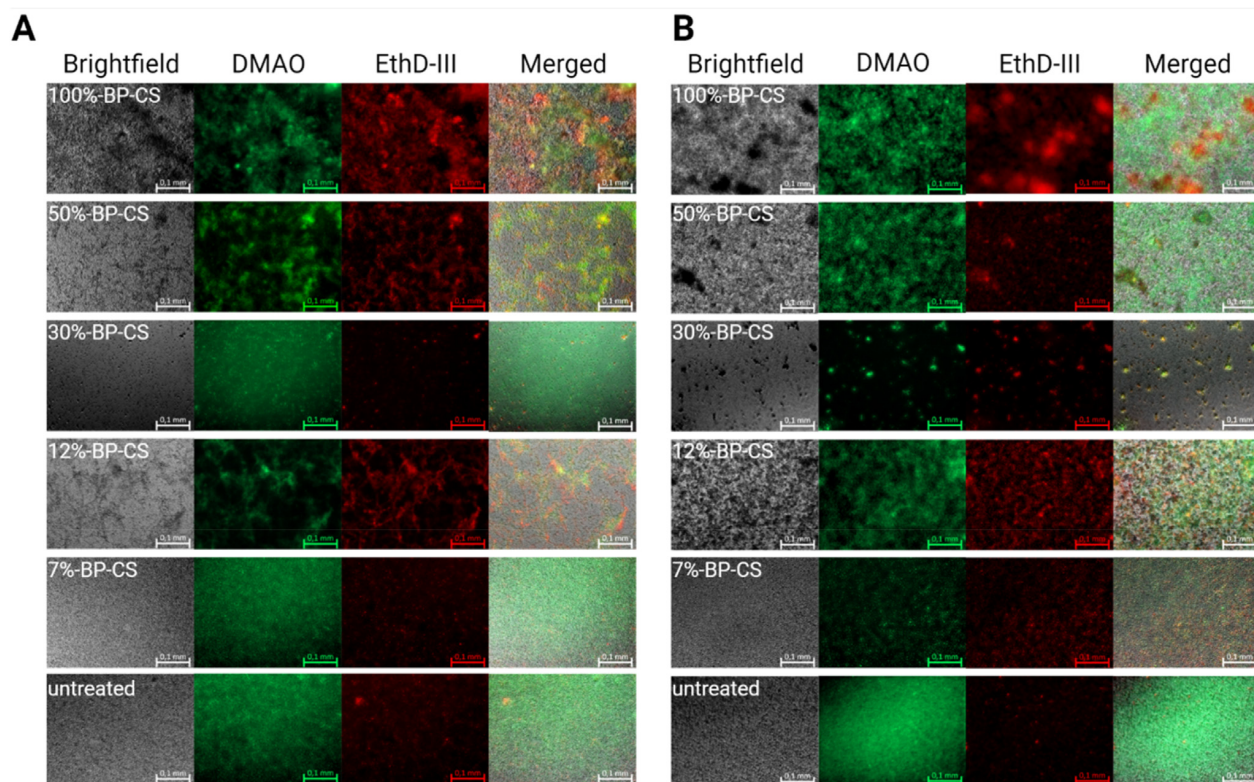


Fig. 7. Representative microscopic images of Live/Dead stained *E. coli* (A) and MRSA (B) after 24 h incubation on the corresponding polymer-coated or untreated surface of a 96-well cell culture plate. Magnification is 200x; scale bar measures 0.1 mm.

crosslinking. Polymer coatings were prepared at mass-to-surface ratios of 625, 312.5, and 62.5 $\mu\text{g}/\text{cm}^2$. Our results revealed a net reduction in antibacterial efficacy of all coatings that paralleled the decreases in mass-to-surface ratios (Figs. S2, 6A, and 6B).

Maximum antibacterial activity was observed for coating of 30%-BP-CS applied at 625 $\mu\text{g}/\text{cm}^2$. Direct contact with this coating (30% benzophenone) resulted in an approximately 5-log reduction of viable *E. coli* or MRSA. Compounds with higher (100%-BP-CS and 50%-BP-CS) and lower (12%-BP-CS and 7%-BP-CS) benzophenone contents were not as effective at limiting bacterial viability (Fig. 6A and B). These results indicate that the antibacterial activity of the cross-linked compound in the form of a coating may be more effective than the individual components in solution. In the case of benzophenone derivatives, crosslinking is critical to ensure a uniform and functional coating.

We also examined biofilm formation on the polymer coatings at 24 and 72 h by crystal violet (CV) staining (Fig. 6E) and Live/Dead staining (Fig. 7). These observations confirmed the results of previous experiments as they revealed that coating 30%-BP-CS was more effective than the other four benzophenone-substituted coatings evaluated. Coating 30%-BP-CS was the only derivative that promoted a reduction in the level of CV stained *E. coli* biofilm between the 24 and 72 h time points, to a point at which it was nearly undetectable. Similar results were obtained in experiments targeting MRSA. However, it is also worth noting that no increases in biofilm formation were observed by CV staining between 24 and 72 h for MRSA in experiments performed with the four additional coatings; experiments performed with coatings 12%-BP-CS and 7%-BP-CS revealed reductions in the amounts of CV stained MRSA biofilms during this time interval. Live/dead staining confirmed that, after 24 h, there was considerably less biofilm on coating 3c

and almost all cells still present were stained as dead. In contrast, the other coatings had developed biofilms, albeit with a higher percentage of dead cells compared to the untreated control. Collectively, the results suggest that these coatings are more effective against biofilms generated by Gram-positive bacteria such as MRSA compared to Gram-negative bacteria, such as *E. coli*.

4. Conclusion

In this study, our findings document the successful functionalization of the free amino groups of chitosan with benzophenone moieties. The degree of functionalization obtained approximately matched the stoichiometrically-calculated ratios. Chemoselective functionalization of the free amino groups via amide formation was confirmed by NMR spectroscopy. Coatings prepared from 30% functionalized derivative, named 30%-BP-CS, were the most effective of the group against the bacterial pathogens MRSA and *E. coli*, which were used as clinically relevant microbial strains in antimicrobial testing. The 30%-BP-CS derivative also exhibited the least cytotoxicity when evaluated in cultures of L-929 fibroblasts, HUVECs, Saos-2 osteoblasts, and Mono Mac-6 monocytes using ISO 10993-5 testing methodology for cytotoxicity assessment. No inflammation was observed in response to the 30%-BP-CS coating in the pyrogen test performed as per ISO 10993-11. Thus, the 30%-BP-CS coating can be considered biologically inert. Interestingly, this 30% functionalized chitosan shows the optimum properties with respect to antimicrobial action and biocompatibility under the UV-crosslinking conditions applied. Different levels of benzophenone substitution (both higher and lower) lead to reduced biocompatibility, a greater potential for inflammation, and diminished antimicrobial activity. This may relate at least in part to differences in

crosslinking efficiency under the applied conditions (3 J/cm², 254 nm), leading to different amounts of uncrosslinked benzophenone residues, which have been shown in the XPS spectra (Fig. 2A). The appropriate combination of these factors may lead to the thinnest possible coating and a smoother surface by minimizing pore formation and the concentration of benzophenone residues that remain uncrosslinked. Previous studies have suggested that the smoothness of the surface is a critical determinant of the biocompatibility and inflammatory potential of biomedical implants [98]. The XPS and IR spectra (Fig. 2) and AFM and SEM measurements (Fig. 3) support this conclusion; these studies revealed that the 30%-BP-CS coating exhibited a relatively smooth surface with no visible pores or sponge-like structures that may promote cell adhesion and inflammation. However, the surface roughness of the 30%-BP-CS coating is slightly higher than the roughness of the 12%-BP-CS coating. This property might also explain the limited capacity for OH-radical quenching (Fig. 4); coatings prepared from 30%-BP-CS derivative display comparatively less active surface area for radical quenching. This can explain the relatively bioinert properties of this coating despite the fact that IC₅₀ of the polymers were within range of those exhibited by the other compounds when they were all examined in solution. However, when applied as a coating, their capacity for growth inhibition differed significantly (Fig. 5). While the exactly optimized parameters for crosslinking conditions and surface properties of the coatings still need more adjustment, overall, our study presents an interesting chemical approach that can be used to generate chitosan-derived coatings for implant materials that are biocompatible, non-inflammatory, and antimicrobial with potential for use in photopatterning applications.

Credit author statement

Max Borgolte: Conceptualization, Methodology, Investigation, Writing – Original Draft, Writing – Review & Editing, Visualization. Oliver Riestler: Methodology, Investigation, Writing – Original Draft, Writing – Review & Editing, Visualization. **Isabel Quint**: Investigation, Writing – Review & Editing. Felix Blendingner: Investigation, Visualization, Writing – Review & Editing. **Volker Bucher**: Resources, Writing – Review & Editing. Stefan Laufer: Resources, Writing – Review & Editing. René Csuk: Resources, Writing – Review & Editing. Luca Scotti: Investigation, Visualization, Resources. Hans-Peter Deigner: Conceptualization, Writing – Review & Editing, Project administration, Funding acquisition, Resources.

Funding

Funding was granted by CoHMed FunctioMed (FKz: 13FH5102IA), CoHMed MS-ToxTest (FKz 13FH5E01IA) and CoHMed PersonaMed (FKz: 13FH5106IA), all BMBF, as well as TriMaBone–Trinationale Forschungsinitiative: 3D-Druck Materialien für resorbierbare Knochen-implantate” (Europäischer Fonds für regionale Entwicklung–EFRE) in the program “Interreg VOberrhein” (Ref: 5115/3.17).

Declaration of competing interest

The authors declare that they have no known competing financial interests or personal relationships that could have appeared to influence the work reported in this paper.

Data availability

No data was used for the research described in the article.

Acknowledgments

We thank Dr. Oliver Podlech, CleanControlling GmbH, for providing us with the L-929 cell line used for biocompatibility testing as well as technical support regarding cell handling and ISO 10993-5 biocompatibility testing. We also thank Dr. Dagmar Martin and Duva Giuliano from the Natural and Medical Sciences Institute (NMI) at the University of Tübingen, Germany, for performing the XPS measurements and gratefully acknowledge their support regarding analysis and discussion of the obtained data. Continuous stimulation by N.C.R. is gratefully acknowledged.

Appendix A. Supplementary data

Supplementary data to this article can be found online at <https://doi.org/10.1016/j.mtchem.2022.101176>.

References

- [1] I.M. Helander, E.L. Nurmiäho-Lassila, R. Ahvenainen, J. Rhoades, S. Roller, Chitosan disrupts the barrier properties of the outer membrane of Gram-negative bacteria, *Int. J. Food Microbiol.* 71 (2001) 235–244, [https://doi.org/10.1016/S0168-1605\(01\)00609-2](https://doi.org/10.1016/S0168-1605(01)00609-2).
- [2] J.Y. Je, S.K. Kim, Chitosan derivatives killed bacteria by disrupting the outer and inner membrane, *J. Agric. Food Chem.* 54 (2006) 6629–6633, <https://doi.org/10.1021/jf061310p>.
- [3] K. Divya, S. Vijayan, T.K. George, M.S. Jisha, Antimicrobial properties of chitosan nanoparticles: mode of action and factors affecting activity, *Fibers Polym.* 18 (2017) 221–230, <https://doi.org/10.1007/s12221-017-6690-1>.
- [4] R.C. Chien, M.T. Yen, J.L. Mau, Antimicrobial and antitumor activities of chitosan from shiitake stipes, compared to commercial chitosan from crab shells, *Carbohydr. Polym.* 138 (2016) 259–264, <https://doi.org/10.1016/j.CARBPOL.2015.11.061>.
- [5] Y. Shai, Mechanism of the binding, insertion and destabilization of phospholipid bilayer membranes by α -helical antimicrobial and cell non-selective membrane-lytic peptides, *Biochim. Biophys. Acta Biomembr.* 1462 (1999) 55–70, [https://doi.org/10.1016/S0005-2736\(99\)00200-X](https://doi.org/10.1016/S0005-2736(99)00200-X).
- [6] K. Matsuzaki, Why and how are peptide–lipid interactions utilized for self-defense? Magainin and tachyplesins as archetypes, *Biochim. Biophys. Acta Biomembr.* 1462 (1999) 1–10, [https://doi.org/10.1016/S0005-2736\(99\)00197-2](https://doi.org/10.1016/S0005-2736(99)00197-2).
- [7] X. Li, X. Feng, S. Yang, G. Fu, T. Wang, Z. Su, Chitosan kills *Escherichia coli* through damage to be of cell membrane mechanism, *Carbohydr. Polym.* 79 (2010) 493–499, <https://doi.org/10.1016/j.carbpol.2009.07.011>.
- [8] R.P. Carlson, R. Taffs, W.M. Davison, P.S. Stewart, Anti-biofilm properties of chitosan-coated surfaces, *J. Biomater. Sci. Polym. Ed.* 19 (2008) 1035–1046, <https://doi.org/10.1163/156856208784909372>.
- [9] X. Fei Liu, Y. Lin Guan, D. Zhi Yang, K. de Yao, Antibacterial Action of Chitosan and Carboxymethylated Chitosan, 2000, <https://doi.org/10.1002/1097-4628>.
- [10] A.J. Varma, S.V. Deshpande, J.F. Kennedy, Metal complexation by chitosan and its derivatives: a review, *Carbohydr. Polym.* 55 (2004) 77–93, <https://doi.org/10.1016/j.carbpol.2003.08.005>.
- [11] P. Sahariah, M. Måsson, Antimicrobial chitosan and chitosan derivatives: a review of the structure–activity relationship, *Biomacromolecules* 18 (2017) 3846–3868, <https://doi.org/10.1021/ACS.BIOMAC.7B01058>.
- [12] Y.C. Chung, H.L. Wang, Y.M. Chen, S.L. Li, Effect of abiotic factors on the antibacterial activity of chitosan against waterborne pathogens, *Bioresour. Technol.* 88 (2003) 179–184, [https://doi.org/10.1016/S0960-8524\(03\)00002-6](https://doi.org/10.1016/S0960-8524(03)00002-6).
- [13] H. Liu, Y. Du, J. Yang, H. Zhu, Structural characterization and antimicrobial activity of chitosan/betaine derivative complex, *Carbohydr. Polym.* 55 (2004) 291–297, <https://doi.org/10.1016/j.CARBPOL.2003.10.001>.
- [14] H. Liu, Y. Du, X. Wang, L. Sun, Chitosan kills bacteria through cell membrane damage, *Int. J. Food Microbiol.* 95 (2004) 147–155, <https://doi.org/10.1016/j.jifoodmicro.2004.01.022>.
- [15] W. Samprasit, R. Kaomongkolgit, M. Sukma, T. Rojanarata, T. Ngawhirunpat, P. Opanasopit, Mucoadhesive electrospun chitosan-based nanofiber mats for dental caries prevention, *Carbohydr. Polym.* 117 (2015) 933–940, <https://doi.org/10.1016/j.CARBPOL.2014.10.026>.
- [16] E.A. Izano, I. Sadovskaya, E. Vinogradov, M.H. Mulks, K. Velliyagounder, C. Ragnath, W.B. Kher, N. Ramasubbu, S. Jabbouri, M.B. Perry, J.B. Kaplan, Poly-N-acetylglucosamine mediates biofilm formation and antibiotic resistance in *Actinobacillus pleuropneumoniae*, *Microb. Pathog.* 43 (2007) 1–9, <https://doi.org/10.1016/j.micpath.2007.02.004>.
- [17] Y. Zheng, N. Pan, Y. Liu, X. Ren, Novel porous chitosan/N-halamide structure with efficient antibacterial and hemostatic properties, *Carbohydr. Polym.* 253 (2021), 117205, <https://doi.org/10.1016/j.CARBPOL.2020.117205>.

- [18] G.M. Luz, L. Boesel, A. Del Campo, J.F. Mano, Micropatterning of bioactive glass nanoparticles on chitosan membranes for spatial controlled biomineralization, *Langmuir* 28 (2012) 6970–6977, <https://doi.org/10.1021/la300667g>.
- [19] Y. Wang, R. Shi, P. Gong, J. Li, J. Li, D. Ao, P. Wang, Y. Yang, Y. Man, Y. Qu, Bioelectric effect of a chitosan bioelectret membrane on bone regeneration in rabbit cranial defects, *J. Bioact. Compat. Polym.* 27 (2012) 122–132, <https://doi.org/10.1177/0883911512436773>.
- [20] I.-Y. Kim, S.-J. Seo, H.-S. Moon, M.-K. Yoo, I.-Y. Park, B.-C. Kim, C.-S. Cho, Chitosan and its derivatives for tissue engineering applications, *Biotechnol. Adv.* 26 (2008) 1–21, <https://doi.org/10.1016/j.biotechadv.2007.07.009>.
- [21] P.R. Sivashankari, M. Prabaharan, Prospects of chitosan-based scaffolds for growth factor release in tissue engineering, *Int. J. Biol. Macromol.* 93 (2016) 1382–1389, <https://doi.org/10.1016/j.ijbiomac.2016.02.043>.
- [22] Z. Liu, H. Wang, Y. Wang, Q. Lin, A. Yao, F. Cao, D. Li, J. Zhou, C. Duan, Z. Du, Y. Wang, C. Wang, The influence of chitosan hydrogel on stem cell engraftment, survival and homing in the ischemic myocardial microenvironment, *Biomaterials* 33 (2012) 3093–3106, <https://doi.org/10.1016/j.biomaterials.2011.12.044>.
- [23] W. Shi, D. Nie, G. Jin, W. Chen, L. Xia, X. Wu, X. Su, X. Xu, L. Ni, X. Zhang, X. Zhang, J. Chen, BDNF blended chitosan scaffolds for human umbilical cord MSC transplants in traumatic brain injury therapy, *Biomaterials* 33 (2012) 3119–3126, <https://doi.org/10.1016/j.biomaterials.2012.01.009>.
- [24] R. Jayakumar, M. Prabaharan, P.T. Sudheesh Kumar, S.V. Nair, H. Tamura, Biomaterials based on chitin and chitosan in wound dressing applications, *Biotechnol. Adv.* 29 (2011) 322–337, <https://doi.org/10.1016/j.biotechadv.2011.01.005>.
- [25] R. Jayakumar, M. Prabaharan, S.V. Nair, S. Tokura, H. Tamura, N. Selvamurugan, Novel carboxymethyl derivatives of chitin and chitosan materials and their biomedical applications, *Prog. Mater. Sci.* 55 (2010) 675–709, <https://doi.org/10.1016/j.pmatsci.2010.03.001>.
- [26] B. Pidhatika, N. Zhao, M. Zinggeler, J. Rühle, Surface-attached dual-functional hydrogel for controlled cell adhesion based on poly(N,N-dimethylacrylamide), *J. Polym. Res.* 26 (2019) 1–12, <https://doi.org/10.1007/s10965-019-1728-2>.
- [27] P. Samyn, M. Biesalski, O. Prucker, J. Rühle, Confining acrylate-benzophenone copolymers into adhesive micropads by photochemical crosslinking, *J. Photochem. Photobiol. Chem.* 377 (2019) 80–91, <https://doi.org/10.1016/j.jphotochem.2019.03.040>.
- [28] F.D. Scherag, R. Niestroj-Pahl, S. Krusekopf, K. Lücke, T. Brandstetter, J. Rühle, Highly selective capture surfaces on medical wires for fishing tumor cells in whole blood, *Anal. Chem.* 89 (2017) 1846–1854, <https://doi.org/10.1021/acs.analchem.6b04219>.
- [29] F.D. Scherag, A. Mader, M. Zinggeler, N. Birsner, R.E. Kneusel, T. Brandstetter, J. Rühle, Blocking-free and substrate-independent serological microarray immunoassays, *Biomacromolecules* 19 (2018) 4641–4649, <https://doi.org/10.1021/acs.biomac.8b01334>.
- [30] L. Yuan, B. Qu, J. Chen, H. Lv, X. Yang, Engineering modifiers bearing benzophenone with enhanced reactivity to construct surface microstructures, *Polym. Chem.* 10 (2019) 4859–4865, <https://doi.org/10.1039/c9py00764d>.
- [31] Y. Iwasaki, S. Bunuasunthon, V.P. Hoven, Protein patterning with antifouling polymer gel platforms generated using visible light irradiation, *Chem. Commun.* 56 (2020) 5472–5475, <https://doi.org/10.1039/d0cc02092c>.
- [32] O. Prucker, C.A. Naumann, J. Rühle, W. Knoll, C.W. Frank, Photochemical attachment of polymer films to solid surfaces via monolayers of benzophenone derivatives, *J. Am. Chem. Soc.* 121 (1999) 8766–8770, <https://doi.org/10.1021/ja990962+>.
- [33] Q. Liu, J.L. Locklin, Photocross-linking kinetics study of benzophenone containing zwitterionic copolymers, *ACS Omega* 5 (2020) 9204–9211, <https://doi.org/10.1021/acsomega.9b04493>.
- [34] K. Ishihara, K. Suzuki, Y. Inoue, K. Fukazawa, Effects of molecular architecture of photoreactive phospholipid polymer on adsorption and reaction on substrate surface under aqueous condition, *J. Biomater. Sci. Polym. Ed.* 32 (2020) 419–437, <https://doi.org/10.1080/09205063.2020.1839340>.
- [35] J. Koc, E. Schönemann, R. Wanka, N. Aldred, A.S. Clare, H. Gardner, G.W. Swain, K. Hunsucker, A. Laschewsky, A. Rosenhahn, Effects of crosslink density in zwitterionic hydrogel coatings on their antifouling performance and susceptibility to silt uptake, *Biofouling* 36 (2020) 646–659, <https://doi.org/10.1080/08927014.2020.1796983>.
- [36] M. Borgolte, O. Riester, T. Kacerova, S. Rentschler, M.S. Schmidt, S. Jacksch, M. Eger, S. Laufer, R. Csuk, H.P. Deigner, Methacryloyl-glcnaC derivatives copolymerized with dimethacrylamide as a novel antibacterial and biocompatible coating, *Pharmaceutics* 13 (2021) 1647, <https://doi.org/10.3390/pharmaceutics13101647>.
- [37] G. Dormán, H. Nakamura, A. Pulsipher, G.D. Prestwich, The life of pi star: exploring the exciting and forbidden worlds of the benzophenone photophore, *Chem. Rev.* 116 (2016) 15284–15398, <https://doi.org/10.1021/acs.chemrev.6b00342>.
- [38] G. Dormán, G.D. Prestwich, Benzophenone photophores in biochemistry, *Biochemistry* 33 (1994) 5661–5673, <https://doi.org/10.1021/bi00185a001>.
- [39] O. Prucker, T. Brandstetter, J. Rühle, Surface-attached hydrogel coatings via C,H-insertion crosslinking for biomedical and bioanalytical applications (Review), *Biointerphases* 13 (2018), 010801, <https://doi.org/10.1116/1.4999786>.
- [40] M.M. Hassan, O.O. Olaoye, Recent advances in chemical biology using benzophenones and diazirines as radical precursors, *Molecules* 25 (2020) 2285, <https://doi.org/10.3390/molecules25102285>.
- [41] H. Orelma, M. Vuoriluoto, L.S. Johansson, J.M. Campbell, I. Filpponen, M. Biesalski, O.J. Rojas, Preparation of photoreactive nanocellulosic materials: via benzophenone grafting, *RSC Adv.* 6 (2016) 85100–85106, <https://doi.org/10.1039/c6ra15015b>.
- [42] G. Dormán, G.D. Prestwich, Benzophenone photophores in biochemistry, *Biochemistry* 33 (1994) 5661–5673, <https://doi.org/10.1021/Bi00185A001/ASSET/Bi00185A001.FP.PNG.V03>.
- [43] M. Körner, O. Prucker, J. Rühle, Kinetics of the generation of surface-attached polymer networks through C, H-insertion reactions, *Macromolecules* 49 (2016) 2438–2447, <https://doi.org/10.1021/acs.macromol.5b02734>.
- [44] M. Morimoto, T. Nakajima, M. Ishikura, Y. Shigemasa, S. Ifuku, H. Saimoto, Synthesis of organosoluble chitosan derivatives with polyphenolic side chains, *Carbohydr. Polym.* 90 (2012) 1259–1264, <https://doi.org/10.1016/j.carbpol.2012.06.067>.
- [45] K.H. Hong, G. Sun, Antimicrobial and chemical detoxifying functions of cotton fabrics containing different benzophenone derivatives, *Carbohydr. Polym.* 71 (2008) 598–605, <https://doi.org/10.1016/j.carbpol.2007.07.004>.
- [46] D. Garcia-Gonzalez, A. Rusinek, T. Jankowiak, A. Arias, Mechanical impact behavior of polyether-ether-ketone (PEEK), *Compos. Struct.* 124 (2015) 88–99, <https://doi.org/10.1016/j.compstruct.2014.12.061>.
- [47] S.M. Kurtz, J.N. Devine, PEEK biomaterials in trauma, orthopedic, and spinal implants, *Biomaterials* 28 (2007) 4845–4869, <https://doi.org/10.1016/j.biomaterials.2007.07.013>.
- [48] A. Godara, D. Raabe, S. Green, The influence of sterilization processes on the micro-mechanical properties of carbon fiber-reinforced PEEK composites for bone implant applications, *Acta Biomater.* 3 (2007) 209–220, <https://doi.org/10.1016/j.actbio.2006.11.005>.
- [49] Lumbar interbody fusion using the brantigan I/F cage for pos... : Spine, (n.d.). https://journals.lww.com/spinejournal/Fulltext/2000/06010/Lumbar_Interbody_Fusion_Using_the_Brantigan_I_F.17.aspx (accessed 15, December 2021).
- [50] D.-Y. Cho, W.-R. Liao, W.-Y. Lee, J.-T. Liu, C.-L. Chiu, P.-C. Sheu, Preliminary experience using a polyetheretherketone (PEEK) cage in the treatment of cervical disc disease, *Neurosurgery* 51 (2002) 1343–1350, <https://doi.org/10.1227/01.NEU.0000309109.71345.19>.
- [51] J.W. Brantigan, A. Neidre, J.S. Toohy, The lumbar I/F cage for posterior lumbar interbody fusion with the variable screw placement system: 10-year results of a food and drug administration clinical trial, *Spine J.* 4 (2004) 681–688, <https://doi.org/10.1016/j.spinee.2004.05.253>.
- [52] J.M. Toth, M. Wang, B.T. Estes, J.L. Scifert, H.B. Seim, A.S. Turner, Polyetheretherketone as a biomaterial for spinal applications, *Biomaterials* 27 (2006) 324–334, <https://doi.org/10.1016/j.biomaterials.2005.07.011>.
- [53] A. Wang, R. Lin, C. Stark, J.H. Dumbleton, Suitability and limitations of carbon fiber reinforced PEEK composites as bearing surfaces for total joint replacements, *Wear* 225–229 (1999) 724–727, [https://doi.org/10.1016/S0043-1648\(99\)00026-5](https://doi.org/10.1016/S0043-1648(99)00026-5).
- [54] A Low Stiffness Composite Biologically Fixed Prosthesis : Clinical Orthopaedics and Related Research®, (n.d.). https://journals.lww.com/clinorthop/Fulltext/2001/12000/A_Low_Stiffness_Composite_Biologically_Fixed.15.aspx (accessed 15 December, 2021).
- [55] S. Akhavan, M.M. Matthiesen, L. Schulte, T. Penoyar, M.J. Kraay, C.M. Rinnac, V.M. Goldberg, Clinical and histologic results related to a low-modulus composite total hip replacement stem, *Journal of Bone and Joint Surgery - Series A* 88 (2006) 1308–1314, <https://doi.org/10.2106/JBJS.E.00316>.
- [56] F. el Halabi, J.F. Rodriguez, L. Rebollo, E. Hurtós, M. Doblare, Mechanical characterization and numerical simulation of polyether-ether-ketone (PEEK) cranial implants, *J. Mech. Behav. Biomed. Mater.* 4 (2011) 1819–1832, <https://doi.org/10.1016/j.jmbbm.2011.05.039>.
- [57] S. Lovald, S.M. Kurtz, Applications of Polyetheretherketone in Trauma, Arthroscopy, and Cranial Defect Repair, *PEEK Biomaterials Handbook*, 2012, pp. 243–260, <https://doi.org/10.1016/B978-1-4377-4463-7.10015-6>.
- [58] T.J. Hoskins, K.D. Dearn, S.N. Kukureka, Mechanical performance of PEEK produced by additive manufacturing, *Polym. Test.* 70 (2018) 511–519, <https://doi.org/10.1016/j.polymertesting.2018.08.008>.
- [59] M. Rinaldi, T. Ghidini, F. Cecchini, A. Brandao, F. Nanni, Additive layer manufacturing of poly (ether ether ketone) via FDM, *Compos. B Eng.* 145 (2018) 162–172, <https://doi.org/10.1016/j.compositesb.2018.03.029>.
- [60] B. Hu, X. Duan, Z. Xing, Z. Xu, C. Du, H. Zhou, R. Chen, B. Shan, Improved design of fused deposition modeling equipment for 3D printing of high-performance PEEK parts, *Mech. Mater.* 137 (2019), 103139, <https://doi.org/10.1016/j.mechmat.2019.103139>.
- [61] S. Berretta, K. Evans, O. Ghita, Additive manufacture of PEEK cranial implants: manufacturing considerations versus accuracy and mechanical performance, *Mater. Des.* 139 (2018) 141–152, <https://doi.org/10.1016/j.matdes.2017.10.078>.
- [62] S. Najeib, Z.K. Bds, S.Z. Bds, M.S.Z. Bds, Bioactivity and osseointegration of PEEK are inferior to those of titanium: a systematic review, *J. Oral Implantol.* 42 (2016) 512–516, <https://doi.org/10.1563/aaid-jo-i-16-00072>.
- [63] F. Blending, D. Seitz, A. Ottensschläger, M. Fleischer, V. Bucher, Atomic layer deposition of bioactive TiO₂ thin films on polyetheretherketone for orthopedic implants, *ACS Appl. Mater. Interfaces* 13 (2021) 3536–3546, <https://doi.org/10.1021/ACSAMI.0C17990>.
- [64] A. Diouf-Lewis, R.D. Farhani, F. Iervolino, J. Pierre, Y. Abderrafai, M. Lévesque, N. Piccirelli, D. Theriault, Design and characterization of carbon fiber-reinforced PEEK/PEI blends for Fused Filament Fabrication additive

- manufacturing, *Mater. Today Commun.* 31 (2022), 103445, <https://doi.org/10.1016/j.mtcomm.2022.103445>.
- [65] B.I. Oladapo, S.A. Zahedi, Improving bioactivity and strength of PEEK composite polymer for bone application, *Mater. Chem. Phys.* 266 (2021), 124485, <https://doi.org/10.1016/j.mtchemphys.2021.124485>.
- [66] K. Hu, Z. Yang, Y. Zhao, Y. Wang, J. Luo, B. Tuo, H. Zhang, Bioinspired surface functionalization of poly(ether ether ketone) for enhancing osteogenesis and bacterial resistance, *Langmuir* 38 (2022) 5924–5933, https://doi.org/10.1021/ACS.LANGMUIR.2C00600/SUPPL_FILE/LA2C00600_SI_002.MP4.
- [67] M. Kyomoto, K. Ishihara, Self-initiated surface graft polymerization of 2-methacryloyloxyethyl phosphorylcholine on poly(ether ether ketone) by photoradiation, *ACS Appl. Mater. Interfaces* 1 (2009) 537–542, https://doi.org/10.1021/AM800260T/ASSET/IMAGES/MEDIUM/AM-2008-00260T_0005.GIF.
- [68] M. Kyomoto, T. Moro, S. Yamane, M. Hashimoto, Y. Takatori, K. Ishihara, Poly(ether-ether-ketone) orthopedic bearing surface modified by self-initiated surface grafting of poly(2-methacryloyloxyethyl phosphorylcholine), *Biomaterials* 34 (2013) 7829–7839, <https://doi.org/10.1016/j.biomaterials.2013.07.023>.
- [69] M. Kyomoto, T. Moro, Y. Takatori, H. Kawaguchi, K. Nakamura, K. Ishihara, Self-initiated surface grafting with poly(2-methacryloyloxyethyl phosphorylcholine) on poly(ether-ether-ketone), *Biomaterials* 31 (2010) 1017–1024, <https://doi.org/10.1016/j.biomaterials.2009.10.055>.
- [70] C.J. Frstrup, K. Jankova, S. Hvilsted, Hydrophilization of poly(ether ether ketone) films by surface-initiated atom transfer radical polymerization, *Polym. Chem.* 1 (2010) 1696–1701, <https://doi.org/10.1039/C0PY00142B>.
- [71] B. Yameen, M. Alvarez, O. Azzaroni, U. Jonas, W. Knoll, Tailoring of poly(ether ether ketone) surface properties via surface-initiated atom transfer radical polymerization, *Langmuir* 25 (2009) 6214–6220, https://doi.org/10.1021/LA900010Z/ASSET/IMAGES/MEDIUM/LA-2009-00010Z_0004.GIF.
- [72] 87: Biological reactivity tests , in vitro, in: *The United States Pharmacopeia. The National Formulary, United States Pharmacopeial Convention, Inc., Rockville, Md, 1979, pp. 92–94.*
- [73] E. Skyttä, T. Mattila-Sandholm, A quantitative method for assessing bacteriocins and other food antimicrobials by automated turbidimetry, *J. Microbiol. Methods* 14 (1991) 77–88, [https://doi.org/10.1016/0167-7012\(91\)90036-P](https://doi.org/10.1016/0167-7012(91)90036-P).
- [74] Japan Food Research Laboratories, ISO, 2011, pp. 1–24. ISO 22196: Measurement of antibacterial activity on plastics and other non-porous surfaces.
- [75] M.F. Queiroz, K.R.T. Melo, D.A. Sabry, G.L. Sasaki, H.A.O. Rocha, Does the use of chitosan contribute to oxalate kidney stone formation? *Mar. Drugs* 13 (2015) 141–158, <https://doi.org/10.3390/MD13010141>, 13 (2014) 141–158.
- [76] Z.G. Tang, R.A. Black, J.M. Curran, J.A. Hunt, N.P. Rhodes, D.F. Williams, Surface properties and biocompatibility of solvent-cast poly[ε-caprolactone] films, *Biomaterials* 25 (2004) 4741–4748, <https://doi.org/10.1016/j.biomaterials.2003.12.003>.
- [77] ISO 10993-5:2009 Biological Evaluation of Medical Devices — Part 5: Tests for in Vitro Cytotoxicity, n.d.
- [78] 88: biological reactivity tests , in vivo, in: *The United States Pharmacopeia. The National Formulary, United States Pharmacopeial Convention, Inc., Rockville, Md, 1979, pp. 94–98.*
- [79] A.D. Baxter, R. Bhogal, J. Bird, J.F. Keily, D.T. Manallack, J.G. Montana, D.A. Owen, W.R. Pitt, R.J. Watson, R.E. Wills, Arylsulphonyl hydroxamic acids: potent and selective matrix metalloproteinase inhibitors, *Bioorg. Med. Chem. Lett* 11 (2001) 1465–1468, [https://doi.org/10.1016/S0960-894X\(01\)00259-1](https://doi.org/10.1016/S0960-894X(01)00259-1).
- [80] E.I. Heath, L.B. Grochow, Clinical potential of matrix metalloprotease inhibitors in cancer therapy, *Drugs* 59 (2000) 1043–1055, <https://doi.org/10.2165/00003495-200059050-00002>.
- [81] S.B. Rodan, Y. Imai, M.A. Thiede, G. Wesolowski, D. Thompson, Z. Bar-Shavit, S. Shull, K. Mann, G.A. Rodan, Characterization of a human osteosarcoma cell line (Saos-2) with osteoblastic properties, *Cancer Res.* 47 (1987) 4961–4966.
- [82] C. Sun, S. bin Feng, Z.W. Cao, J.J. Bei, Q. Chen, X.J. Xu, Z. Zhou, Z.P. Yu, H.Y. Hu, Up-regulated expression of matrix metalloproteinases in endothelial cells mediates platelet microvesicle-induced angiogenesis, *Cell. Physiol. Biochem.* 41 (2017) 2319–2332, <https://doi.org/10.1159/000475651>.
- [83] T. Mori, M. Okumura, M. Matsuura, K. Ueno, S. Tokura, Y. Okamoto, S. Minami, T. Fujinaga, Effects of chitin and its derivatives on the proliferation and cytokine production of fibroblasts in vitro, *Biomaterials* 18 (1997) 947–951, [https://doi.org/10.1016/S0142-9612\(97\)00017-3](https://doi.org/10.1016/S0142-9612(97)00017-3).
- [84] J. Brown, Using the monocyte activation test as a stand-alone release test for medical devices, *ALTEX* (2021) 151–156, <https://doi.org/10.14573/altex.2012021>.
- [85] Y. Nakagawa, H. Maeda, T. Murai, Evaluation of the in vitro pyrogen test system based on proinflammatory cytokine release from human monocytes: comparison with a human whole blood culture test system and with the rabbit pyrogen test, *Clin. Diagn. Lab. Immunol.* 9 (2002) 588–597, <https://doi.org/10.1128/CDLI.9.3.588-597.2002>.
- [86] Y.v. Chaly, R.S. Selvan, K.v. Fegeding, T.S. Kolesnikova, N.N. Voitenok, Expression of IL-8 gene in human monocytes and lymphocytes: differential regulation by tnf and IL-1, *Cytokine* 12 (2000) 636–643, <https://doi.org/10.1006/CYTO.1999.0664>.
- [87] H.-Y. Hsu, M.-H. Wen, Lipopolysaccharide-mediated reactive oxygen species and signal transduction in the regulation of interleukin-1 gene expression, *J. Biol. Chem.* 277 (2002) 22131–22139, <https://doi.org/10.1074/jbc.M111883200>.
- [88] H. Yuan, C.N. Perry, C. Huang, E. Iwai-Kanai, R.S. Carreira, C.C. Glembotski, R.A. Gottlieb, LPS-induced autophagy is mediated by oxidative signaling in cardiomyocytes and is associated with cryoprotection, *Am. J. Physiol. Heart Circ. Physiol.* (2009) 296, <https://doi.org/10.1152/AJPHEART.01051.2008/ASSET/IMAGES/LARGE/ZH40030987000009.JPG>.
- [89] J.G. Gray, G. Chandra, W.C. Clay, S.W. Stinnett, S.A. Haneline, J.J. Lorenz, I.R. Patel, G. Bruce Wisely, P.J. Furdon, J.D. Taylor, T.A. Kost, A CRE/ATF-like site in the upstream regulatory sequence of the human interleukin 1 beta gene is necessary for induction in U937 and THP-1 monocytic cell lines, *Mol. Cell Biol.* 13 (1993) 6678–6689, <https://doi.org/10.1128/MCB.13.11.6678-6689.1993>.
- [90] K. Li, R. Xing, S. Liu, R. Li, Y. Qin, X. Meng, P. Li, Separation of chito-oligomers with several degrees of polymerization and study of their antioxidant activity, *Carbohydr. Polym.* 88 (2012) 896–903, <https://doi.org/10.1016/j.carbpol.2012.01.033>.
- [91] H. Anggani, E. Hasriati, E. Winiati Bachtiar, Evaluation of IL-1 α and IL-1 β , COX-2, and iNOS mRNA expression in orthodontic patients given chitosan mouthwash during treatment with miniscrew, *J. Int. Soc. Prev. Community Dent.* 11 (2021) 561–565, https://doi.org/10.4103/JISPCD.JISPCD_163_21.
- [92] T.-C. Chou, E. Fu, E.-C. Shen, Chitosan inhibits prostaglandin E2 formation and cyclooxygenase-2 induction in lipopolysaccharide-treated RAW 264.7 macrophages, *Biochem. Biophys. Res. Commun.* 308 (2003) 403–407, [https://doi.org/10.1016/S0006-291X\(03\)01407-4](https://doi.org/10.1016/S0006-291X(03)01407-4).
- [93] G.-W. Oh, S.-C. Ko, J.-Y. Je, Y.-M. Kim, J. Oh, W.-K. Jung, Fabrication, characterization and determination of biological activities of poly(ε-caprolactone)/chitosan-caffeic acid composite fibrous mat for wound dressing application, *Int. J. Biol. Macromol.* 93 (2016) 1549–1558, <https://doi.org/10.1016/j.ijbiomac.2016.06.065>.
- [94] M. Valko, K. Jomova, C.J. Rhodes, K. Kuča, K. Musilek, Redox- and Non-redox-metal-induced Formation of Free Radicals and Their Role in Human Disease, 2016, <https://doi.org/10.1007/s00204-015-1579-5>.
- [95] Z. Li, F. Yang, R. Yang, Synthesis and characterization of chitosan derivatives with dual-antibacterial functional groups, *Int. J. Biol. Macromol.* 75 (2015) 378–387, <https://doi.org/10.1016/j.ijbiomac.2015.01.056>.
- [96] L. Hu, X. Meng, R. Xing, S. Liu, X. Chen, Y. Qin, H. Yu, P. Li, Design, synthesis and antimicrobial activity of 6-N-substituted chitosan derivatives, *Bioorg. Med. Chem. Lett* 26 (2016) 4548–4551, <https://doi.org/10.1016/j.bmcl.2015.08.047>.
- [97] H. Liu, P. Sun, H. Liu, S. Yang, L. Wang, Z. Wang, Acute toxicity of benzophenone-type UV filters for Photobacterium phosphoreum and Daphnia magna: QSAR analysis, interspecies relationship and integrated assessment, *Chemosphere* 135 (2015) 182–188, <https://doi.org/10.1016/j.chemosphere.2015.04.036>.
- [98] A.K. Refai, M. Textor, D.M. Brunette, J.D. Waterfield, Effect of titanium surface topography on macrophage activation and secretion of proinflammatory cytokines and chemokines, *J. Biomed. Mater. Res.* 70A (2004) 194–205, <https://doi.org/10.1002/jbm.a.30075>.

Supporting Information

Synthesis of a biocompatible benzophenone-substituted chitosan hydrogel as novel coating for PEEK with extraordinary strong antibacterial and anti-biofilm properties

Max Borgolte^{1,2}, Oliver Riester^{1,3}, Isabel Quint^{1,3}, Felix Blendinger^{4,5}, Volker Bucher⁴, Stefan Laufer^{3,6}, René Csuk², Luca Scotti⁷ and Hans-Peter Deigner^{*1,8,9}

¹ Institute of Precision Medicine, Furtwangen University, Jakob-Kienzle Str. 17, 78054 Villingen-Schwenningen, Germany

² Martin-Luther University Halle-Wittenberg, Organic Chemistry, Kurt-Mothes-Str. 2, 06120, Halle, Saale, Germany

³ Institute of Pharmaceutical Sciences, Department of Pharmacy and Biochemistry, Eberhard-Karls-University Tuebingen, Auf der Morgenstelle 8, Tuebingen, 72076, Germany

⁴ Institute for Microsystems Technology (iMST), Furtwangen University, Neckartal 142, 78628 Rottweil, Germany

⁵ Institute for Applied Physics, Eberhard Karls University Tuebingen, Auf der Morgenstelle 8, 72076 Tuebingen, Germany

⁶ Tuebingen Center for Academic Drug Discovery & Development (TüCAD2), 72076 Tuebingen, Germany

⁷ Department of Medical, Oral and Biotechnological Sciences, University "G. d'Annunzio" of Chieti-Pescara, Via dei Vestini, 66100 Chieti, Italy

⁸ Faculty of Science, Eberhard Karls University Tuebingen, Auf der Morgenstelle 8, 72076 Tuebingen, Germany

⁹ EXIM Department, Fraunhofer Institute IZI (Leipzig), Schillingallee 68, 18057 Rostock, Germany

* Correspondence: dei@hs-furtwangen.de

Abstract: Chitosan derivatives substituted with benzophenone groups that can be cross-linked by ultraviolet light were synthesized as coatings for PEEK substrates used in the construction of lumbar cages. The IC₉₀ values of the benzophenone-modified chitosan polymers in solution before crosslinking were in the same range as those reported for native chitosan. The resulting hydrogel surface after crosslinking exhibited excellent antimicrobial properties and was highly effective (up to 5 log-fold) against clinically relevant strains of methicillin-resistant *S. aureus* and *E. coli*. As a result, the coated surface also significantly reduced biofilm formation. The coatings show good biocompatibility with numerous cell lines as well as low levels of cytotoxicity (ISO 10993-5) and pyrogenicity (ISO 10993-11). The coatings also exhibited strong antioxidant properties toward formed hydroxyl radicals in an in-vitro Fenton reaction. Overall, substitution of chitosan with benzophenone residues is an interesting and important approach to the functionalization of materials used for medical implants that are prone to microbial contamination and mechanical failure. Biocompatible antimicrobial coatings might also be employed in photopatterning methods used in the design of medical devices.

Table of Contents

1.	Synthesis	2
1.1	Calibration curve of 4-benzoyl-benzoic acid in EtOH	2
2.	Surface characterization	3
2.1	XPS surface characterization	3
2.2	SEM-EDS surface characterization	4
3.	Surface topology	5
3.1	Microscopic images (200 x magnification) of the coatings	5
4.	Microbiology	6
4.1	Antibacterial assay for the evaluation of coatings	6
4.2	Bacteriostatic Assay	7

1. Synthesis

1.1 Calibration curve of 4-benzoyl-benzoic acid in EtOH

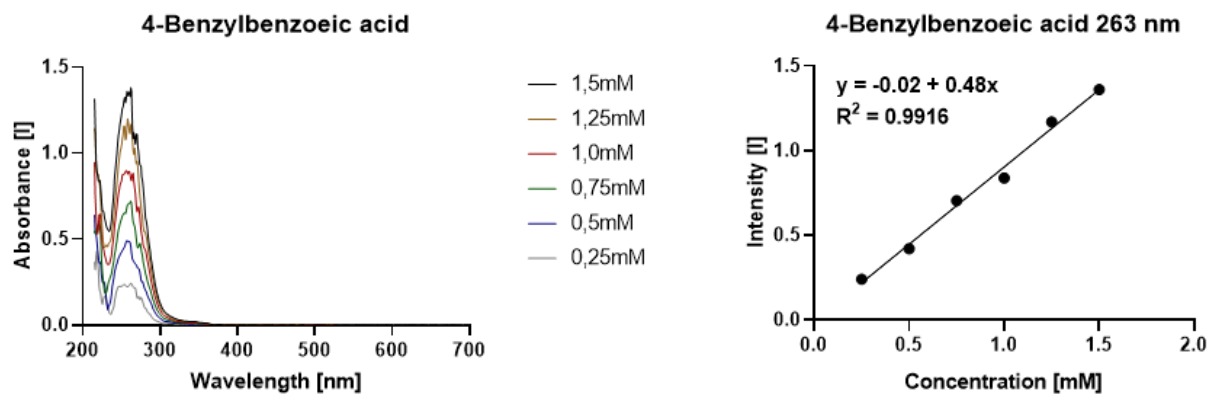


Figure S1. Full spectrum (left) and calibration curve with corresponding formula calculated with maxima at 263 nm of 4-benzoyl-benzoic acid in EtOH, used for calculation of the degree of substitution of the benzophenone-chitosan derivatives.

2. Surface characterization

2.1 XPS surface characterization

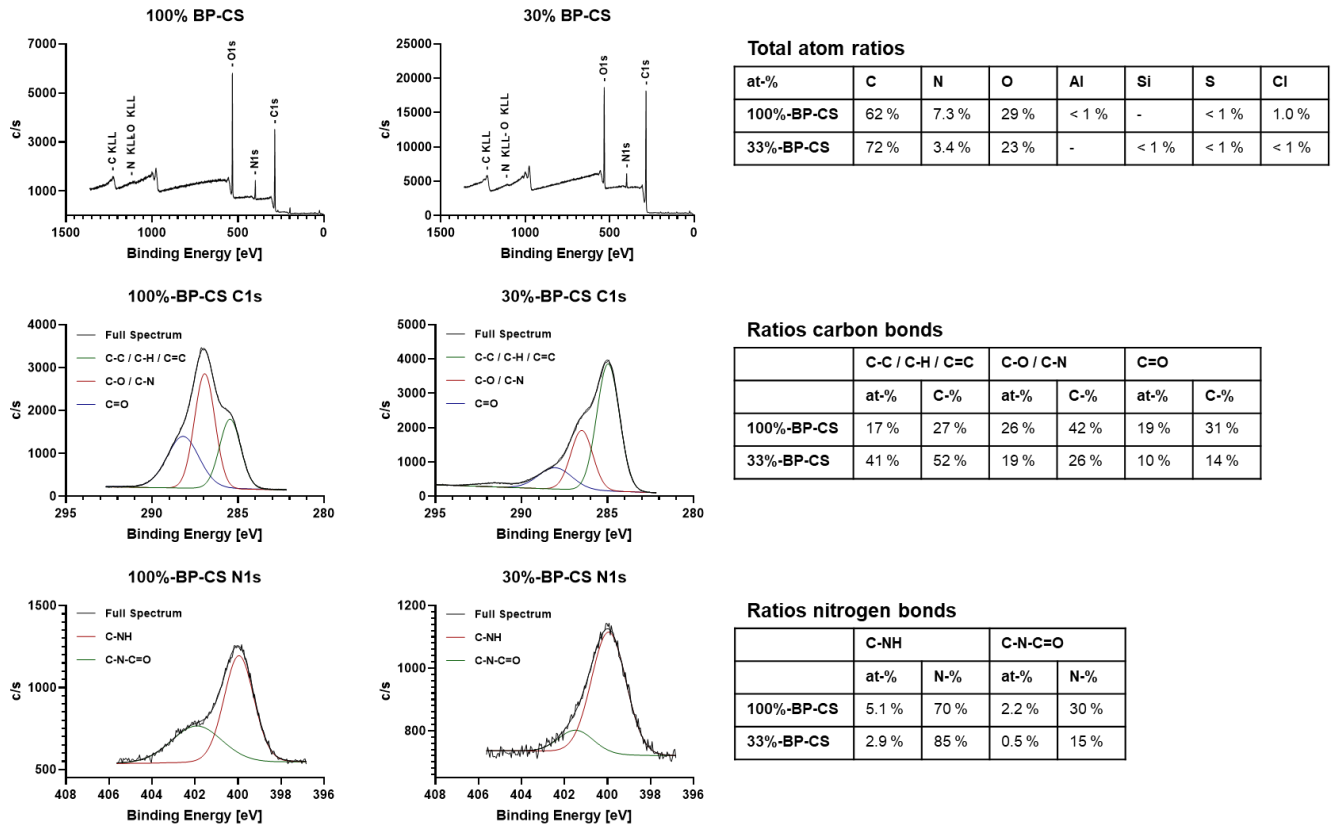
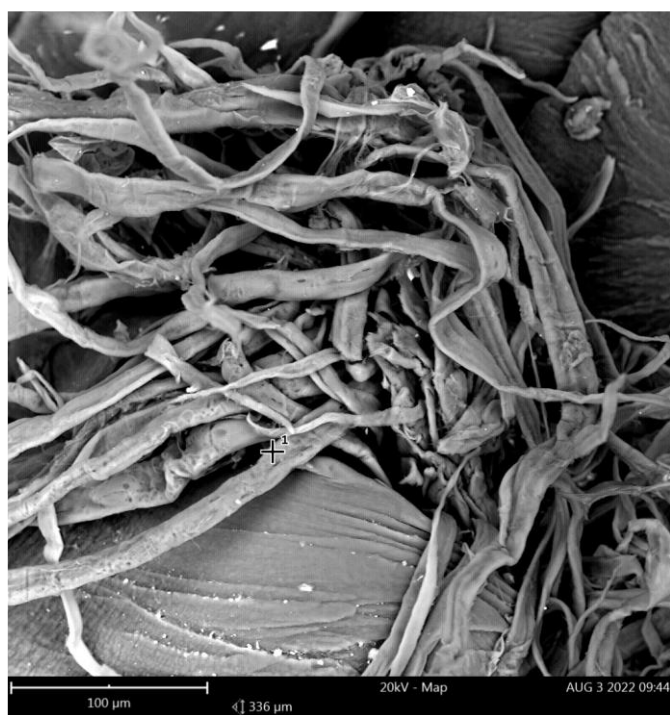


Figure S2. XPS spectra of 100%-BP-CS and 33%-BP-CS coating, together with calculated ratios of the atoms in the coating.

2.2 SEM-EDS surface characterization



Element	Atomic conc.	Weight conc.	Oxide Symbol	Stoich wt conc.
O	58.54 %	64.38 %		
C	31.75 %	26.21 %		
N	9.64 %	9.28 %		
Si	0.06 %	0.12 %	SiO ₂	0.74 %

Figure S3. SEM-EDS surface characterization of the 100%-BP-CS coating and the corresponding atomic concentrations. Area of measurement is marked in the SEM image.

3. Surface topology

3.1 Microscopic images (200 x magnification) of the coatings

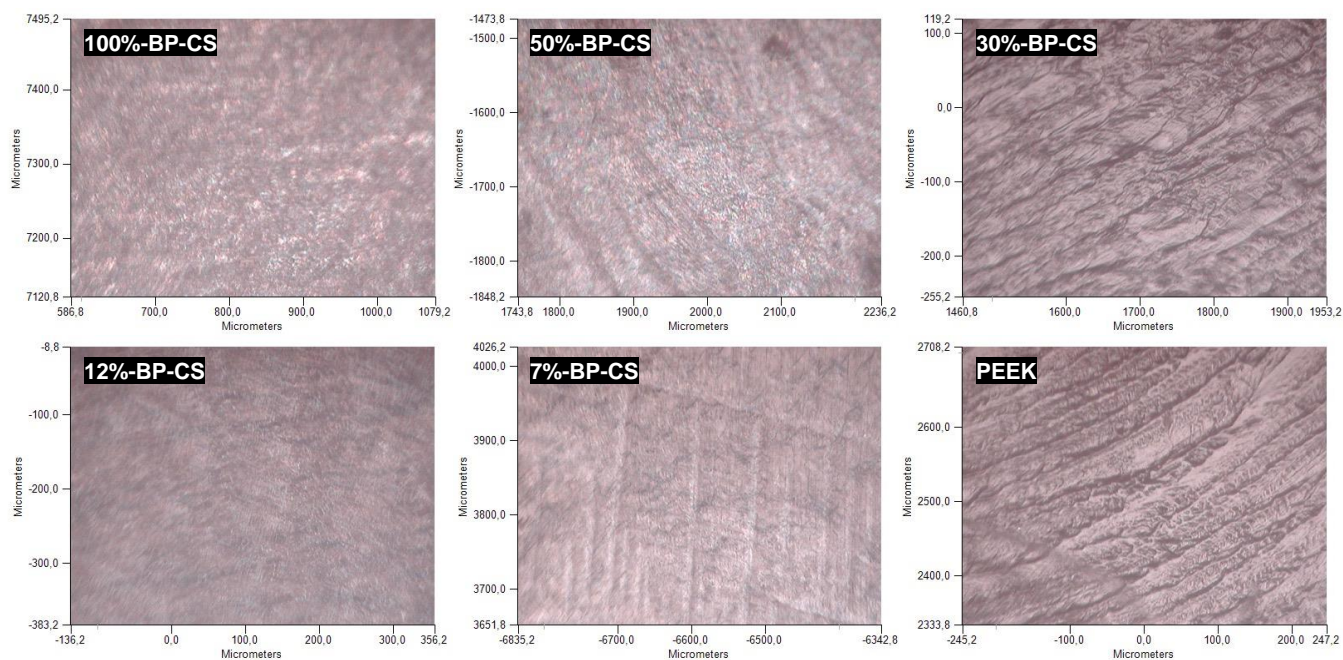


Figure S4. Microscopic images of the coatings, taken with 200x magnification using the PerkinElmer IR Microscope. The shown areas were used for IR measurements of the coating.

4. Microbiology

4.1 Antibacterial assay for the evaluation of coatings

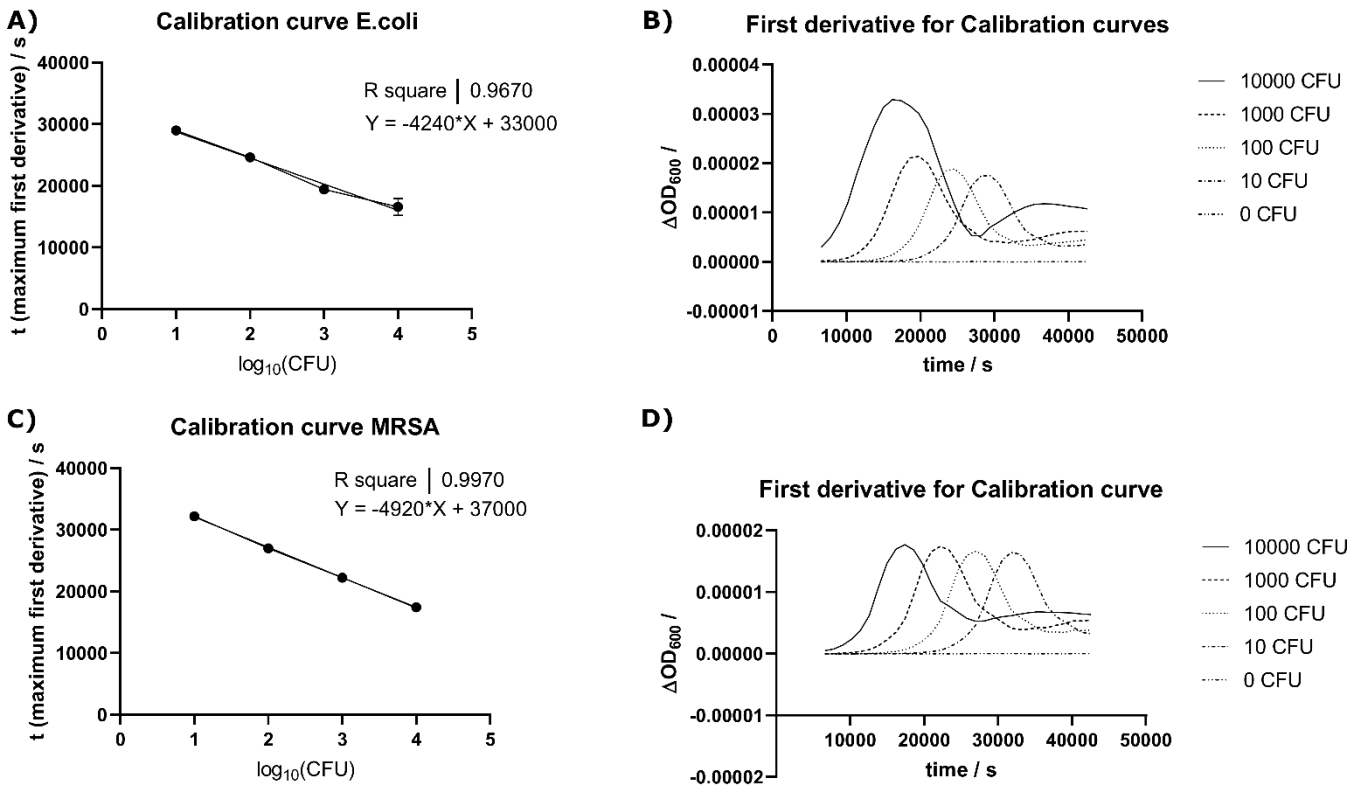


Figure S5. Calibration curves of *Escherichia coli* (A) and *Staphylococcus aureus* (C) for the correlation between the logarithmic colony forming units (CFU) and the time needed to reach the growth curve's maximum of the first derivative. The calculated first derivatives for *Escherichia coli* (B) and *Staphylococcus aureus* (D).

4.2 Bacteriostatic Assay

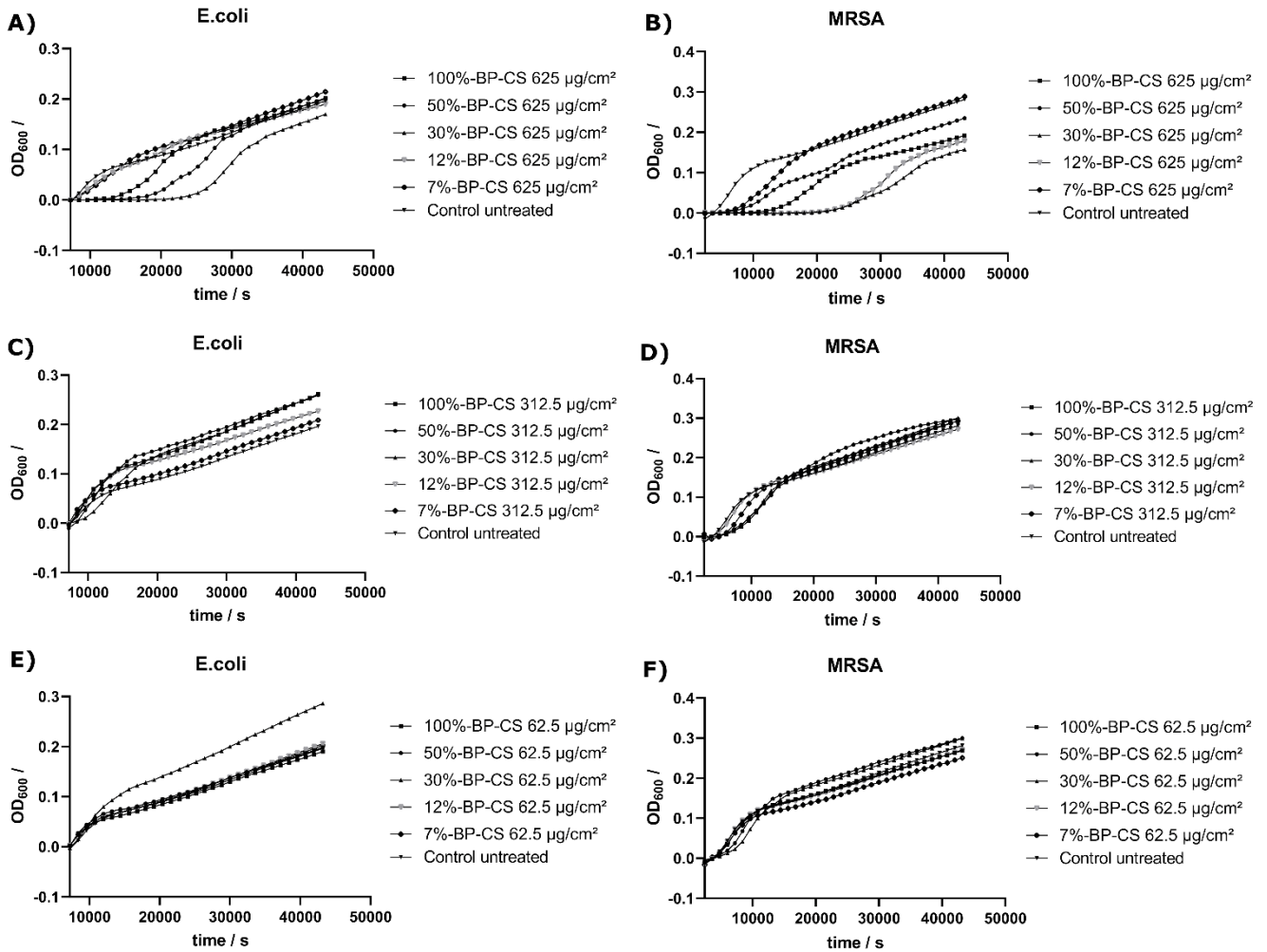


Figure S6. Growth curves of alive bacteria after 24 h incubation in direct contact with polymer coatings. Three different concentrations were used in the casting process: 625 $\mu\text{g}/\text{cm}^2$ (A, B), 312.5 $\mu\text{g}/\text{cm}^2$ (C, D) and 62.5 $\mu\text{g}/\text{cm}^2$ (E, F). They were tested with bacterial solution of *Staphylococcus aureus* (B, D, F) and *Escherichia coli* (A, C, E).

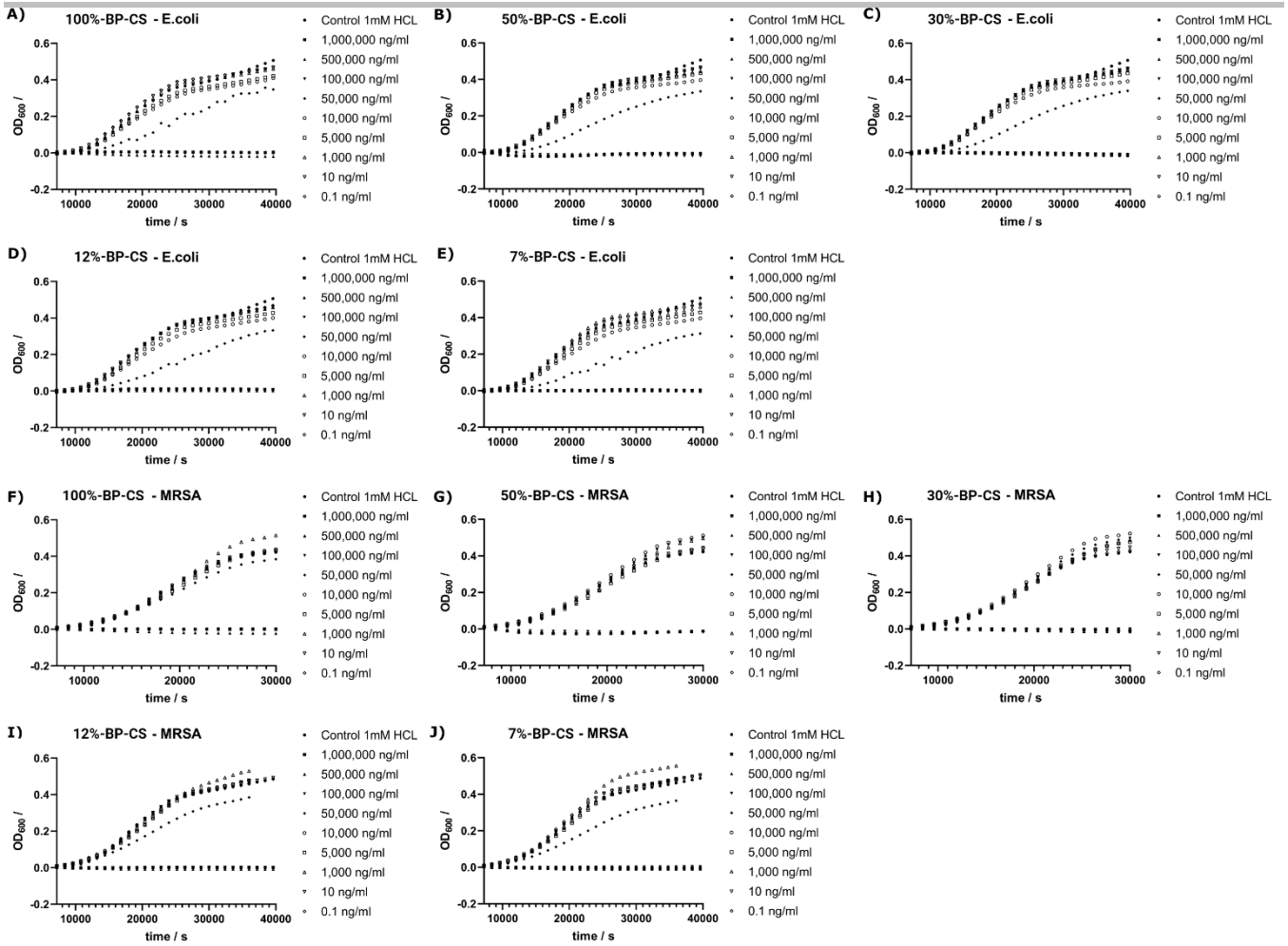
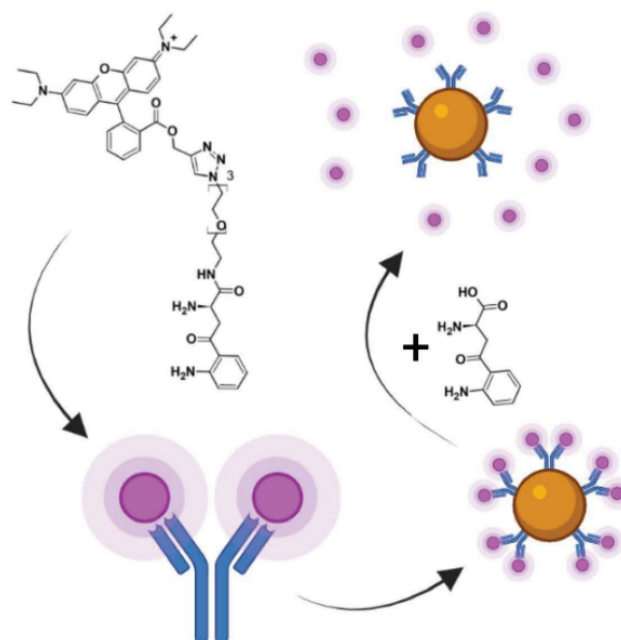


Figure S7. Growth curves of *Escherichia coli* (A - E) and *Staphylococcus aureus* (F - J) treated with various concentrations of the chitosan derivatives solubilized in 1 mM HCl.

P-3: A Fluorescence-Based Competitive Antibody Binding Assay for Kynurenine, a Potential Biomarker of Kidney Transplant Failure

Borgolte, M.; Quint, I.; Kaiser, L.; Csuk, R.; Deigner, H.-P. A Fluorescence-Based Competitive Antibody Binding Assay for Kynurenine, a Potential Biomarker of Kidney Transplant Failure. *Diagnostics* **2022**, *12*, 1380.

Graphical Abstract



Abstract

Kynurenine is a tryptophan metabolite linked to several inflammatory processes including transplant failure, a significant challenge in transplant medicine. The detection of small molecules such as kynurenine, however, is often complex and time consuming. Herein, we report the successful synthesis of a fluorescently labelled kynurenine derivative, showing proper fluorescence and antikynurenine antibody binding behavior in a magnetic bead immunoassay (MIA). The fluorescent kynurenine–rhodamine B conjugate shows a K_D -value of $5.9 \mu\text{M}$ as well as IC_{50} values of $4.0 \mu\text{M}$ in PBS and $10.2 \mu\text{M}$ in saliva. We thus introduce a rapid test for kynurenine as a potential biomarker for kidney transplant failure

Keywords

Transplant failure; transplant medicine; biomarkers; fluorescent probes; fluorescence; kynurenine; amino acids; rapid testing

Article

A Fluorescence-Based Competitive Antibody Binding Assay for Kynurenine, a Potential Biomarker of Kidney Transplant Failure

Max Borgolte ^{1,2}, Isabel Quint ^{1,3}, Lars Kaiser ^{1,4}, René Csuk ² and Hans-Peter Deigner ^{1,5,*}

¹ Institute of Precision Medicine, Furtwangen University, Jakob-Kienzle Str. 17, 78054 Villingen-Schwenningen, Germany; box@hs-furtwangen.de (M.B.); i.quint@hs-furtwangen.de (I.Q.); kal@hs-furtwangen.de (L.K.)

² Institute of Organic Chemistry, Martin-Luther University Halle-Wittenberg, Kurt-Mothes-Str. 2, 06120 Halle (Saale), Germany; rene.csuk@chemie.uni-halle.de

³ Faculty of Science, Eberhard Karls University Tuebingen, Auf der Morgenstelle 8, 72076 Tuebingen, Germany

⁴ Institute of Pharmaceutical Sciences, University of Freiburg, Albertstraße 25, 79104 Freiburg im Breisgau, Germany

⁵ EXIM Department, Fraunhofer Institute IZI (Leipzig), Schillingallee 68, 18057 Rostock, Germany

* Correspondence: dei@hs-furtwangen.de

Abstract: Kynurenine is a tryptophan metabolite linked to several inflammatory processes including transplant failure, a significant challenge in transplant medicine. The detection of small molecules such as kynurenine, however, is often complex and time consuming. Herein, we report the successful synthesis of a fluorescently labelled kynurenine derivative, showing proper fluorescence and anti-kynurenine antibody binding behavior in a magnetic bead immunoassay (MIA). The fluorescent kynurenine–rhodamine B conjugate shows a K_D -value of 5.9 μM as well as IC_{50} values of 4.0 μM in PBS and 10.2 μM in saliva. We thus introduce a rapid test for kynurenine as a potential biomarker for kidney transplant failure.

Keywords: transplant failure; transplant medicine; biomarkers; fluorescent probes; fluorescence; kynurenine; amino acids; rapid testing



check for updates

Citation: Borgolte, M.; Quint, I.; Kaiser, L.; Csuk, R.; Deigner, H.-P. A Fluorescence-Based Competitive Antibody Binding Assay for Kynurenine, a Potential Biomarker of Kidney Transplant Failure. *Diagnostics* **2022**, *12*, 1380. <https://doi.org/10.3390/diagnostics12061380>

Academic Editors: Luca Morelli and Nicola Longo

Received: 22 March 2022

Accepted: 29 May 2022

Published: 2 June 2022

Publisher's Note: MDPI stays neutral with regard to jurisdictional claims in published maps and institutional affiliations.



Copyright: © 2022 by the authors. Licensee MDPI, Basel, Switzerland. This article is an open access article distributed under the terms and conditions of the Creative Commons Attribution (CC BY) license (<https://creativecommons.org/licenses/by/4.0/>).

1. Introduction

Kynurenine is a metabolite of the tryptophan degradation pathway linked to several inflammatory, metabolic, oncogenic [1] as well as psychiatric disorders [2,3]. While some tryptophan is metabolized to serotonin [4], 95% of the dietary tryptophan is metabolized to the kynurenine pathway (KP) via the enzyme class of indolamine-2,3-dioxygenases (IDOs) [5–7], followed by a cascade of degradation enzymes with quinolinic acid as the final product [8]. The activity of the IDO enzymes is regulated through immunological factors such as pathogenic microorganisms and LPS [9–11], inflammatory cytokines [12,13], or IL-1 and TNF- α [14]. Elevated kynurenine levels also downregulate immune activation and convey anti-inflammatory activity [15–18], demonstrating a feedback-loop-like behavior.

The link between inflammatory response and elevated kynurenine levels in serum via upregulation of IDO by pro-inflammatory factors renders kynurenine an interesting biomarker for clinically relevant inflammatory processes. Upregulated IDO and, therefore, elevated kynurenine levels of $3.9 \pm 2.1 \mu\text{M}$ in serum have been found in the case of chronic kidney disease (CKD) in patients in the pre-dialysis stage. Values increase along with CKD severity up to $5.6 \pm 2.3 \mu\text{M}$ because of chronic inflammation during CKD progression [19–22]. Elevated kynurenine levels are related not only to CKD but also to inflammatory processes after kidney transplantation; they are inversely correlated with kidney function [23,24]. In a study from 2007 by Buczko et al., plasma and saliva kynurenine levels from uremic patients were compared, showing reproducible results and correlations among saliva and serum kynurenine levels [25]. Due to this correlation in serum and saliva

kynurenine found by Buczko et al. [25] and the association with inflammation and IDO expression both in kidney failure during chronic kidney disease and kidney transplant rejection [22,26,27], and due to the findings that kynurenine is discussed as a biomarker for renal allograft failure in the literature [28,29], here, we focus on kynurenine determined from saliva as a potential biomarker for kidney transplant rejection. In patients with transplant rejection, L-kynurenine levels of $17.4 \pm 8.4 \mu\text{M}$ for serum and $4.6 \pm 1.6 \mu\text{M}$ for saliva were measured, compared to control groups with serum levels of $2.7 \pm 0.4 \mu\text{M}$ and $0.7 \pm 0.4 \mu\text{M}$ in saliva [23,25,28–30].

Apart from transplant failure, elevated kynurenine levels have also been linked to titanium dental implants and to bone-osseointegration processes [31], as well as to the implantation of a left ventricular assist device, showing that kynurenine as a metabolite is linked to implant failure as well [32].

Most approaches in clinical trials to quantifying kynurenine from different tissues are focused on LC-MS [33–35] or GC-MS [36] methods, displaying clinical impracticability and delayed diagnosis. Apart from these, Ungor et al., 2019, presented fluorescent gold nanoclusters able to detect kynurenine in physiological concentrations in PBS with a quenching mechanism [37]. Another approach is the usage of fluorescently labelled kynurenine derivatives, as shown by Klockow et al., 2013, who labelled kynurenine with a coumarin aldehyde scaffold, showing fluorescence while undergoing a shift in pH [38]. Other approaches for potential rapid testing, using the kynurenine pathway for diagnosis, focus on quantifying the IDO activity instead of measuring kynurenine directly [39].

To date and due to the small size of the kynurenine molecule, no fluorescently labelled kynurenine derivatives bound to an anti-kynurenine antibody are described in the literature. Likewise, there is no functional bioassay based on antibody binding of kynurenine described in the literature. Herein, we report the synthesis of a fluorescent, rhodamine B-labelled kynurenine derivative and demonstrate its binding ability to an anti-kynurenine antibody. We demonstrate that this denotes a promising approach for the development of a competitive kynurenine antibody-binding assay and ultimately a kynurenine rapid test from saliva and possibly other body fluids.

2. Materials and Methods

2.1. General Experimental

TLC was carried out on Silica Gel 60 F254 (Merck, layer thickness 0.2 mm) with detection by UV light (254 nm) or by charring with 1% KMnO_4 in 1N NaOH. Flash column chromatography (FC) was performed on M&N Silica Gel 60 (0.063–0.200 mm). ^1H NMR and ^{13}C NMR spectra were recorded on a Bruker Avance I 200 (200 MHz), Bruker Avance II 400 (400 MHz, both Bruker, Billerica, MA, USA), or Varian Unity 500 (500 MHz) spectrometer (Varian Inc., Palo Alto, CA, USA). Chemical shifts are reported in parts per million relative to solvent signals (CDCl_3 : $\delta\text{H} = 7.26$ ppm, $\delta\text{C} = 77.0$ ppm; $\text{DMSO}-d_6$: $\delta\text{H} = 2.49$ ppm, $\delta\text{C} = 39.7$ ppm). Signals were assigned by first-order analysis and assignments were supported where feasible by 2-dimensional ^1H , ^1H and ^1H , ^{13}C correlation spectroscopy. Coupling constants are reported in hertz. UV/vis spectra were recorded on a PerkinElmer Lambda XLS+ UV/vis spectrometer (PerkinElmer, Waltham, MA, USA) in a 10.00 mm QS quartz cuvette. Fluorescence was recorded on a Tecan Infinite M200 multiplate reader in commercially available 96-well multiter plates. Chemicals and reagents were purchased from Acros Organics, Alfa Aesar, Sigma-Aldrich, Carl Roth, Carbolution or ABCR and were used without further purification.

2.2. Synthesis of Kynurenine–Rhodamine B Conjugates

2.2.1. [6-Diethylamino-9-(2-prop-2-ynylloxycarbonyl-phenyl)-xanthen-3-ylidene]-diethylammonium; Chloride **1**

Rhodamine B (10 g, 20.9 mmol, 1 eq) was dissolved in dry CH_2Cl_2 (250 mL) under N_2 atmosphere. EDC (4.4 g, 22.99 mmol, 1.1 eq) and DMAP (0.51 g, 4.18 mmol, 0.2 eq) were

added, and the mixture obtained was stirred for 15 min at room temperature. After the addition of propargyl alcohol (1.33 mL, 22.99 mmol, 1.1 eq) and after stirring overnight at room temperature, the mixture was washed 2x with 1M HCl (250 mL) and 1x with brine (250 mL). Drying the organic layer over Na₂SO₄ and evaporating the solvent yielded the crude product. Purification via flash column chromatography (CH₂Cl₂: MeOH 9:1) gave the final product: violet powder (6.08 g, 56%).

¹H-NMR (CDCl₃, 400 MHz): 8.66 (d, *J* = 7.9 Hz, 1 H, Ar-H), 7.88 (t, *J* = 7.6 Hz, 1 H, Ar-H), 7.78 (t, *J* = 7.7 Hz, 1 H, Ar-H), 7.38 (d, *J* = 7.6 Hz, 1 H, Ar-H), 7.09 (d, *J* = 9.4 Hz, Ar-H, 1 H), 6.95 (d, *J* = 9.6 Hz, Ar-H, 1 H), 6.88 (s, Ar-H, 1 H), 4.65 (d, *J* = 1.3 Hz, CH₂, 2 H), 3.68 (q, *J* = 7.1, CH₂, 8 H), 2.46 (s, CH, 1 H), 1.36 (t, *J* = 7.1, CH₃, 12 H).

¹³C-NMR (DMSO, 50 MHz): 164.4 (C(=O)O), 157.6 (Ar-C), 155.6 (Ar-C), 134.0 (Ar-C), 133.8 (Ar-C), 131.3 (Ar-C), 131.3 (Ar-C), 131.0 (Ar-C), 129.3 (Ar-C), 115.1 (Ar-C), 113.4 (Ar-C), 107.4 (Ar-C), 96.4 (Ar-C), 78.5 (C), 77.8 (CH), 53.3 (CH₂), 45.8 (CH₂), 12.9 (CH₃).

2.2.2. 4-(2-Amino-phenyl)-2-tert-butoxycarbonylamino-4-oxo-butyric Acid 2

NH₂ protection of kynurenine was carried out by Boc-chemistry following Schotten-Baumann conditions: kynurenine (500 mg, 2.4 mmol, 1 eq) was dissolved in a water/THF 1:1 mixture containing NaOH (288 mg, 7.2 mmol, 3 eq). After the solution turned clear, Boc₂O (1.55 mL, 7.2 mmol, 3 eq) was added dropwise at 0 °C, and the reaction was monitored by TLC. Complete conversion was observed after 90 min. Acidification using 10% HCl, followed by 3 extractions with ethyl acetate, drying of the organic layer and evaporation of the solvent yielded the crude product: a yellowish oil. Column chromatography (ethyl acetate) yielded the pure product: a yellowish powder (327.7 mg, 44%).

¹H-NMR (400 MHz, CDCl₃): 7.73 (d, *J* = 8.0 Hz, 1H, Ar-H), 7.34 (t, *J* = 7.6 Hz, 1H, Ar-H), 6.83–6.72 (m, 2H, Ar-H), 5.64 (d, *J* = 8.7 Hz, 1H, CH), 4.67 (ddd, *J* = 12.8, 8.5, 4.3 Hz, 1H, CH), 3.80–3.69 (m, 2H, CH₂), 3.53 (dd, *J* = 18.0, 3.8 Hz, 1H, CH), 1.45 (s, 9H, 3x CH₃).

¹³C-NMR (100 MHz, CDCl₃): 199.54 (Ar-C(=O)), 172.43 (C(C=O)OH), 155.68 (Boc-C(=O)), 149.45 (Ar-C), 134.96 (Ar-C), 131.08 (Ar-C), 125.83 (Ar-C), 118.10 (Ar-C), 116.73 (Ar-C), 69.98 (Boc-*tert*-C), 52.60 (CH), 41.47 (CH₂), 28.34 (CH₃).

2.2.3. [3-(2-Amino-phenyl)-1-(2-[2-(2-azido-ethoxy)-ethoxy]-ethoxy)-ethylcarbamoyl]-3-oxo-propyl]-carbamic Acid Tert-Butyl Ester 3

Boc-protected kynurenine **1** (318.9 mg, 1.03 mmol, 1 eq) and the corresponding azido-linker (248.68 mg, 1.14 mmol, 1.1 eq) were dissolved in CH₂Cl₂ (50 mL). EDC (197.45 mg, 1.03 mmol, 1 eq) and DMAP (25.17 mg, 0.206 mmol, 0.2 eq) were added, and the mixture was stirred at room temperature for 48 h. Washing 3× with 2 M NaOH (80 mL) followed by washing with brine (80 mL), drying over Na₂SO₄ and evaporation yielded the crude product. Column chromatography (ethyl acetate) yielded the pure product: an orange solid, which was used directly in the next step without further analysis (175.11 mg, 33%).

2.2.4. (9-[2-[1-(2-[2-[4-(2-Amino-phenyl)-2-tert-butoxycarbonylamino-4-oxo-butyrylamino]-ethoxy)-ethyl]-1H-[1,2,3]triazol-4-ylmethoxycarbonyl]-phenyl]-6-diethylamino-xanthen-3-ylidene)-diethyl-ammonium Salt 4

Azido functionalized Boc-L-Kynurenine **3** (166 mg, 326.6 μmol, 1 eq) and propargyl rhodamine B **1** (169 mg, 326.6 μmol, 1 eq) were dissolved in 30 mL of a mixture of CH₂Cl₂/MeOH/H₂O 10:10:3. After adding an aqueous CuSO₄ solution (262 μL, 0.5 M, 130.64 μmol, 0.4 eq), TBTA (18 mg, 32.66 μmol, 0.1 eq) and Na ascorbate (142 mg, 718.52 μmol, 2.2 eq), the mixture was heated to 60 °C for 16 h. After cooling down, 20 mL of ddH₂O was added and the mixture was extracted 3 times with 50 mL CH₂Cl₂, followed by drying over Na₂SO₄ and evaporation of the solvent. The pure product was obtained after column chromatography (CH₂Cl₂/MeOH 3:1) as a pink powder (302.5 mg, 90%).

¹H-NMR (DMSO, 500 MHz): 8.20 (dd, *J* = 7.9, 1.0 Hz, 1H, Ar-H), 7.91–7.85 (m, 3H, Ar-H), 7.83–7.79 (m, 2H, Ar-H), 7.47 (dd, *J* = 7.6, 0.8 Hz, 1H, Ar-H), 7.08–7.00 (m, 2H, Ar-H), 6.97–6.90 (m, 5H, Ar-H), 5.04 (s, 2H, Ar-CH₂), 4.65 (d, *J* = 2.4 Hz, 1H, CH₂), 4.44 (t, *J* = 5.2 Hz, 2H, Triazol-CH₂), 3.74 (t, *J* = 5.2 Hz, 2H, O-CH₂), 3.63 (dd, *J* = 13.9, 6.7 Hz, 8H, 4x

RhB-CH₂), 3.48–3.45 (m, 2H, O-CH₂), 3.44–3.40 (m, 6H, 3 × O-CH₂), 3.30 (t, *J* = 6.4 Hz, 2H, O-CH₂), 3.00 (dd, *J* = 12.0, 6.0 Hz, 2H, CH₂), 1.33 (s, 9H, 3 × Boc-CH₃), 1.20 (t, *J* = 6.7 Hz, 12H, 4 × RhB-CH₃).

¹³C-NMR (DMSO, 125 MHz): 198.9 (Ar-C(=O)), 172.1 (C(=O)-NH), 164.9 (C(=O)-O), 157.8 (Ar-H), 157.5 (Boc-C(=O)), 156.0 (Ar-C), 155.6 (Ar-C), 155.5 (Ar-C), 141.04 (Triazol-Ar-C), 134.6 (Ar-C), 133.9 (Ar-C), 133.8 (Ar-C), 133.7 (Ar-C), 131.3 (Ar-C), 131.2 (Ar-C), 131.0 (Ar-C), 130.9 (Ar-C), 129.6 (Ar-C), 129.2 (Ar-C), 125.3 (Triazol-Ar-C), 115.0 (Ar-C), 114.9 (Ar-C), 114.8 (Ar-C), 113.3 (Ar-C), 96.3 (Ar-C), 78.4 (*tert.*-C), 78.0 (NH(Boc)-CH), 77.8 (O-CH₂), 70.1 (O-CH₂), 70.0 (O-CH₂), 69.9 (O-CH₂), 69.6 (O-CH₂), 69.3 (O-CH₂), 68.0 (O-CH₂), 58.6 (Ar-CH₂), 53.2 (RhB-CH₂), 49.8 (Ar-CH₂), 45.8 (N-CH₂), 28.7 (Boc-CH₃), 12.9 (RhB-CH₃).

2.2.5. (9-[2-[1-(2-[2-[2-Amino-4-(2-amino-phenyl)-4-oxo-butyrylamino]-ethoxy]-ethyl)-1H-[1,2,3]triazol-4-ylmethoxycarbonyl]-phenyl]-6-diethylamino-xanthen-3-ylidene)-diethyl-ammonium Salt 5

Boc-deprotection of rhodamine B-kynurenin conjugate **4** was carried out by dissolving conjugate **4** in 6 mL of CH₂Cl₂ containing 25% trifluoroacetic acid. After stirring at room temperature for 1 h, the solution was precipitated in 50 mL ice cold Et₂O and centrifuged for 5 min at 4 °C and max speed. The precipitate was dissolved in ddH₂O and lyophilized. Purification by HPLC yielded the pure product: a pink solid (60.5 mg, 26%).

¹H-NMR (DMSO, 500 MHz): 8.20 (dd, *J* = 8.0, 1.4, 1H, Ar-H), 8.11 (s, 1H, C(=O)NH), 7.93–7.84 (m, 3H, Ar-H), 7.85–7.78 (m, 2H, Ar-H), 7.47 (dd, *J* = 7.7, 1.4, 1H, Ar-H), 7.05–6.99 (m, 3H, Ar-H), 6.97–6.89 (m, 5H, Ar-H), 5.05 (d, *J* = 4.4, 3H, Ar-CH₂ + CH), 4.47–4.41 (m, 2H, Ar-CH₂), 3.75 (t, *J* = 5.2, 2H, O-CH₂), 3.63 (q, *J* = 6.9, 8H, RhB-CH₂), 3.54 (d, *J* = 5.6, 2H, O-CH₂), 3.50–3.42 (m, 8H, O-CH₂), 2.92 (q, *J* = 5.6, 2H, O-CH₂), 1.20 (t, *J* = 7.0, 12H, RhB-CH₃).

¹³C-NMR (DMSO, 125 MHz): 197.3 (Ar-C(=O)), 168.8 (C(=O)-NH), 164.9 (C(=O)-O), 158.2 (Ar-C), 157.9 (Ar-C), 157.5 (Ar-C), 155.5 (Ar-C), 141.1 (Triazol-Ar-C), 133.2 (Ar-C), 133.7 (Ar-C), 131.2 (Ar-C), 130.9 (Ar-C), 129.6 (Ar-C), 125.3 (Triazol-Ar-C), 117.5 (Ar-C), 114.9 (Ar-C), 113.3 (Ar-C), 96.3 (Ar-C), 70.1 (O-CH₂), 70.0 (O-CH₂), 69.9 (O-CH₂), 69.0 (O-CH₂), 67.1 (O-CH₂), 58.6 (Ar-CH₂), 49.8 (Ar-CH₂), 45.7 N-CH₂, 12.87 (CH₃).

2.2.6. (6-Diethylamino-9-[2-[1-(2-[2-(2-hydroxy-ethoxy)-ethoxy]-ethoxy)-ethyl]-1H-[1,2,3]triazol-4-ylmethoxycarbonyl]-phenyl]-xanthen-3-ylidene)-diethyl-ammonium Salt 6

Propargyl rhodamine B **1** (100 mg, 193.4 μmol, 1 eq) and azidotetraethylene glycol (42.4 mg, 193.4 μmol, 1 eq, synthesized according to the literature [40]) were dissolved in 25 mL of a mixture of CH₂Cl₂/MeOH/H₂O 10:10:3. A solution of CuSO₄ in H₂O (0.5 M, 15.5 μL, 7.74 μmol, 0.04 eq) was added, TBTA (1 mg, 1.93 μmol, 0.01 eq) and Na ascorbate (8.4 mg, 42.6 μmol, 0.22 eq) were added, and the mixture was heated to 60 °C. The reaction was monitored by TLC. After 16 h, the mixture was left to cool down, followed by the addition of 25 mL of ddH₂O. Extraction with 50 mL of CH₂Cl₂ 3 times, followed by drying over Na₂SO₄, gave the crude product. Column chromatography (CH₂Cl₂/MeOH 3:1) gave the pure product: a pink oil (135.8 mg, 95%).

¹H-NMR (DMSO, 500 MHz): 8.22 (d, *J* = 8.0 Hz, 1H, Ar-H), 7.89 (t, *J* = 5.2 Hz, 2H, Ar-H), 7.82 (t, *J* = 7.9 Hz, 1H, Ar-H), 7.48 (d, *J* = 7.5 Hz, 1H, Ar-H), 7.04 (dd, *J* = 9.5, 2.2 Hz, 2H, Ar-H), 6.96 (s, 1H, Ar-H), 6.95–6.92 (m, 3H, Ar-H), 5.06 (s, 2H, Ar-CH₂), 4.56 (s, 1H, OH), 4.45 (t, *J* = 5.2 Hz, 2H, O-CH₂), 3.76 (t, *J* = 5.2 Hz, 2H, O-CH₂), 3.65 (q, *J* = 6.8 Hz, 8H, CH₂), 3.49 (dd, *J* = 5.6, 3.1 Hz, 2H, O-CH₂), 3.46–3.41 (m, 6H, O-CH₂), 3.37–3.34 (m, 2H, O-CH₂), 1.22 (t, *J* = 6.8 Hz, 12H, CH₃).

¹³C-NMR (DMSO, 125 MHz): 164.88 (C(=O)), 157.88 (Ar-H), 157.53 (Ar-H), 155.53 (Ar-H), 141.05 (Ar-H), 133.71 (Ar-H), 131.24 (Ar-H), 130.93 (Ar-H), 129.67 (Ar-H), 125.36 (Ar-H), 114.94 (Ar-H), 113.32 (Ar-H), 96.29 (Ar-H), 72.75 (CH₂), 70.21 (CH₂), 70.17 (CH₂), 70.05 (CH₂), 69.97 (CH₂), 69.01 (CH₂), 66.81 (CH₂), 60.63 (CH₂), 58.63 (CH₂), 49.77 (CH₂), 45.76 (CH₂), 12.89 (CH₃).

2.3. Magnetic Bead Immunoassay (MIA)

2.3.1. Antibody Biotinylation

A total of 1 μL of a 6 mg/mL Biotin-NHS solution (NHS-dPEG[®]12-biotin, Sigma Aldrich, Taufkirchen, Germany) was added to 100 μL of an anti-kynurenine antibody (monoclonal Mouse IgG1a k chain anti-kynurenine antibody, clone 3D4-F2, ImmuSmol SAS, 0.5 mg/mL). The mixture was incubated for 50 min at room temperature with gentle shaking. Excess Biotin-NHS was removed using a VivaSpin 500 centrifugal concentrator with 10 kDa MWCO (Sigma Aldrich).

2.3.2. Bead Preparation

For bead activation, 50 μL of magnetic beads (Dynabeads[™] MyOne[™] Streptavidin C1 magnetic beads 10 mg/mL, Thermo Fisher Scientific, Schwerte, Germany) was diluted to 1 mg/mL with 450 μL of PBS and pelleted on a magnetic rack for 2 min. The supernatant was discarded, and the beads were washed three times with 500 μL PBS. After the last washing step, 20 μL of the supernatant was replaced with 20 μL biotinylated antibody (0.5 mg/mL). The mixture was incubated for 30 min at RT under gentle shaking. The reaction was blocked by washing the beads three times with PBS containing 1.5% BSA and 0.5% Tween-20. The final concentration was 20 μg of antibody per 1 mg of beads.

2.3.3. Immunoassay Conjugate Binding

For 3 h at RT, 0–100 μM rhodamine B–kynurenine conjugate **5** or rhodamine B-PEG-Linker **6** was incubated with 50 μL of antibody-conjugated magnetic beads and 50 μL of PBS (1:3 dilution). The beads were pelleted on a magnetic rack, and the unbound rhodamine B in the supernatant was quantified in a 96-well-plate with a fluorescence measurement of 100 μL of supernatant at 561 nm excitation and 592 nm emission, using a Tecan Infinite M200 multiplate reader. A standard curve of rhodamine B fluorescence intensity between 0 and 100 μM diluted 1:3 in PBS was used for the calculation of bead-bound conjugate **5** or **6**.

2.3.4. Competition between Rhodamine B–Kynurenine Conjugate and Native Kynurenine

Fifty microliters of antibody coupled beads was incubated with 50 μL of 12 μM rhodamine B–kynurenine conjugate **5** and 50 μL of spiked PBS or artificial saliva (Sigma Aldrich, SAE0149) containing 0–250 μM native L-kynurenine for 3 h at RT on a hula shaker (1:3 dilution). Beads were pelleted on a magnet and fluorescence intensity of unbound rhodamine B–kynurenine conjugate **5** in 100 μL supernatant was measured in a Tecan Infinite M200 multiplate reader at 561 nm excitation and 592 nm emission. Bead-bound L-kynurenine was indirectly calculated by calculating the amount of displaced rhodamine B–kynurenine conjugate **5**. Therefore, the fluorescence intensity of bound rhodamine B–kynurenine conjugate **5** without L-kynurenine was subtracted from the fluorescence intensity of samples with different L-kynurenine concentrations.

3. Results and Discussion

3.1. Synthesis of Fluorescent Kynurenine Conjugates

Chemical synthesis of the fluorescent L-kynurenine–rhodamine B conjugate was carried out as shown in Figure 1. First, commercial rhodamine B was reacted with propargyl alcohol to the corresponding rhodamine B propargyl ester **1** using Steglich esterification by EDC and DMAP, which was used as the fluorescent probe for click-conjugates **5** and **6**.

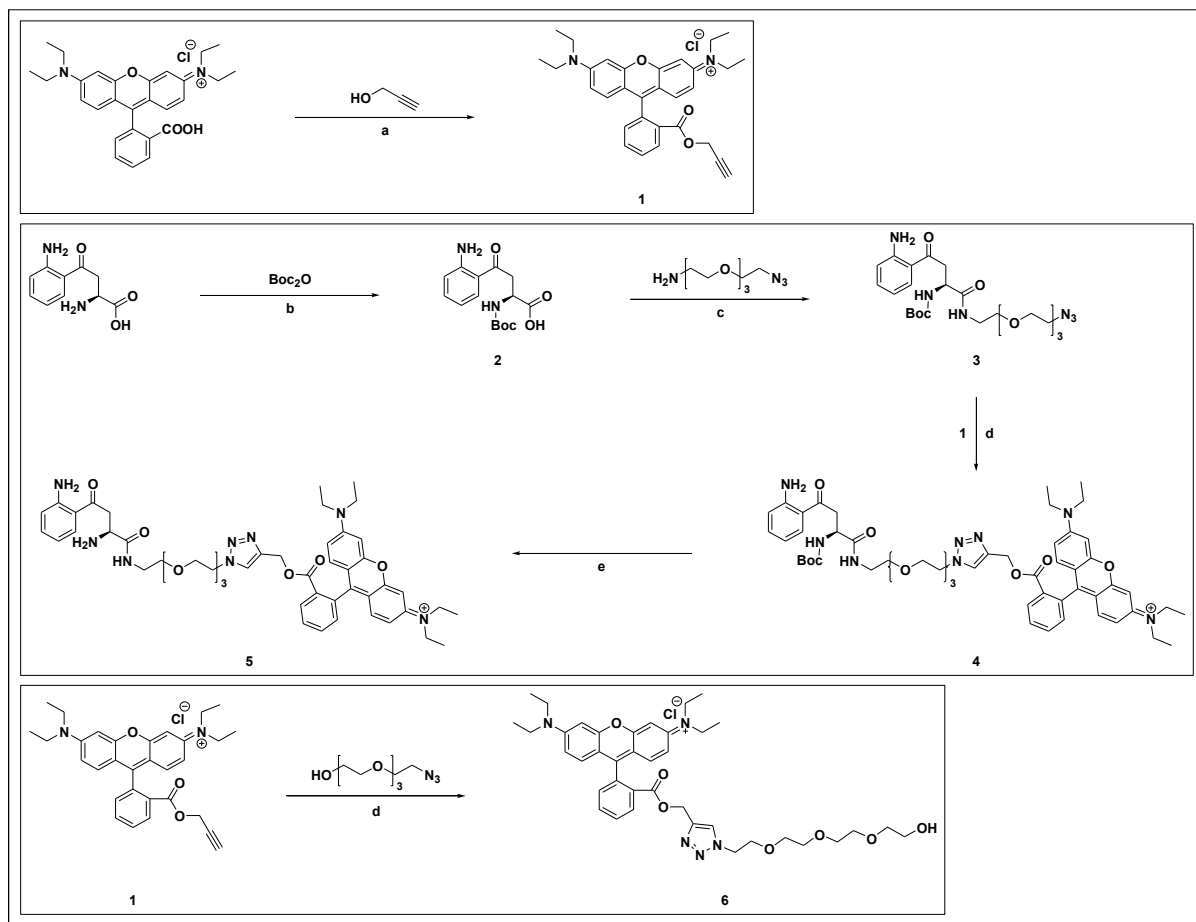


Figure 1. Route of synthesis for the fluorescent labelled kynurenine probe. Rhodamine B was reacted with propargyl alcohol to rhodamine B propargyl ester **1**, which was reacted with an azido tetraethylene glycol linker to afford **6** or with azido-kynurenine to yield product **5**. Reaction conditions: (a) EDC, DMAP, CH_2Cl_2 , RT, overnight; (b) NaOH, $\text{H}_2\text{O}/\text{THF}$ 1:1, RT, 90 min; (c) EDC, DMAP, CH_2Cl_2 , RT, 48 h; (d) **1**, CuSO_4 , TBTA, Na ascorbate, $\text{H}_2\text{O}/\text{MeOH}/\text{CH}_2\text{Cl}_2$ 10:10:3, 16 h; and (e) $\text{CH}_2\text{Cl}_2/\text{TFA}$ 4:1, RT, 1 h.

For the azido tetraethylene glycol L-kynurenine derivative **3**, Boc-protection of the primary amine of kynurenine was carried out to obtain product **2**, followed by attaching an amino-azido-tetraethylene glycol linker, synthesized according to a published protocol [41] yielding the azido-4EG-L-kynurenine derivative **3**. Click reaction of **3** with **1** gave product **4**, followed by Boc-deprotection to the fluorescent kynurenine probe **5**. To study the effect of the linker as well as the rhodamine B moiety on antibody binding, rhodamine B clickamer **6** containing only a tetraethylene glycol linker [40] was prepared, following the same reaction conditions as for product **4**.

3.2. Spectral Properties

To determine emission and absorption maxima for the synthesized rhodamine B click-conjugates, UV/vis spectra of the compounds were recorded in dd H_2O (cf. Figure 2). The absorption maximum of rhodamine B is at 554 nm [42] while the absorption maxima of the rhodamine B conjugates **5** and **6**, containing a benzoic ester instead of a free benzoic acid at the rhodamine's benzoic acid residue, is slightly shifted to 560 nm. Emission maxima were determined to be at 586 nm for the L-Kyn-4EG-RhB probe **5**, while the 4EG-RhB clickamer

6 shows an emission maximum of 584 nm, indicating suitable absorption and emission properties for immunoassays.

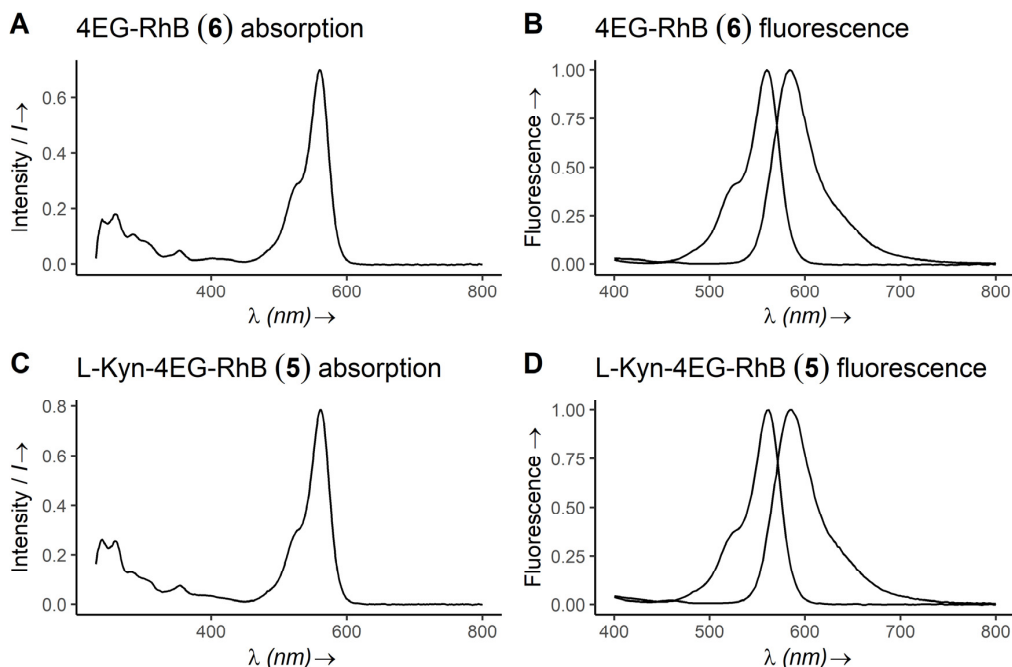


Figure 2. Absorption (A,C) and fluorescence (B,D) spectra of compounds **5** and **6**, measured in ddH₂O. Absorption maxima of compounds **5** and **6** are shifted slightly to 560 nm in the comparison at 554 nm for native rhodamine B [42]. Fluorescence maxima are 586 nm.

3.3. Magnetic Bead Immunoassay (MIA)

To determine the antibody binding capabilities of the synthesized fluorescent L-kynurenine conjugate, we elucidated the antibody binding capability of fluorescent conjugates **5** and **6** as well as their competitive binding capability by using magnetic bead-bound anti-kynurenine antibodies, followed by incubation with the fluorescent conjugates and the subsequent fluorescence measurements of unbound conjugate in the supernatant. The tetraethylene glycol rhodamine B clickamer **6** was used as a negative control to exclude unspecific interactions between the rhodamine B or the tetraethylene glycol linker with the antibody. Antibody binding data are shown in Figure 3. As the magnetic beads are suspended in solution, the surface coated with antibodies is effectively increased, leading to increased assay sensitivity and favorable binding kinetics and, therefore, more accurate data on competition between fluorescent probe **5** and native L-kynurenine.

To this end, antibodies were bound to magnetic beads in 1 μ m diameter, followed by incubation with the target compounds, pelleted via magnet and the fluorescence measured in the supernatant. In the competitive assay, 0–83 μ M L-kynurenine was incubated together with either 4 μ M RhB-4EG-L-Kyn conjugate **5**, followed by a pelleting of the beads and the measurement of the fluorescence in the supernatant. The binding curves of **5** and **6** as well as the competitive binding curve are shown in Figures 3 and 4.

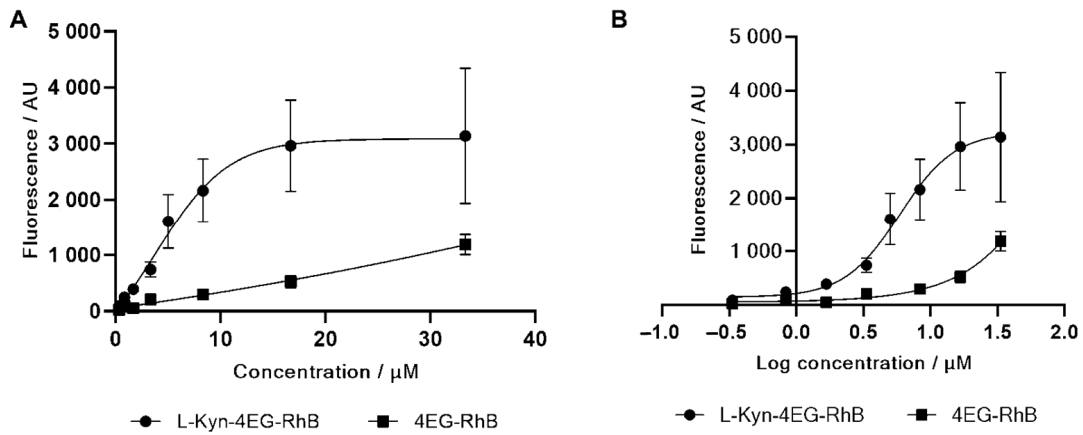


Figure 3. Binding assay of L-Kyn-4EG-RhB conjugate 5 and 4EG-RhB control 6 with antibody-coated magnetic beads (A) Concentration in micromole per liter and (B) logarithmic analyte concentration. Binding of the conjugate 5 to the antibody is significantly stronger than binding of the 4EG-RhB control 6. A specific binding of the conjugate to the antibody is concluded.

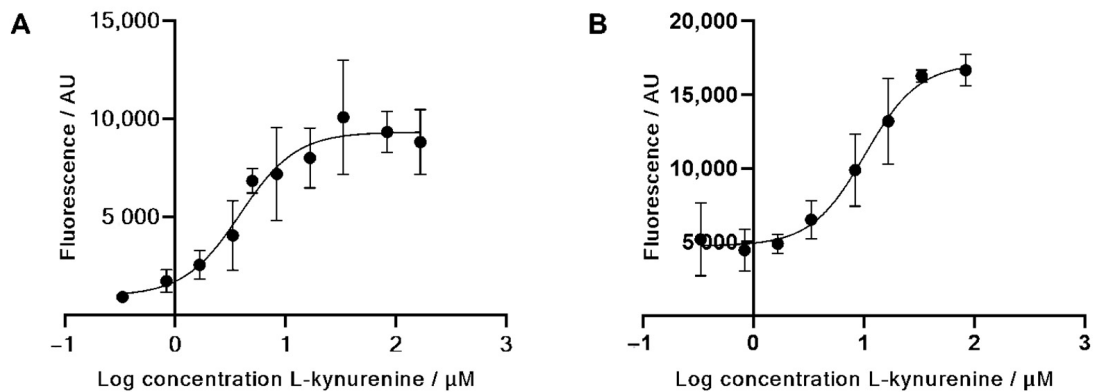


Figure 4. Competitive antibody binding assay in magnetic bead assay of the L-kynurenine–rhodamine B conjugate 5 against native L-kynurenine in (A) PBS and (B) artificial saliva. Fluorescence of the solution increases with increasing L-kynurenine concentration, meaning native kynurenine competes in antibody binding against the kynurenine conjugate.

With increasing concentration of the fluorescent L-kynurenine conjugate 5, the measured fluorescence in the supernatant decreases since more fluorescent conjugates bind to the antibody. Figure 3A shows the difference in fluorescence intensity between L-kynurenine conjugate 5 and 4EG-RhB clickamer 6 with and without incubation with the bead-bound antibodies. In higher concentrations, the 4EG-RhB clickamer 6 binding affinity also increases, probably due to unspecific interactions between either the linker or the rhodamine B residue. Apart from this, the difference in measured fluorescence for the L-kynurenine conjugate 5 is significantly stronger, showing a K_D -value of $5.9 \mu\text{M}$, and therefore, unspecific interactions between the 4EG-RhB clickamer 6 and the magnetic bead-bound antibody can be neglected.

As shown in Figure 4, the competitive binding assay shows a proper increase in fluorescence along with increasing concentrations of native L-kynurenine in both PBS and artificial saliva. Increasing fluorescence levels are caused by the displacement of the fluorescent conjugate through native kynurenine. The IC_{50} values of this competition were calculated to be $4.0 \mu\text{M}$ in PBS and $10.2 \mu\text{M}$ in saliva. As expected, the IC_{50} value in saliva

is higher than in PBS due to interfering components such as enzymes and proteins in saliva samples.

4. Conclusions

We successfully synthesized a fluorescent kynurenine conjugate based on rhodamine B with unique antibody binding properties, a promising component of a future rapid diagnostic test for kynurenine, a metabolite with a clinically relevant marker for the diagnosis of distinct diseases. Spectral properties of the products were elucidated, showing only a slight shift of 6 nm in the fluorescence emission maximum when compared to native rhodamine B. The antibody binding was investigated, and the magnetic bead assay showed a good sensitivity with a K_D -value of 5.9 μM for the L-kynurenine conjugate 5 and IC50 values of 4.0 μM in PBS and 10.2 μM in saliva for the competitive assay. Since an increase in kynurenine levels in saliva to $4.6 \pm 1.6 \mu\text{M}$ under pathological conditions, compared to $0.7 \pm 0.4 \mu\text{M}$ in the healthy subject, are observed [30], it thus is possible to detect metabolite changes with statistical significance by using repeated measurements. This allows for the detection of transplant rejection in a clinical setting subject to validation in clinical trials. In addition, this approach offers the possibility of using other body fluids such as blood serum, where kynurenine levels are much higher with $17.4 \pm 8.4 \mu\text{M}$ for serum compared to $4.6 \pm 1.6 \mu\text{M}$ for saliva [30], even though the influence of matrix proteins and other metabolites from serum would have to be investigated in more detail for this to obtain reliable measurements. Since the current standard methods for kynurenine detection are based on liquid chromatography, they are not practical for routine diagnostics; likewise, no clinically applied functional bioassay based on antibody binding of kynurenine exists. Together, our investigations provide a promising approach towards future rapid tests for kynurenine. Here, we introduced a microbead competitive assay allowing for the determination of L-kynurenine metabolites directly from saliva, thus avoiding the use of invasive procedures and expensive equipment.

Author Contributions: Conceptualization, H.-P.D.; methodology, M.B. and I.Q.; investigation, M.B. and I.Q.; resources, H.-P.D. and R.C.; data curation, M.B. and I.Q.; writing—original draft preparation, M.B. and I.Q.; writing—review and editing, M.B., I.Q., L.K. and H.-P.D.; visualization, M.B., I.Q. and L.K.; supervision, H.-P.D.; project administration, H.-P.D.; funding acquisition, H.-P.D. All authors have read and agreed to the published version of the manuscript.

Funding: This research was funded by the Ministry of Economics, Labor and Housing Baden-Württemberg, Germany, TechPat nano, grant number 35-4223.10/10 and by the Federal Ministry for Economic Affairs and Climate Action, Germany, InfektResonator, IGF-grant number 20934 N. The article processing charge was funded by the Baden-Württemberg Ministry of Science, Research and Culture and the Furtwangen University in the funding program Open Access Publishing.

Institutional Review Board Statement: Not applicable.

Informed Consent Statement: Not applicable.

Data Availability Statement: Not applicable.

Acknowledgments: We thank Doris Benz-Schreger for her tremendous and continuous support.

Conflicts of Interest: The authors declare no conflict of interest. The funders had no role in the design of the study; in the collection, analyses, or interpretation of data; in the writing of the manuscript; or in the decision to publish the results.

References

1. Adams, S.; Teo, C.; McDonald, K.L.; Zinger, A.; Bustamante, S.; Lim, C.K.; Sundaram, G.; Braidy, N.; Brew, B.J.; Guillemin, G.J. Involvement of the Kynurenine Pathway in Human Glioma Pathophysiology. *PLoS ONE* **2014**, *9*, e112945. [[CrossRef](#)] [[PubMed](#)]
2. Cervenka, I.; Agudelo, L.Z.; Ruas, J.L. Kynurenines: Tryptophan's Metabolites in Exercise, Inflammation, and Mental Health. *Science* **2017**, *357*, eaaf9794. [[CrossRef](#)] [[PubMed](#)]
3. Dantzer, R. Role of the Kynurenine Metabolism Pathway in Inflammation-Induced Depression—Preclinical Approaches. *Curr. Top. Behav. Neurosci.* **2017**, *31*, 117. [[CrossRef](#)] [[PubMed](#)]

4. Badawy, A.A.-B. Kynurenine Pathway of Tryptophan Metabolism: Regulatory and Functional Aspects. *Int. J. Tryptophan Res.* **2017**, *10*. [[CrossRef](#)]
5. Badawy, A.A.-B. Tryptophan Metabolism in Alcoholism. *Nutr. Res. Rev.* **2002**, *15*, 123–152. [[CrossRef](#)]
6. Bender, D.A. Biochemistry of Tryptophan in Health and Disease. *Mol. Asp. Med.* **1983**, *6*, 101–197. [[CrossRef](#)]
7. Ball, H.J.; Yuasa, H.J.; Austin, C.J.; Weiser, S.; Hunt, N.H. Indoleamine 2,3-Dioxygenase-2; a New Enzyme in the Kynurenine Pathway. *Int. J. Biochem. Cell Biol.* **2009**, *41*, 467–471. [[CrossRef](#)]
8. Stone, T.W.; Stoy, N.; Darlington, L.G. An Expanding Range of Targets for Kynurenine Metabolites of Tryptophan. *Trends Pharmacol. Sci.* **2013**, *34*, 136–143. [[CrossRef](#)]
9. Fujigaki, S.; Saito, K.; Sekikawa, K.; Tone, S.; Takikawa, O.; Fujii, H.; Wada, H.; Noma, A.; Seishima, M. Lipopolysaccharide Induction of Indoleamine 2,3-Dioxygenase Is Mediated Dominantly by an IFN- γ -Independent Mechanism. *Eur. J. Immunol.* **2001**, *31*, 2313–2318. [[CrossRef](#)]
10. Divanovic, S.; Sawtell, N.M.; Trompette, A.; Warning, J.I.; Dias, A.; Cooper, A.M.; Yap, G.S.; Arditi, M.; Shimada, K.; DuHadaway, J.B.; et al. Opposing Biological Functions of Tryptophan Catabolizing Enzymes During Intracellular Infection. *J. Infect. Dis.* **2012**, *205*, 152–161. [[CrossRef](#)]
11. Suzuki, Y.; Suda, T.; Asada, K.; Miwa, S.; Suzuki, M.; Fujie, M.; Furuhashi, K.; Nakamura, Y.; Inui, N.; Shirai, T.; et al. Serum Indoleamine 2,3-Dioxygenase Activity Predicts Prognosis of Pulmonary Tuberculosis. *Clin. Vaccine Immunol.* **2012**, *19*, 436–442. [[CrossRef](#)] [[PubMed](#)]
12. Taylor, M.W.; Feng, G. Relationship between Interferon-Gamma, Indoleamine 2,3-Dioxygenase, and Tryptophan Catabolism. *FASEB J. Off. Publ. Fed. Am. Soc. Exp. Biol.* **1991**, *5*, 2516–2522. [[CrossRef](#)]
13. Hassanain, H.H.; Chon, S.; Gupta, S.L. Differential Regulation of Human Indoleamine 2,3-Dioxygenase Gene Expression by Interferons-Gamma and -Alpha. Analysis of the Regulatory Region of the Gene and Identification of an Interferon-Gamma-Inducible DNA-Binding Factor. *J. Biol. Chem.* **1993**, *268*, 5077–5084. [[CrossRef](#)]
14. Babcock, T.A.; Carlin, J.M. Transcriptional Activation of Indoleamine Dioxygenase by Interleukin 1 and Tumor Necrosis Factor α in Interferon-Treated Epithelial Cells. *Cytokine* **2000**, *12*, 588–594. [[CrossRef](#)]
15. Fallarino, F.; Grohmann, U.; Vacca, C.; Bianchi, R.; Orabona, C.; Spreca, A.; Fioretti, M.C.; Puccetti, P. T Cell Apoptosis by Tryptophan Catabolism. *Cell Death Differ.* **2002**, *9*, 1069–1077. [[CrossRef](#)]
16. Hill, M.; Tanguy-Royer, S.; Royer, P.; Chauveau, C.; Asghar, K.; Tesson, L.; Lavainne, F.; Rémy, S.; Brion, R.; Hubert, F.X.; et al. IDO Expands Human CD4⁺CD25^{high} Regulatory T Cells by Promoting Maturation of LPS-Treated Dendritic Cells. *Eur. J. Immunol.* **2007**, *37*, 3054–3062. [[CrossRef](#)]
17. Mellor, A.L.; Munn, D.H. IDO Expression by Dendritic Cells: Tolerance and Tryptophan Catabolism. *Nat. Rev. Immunol.* **2004**, *4*, 762–774. [[CrossRef](#)]
18. Wood, K.J.; Sawitzki, B. Interferon γ : A Crucial Role in the Function of Induced Regulatory T Cells in Vivo. *Trends Immunol.* **2006**, *27*, 183–187. [[CrossRef](#)]
19. Schefold, J.C.; Zeden, J.-P.; Fotopoulou, C.; von Haehling, S.; Pchowski, R.; Hasper, D.; Volk, H.-D.; Schuett, C.; Reinke, P. Increased Indoleamine 2,3-Dioxygenase (IDO) Activity and Elevated Serum Levels of Tryptophan Catabolites in Patients with Chronic Kidney Disease: A Possible Link between Chronic Inflammation and Uraemic Symptoms. *Nephrol. Dial. Transplant.* **2009**, *24*, 1901–1908. [[CrossRef](#)]
20. Bao, Y.-S.; Ji, Y.; Zhao, S.-L.; Ma, L.-L.; Xie, R.-J.; Na, S.-P. Serum Levels and Activity of Indoleamine 2,3-Dioxygenase and Tryptophanyl-TRNA Synthetase and Their Association with Disease Severity in Patients with Chronic Kidney Disease. *Biomarkers* **2013**, *18*, 379–385. [[CrossRef](#)]
21. Gagnebin, Y.; Jaques, D.A.; Rudaz, S.; de Seigneux, S.; Boccard, J.; Ponte, B. Exploring Blood Alterations in Chronic Kidney Disease and Haemodialysis Using Metabolomics. *Sci. Rep.* **2020**, *10*, 19502. [[CrossRef](#)] [[PubMed](#)]
22. Konje, V.C.; Rajendiran, T.M.; Bellovich, K.; Gadegbeku, C.A.; Gipson, D.S.; Afshinnia, F.; Mathew, A.V. Tryptophan Levels Associate with Incident Cardiovascular Disease in Chronic Kidney Disease. *Clin. Kidney J.* **2021**, *14*, 1097–1105. [[CrossRef](#)] [[PubMed](#)]
23. Marzinzig, M. Dynamics and Diagnostic Relevance of Kynurenine Serum Level after Kidney Transplantation. *Ann. Transplant.* **2015**, *20*, 327–337. [[CrossRef](#)] [[PubMed](#)]
24. Lahdou, I.; Sadeghi, M.; Daniel, V.; Schenk, M.; Renner, F.; Weimer, R.; Löb, S.; Schmidt, J.; Mehrabi, A.; Schnitzler, P.; et al. Increased Pretransplantation Plasma Kynurenine Levels Do Not Protect from but Predict Acute Kidney Allograft Rejection. *Hum. Immunol.* **2010**, *71*, 1067–1072. [[CrossRef](#)] [[PubMed](#)]
25. Buczko, P.; Tankiewicz-Kwedlo, A.; Buraczewska, A.; Mysliwiec, M.; Pawlak, D. Accumulation of Kynurenine Pathway Metabolites in Saliva and Plasma of Uremic Patients Accumulation of Kynurenine Pathway Metabolites in Saliva and Plasma of Uremic Patients. *Pharmacol. Rep.* **2007**, *59*, 199–204.
26. Debnath, S.; Velagapudi, C.; Redus, L.; Thameem, F.; Kasinath, B.; Hura, C.E.; Lorenzo, C.; Abboud, H.E.; O'Connor, J.C. Tryptophan Metabolism in Patients With Chronic Kidney Disease Secondary to Type 2 Diabetes: Relationship to Inflammatory Markers. *Int. J. Tryptophan Res.* **2017**, *10*, 1178646917694600. [[CrossRef](#)]
27. Lee, H.; Jang, H.B.; Yoo, M.G.; Park, S.I.; Lee, H.J. Amino Acid Metabolites Associated with Chronic Kidney Disease: An Eight-Year Follow-Up Korean Epidemiology Study. *Biomedicines* **2020**, *8*, 222. [[CrossRef](#)]

28. Brandacher, G.; Cakar, F.; Winkler, C.; Schneeberger, S.; Obrist, P.; Bösmüller, C.; Werner-Felmayer, G.; Werner, E.R.; Bonatti, H.; Margreiter, R.; et al. Non-Invasive Monitoring of Kidney Allograft Rejection through IDO Metabolism Evaluation. *Kidney Int.* **2007**, *71*, 60–67. [[CrossRef](#)]
29. Holmes, E.W.; Russell, P.M.; Kinzler, G.J.; Reckard, C.R.; Flanigan, R.C.; Thompson, K.D.; Bermes, E.W. Oxidative Tryptophan Metabolism in Renal Allograft Recipients: Increased Kynurenine Synthesis Is Associated with Inflammation and OKT3 Therapy. *Cytokine* **1992**, *4*, 205–213. [[CrossRef](#)]
30. Kaden, J.; Abendroth, D.; Marzinzig, M.; May, G. Untersuchungen Zur Dynamik Der Indolamin 2,3-Dioxygenase Bei Patienten Mit Unterschiedlichen Verläufen Nach Nierentransplantation. *Transplant. Organ Dtsch. Transplant.* **2007**, *19*, 110–116.
31. Merino, J.J.; Cabaña-Muñoz, M.E.; Gasca, A.T.; Garcimartín, A.; Benedí, J.; Camacho-Alonso, F.; Parmigiani-Izquierdo, J.M. Elevated Systemic L-Kynurenine/L-Tryptophan Ratio and Increased IL-1 Beta and Chemokine (CX3CL1, MCP-1) Proinflammatory Mediators in Patients with Long-Term Titanium Dental Implants. *J. Clin. Med.* **2019**, *8*, 1368. [[CrossRef](#)] [[PubMed](#)]
32. Clendenen, N.; Cornwell, W.; Pal, J.; Weitzel, N. Acute Metabolomic Changes after Implantation of a Left Ventricular Assist Device. *J. Heart Lung Transplant.* **2019**, *38*, S245. [[CrossRef](#)]
33. Linderholm, K.R.; Skogh, E.; Olsson, S.K.; Dahl, M.-L.; Holtze, M.; Engberg, G.; Samuelsson, M.; Erhardt, S. Increased Levels of Kynurenine and Kynurenic Acid in the CSF of Patients With Schizophrenia. *Schizophr. Bull.* **2012**, *38*, 426–432. [[CrossRef](#)] [[PubMed](#)]
34. Flieger, J.; Świącz-Zubilewicz, A.; Śniegocki, T.; Dolar-Szczasny, J.; Pizoń, M. Determination of Tryptophan and Its Major Metabolites in Fluid from the Anterior Chamber of the Eye in Diabetic Patients with Cataract by Liquid Chromatography Mass Spectrometry (LC-MS/MS). *Molecules* **2018**, *23*, 3012. [[CrossRef](#)] [[PubMed](#)]
35. Sundaram, G.; Brew, B.J.; Jones, S.P.; Adams, S.; Lim, C.K.; Guillemain, G.J. Quinolinic Acid Toxicity on Oligodendroglial Cells: Relevance for Multiple Sclerosis and Therapeutic Strategies. *J. Neuroinflamm.* **2014**, *11*, 204. [[CrossRef](#)]
36. Notarangelo, F.M.; Wu, H.Q.; Macherone, A.; Graham, D.R.; Schwarcz, R. Gas Chromatography/Tandem Mass Spectrometry Detection of Extracellular Kynurenine and Related Metabolites in Normal and Lesioned Rat Brain. *Anal. Biochem.* **2012**, *421*, 573–581. [[CrossRef](#)]
37. Ungor, D.; Horváth, K.; Dékány, I.; Csapó, E. Red-Emitting Gold Nanoclusters for Rapid Fluorescence Sensing of Tryptophan Metabolites. *Sens. Actuators B Chem.* **2019**, *288*, 728–733. [[CrossRef](#)]
38. Klockow, J.L.; Glass, T.E. Development of a Fluorescent Chemosensor for the Detection of Kynurenine. *Org. Lett.* **2013**, *15*, 235–237. [[CrossRef](#)]
39. Seegers, N.; van Doornmalen, A.M.; Uitdehaag, J.C.M.; de Man, J.; Buijsman, R.C.; Zaman, G.J.R. High-Throughput Fluorescence-Based Screening Assays for Tryptophan-Catabolizing Enzymes. *SLAS Discov. Adv. Sci. Drug Discov.* **2014**, *19*, 1266–1274. [[CrossRef](#)]
40. Mahou, R.; Wandrey, C. Versatile Route to Synthesize Heterobifunctional Poly(Ethylene Glycol) of Variable Functionality for Subsequent Pegylation. *Polymers* **2012**, *4*, 561–589. [[CrossRef](#)]
41. Niskanen, J.; Karesoja, M.; Aseyev, V.; Qiu, X.-P.; Winnik, F.M.; Tenhu, H. Thermal Response of a PVCL-HA Conjugate. *J. Polym. Sci. Part A Polym. Chem.* **2016**, *54*, 425–436. [[CrossRef](#)]
42. Helttunen, K.; Prus, P.; Luostarinen, M.; Nissinen, M. Interaction of Aminomethylated Resorcinarenes with Rhodamine B. *New J. Chem.* **2009**, *33*, 1148. [[CrossRef](#)]

Lebenslauf

Persönliche Daten

Name: Max Borgolte

Geburtsdatum: 23.03.1992

Geburtsort: Holzminden

Staatsangehörigkeit: deutsch

Berufslaufbahn

seit 07/2017 Wissenschaftlicher Mitarbeiter an der Fakultät Medical and Life Sciences, Institute of Precision Medicine in der Arbeitsgruppe von Herrn Prof. Hans-Peter Deigner

Bildungsweg

seit 07/2021 Promotionsstudium am Institut für Chemie im Bereich Organische Chemie, Martin-Luther-Universität Halle-Wittenberg unter Leitung von Herrn Prof. René Csuk

10/2013 - 02/2016 Master of Science (M. Sc.) Chemie, Universität Stuttgart, Masterarbeit am Institut für Biochemie unter Leitung von Herrn Prof. Albert Jeltsch

10/2010 – 09/2013 Bachelor of Science (B. Sc.) Chemie, Universität Paderborn, Bachelorarbeit am Institut für Organische Chemie unter Leitung von Herrn Prof. René Wilhelm

06/2010 Fachhochschulreife, Fachoberschule Wirtschaft und Verwaltung, Georg-von-Langen-Schule Holzminden

Publikationsliste

Erstautor

„Synthesis of a biocompatible benzophenone-substituted chitosan hydrogel as novel coating for PEEK with extraordinary strong antibacterial and anti-biofilm properties“

Borgolte, M.; Riester, O.; Quint, I.; Blendinger, F.; Bucher, V.; Laufer, S.; Csuk, R.; Scotti, L.; Deigner H.-P. *Mater. Today Chem.* **2022**, 26, 101176.

„A Fluorescence-Based Competitive Antibody Binding Assay for Kynurenine, a Potential Biomarker of Kidney Transplant Failure“

Borgolte, M.; Quint, I.; Kaiser, L.; Csuk, R.; Deigner, H.-P. *Diagnostics* **2022**, 12, 1380.

„Methacryloyl-GlcNAc Derivatives Copolymerized with Dimethacrylamide as a Novel Antibacterial and Biocompatible Coating“

Borgolte, M.; Riester, O.; Kacerova, T.; Rentschler, S.; Schmidt, M.S.; Jacksch, S.; Egert, M.; Laufer, S.; Csuk, R.; Deigner, H.-P. *Pharmaceutics* **2021**, 13, 1647.

Co-Autor

„Challenges in Bone Tissue Regeneration: Stem Cell Therapy, Biofunctionality and Antimicrobial Properties of Novel Materials and Its Evolution.“

Riester, O.; **Borgolte, M.**; Csuk, R.; Deigner, H.P. *Int. J. Mol. Sci.* 2021, 22, 1–25.

Erklärung über den Autorenanteil

Publikation 1: „**Synthesis of a biocompatible benzophenone-substituted chitosan hydrogel as novel coating for PEEK with extraordinary strong antibacterial and anti-biofilm properties**“

Borgolte, M.; Riester, O.; Kacerova, T.; Rentschler, S.; Schmidt, M.S.; Jacksch, S.; Egert, M.; Laufer, S.; Csuk, R.; Deigner, H.-P. *Pharmaceutics* **2021**, *13*, 1647.

Der Großteil der Synthese der Polymere und deren Vorstufen sowie die Auswertung der zugehörigen analytischen Daten wurden von mir durchgeführt. Ein Teil der Polymersynthesen wurde von Tereza Kacerova im Rahmen ihres Forschungspraktikums durchgeführt. NMR Messungen erfolgten zum Teil seitens R. Csuk, die Auswertung der Daten wurde von mir durchgeführt. Die Beschichtung der Oberflächen und die Auswertung der Messdaten (IR, SEM, AFM) wurden von mir durchgeführt. Die Experimente zur Biokompatibilität und die zugehörige Datenauswertung wurde von mir durchgeführt. Die Experimente zur antimikrobiellen Aktivität der Polymere wurden von O. Riester durchgeführt. Die Betreuung hinsichtlich praktischer und theoretischer Aspekte erfolgte durch R. Csuk und H.-P. Deigner.

Publikation 2: „**A Fluorescence-Based Competitive Antibody Binding Assay for Kynurenine, a Potential Biomarker of Kidney Transplant Failure**“

Borgolte, M.; Quint, I.; Kaiser, L.; Csuk, R.; Deigner, H.-P. *Diagnostics* **2022**, *12*, 1380.

Die chemische Synthese und die chemische Charakterisierung der Verbindungen wurden von mir durchgeführt. NMR Messungen erfolgten seitens R. Csuk, wobei die Auswertung der Daten von mir durchgeführt wurde. Die Arbeiten zur Antikörperbindung und IC50 Werten sowie deren Auswertung erfolgte von I. Quint. R. Csuk und H.-P. Deigner betreuten die praktischen und theoretischen Aspekte der Arbeit.

Publikation 3: „**Synthesis of a biocompatible benzophenone-substituted chitosan hydrogel as novel coating for PEEK with extraordinary strong antibacterial and anti-biofilm properties**“

Borgolte, M.; Riester, O.; Quint, I.; Blendinger, F.; Bucher, V.; Laufer, S.; Csuk, R.; Scotti, L.; Deigner H.-P. *Mater. Today Chem.* **2022**, *26*, 101176.

Die chemische Synthese und Charakterisierung der Benzophenon-Chitosan Derivate wurde von mir durchgeführt, ebenso die Beschichtung der Oberflächen und die Auswertung der zugehörigen Daten. Die Auswertung der Oberflächencharakterisierung (IR, XPS, SEM-EDS, SEM, AFM, etc.) wurde von mir durchgeführt. Die NMR Messungen erfolgten seitens R. Csuk, die Auswertung der Daten wurde von mir durchgeführt. Die Experimente zur Biokompatibilität und die zugehörige Datenauswertung wurden ebenso von mir durchgeführt. Die Experimente zur antimikrobiellen Aktivität und die Auswertung der Daten wurden von O. Riester durchgeführt. R. Csuk und H.-P. Degner betreuten die theoretischen und praktischen Aspekte der Arbeit.

Selbstständigkeitserklärung

Hiermit versichere ich, dass ich die vorliegende Arbeit selbständig und nur mit den angegebenen Hilfsmitteln angefertigt habe, und dass ich alle Stellen, die dem Wortlaut oder dem Sinn nach anderen Werken, auch elektronischen Medien, entnommen sind, durch Angabe der Quellen als Entlehnung kenntlich gemacht habe.

Villingen-Schwenningen, den 13. März 2023

Max Borgolte
